

# **Thermal and Photo Stability of Tungsten Polyoxometalate-surfactant Hybrid Compounds**

Aaron Victor Colusso  
Doctor of Philosophy

University of Technology Sydney  
Faculty of Science

2018

## **Certificate of original authorship**

I, Aaron Victor Colusso declare that this thesis is submitted in fulfilment of the requirements for the award of Doctor of Philosophy, in the Faculty of Science at the University of Technology Sydney.

This thesis is wholly my own work unless otherwise referenced or acknowledged. In addition, I certify that all information sources and literature used are indicated in the thesis. This document has not been submitted for qualifications at any other academic institution. This research is supported by a UTS Doctoral Scholarship from the Graduate Research School and by an Australian Government Research Training Program Scholarship.

Signature:

Production Note:  
Signature removed prior to publication.

Date: 18/10/2018

## Acknowledgements

There have been many individuals that have helped me through my journey to complete my PhD, without whom the work presented in this thesis would be of a much lower standard, or absent. First and foremost, I would like to thank my supervisors, Prof Michael Cortie and A/Prof Andrew McDonagh, who have provided me a solid foundation from which I can hypothesize and experiment. Their continued support and interest in my work, from the first day of my Honours year to today, has kept me motivated and inspired with my research. The many conversations shared over numerous coffees have always been thoroughly appreciated and have allowed me to form relationships with them and other colleagues beyond the merely professional.

I would also like to thank many members of the Science Faculty- without their contributions many experiments would have otherwise been impossible. In particular I would like to thank Dr Ronald Shimmon, who always made sure that I had the capacity to perform my experiments or pointed me towards someone who could help. A big thank you to Dr Angus Gentle, who has continually been a reliable source of expertise when it comes to experimental design and set-up. Mr Alex Angeloski has also always been able to aid me with the completion of many experiments, despite his mutual position as a fellow busy PhD student. The imaging expertise of Dr Annette Dowd has also immensely aided my PhD, and all of my papers would not be what they are without her TEM images. I am also very grateful to the Australian Synchrotron for the provision of beam time. Thanks especially go to beam line scientist Dr Justin Kimpton and his team.

Many of my fellow students have also provided me with support throughout this journey, including Mr Chris Elbadawi, Mr Daniel Pasin, Ms Maryna Bilokur, Mr Marc Gali Labarias and Ms Alba Garcia. Whether it be lending their brain and specific expertise to solve a particular research puzzle, or just being a sympathetic ear in which to direct frustrations, their presence has been thoroughly appreciated.

Last, but not least, I would like to thank my parents and extended family for their continued support through my many years of education, without whom I could not have even started this PhD. They have always pushed me to excel in the field of my choosing and have made sure that I have the capacity to be the best scientist I can be. My beautiful fiancé Fumie, that I met whilst completing my PhD, has also been a source of strength and motivation. She has given me great cause to excel just beyond the mere desires of individual pursuits.

## **Thesis Overview**

Each chapter of this Thesis contains an individual topic investigated and described in detail. Chapters 3 to 6 contain theory specific to the topic being discussed within it, followed by experimental results, analysis and conclusions. In this way, each chapter is able stand alone as an individual piece of work. A list of my publications related to the work covered in this thesis follows this statement, which is then followed by a statement regarding the contribution of the authors listed in them. A complete List of Abbreviations and Symbols used in this work is also provided, along with a Table of Contents and a List of Figures and Tables for ease of navigation. An Abstract of my completed work is given before the chapters are listed in sequence, from 1 through to 7. Chapter 1 gives a brief, general introduction on the topic of polyoxometalates. Chapter 2 contains the methods and materials employed to complete my PhD. Chapters 3 to 6 contain the specific topics of my project, which will be generically introduced in Chapter 1. Chapter 7 contains general conclusions of this work, as well as some ideas for possible future work. All references used to study and support the content of my PhD are presented in the Bibliography at the end of this thesis.

## List of Publications

### 1<sup>st</sup> Publication

Colusso, A. Cortie, M. Dowd, A. McDonagh, A., Thermal stability of mesoscopic compounds of cetyltrimethylammonium and Keggin metatungstates. *Dalton Trans.* **2017**, 46, 11053–11062.<sup>1</sup>

### 2<sup>nd</sup> Publication

Colusso, A. McDonagh, A. Gentle, A. Cortie, M., Photomechanical photochromism in a cetyltrimethylammonium isopolytungstate. *RSC Adv.* **2018**, 8, 18776-18783.<sup>2</sup>

### 3<sup>rd</sup> Publication

Colusso, A. McDonagh, A. Gentle, A. Cortie, M., X-ray induced reduction of a surfactant/polyoxotungstate hybrid compound, **2018**, DOI: 10.1002/sia.6516.<sup>3</sup>

In all of my publications, my principal supervisor M. Cortie and co-supervisor A. McDonagh aided me with the sequence of sections and arguments in the paper and overall construction. Help in the interpretation of data was also given, with M. Cortie helping me mainly with problems regarding x-ray diffraction and materials science, and A. McDonagh with problems regarding chemistry. Direction regarding the best way to visualize data in appropriate figures was also given by both supervisors.

Contributors to my first publication other than myself and my supervisors include A. Dowd who collected the transmission electron micrographs displayed within.

Contributors to my second publication other than myself include my supervisors and A. Gentle who aided with the design and set-up of the photochromic hysteresis study.

There are no additional contributors, apart from my supervisors, to my third publication.

# Table of Contents

<b>Thermal and Photo Stability of Tungsten Polyoxometalate-surfactant Hybrid Compounds</b> .....	i
<b>Certificate of original authorship</b> .....	ii
<b>Acknowledgements</b> .....	iii
<b>Thesis Overview</b> .....	iv
<b>List of Publications</b> .....	v
<b>1<sup>st</sup> Publication</b> .....	v
<b>2<sup>nd</sup> Publication</b> .....	v
<b>Table of Contents</b> .....	vi
<b>List of Abbreviations and Symbols</b> .....	x
<b>List of Abbreviations</b> .....	x
<b>List of Symbols</b> .....	xi
<b>List of Figures</b> .....	xiii
<b>List of Tables</b> .....	xix
<b>Abstract</b> .....	xxi
<b>Chapter 1. Introduction</b> .....	1
<b>1.1 Structure and nomenclature of common transition-metal oxo-anion clusters</b> .....	1
<b>1.2 A brief review of polyoxometalate properties and current and possible applications</b> .....	8
<b>1.3 Surfactant-polyoxometalate hybrid compounds</b> .....	10
<b>1.4 Thermal Stability of surfactant-polyoxometalate structures</b> .....	13
<b>1.5 Introduction to photochromism</b> .....	14
<b>1.6 Photochromic quality and the photochromic cycle</b> .....	16
<b>1.7 <i>In situ</i> photo-reduction of TMO-hybrids during X-ray-based measurements</b> .....	17
<b>1.8 Chapter overviews</b> .....	18
<b>Chapter 2. Methods and Materials</b> .....	20
<b>2.1 Chemical synthesis</b> .....	20
<b>2.1.1 Synthesis of CTA-W<sub>12</sub></b> .....	20
<b>2.1.2 Synthesis of CTA-WO<sub>3</sub></b> .....	22
<b>2.1.3 Soxhlet extraction</b> .....	23
<b>2.2 Characterization techniques</b> .....	24
<b>2.2.1 Powder X-ray diffraction</b> .....	24
<b>2.2.2 UV-visible spectroscopy</b> .....	27

2.2.3 Scanning electron microscopy.....	28
2.2.4 Transmission electron microscopy .....	29
2.2.5 X-ray photoelectron spectroscopy .....	29
2.2.6 Infrared and Fourier transform infrared spectroscopy .....	30
2.2.7 Raman spectroscopy .....	32
2.2.8 Thermogravimetric analysis and differential thermal analysis.....	33
2.2.9 Nuclear magnetic resonance spectroscopy.....	34
2.2.10 Microanalysis/combustion analysis .....	35
2.2.11 CTA-W <sub>12</sub> photochromism investigation.....	35
2.2.12 Hysteresis study.....	36
2.2.13 Gas chromatography-mass spectrometry .....	37
<b>Chapter 3. Synthesis of CTA-W<sub>12</sub>.....</b>	<b>39</b>
3.1 Background Theory .....	39
3.1.1 Aqueous tungstate equilibria .....	39
3.1.2 Tungstate-quaternary ammonium equilibria and Keggin cluster formation.....	41
3.1.3 Surfactant-polyoxometalate chemistry .....	43
3.1.4 Surfactant-polyoxometalate packing.....	44
3.1.5 The SEP lamellar phase and the 1:4 ratio .....	48
3.1.6 Solvent effects .....	53
3.2 Synthesis of CTA-W <sub>12</sub> .....	55
3.2.1 Characterization of CTA-W <sub>12</sub> .....	55
3.2.2 Synthesis and characterization of layered tungsten hydroxides .....	59
3.2.3 Synthesis of other tungstate-CTA compounds .....	66
3.2.4 CTA-tungstate products from high pH solutions.....	77
3.3 Tungstate-CTA <sup>+</sup> solution dynamics.....	78
3.3.1 Tungstate-CTA equilibria .....	78
3.3.2 Conversion of CTA-WO <sub>3</sub> to CTA-W <sub>12</sub> .....	79
3.4 Structural characterization of CTA-W <sub>12</sub> .....	82
3.4.1 P-XRD, SEM and TEM of CTA-W <sub>12</sub> .....	83
3.4.2 Hyper-digitation of CTA-W <sub>12</sub> .....	86
3.5 Conclusions: surfactant-mediated aqueous synthesis of Keggin polytungstates.....	87
<b>Chapter 4. Thermal Stability and Decomposition of Surfactant-Polyoxometalate Frameworks</b>	
.....	89

4.1 Background Theory .....	89
4.1.1 Calcination of surfactant-metal-oxide precursors .....	89
4.1.2 Thermal stability of organic spacers including alkyl-ammonium surfactants .....	92
4.1.3 Keggin fragmentation .....	95
4.1.4 Crystallographic phases of $WO_x$ .....	99
4.1.5 Hexagonal tungsten oxides .....	103
4.2 Thermal decomposition of CTA-Br .....	106
4.3 Thermal decomposition of CTA- $W_{12}$ .....	109
4.3.1 Dehydration and expansion – phases I - III.....	109
4.3.2 Lamellar decomposition – phase IV .....	113
4.3.3 Keggin fragmentation and adoption of HCP structure – phase V.....	115
4.3.4 Bulk-oxide formation .....	119
4.3.5 Effect of environment on CTA- $W_{12}$ thermal decomposition.....	121
4.4 Thermal Decomposition of CTA- $WO_3$ .....	123
4.4.1 Lamellar phases of CTA- $WO_3$ , phases I – III.....	124
4.4.2 Lamellar decomposition and bulk-oxide formation.....	127
4.4.3 Effect of environment .....	128
4.4.4 Comparison to CTA- $W_{12}$ thermal decomposition.....	129
4.5 Phase V (CTA- $W_{12}$ thermal decomposition intermediate).....	132
4.5.1 Soxhlet extraction.....	134
4.5.2 Analysis of fractions.....	136
4.5.3 Characterization of fractions .....	145
4.6 Conclusion: Formation of $WO_x$ from the thermal decomposition of CTA- $W_{12}$ .....	147
Chapter 5. Photochromism of Quaternary Alkyl-Ammonium Polyoxometalate Hybrids .....	150
5.1 Background Theory .....	150
5.1.1 Structure of the Keggin anion.....	150
5.1.2 Band-gap structure of the Keggin anion.....	152
5.1.3 Electronic structure of the Keggin anion .....	154
5.1.4 Photochromism of POM materials .....	156
5.1.5 Photocatalysis of POMs .....	159
5.1.6 Photochromism of quaternary-ammonium POM hybrids.....	162
5.2 Photochromism of CTA- $W_{12}$ .....	165
5.2.1 Colouration of CTA- $W_{12}$ in alcohols .....	165
5.2.2 Colouration of CTA- $W_{12}$ in air .....	167

5.2.3 XPS of CTA-W <sub>12</sub> .....	170
<b>5.3 Reversibility of CTA-W<sub>12</sub> photochromism .....</b>	<b>172</b>
5.3.1 Hysteresis study of CTA-W <sub>12</sub> photochromism .....	173
5.3.2 Chemical changes to CTA-W <sub>12</sub> during photochromism .....	174
5.3.3 Long-lived W <sup>5+/4+</sup> sites.....	180
5.3.4 Products of CTA-W <sub>12</sub> photochromism.....	182
<b>5.4 Structural changes during CTA-W<sub>12</sub> photochromism.....</b>	<b>185</b>
5.4.1 CTA-W <sub>12</sub> photo-decomposition.....	185
5.4.2 Lattice expansion and contraction during photochromism .....	188
<b>5.5 Conclusion: Photochromism of quaternary-ammonium polytungstate hybrids.....</b>	<b>191</b>
<b>Chapter 6. Photochromic Reduction During XPS Measurements .....</b>	<b>193</b>
6.1 Background theory .....	193
6.1.1 X-ray/Matter interactions .....	193
6.1.2 Measurement induced x-ray damage .....	195
6.1.3 Photoreduction during x-ray measurements .....	198
6.1.4 X-ray photoreduction of organic-inorganic hybrids.....	200
6.2 XPS-induced reduction of CTA-W <sub>12</sub> .....	202
6.2.1 W4f core-level spectra during XPS induced reduction.....	203
6.2.2 Kinetics of XPS induced reduction.....	206
6.2.3 Binding Energy of W oxidation-states during XPS induced reduction.....	207
6.3.1 Probable causes of XPS induced Reduction .....	209
6.4.1 Conclusions: XPS measurements of metal-oxide based inorganic-organic hybrids ...	210
<b>Chapter 7. Conclusions and prospective future work .....</b>	<b>212</b>
7.1. Conclusions.....	212
7.2. Future Work.....	216
<b>References.....</b>	<b>217</b>

# List of Abbreviations and Symbols

## List of Abbreviations

ATR	Attenuated total reflectance
CD	Conduction-band
CIF	Crystallographic Information File
CT	Charge-transfer
CTA <sup>+</sup>	Cetyltrimethylammonium cation, C <sub>16</sub> H <sub>33</sub> N(CH <sub>3</sub> ) <sub>3</sub> <sup>+</sup>
CTA-W <sub>12</sub>	Studied surfactant-polyoxometalate material, (C <sub>19</sub> H <sub>42</sub> N) <sub>7</sub> Cl.[H <sub>2</sub> W <sub>12</sub> O <sub>40</sub> ].2H <sub>2</sub> O
CTA-WO <sub>3</sub>	Studied surfactant-tungsten oxide material, (CTA).6[WO <sub>3</sub> ].7H <sub>2</sub> O
DODA <sup>+</sup>	Dimethyldioctadecylammonium cation, (C <sub>18</sub> H <sub>37</sub> ) <sub>2</sub> N(CH <sub>3</sub> ) <sub>2</sub> <sup>+</sup>
DNA	Deoxyribonucleic acid
DTA	Differential thermal analysis
DTG	Differential thermogravimetric
EDX	Energy-dispersive X-ray
EtOH	Ethanol
FT-IR	Fourier-transform infrared
GC	Gas chromatography
GC-MS	Gas chromatography-mass spectrometry
HATB	Hexagonal ammonium tungsten bronze
HTB	Hexagonal tungsten bronze
HCP	Hexagonal-close-packed
HOMO	Highest occupied molecular orbital
ICDD	International Centre for Diffraction Data
IR	Infrared
IVCT	Inter-valence charge-transfer
JCPDF	Joint Committee on Powder Diffraction File
L→M	Ligand-to-metal
LMCT	Ligand-to-metal charge-transfer
LUMO	Lowest unoccupied molecular orbital
MeOH	Methanol
MS	Mass spectrometry
MCM	Mobil Composition of Matter

NIR	Near-infrared
NMR	Nuclear magnetic resonance
O→M	Oxygen-to-metal
P-XRD	Powder X-ray diffraction
PhD	Doctorate of philosophy
POM	Polyoxometalate
RBF	Round-bottom flask
RT	Room temperature
SAXS	Small angle x-ray scattering
SE	Secondary electron
SEC	Surfactant encapsulated cluster
SEM	Scanning Electron Microscope
SEP	Surfactant encapsulated polyoxometalate
Surfactant	Surface acting agent
TBA <sup>+</sup>	Tetrabutylammonium cation, N(C <sub>2</sub> H <sub>5</sub> ) <sub>4</sub> <sup>+</sup>
TGA	Thermogravimetric analysis
TMA <sup>+</sup>	Tetramethylammonium cation, N(CH <sub>3</sub> ) <sub>4</sub> <sup>+</sup>
TrMA <sup>+</sup>	Trimethylammonium cation, HN(CH <sub>3</sub> ) <sub>3</sub> <sup>+</sup>
UHV	Ultra-high Vacuum
UV	Ultraviolet
UV-vis	Ultraviolet-visible
VB	Valence-band
XPS	X-ray photoelectron spectroscopy
XRD	X-ray diffraction

### **List of Symbols**

<i>a</i>	Scaling factor
<i>A</i> <sub>0</sub>	Effective surfactant head-group cross-sectional area
<i>b</i>	Scaling factor
<i>c</i>	Rate of photo-colouration or bleaching
CTA <sub><i>m</i></sub>	Fraction of micellized CTA <sup>+</sup> surfactants
ΔAbs.	Change in absorbance
ΔR	Change in reflectance

$\Delta T$	Change in transmittance
$e^-$	Electron
$E_g$	Energy difference across a molecular orbital band-gap
$E_\gamma$	Photon energy
$g$	Surfactant packing parameter
$\gamma$	Photon
$h^+$	Electron hole
$I$	Collected light-spectrum intensity
$I_0$	Light-spectrum intensity of a known standard material
$k_{aq}$	Rate of reaction outside a surfactant micelle in an aqueous solution
$k_m$	Rate of reaction within a surfactant micelle in an aqueous solution
$K_{OH}^{Cl}$	rate of exchange between $Cl^-$ and $OH^-$ anions across a micelle interface
$K_{OH}^X$	Rate of exchange between halide and $OH^-$ anions across a micelle interface
$l$	Curvature elastic energy
$n$	Oxidation state
$n$	Surfactant packing number
$[OH_{aq}^-]$	Concentration of $OH^-$ anions in aqueous solution
$[OH_m^-]$	Concentration of $OH^-$ anions within a surfactant micelle
$p$	Probability of x-ray interaction with an atom
$t$	Time in seconds
$t_{1/2}$	Time taken to photo-colour or bleach to half the full extent
$V$	Surfactant alkyl-tail volume
$[X_{aq}^-]$	Concentration of halide anions in aqueous solution
$[X_m^-]$	Concentration of halide anions in a surfactant micelle
$y$	Diffuse reflectance or transmittance
$Z$	Atomic number

## List of Figures

**Figure 1.1.1.** Depiction of the Lindqvist polyoxometalate.

**Figure 1.1.2.** Depiction of a mixed-addenda Lindqvist polyoxometalate.

**Figure 1.1.3.** Depiction of the Dawson polyoxometalate.

**Figure 1.1.4.** Depiction of a lacunary polyoxometalate based on the combination of Lindqvist polyoxometalate derivatives.

**Figure 1.1.5.** Example of the many ways that polyoxometalates can be further functionalized by the attachment of organic groups.

**Figure 1.1.6.** Depiction of the ‘recipe-based’ method to synthesize ionic polyoxometalate-hybrid compounds.

**Figure 1.1.7.** Depiction of the Keggin anion.

**Figure 1.1.8.** Illustration of the predictability of surfactant-polyoxometalate self-assembly via manipulable parameters such as cation-anion charge-balancing.

**Figure 2.1.1.** Depiction of a Soxhlet apparatus.

**Figure 2.2.1.** Experimental set-up for CTA- $W_{12}$  hysteresis study.

**Figure 3.1.1.** Tungstate equilibrium scheme devised by J. Hastings and O. Howarth.

**Figure 3.1.2.** Processes methyl-ammonium concentration-dependent precipitation of tungsten octahedra from aqueous solutions.

**Figure 3.1.3.** Curvature elastic energy versus surfactant-tail volume of different length surfactants.

**Figure 3.1.4.** Keggin anions within the hydrophilic layer of  $(CTA)_4[SiW_{12}O_{40}]$ . (a) Keggin anions form a pseudo hexagonal pattern within the layer, separated by the mutually pseudo-hexagonally arranged dimers of cations quaternary-ammonium head-groups. (b) View of the same layer parallel to the  $b$ -axis. (c) Simplified diagram of the pseudo-hexagonally arranged species.

**Figure 3.1.5.** View of  $(CTA)_5(CH_3CN)_4[H_xSiMo_{12}O_{40}]$  down the  $a$ -axis highlighting the interdigitation, tilting and individuality of the hydrophobic alkyl-chains.

**Figure 3.1.6.** (a) Lamellar width as a function of the POM anionic charge. (b) Additional surfactants beyond a 1:4 POM:alkyl-chain ratio increases lamellar width due to surfactant binding to bottom surface of POMs.

**Figure 3.1.7.** Solvent-dependent reversible transformations of  $(\text{DODA})_3[\text{PW}_{12}\text{O}_{40}]$  structures in butanol/chloroform mixtures.

**Figure 3.2.1.** Raman spectrum of CTA- $\text{W}_{12}$ .

**Figure 3.2.2.** ATR FT-IR spectra of CTA- $\text{W}_{12}$ .

**Figure 3.2.3.** P-XRD pattern of CTA- $\text{W}_{12}$ .

**Figure 3.2.4.** Powder XRD pattern of CTA- $\text{WO}_3$ .

**Figure 3.2.5.** Raman spectrum of CTA- $\text{WO}_3$ .

**Figure 3.2.6.** FT-IR Spectrum of CTA- $\text{WO}_3$  in a KBr pellet.

**Figure 3.2.7.** SEM image of CTA- $\text{WO}_3$ .

**Figure 3.2.8.** P-XRD pattern of the product of  $\text{WO}_3 \cdot 2\text{H}_2\text{O}$ .

**Figure 3.2.9.** Raman spectrum of  $\text{WO}_3 \cdot 2\text{H}_2\text{O}$ .

**Figure 3.2.10.** FT-IR spectrum of  $\text{WO}_3 \cdot 2\text{H}_2\text{O}$  collected in a KBr pellet.

**Figure 3.2.11.** P-XRD patterns of products of CTA- $\text{WO}_3$  colloidal suspensions raised to pH 4 and pH 7.

**Figure 3.2.12.** Raman spectra of samples as described in Figure 3.2.11.

**Figure 3.2.13.** ATR FT-IR of samples as described in Figure 3.2.11.

**Figure 3.2.14.** P-XRD pattern of  $\text{WO}_3 \cdot 2\text{H}_2\text{O}$  suspension alkalized to pH 4 followed by addition of CTA-Br.

**Figure 3.2.15.** Raman spectra of sample as described in Figure 3.2.14.

**Figure 3.2.16.** ATR FT-IR spectrum of sample as described in Figure 3.2.14.

**Figure 3.2.17.** P-XRD of a CTA- $\text{W}_{12}$  suspension alkalized to pH 8, followed by acidification to pH 4 and pH 7.

**Figure 3.2.18.** Raman spectra of the samples as described in Figure 3.2.17.

**Figure 3.2.19.** ATR FT-IR of the samples as described in Figure 3.2.17.

**Figure 3.2.20.** (a) XRD patterns of CTA-Para and  $(\text{NH}_4)_{10}[\text{H}_2\text{W}_{12}\text{O}_{42}] \cdot 10\text{H}_2\text{O}$  (b) Raman spectra of CTA-Para and  $(\text{NH}_4)_{10}[\text{H}_2\text{W}_{12}\text{O}_{42}] \cdot 10\text{H}_2\text{O}$ .

**Figure 3.3.1.** (a) TGA and DTA of CTA- $\text{WO}_3$  (b) TGA and DTA of B4 (c) TGA and DTA of B7 (d) Organic (CTA<sup>+</sup>) fraction of sample versus synthesis pH

**Figure 3.4.1.** (a) Lamellar structure of CTA- $\text{W}_{12}$  depicting the  $[\text{H}_2\text{W}_{12}\text{O}_{40}]^{6-}$  clusters separated by the interdigitated surfactant tails of CTA<sup>+</sup>. (b) 2D pseudo-hexagonal arrangement of the POMs within the hydrophilic layer.

**Figure 3.4.2.** (a) SEM image of CTA-W<sub>12</sub>. (b) and (c) TEM images of CTA-W<sub>12</sub>. (d) Typical 35nm contrast-dependent length section used to calculate interlamellar distance of CTA-W<sub>12</sub>.

**Figure 3.4.3.** Distortion within the 2D pseudo-hexagonal arrangement of anionic POMs across the (001) plane due to the POM:surfactant ratio exceeding 1:4 (a), as compared to the more symmetrical arrangement within a 1:4 SEP (b).

**Figure 4.1.1.** Production of MCM-41 catalytic substrate.

**Figure 4.1.2.** Mesostructure representations of (a) hexagonally arranged silicates (MCM-41), (b) cubically arranged silicates (MCM-48) and (c) meso-lamellar arranged silicates (MCM-50).

**Figure 4.1.3.** Hoffman degradation mechanism of CTA<sup>+</sup>.

**Figure 4.1.4.** Thermodynamics of CTA<sup>+</sup> decomposition.

**Figure 4.1.5.** Model of Keggin anion fragmentation and condensation.

**Figure 4.1.6.** Temperature dependent phases of WO<sub>3</sub>.

**Figure 4.1.7.** (a) WO<sub>6</sub> octahedral network of monoclinic  $\gamma$ -WO<sub>3</sub>, and (b) distorted WO<sub>5</sub>(OH<sub>2</sub>) alternating octahedral network.

**Figure 4.1.8.** (a) Structural representation of WO<sub>3</sub>·2H<sub>2</sub>O, depicting sheets of alternating WO<sub>5</sub>(OH<sub>2</sub>) octahedra and intercalated H<sub>2</sub>O. (b) Hydrogen-bonded network of intercalated H<sub>2</sub>O monolayer. (c) Sheet of WO<sub>5</sub>(OH<sub>2</sub>) octahedra highlighting the alternating positions of the coordinated water.

**Figure 4.1.9.** Crystallographic structure of the h-WO<sub>3</sub> phase.

**Figure 4.1.10.** Complete removal of cations from results in the collapse of the porous hexagonal structure into the condensed m-WO<sub>3</sub> phase.

**Figure 4.2.1.** Molecular structure of the surfactant CTA-Br, indicating all non-equivalent chemical environments of the C and H atoms.

**Figure 4.2.2.** TGA, DTG and DTA of CTA-Br heated in air.

**Figure 4.3.1.** TGA, DTG and DTA of CTA-W<sub>12</sub> in air.

**Figure 4.3.2.** (a) Heat map of CTA-W<sub>12</sub> thermal decomposition consisting of *in situ* synchrotron P-XRD patterns (b) Stacked P-XRD plot of CTA-W<sub>12</sub> thermal decomposition containing the distinct phases.

**Figure 4.3.3.** *Ex-situ* ATR FT-IR spectra of the phases present across CTA-W<sub>12</sub> thermal decomposition.

**Figure 4.3.4.** (002) Peak position as a function of temperature illustrating interlamellar expansion from 30 to 220°C.

**Figure 4.3.5.** Measured and calculated XRD patterns of phase V, compared with a similar HCP array of Au atoms.

**Figure 4.3.6.** *ex-situ* ATR FT-IR spectra of phase V from 270 to 310°C.

**Figure 3.3.7.** Depiction of the multi-step process of Keggin anion decomposition over the course of phase V, involving separation into edge-sharing trimers before condensing into larger edge-sharing isoplytungstates.

**Figure 4.3.8.** (a) Conversion of phase V to VI to VII to VIII during thermal decomposition, and (b) increase in amorphous background with stability ranges of various phases superimposed.

**Figure 4.3.9.** TGA, DTG and DTA of CTA-W<sub>12</sub> in N<sub>2</sub>.

**Figure 4.3.10.** P-XRD of the product produced from (a) TGA in air (Figure 3.3.1) and (b) TGA in N<sub>2</sub> (Figure 3.3.9).

**Figure 4.4.1.** (a) Heat map of CTA-WO<sub>3</sub> thermal decomposition consisting of *in situ* synchrotron P-XRD patterns (b) Stacked P-XRD plot of CTA-WO<sub>3</sub> thermal decomposition containing the distinct phases.

**Figure 4.4.2.** TGA, DTG and DTA of CTA-WO<sub>3</sub> in air.

**Figure 4.4.3.** TGA, DTG and DTA of CTA-WO<sub>3</sub> in N<sub>2</sub>.

**Figure 4.4.4.** Comparison of DTG curves of CTA-W<sub>12</sub> and CTA-WO<sub>3</sub> in air.

**Figure 4.5.1.** SEM image of phase V.

**Figure 4.5.2.** FT-IR spectra of phase V (310°C) as-prepared, after Soxhlet extraction and the soluble fraction that was removed in CHCl<sub>3</sub>.

**Figure 4.5.3.** Labelled <sup>1</sup>H-NMR of (a) CTA-W<sub>12</sub> as prepared and (b) CHCl<sub>3</sub> soluble fraction of phase V in CDCl<sub>3</sub>.

**Figure 4.5.4.** TGA and DTA of the CHCl<sub>3</sub> insoluble (a) and soluble (b) fractions of phase V, (c) comparative DTA of insoluble and soluble fractions, and (d) comparative DTG of insoluble and soluble fractions.

**Figure 4.5.5.** (a) TGA and DTA of the CHCl<sub>3</sub> insoluble fraction, (b) TGA and DTG of CHCl<sub>3</sub> insoluble fraction, (c) TGA and DTA of the CHCl<sub>3</sub> soluble fraction, (d) TGA and DTG of CHCl<sub>3</sub> soluble fraction, (e) DTA of the insoluble and soluble fractions and (f) DTG of the

insoluble and soluble fractions. All measurements performed at the slower heating rate of 1°C/min (as compared to 5°C/min).

**Figure 4.5.6.** P-XRD patterns of phase V as prepared, after Soxhlet extraction with CHCl<sub>3</sub>, and the extracted residue from the Soxhlet apparatus.

**Figure 4.5.7.** RAMAN spectra of phase V, phase V after Soxhlet extraction with CHCl<sub>3</sub>, and the extracted residue.

**Figure 4.5.8.** FT-IR spectra of phase V, and its respective CHCl<sub>3</sub> soluble and CHCl<sub>3</sub> insoluble fractions.

**Figure 5.1.1.** Octahedral representations of WO<sub>6</sub><sup>6-</sup> in the bulk state with an idealised *O<sub>h</sub>* symmetry and at the surface with a distorted *C<sub>s</sub>* symmetry.

**Figure 5.1.2.** Structure of the Keggin anion depicting the edge-sharing capping trimers and the corner-sharing equatorial ring that comprise the anion, as well as the types of oxygen bonds that connect the octahedra.

**Figure 5.1.3.** Splitting of the *t<sub>2g</sub>* d-orbitals in Keggin and other polyoxometalates due to the distortion of MO<sub>6</sub> octahedra away from idealised *O<sub>h</sub>* symmetry.

**Figure 5.1.4.** (a) Structure of the Keggin-anion, (b) ionic representation of the Keggin structure, and (c) example of one of the closed -O<sup>2-</sup>-W<sup>6+</sup>-O<sup>2-</sup>- loops formed within the anion's cyclic-geometry.

**Figure 5.1.5.** Formation of the photo-coloured charge-transfer complex from the bleached state in typical alkyl-ammonium-POM photochromic materials.

**Figure 5.1.6.** Diagram of photon-absorption instigated electronic d-d transitions of excited electrons within the distorted W 5d band.

**Figure 5.1.7.** Photo-catalysed C-H bond activation-mediated reactions of organic molecules and the decatungstate anion, [W<sub>10</sub>O<sub>32</sub>]<sup>4-</sup>.

**Figure 5.1.7.** FT-IR spectra of (a) H<sub>3</sub>PMO<sub>12</sub>O<sub>40</sub>, (b) pristine (DODA)<sub>3</sub>[PMO<sub>12</sub>O<sub>40</sub>] film, (c) (DODA)<sub>3</sub>[PMO<sub>12</sub>O<sub>40</sub>] after UV irradiation, (d) (DODA)<sub>3</sub>[PMO<sub>12</sub>O<sub>40</sub>] film after heating photo-coloured film in air, and (e) after further UV irradiation of the bleached film.

**Figure 5.2.1.** UV-vis spectra of CTA-W<sub>12</sub> in MeOH as-prepared and after UV irradiation.

**Insert:** Quartz cuvette containing the described photo-reduced CTA-W<sub>12</sub> in MeOH.

**Figure 5.2.2.** (a) CTA-W<sub>12</sub> particles directly after UV irradiation displaying both coloured and as-prepared/bleached states, (b) UV-vis reflectance spectra of CTA-W<sub>12</sub> as prepared and after UV irradiation.

**Figure 4.2.3.** (a) Colouration rate of CTA-W<sub>12</sub> and (b) bleaching rate of coloured CTA-W<sub>12</sub>.

**Figure 5.2.4.** XPS of CTA-W<sub>12</sub> as-prepared (a) and directly after UV irradiation (b).

**Figure 5.3.1.** UV-vis reflectance spectra of CTA-W<sub>12</sub> as-prepared, directly after UV irradiation, bleached and after a subsequent UV irradiation.

**Figure 5.3.2.** Hysteresis study of CTA-W<sub>12</sub> photochromism.

**Figure 5.3.3.** XPS spectra of CTA-W<sub>12</sub> including C1s, O1s and N1s spectra in un-irradiated and UV irradiated samples.

**Figure 5.3.4.** (a) ATR FT-IR spectra of CTA-W<sub>12</sub> as-prepared, and after two, four and six photochromic cycles. (b)  $\nu(\text{C}=\text{O})$ : $\nu(\text{W}-\text{O}_b-\text{W})$  peak-area ratio vs total exposure time.

**Figure 5.3.5.** ATR FT-IR spectra of CTA-W<sub>12</sub> as-prepared and after 18 photochromic cycles.

**Figure 5.3.6.** Intensities of  $\nu_{\text{as}}(-\text{CH}_2)$ ,  $\nu_{\text{ss}}(-\text{CH}_2)$ ,  $\nu(\text{C}=\text{O})$  and  $\nu(\text{C}-\text{OH})$  FT-IR bands vs number of photochromic cycles.

**Figure 5.3.7.** (a) ATR FT-IR spectra of CTA-Br as-received and after two, four and six UV irradiation. (b)  $\nu(\text{C}=\text{O})$  intensity in CTA-Br and CTA-W<sub>12</sub> vs number of UV irradiation cycles.

**Figure 5.3.8.** Raman spectra of CTA-W<sub>12</sub> as-prepared and after 18 photochromic cycles.

**Figure 5.3.9.** GC-MS spectra of CTA-W<sub>12</sub> after UV irradiation. (a) GC of irradiated CTA-W<sub>12</sub> in CHCl<sub>3</sub> (b) Mass spectrum of 1-hexadecanol (c) Mass spectrum of hexadecylamine (d) GC of un-irradiated CTA-W<sub>12</sub>.

**Figure 5.4.1.** *In-situ* low-angle synchrotron P-XRD patterns of CTA-W<sub>12</sub> at 4min, 40min, 80min, 120min, 160min, 200min and 220 min of UV irradiation time. **Insert:** (001) and (110) peak intensities vs irradiation time.

**Figure 5.4.2.** (001) peak intensity vs X-ray only irradiation, X-ray with intermittent UV irradiation, and continuous UV and X-ray irradiation.

**Figure 5.4.3.** (001) peak intensity for each UV ON-OFF cycle.

**Figure 5.4.4.** Thermal expansion of CTA-W<sub>12</sub> in the [001] direction from 25 to 90°C.

**Figure 5.4.5.** Interlamellar spacing vs X-ray-only irradiation time, X-ray and intermittent UV irradiation, and continuous X-ray and UV irradiation.

**Figure 6.1.1.** Diagram of possible x-ray/matter interactions.

**Figure 6.1.2.** Examples of x-ray induced damage that can be induced by measurement of a sample.

**Figure 6.1.3.** Process of ‘Coulombic explosion’ in ionic compounds.

**Figure 6.1.4.** Diagram of present organic material accelerating oxygen-vacancy generation and x-ray photoreduction of chromium oxides by reaction with photo-oxidized O<sup>+</sup> species.

**Figure 6.2.1.** The first, fifteenth, thirtieth and fiftieth scans of the W4f core-level XPS spectra in CTA-W<sub>12</sub>.

**Figure 6.2.2.** Relative concentration of W<sup>6+</sup>, W<sup>5+</sup> and W<sup>4+</sup> oxidation states as a function of XPS scan time.

**Figure 6.2.3.** Surface plot (a) and coloured heat-map (b) of W4f x-ray photoelectron intensity as a function of XPS scan number.

## List of Tables

**Table 1.1.1.** Notable examples of literature on surfactant-POM hybrids highly-relevant to the subjects covered in this thesis.

**Table 3.1.1.** Value of the surfactant-packing parameter, *g*, within curved and flat mesophases.

**Table 3.2.1.** Comparison between theoretical and experimental C,H&N micro-analysis data of CTA-W<sub>12</sub> based on the empirical formula (CTA)<sub>7</sub>[H<sub>2</sub>W<sub>12</sub>O<sub>40</sub>]Cl.2H<sub>2</sub>O.

**Table 3.2.2.** Comparison between theoretical and experimental TGA data of CTA-W<sub>12</sub> based on the empirical formula (CTA)<sub>7</sub>[H<sub>2</sub>W<sub>12</sub>O<sub>40</sub>]Cl.2H<sub>2</sub>O.

**Table 3.2.3.** Measured and theoretical C,H&N micro-analysis of CTA-WO<sub>3</sub> based on the empirical formula (CTA)<sub>6</sub>[WO<sub>3</sub>].7H<sub>2</sub>O.

**Table 3.2.4.** Measured and theoretical volatile organic (CTA<sup>+</sup>), non-volatile (WO<sub>3</sub>) and hydration (H<sub>2</sub>O) content based on the empirical formula (CTA)<sub>6</sub>[WO<sub>3</sub>].7H<sub>2</sub>O as measured by CTA.

**Table 4.1.1.** Bond energies within alkyl-ammonium molecules.

**Table 4.4.1.** Comparison of CTA-W<sub>12</sub> and CTA-WO<sub>3</sub> thermal decomposition events in air.

**Table 4.5.1.** Comparison between volatile (organic and water) and non-volatile ( $\text{WO}_3$ ) content of  $\text{CHCl}_3$  insoluble and  $\text{CHCl}_3$  soluble fractions of phase V as measured by TGA.

**Table 4.5.2.** Comparison between experimental C,H&N micro-analysis and theoretical calculations based on the empirical formula  $(\text{TMA})_{2.5}\text{H}_{3.5}[\text{W}_7\text{O}_{24}]$ .

**Table 6.2.1.** Relative concentration of  $\text{W}^{6+}$ ,  $\text{W}^{5+}$  and  $\text{W}^{4+}$  oxidation states across successive XPS scans.

## Abstract

Inorganic-organic polyoxometalate-hybrid materials have attracted increased interest from researchers in recent years due their favourable photo-redox properties. These compounds have the potential to serve in a wide range of applications including photo-catalysis, gas-sensing and medicine. However, limited thermal and photo-chemical stability of these systems has restricted further development into other applications, such as photochromic technologies.

This thesis focuses on the synthesis and thermal and photochemical stability of the polyoxometalate-hybrid designated CTA-W<sub>12</sub>, formed from the metatungstate anion, [H<sub>2</sub>W<sub>12</sub>O<sub>40</sub>]<sup>6-</sup> and the cationic surfactant cetyltrimethylammonium, (C<sub>16</sub>H<sub>33</sub>)N(CH<sub>3</sub>)<sub>3</sub><sup>+</sup> (CTA<sup>+</sup>). Only a narrow window of synthesis conditions actually leads to the production of the studied material because the products produced are very sensitive to pH, temperature, sequence of reactions steps and time. The CTA-W<sub>12</sub> exhibits a lamellar bilayer structure, consisting of 2D sheets of hexagonally arranged polyoxometalate anions separated by interdigitated surfactant alkyl-tails.

The thermal stability of CTA-W<sub>12</sub> was studied using a battery of techniques, including *in situ* synchrotron x-ray diffraction. It was found that the salt went through seven phase and/or chemical transitions from room-temperature to 800°C within the enclosed environment of the quartz capillary. The lamellar structure persisted for the first three transitions and was destroyed by the fifth at 230°C, when the polyoxometalates fragmented and assumed a hexagonally-close-packed (HCP) arrangement. By ~350°C, the fragments reorganized into the bulk tungsten-suboxide W<sub>17</sub>O<sub>47</sub> and by ~550°C all organic material was removed from the sample. At ~600°C the sample underwent a final transition to monoclinic WO<sub>2</sub>. The HCP fifth phase was further studied due to its high crystallinity and was found to be comprised of two types of polyanion fragments, alluding to the complex decomposition kinetics of polyoxometalates and inorganic-organic hybrids.

The photochromism of CTA-W<sub>12</sub> highlighted the photochemical instability of the inorganic-organic polyoxometalate hybrid. Multiple cycles of irradiation followed by recovery were applied to elucidate the behaviour of the material. The first four photochromic cycles coincided with a slight discoloration of the bleached state, detrimentally affecting

photochromic performance slightly. This was ascribed to irreversible oxidation to organic CTA<sup>+</sup> which caused a yellowing of the material, as well the production of long-lived W<sup>5+</sup> sites deep within the material which could not be re-oxidized by atmospheric O<sub>2</sub>. The material maintained reasonable photochromic performance beyond four cycles, which was attributed to the production of more reversible proton-transfer groups, as compared to CH<sub>2/3</sub>, and an equilibrium between the production of long-lived W<sup>5+</sup> sites and the diffusion of O<sub>2</sub> into the material. Lattice expansion and amorphization (which was partially reversed during bleaching) was observed to mutually occur with photo-colouration, as evidenced by XRD. The accumulation of strain in the sample, as indicated by the expansion in lattice parameter along the [001] direction, may represent a new photomechanical phenomenon. The photochemical instability of CTA-W<sub>12</sub> was further revealed during XPS measurements, which caused progressive reduction of tungsten centres with each successive measurement due to the ionizing effect of the X-ray radiation in combination with the high vacuum environment of the instrument.

The project has provided detailed insight into the synthesis, thermal stability and photochemical properties of CTA-W<sub>12</sub>. The mechanism of photochromism, and the reasons for its partial irreversibility, were found. A new photomechanical phenomenon was uncovered and investigated. The new insights provided by the project will facilitate future attempts to develop applications for these and related inorganic-organic hybrid compounds.

## Chapter 1. Introduction

The information presented in this chapter provides a brief introduction on the topic of polyoxometalates in order to familiarize the reader with the field. The nomenclature used to define different polyoxometalates, a brief overview of their properties, and current and possible future applications will be provided. Greater detail on the specific topics covered within this thesis, including specific theory and the current gaps in the knowledge, will be given at the beginning of each chapter.

### **1.1 Structure and nomenclature of common transition-metal oxo-anion clusters**

As will be discussed in detail in the following chapters, octahedra comprised of group V or VI transition-metal cations surrounded by oxygen ligands are able to bond together in linked cyclic arrangements which form discrete anionic macro-molecular clusters. The metallic atoms at the centre of octahedra are referred to as *addenda atoms*. The clusters can further be categorized based upon their chemical make-up. If the anion only contains transition-metal octahedra, it is termed an *isopolyanion*. The simplest isopolyanion, termed the Lindqvist anion,  $[M_6O_{19}]^{n-}$  (where M = group V or VI transition-metal) is pictured below in Figure 1.1.1 comprising of six octahedra bonded to each other by their edges to form a square bipyramidal structure.

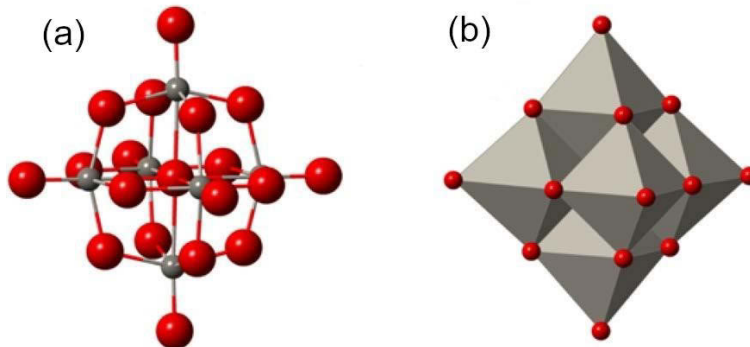


**Figure 1.1.1.** The Lindqvist anion. (a) Ball-and-stick representation where grey spheres represent a group V or VI transition-metal and red spheres represent oxygen. (b) Octahedral representation where the grey octahedra represent the metal cations and its bonds to the oxygen atoms in red.<sup>4</sup>

A cluster can be comprised of a single type of addenda atom, or differing types resulting in *mixed-addenda* clusters. Figure 1.1.3 below displays a mixed-addenda Lindqvist structure comprising of one vanadium octahedra and five molybdenum octahedra.

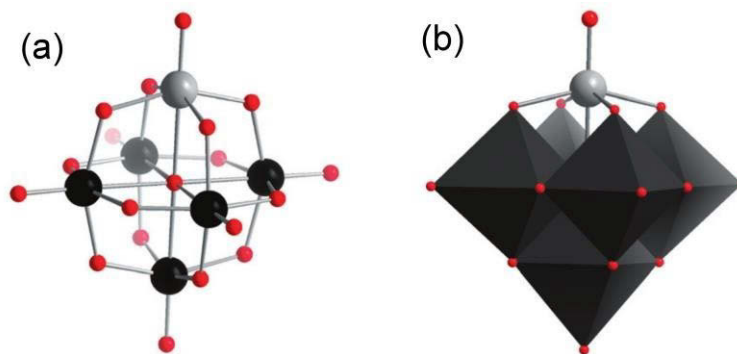


**Figure 1.1.2.** A vanadium-substituted mixed-addenda Lindqvist cluster, comprised of four molybdenum octahedra and one vanadium octahedra. (a) Ball-and-stick model where molybdenum cations are represented as black spheres, the vanadium cation as a grey spheres and oxygen ligands as red spheres (b) Octahedral representation where molybdenum octahedra and their bonds to the oxygen ligands are represented by black octahedra, the vanadium cation is represented as a grey sphere and the oxygen ligands are represented by red spheres.<sup>5</sup>

Isopolyanions tend to have a high anionic charge, which can be countered by protons and other cationic acidic groups and is the reason they are also routinely referred to as *heteropoly acids*. The term isopolyanion can be altered to further reflect the dominant transition-metal present in the cluster, such as *isopolytungstate* if the cluster is largely comprised of tungstate octahedra, or *isopolymolybdate* if molybdenum cations are predominant. If a cluster contains another type of atom within its interior, termed a *hetero-atom*, then the cluster is called a *polyoxometalate* (POM). The term polyoxometalate can be further altered in the same way as the term isopolyanion, producing names such as *polyoxotungstate*, *polyoxomolybdate* and so on. Alternatively, these terms can also be altered to reflect the type of hetero-atom present, producing terms such as *phosphotungstic acid* and *silicotungstic acid*. The *Dawson-type* polyoxometalate,  $[X_2M_{18}O_{62}]^{n-}$ , where X = the hetero-atom and M = tungsten or molybdenum cations, is pictured in Figure 1.1.3.

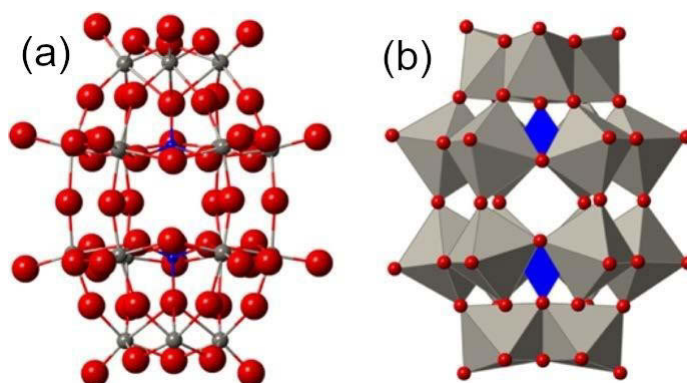


**Figure 1.1.3.** The Dawson polyoxometalate represented with a (a) ball-and-stick model where grey spheres represent transition-metal cations, red spheres represent oxygen ligands and blue spheres represent the hetero-atoms, and (b) octahedral model where grey octahedra represent transition-metal cations and their bonds to the oxygen ligands (red spheres) and blue triangles represent the hetero-atoms and their bonds to the outer oxo-anion cage.<sup>4</sup>

Defect POM structures in which some metal atoms are removed are termed *lacunary* POMs. The vacant octahedra site where the metal atom was removed may be left vacant or substituted with other elements or molecules. Lacunary POMs may also be joined to other lacunary POMs to create new, further functionalized anions. Figure 1.1.4 displays a lacunary

POM were two Lindqvist isopolytungstates, that both contain vacant octahedra, are joined together via a lanthanide ( $\text{Ln}^{3+}$ ) cation at their respective vacant sites to form the pictured  $[\text{Ln}(\text{W}_5\text{O}_{18})_2]^{9-}$  anion.

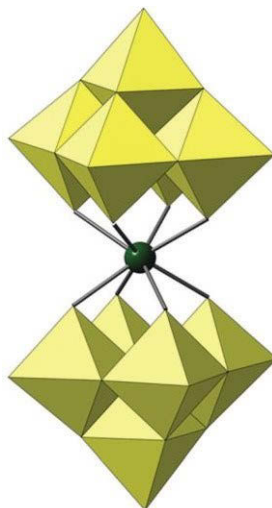


**Figure 1.1.4.** A lacunary POM where two defect Lindqvist isopolytungstates are joined together via a lanthanide ( $\text{Ln}^{3+}$ ) at their respective vacant sites.<sup>6</sup>

In a similar way, the terminal oxygen bonds on the surface of POMs can also be substituted for other appropriate ligands. The attachment of organic molecules to such sites allows for a greatly improved variety of functionalization, owing to the mutual properties of the inorganic anion and the attached organic group. Clusters that are connected to organic moieties, other clusters, metallic nanoparticles, or any other functional group are termed *hybrid polyoxometalates*. Such hybrid-functionalization has become widespread across the discipline of POM-based research, due to the wide variety of structures and properties that result. An example of such varied functionalization possibilities is displayed in Figure 1.1.5, which displays a myriad of organic molecules that can be attached to the Lindqvist structure.

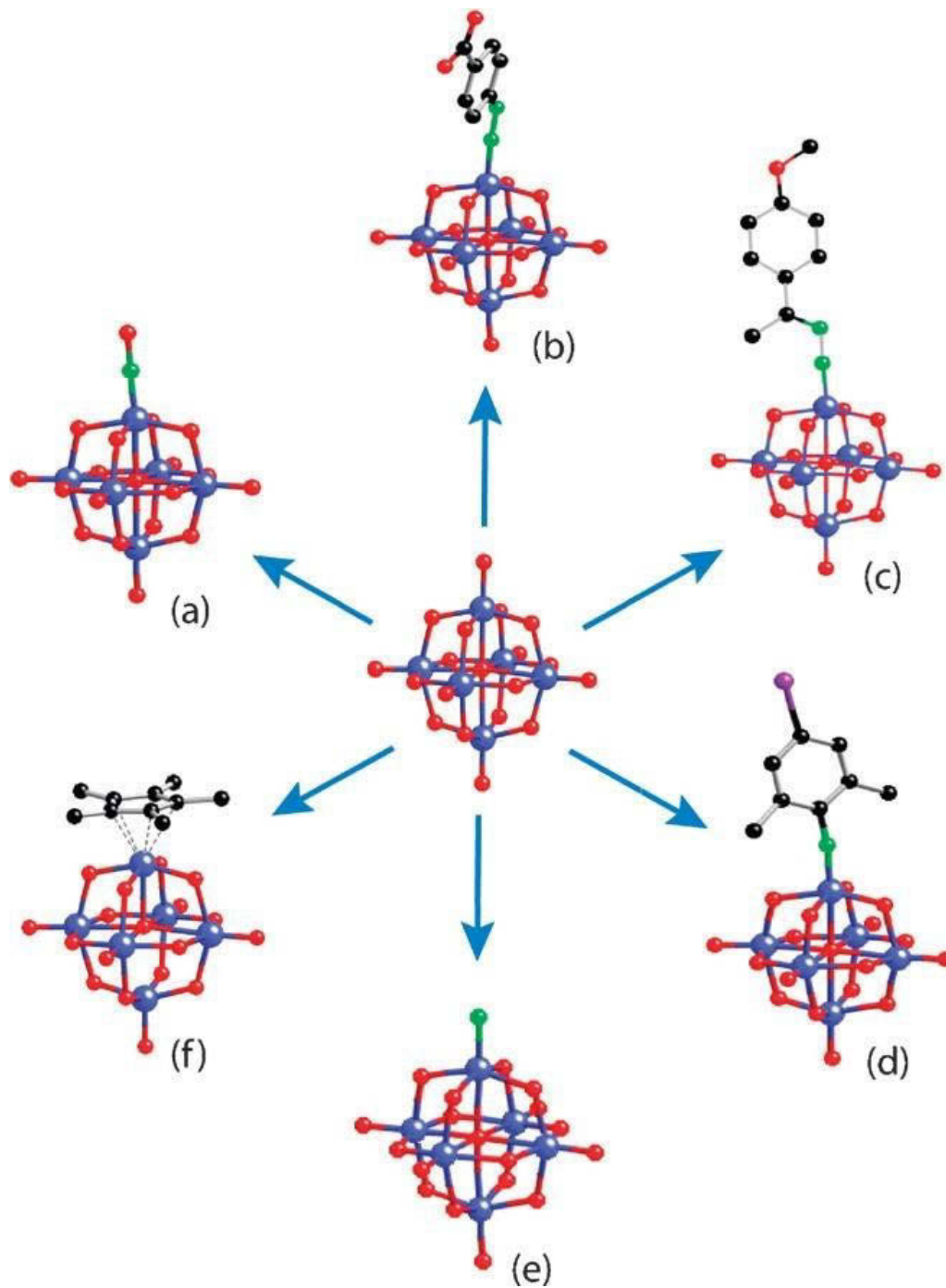


**Figure 1.1.5.** The terminal oxygen ligand in POMs can be substituted for a wide variety of appropriate groups, including organic molecules, leading to vast array of functionalization possibilities.<sup>7</sup>

Organic molecules can be added to materials containing POMs to form hybrid compounds via electrostatic means, as opposed to the covalent attachments described previously. This is

easily achieved do the negative charge of the inorganic anions and the (typically) positive charge of suitable organic cations. Furthermore, as will be further described in Section 3.1, due to the (typical) hydrophilicity of POMs, and the (typical) hydrophobicity of organic molecules, many architectures are readily synthesized via predictable and manipulable self-assembly techniques. Other ionic species can also be added to such systems to further functionalize these materials. The typical synthesis method to produce ionically bound POM hybrid compounds is described in Figure 1.1.6.

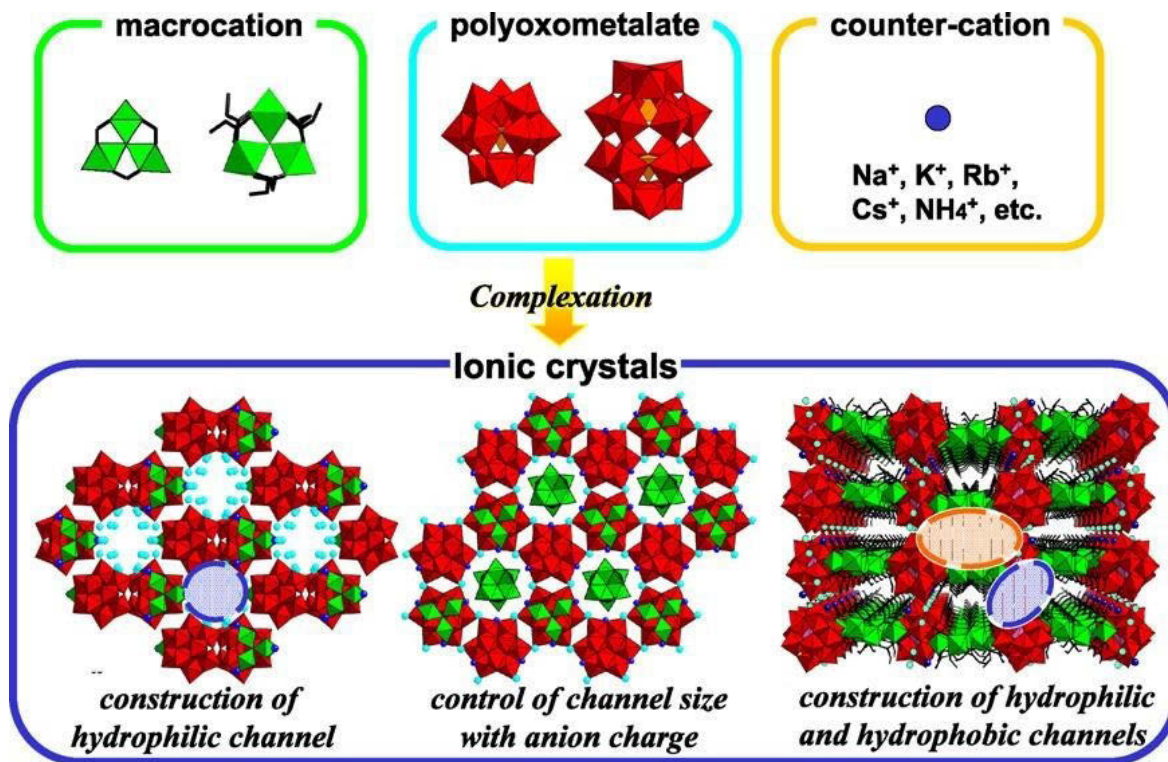


**Figure 1.1.6.** Ionically-bound POM hybrid compounds are typically synthesized via ‘recipe-based’ approaches that take advantage of self-assembly techniques driven by attractive anionic-cationic and repulsive hydrophobic-hydrophilic forces.<sup>8</sup>

Organic hybrid POMs can be categorized into two classes dependent upon the type of interaction between the POM and the added moiety, as will be further described in the next section.

Due to the prolific production of different exotic clusters and hybrid POMs, many of the previous terms have fallen out of regular use, and the term ‘polyoxometalate’ has become

synonymous with any discrete transition-metal-oxide cluster. In the present work, the term ‘polyoxometalate’ will also describe any discrete transition-metal-oxide cluster. Other previously described terms will also be used when appropriate to further clarify the nature of a specific cluster.

By far the most studied POM is the Keggin anion, Figure 1.1.7, due to the anions favourable photo-redox properties and its relative resistance to electronic stress. It is comprised of 12 group V or VI transition-metal octahedra which are organised into cyclic arrangements which form the near-spherical cluster  $[XM_{12}O_{42}]^{n-}$  pictured below.

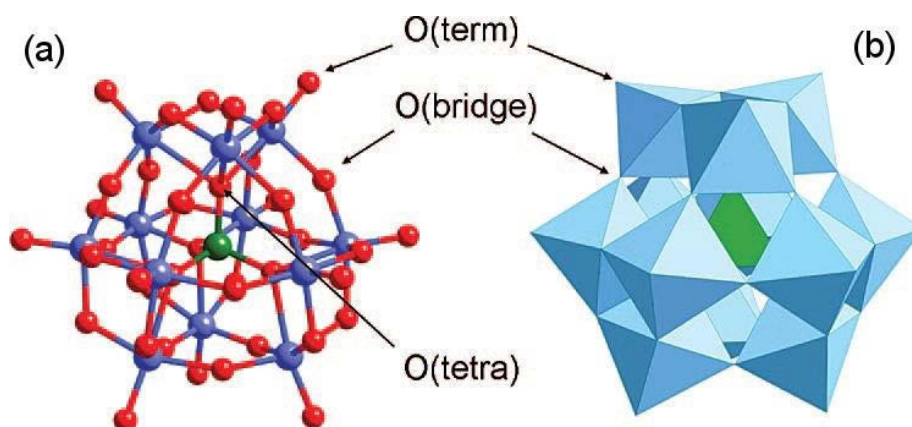


**Figure 1.1.7.** Models of the Keggin anion with the types of oxygen bonds labelled. (a)

Ball-and-stick model where purple spheres represent group V or VI transition-metal cations, red spheres represent oxygen and the green-sphere represent the hetero-atom. (b)

Octahedral model where blue octahedra represent the transition-metal cations and the oxygen ligands bonded to them, and the green triangle at the centre of the cluster represents the hetero-atom.<sup>9</sup>

As will be discussed further in Chapter 5, the favourable electronic properties of the Keggin anion arise due to the bonding within the cluster, which is also displayed in Figure 1.1.7. These bonds include terminal oxygen on the outer surface of the cluster double-bonded to the transition-metal, internal bonds between the hetero-atom and the inner oxo-ligands (termed ‘*tetra*’ in Figure 1.1.7. due to the four bonds made between the hetero-atom and the inner oxo-ligands), and bridging bonds between the octahedra. These bridging bonds can either involve corner-sharing or edge-sharing between the octahedra. The Keggin anion, and

its hybrid derivatives will also attract the focus of the work presented in this thesis and will be studied in detail over the proceeding chapters.

## **1.2 A brief review of polyoxometalate properties and current and possible applications**

Polyoxometalates (POMs) are discrete clusters of group V and VI metal-oxide octahedra. The significant mixing between the metallic and oxo-ligand orbitals allows electrons promoted to the HOMO to delocalize across multiple octahedral sites, and as a result these clusters exhibit favourable redox properties.<sup>10</sup> A POMs solubility in aqueous media or organic solvents is highly dependent on the types of counter-cations present. Due to this versatility, POMs have attracted significant research within the last few decades, which has culminated in their application across an array of commercial technologies.

By far the most studied type of POM-based materials are those that include organic components to form organic-inorganic hybrids. Such functionalization has led to POM applications in homogeneous<sup>11,12</sup> and heterogeneous<sup>13</sup> catalysis, photocatalysis,<sup>14-16</sup> chemical sensors,<sup>17,18</sup> solar-cells,<sup>19,20</sup> electro- and photo-chromism,<sup>21-24</sup> magnetism<sup>6,25</sup> and medicine.<sup>26</sup> In many cases the application takes advantage of the POM's desirable (photo-)redox properties, pairing it with designed organic entities to produce desired functionality.

Hybrid POM-organic materials can be separated into two categories; Class I and Class II.<sup>7,27</sup> Class I hybrids contain a non-covalent bond between the POM and the organic component and therefore are affixed by electrostatic interactions, such as coulombically between the anionic POM and cationic organic (e.g. the bond between an anionic POM and a cationic quaternary-amine), or van der Waals forces (e.g. attraction between affixed alkyl-tails).<sup>28-32</sup> Class II hybrids contain a covalent bond between the inorganic POM and organic component, typically through substitution of a surface M=O oxo-site (commonly by N) or substitution of a complete MO<sub>6</sub> octahedra (Where M = group V or IV transition-metal).<sup>7, 33,</sup>

34

Orbital-mixing between the metal and oxo-ligands not only gives rise to electronic delocalization but also imparts significant structural and oxidative stability to the MO<sub>6</sub> cyclic cages within these clusters. This allows POMs to function as electron reservoirs, donating or accepting electrical charge to drive chemical reactions. The basic terminal M=O sites that cover the surface of POMs are able to accept and donate protons, becoming acidic or basic

in response to pH change and/or changes in anionic charge. By manipulating these charge transfers to occur at specific surface-sites and potentials, POMs have been employed to catalyze many researched and industrial reactions.<sup>12, 35, 36</sup> In particular POMs have seen substantial applications within oxidative organic and acid catalysis.<sup>7, 36-38</sup> Furthermore, functionalization of POMs by the grafting of organic species, addenda atoms or even other POM units can fine-tune the functional structure of the hybrid promoting catalytic-selectivity towards engineered reactions.<sup>7, 39-43</sup> Their insertion into organic-matrices allows for further increases in reaction selectivity due to the tunability of pore-sizes as well as ease of recovery/recyclability.<sup>44-47</sup> Because of these attractive redox and stability properties, catalysis is by far the largest industrial and commercial application of POMs.

POMs undergo photo-reduction via the absorption of above band-gap radiation which results in the excitation of an electron from the HOMO (O 2p orbital) to the LUMO (metallic d-orbitals), otherwise known as an oxygen-to-metal ligand-to-metal charge transfer (O→M LMCT). This process results in an electron-hole ( $h^+$ ) being formed at the oxidized oxo-ligand and a reduced  $M^{(n-1)+}$  site (where n = previously more oxidized state). In the proximity of an appropriate organic species, the reduced  $M^{(n-1)+}$  centre is able to attract a hydrogen atom from a neighbouring organic molecule, resulting in a highly reactive organic radical.<sup>14, 16, 48</sup> Due to this mechanism, POMs have also seen employment as photocatalysts, especially the decatungstate anion,  $[W_{10}O_{32}]^{4-}$ .<sup>15, 49-51</sup> Doping of the POM with appropriate metallic cations (such as  $Cd^{2+}$ ,  $Ce^{3+}$  and  $Mn^{+}$ )<sup>52-54</sup>, decoration with plasmonic metallic nanoparticles<sup>55-57</sup> or attachment to visible-light-absorbing dyes can alter the band-gap or absorption spectrum and allow for capture of longer wavelengths resulting in visible-light active catalysis.

The inter-valence charge transfer process that allows for the delocalization of promoted HOMO level electrons across a reduced cluster is a thermally activated process which, at room-temperature, can be instigated by the absorption of visible and near-infrared light.<sup>21, 24, 58, 59</sup> The energy required to instigate this process typically corresponds to that of red light, and is the reason why reduced POMs are regularly referred to as *heteropoly blues* (because red light is absorbed leaving a blue colour to the eye). The energy required to cause an O→M LMCT and populate the d-orbitals corresponds to UV light, and therefore sunlight can be used to drive the photo-reduction process in many POM-based materials. Once the source of UV irradiation is removed, the electrons within photo-coloured, reduced POMs are

scavenged by oxidizing species, such as O<sub>2</sub>, returning the cluster back to its original oxidized colour and state. This light-instigated reduction and subsequent *bleaching* of the coloured state is termed *photochromism* and has attracted the attention of researchers due to the possible application of these materials in window-coatings, light-writable surfaces, and so on. Of course, this reduction and oxidization can also be driven by an electric current, a processes which is termed *electrochromism*.<sup>58, 60</sup>

The structural stability of POMs upon multiple reductions and their high selectivity towards targeted organic substrates make them attractive candidates for use in liquid and gas-phase chemical sensors.<sup>17, 18, 61</sup> Because of this stability, the structure of a POM is largely retained after fixture to the sensor surface.<sup>17, 18</sup> Additional functionalization via molecular or ionic attachment, or insertion into porous-matrices with tailored pore-sizes can further increase selectivity. Attachment to conductive materials (including appropriate polymers) takes advantage of POM's reduction dependent conductivity, allowing for a concentration-dependent linear electrical response from the analyte to the transducer.<sup>17</sup>

The paramagnetic properties of the HUMO level electrons within partially occupied d-orbitals of the M<sup>(n-1)+</sup> sites imparts the reduced POM cluster interesting paramagnetic properties.<sup>6, 25, 62</sup> Furthermore, ferromagnetic species cationic magnetic species, such as Co<sup>2+</sup> and Fe<sup>3+</sup>, can serve as the POMs heteroatom, imparting ferromagnetism to the materials which contain these clusters. The small size and discrete nature of magnetic POMs has seen research of these units as molecular spintronic devices which may see their eventual application in quantum computing.<sup>6</sup>

Due to their discreteness, favourable redox properties and ease of functionalization, POMs have also seen some applications in medicine,<sup>26</sup> with POM units being incorporated into ant-viral and anti-cancer treatments.

### **1.3 Surfactant-polyoxometalate hybrid compounds**

As previously mention in Section 1.1, class II ionically-bound organic-POM hybrid compounds are easily synthesized via manipulable self-assembly techniques. Typically, the ionically attached organic group is a cationic surfactant, which allows the organic groups interaction with the inorganic POM to be dependent upon predictable attractive electrostatic anion-cation and repulsive hydrophobic-hydrophilic forces.<sup>63</sup> Figure 1.1.8 highlights this

predictability and manipulability, where, given the pictured cationic surfactant, different mesostructures are produced dependent on POM anionic charge.

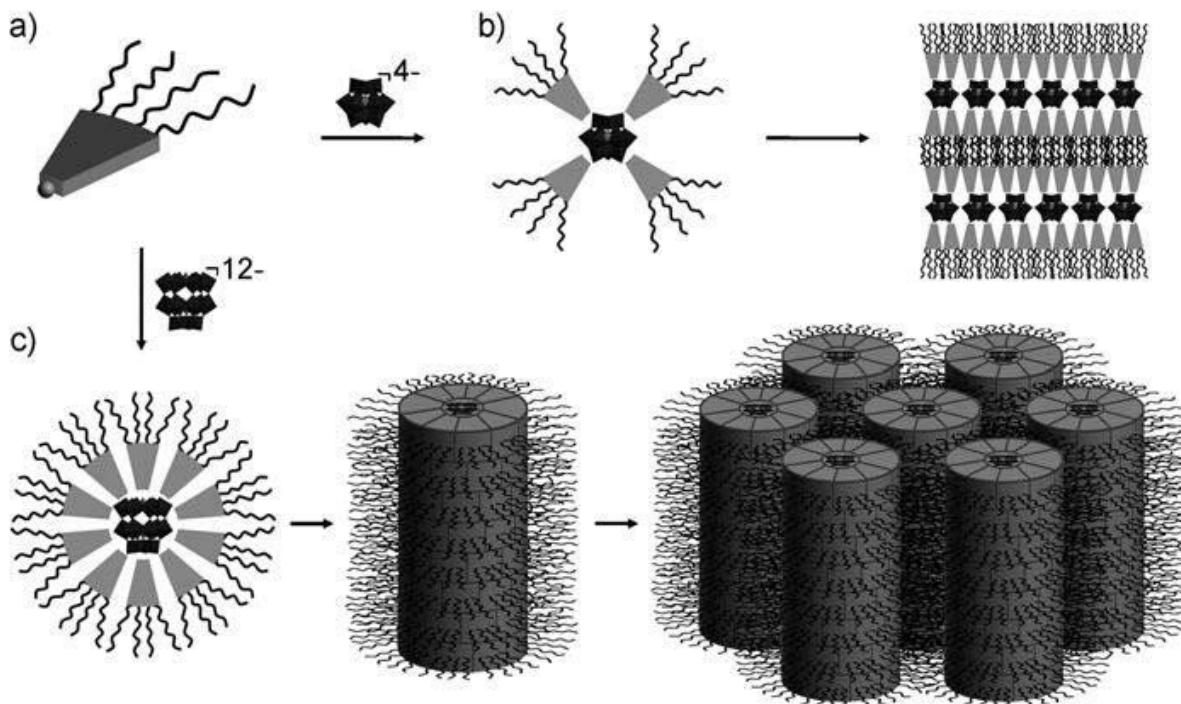


**Figure 1.1.8.** Surfactant-POM hybrid materials are synthesized via predictable self-assembly techniques which are dependent on manipulable parameters such as surfactant cationic charge and POM anionic charge.<sup>64</sup>

This relative ease of synthesis, as compared to their covalently-bound class I counterparts, has led to the production of a wide number of surfactant-POM-based materials for a variety of applications including (photo-)catalysis,<sup>65</sup> medicine,<sup>31</sup> ionic/molecular sieves<sup>8</sup> and electro- and photo-chromism.<sup>32</sup>

The reason for the ionic attachment of surfactants is varied and can include the desire to add the functionality of an organic functional-group,<sup>30</sup> alter the solubility of the anion-complex in a desired solution<sup>41</sup> or to create specific architectures derived from the organization of the combined ionic species.<sup>31, 66</sup> Once synthesized, these materials can be further manipulated by stimuli such as light,<sup>67</sup> changes in pH and solvent effects,<sup>68, 69</sup> which adds further functionality these clusters.

In the work presented within this thesis, a number of different subjects relating to surfactant-POM hybrids will be studied. This includes an investigation into the solution chemistry which forms some of these structures, their thermal stability and decomposition, their possible application as photochromic materials, as well as their interaction with X-rays which are regularly used to measure the properties of these materials.

Table 1.1.1 displayed below contains examples of literature that will aid the reader in understanding the current scene surrounding the study of the subjects covered within this thesis.

**Table 1.1.1.** Notable examples of literature on surfactant-POM hybrids highly-relevant to the subjects covered in this thesis.

<b>Subject(s) Covered</b>	<b>Publication</b>	<b>Reference within this work</b>
General Overview	Dolbecq, A.; Dumas, E.; Mayer, C.; Mialane, P., Hybrid Organic-Inorganic Polyoxometalate Compounds: From Structural Diversity to Applications. <i>Chem. Rev.</i> <b>2010</b> , 110, 6009–6048.	27
Synthesis and structure of POM hybrids	Zhang, T.; Brown, J.; Oakley, R.; Faul, C., Towards Functional Nanostructures: Ionic Self-Assembly of Polyoxometalates and Surfactants. <i>Current Opinion in Colloid &amp; Interface Science</i> <b>2009</b> , 14, 62–70.	32
Synthesis and structure of POM hybrids/ Catalysis	Nisar, A.; Wang, X., Surfactant-Encapsulated Polyoxometalate Building Blocks: Controlled Assembly and Their Catalytic Properties. <i>Dalton Trans.</i> <b>2012</b> , 41, 9832–9845.	30

Photochromism	Dessapt, R.; Collet, M.; Coue', V.; Bujoli-Doeuff, M.; Jobic, S.; C. Lee; M. Whangbo, Kinetics of Coloration in Photochromic Organoammonium Polyoxomolybdates. <i>Inorg. Chem.</i> <b>2009</b> , 48, 574-580.	70
Photochromism	Yamase, T., Photo- and electrochromism of polyoxometalates and related materials. <i>Chem. Rev.</i> <b>1998</b> , 98, 307-325.	58
Thermal Stability	Mestl, G.; Ilkenhans, T.; Spielbauer, D.; Dieterle, M.; Timpe, O.; Kröhnerta, J.; Jentoft, F.; Knözinger, H.; Schlögl, R., Thermally and Chemically Induced Structural Transformations of Keggin-type Heteropoly Acid Catalysts. <i>Appl. Catal. A</i> <b>2001</b> , 210, 13-34.	71
Thermal Stability/ Structure	Soler-Illia, G.; Sanchez, C.; Lebeau, B.; Patarin, J., Chemical Strategies To Design Textured Materials: from Microporous and Mesoporous Oxides to Nanonetworks and Hierarchical Structures. <i>Chem. Rev.</i> <b>2002</b> , 102, 4093-4138.	72
Photochromism/ <i>in situ</i> X-ray photoreduction	Feng, W.; Ding, Y.; Liu, Y.; Lu, R., The photochromic process of polyoxometalate-based nanocomposite thin film by <i>in situ</i> AFM and spectroscopy. <i>Mater. Chem. Phys.</i> <b>2006</b> , 98, 347-352.	73

#### **1.4 Thermal Stability of surfactant-polyoxometalate structures**

As described above, POMs and POM-hybrid materials have seen numerous applications across a wide array of fields and are currently being researched in others, however, their thermal and chemical stability has restricted further application and/or performance in certain applications.

For example, POMs are prone to undergo an irreversible transformation to their bulk-oxide counterparts at high temperatures.<sup>71, 74, 75</sup> This has limited their performance in catalysis applications due to the limitation on reaction temperatures.<sup>75, 76</sup> Production of highly-porous,

high surface-area  $\text{WO}_x$  materials from widely available surfactant-anion self-assembly techniques (described in the previous chapter) would be of significant interest considering the potent (photo-)catalytic properties of tungsten oxides.<sup>77, 78</sup> Unfortunately, the production of porous crystalline  $\text{WO}_x$  from surfactant-encapsulated polyoxometalate (SE-POM) precursors is very difficult. This is because  $\text{WO}_x$  networks produced from the calcination of SE-POMs tend to collapse upon complete organic-template removal, and/or at elevated temperatures ( $> 400^\circ\text{C}$ ).<sup>72, 79, 80</sup> However, this chemical instability has been exploited in other fields, and isopolyanions are regularly used as precursors to deposit their oxide counterparts on substrates.<sup>81-83</sup>

Current understanding as to why porous crystalline  $\text{WO}_x$  is unstable towards organic-template removal and elevated temperatures is incomplete and, to date, few publications that address this question have been produced.<sup>80, 84</sup> A more complete understanding of SE-POM calcination or thermal decomposition, including inorganic phase transformations and surfactant degradation mechanisms, would help address this current gap.

Within this thesis, the thermal stability of a simple surfactant-POM hybrid will be presented, along with the temperature dependent structural and chemical transformations that accompany the compounds thermal decomposition. A decomposition intermediate will also be further studied to investigate its viability as a porous  $\text{WO}_x$  material.

## **1.5 Introduction to photochromism**

Photochromism is the change of a material's absorption spectrum in response to incident electromagnetic radiation. Since this electromagnetic radiation can be provided from the sun (or other ambient sources), photochromic devices are examples of *passive technologies*, meaning that they do not directly require human input to operate. This is advantageous in some applications. One such potential application of this passive technology is transition window-coatings, where these coatings would be dark-coloured during the brightness of the day, limiting the transmission of infrared heating, but transparent at night-time in the absence of incident UV irradiation.<sup>23, 85</sup> Currently, similar functionality is available from *electrochromism*, an example of an active technology that requires the application of an external electrochemical circuit to operate.<sup>23, 86, 87</sup> The need for electrodes makes

electrochromic devices expensive. It is for this reason that the production of commercially viable *photochromic* materials is highly desirable.

Changes in absorption spectra are not the only phenomena that occur in photochromic materials during their colour variation. The transfer of charge that is instigated by the light absorption is useful in the field of photo-catalysis, where many polyoxometalates and their hybridised materials have found commercial applications.<sup>16, 19, 88</sup> Multiple other changes also occur within TMOs upon their interaction with light and subsequent change in optical properties (photochromism), including changes in conductivity<sup>18</sup>, hydrophobicity/hydrophilicity<sup>89, 90</sup>, magnetism<sup>91</sup> and chemical sensitivity.<sup>18, 61</sup> Therefore, advances in the understanding of photochromism has benefits beyond mere colour change. As such, further research of passive TMO-based photochromic materials is beneficial to many fields and has far-reaching impact in scientific research and wider society.

However, the photochromic process in organic-inorganic POM-hybrid materials is not yet completely understood, and so far, these materials have not seen application in commercial photochromic devices. Coloured POM-hybrids are also slow to bleach, with many of these materials taking days to completely de-colour.<sup>21, 92-95</sup> This is obviously disadvantageous in window-coating applications as photo-coloured windows would not bleach over the course of one night. Heating the coloured material or exposure to high oxygen partial-pressures can greatly decrease bleaching times, however, these methods also cause a reduced change in absorbance ( $\Delta$ Abs.) in the following photochromic cycles.<sup>21</sup>

POM-hybrid materials often suffer from photochromic fatigue, meaning that they gradually lose function with increasing numbers of photochromic cycles.<sup>58, 92-94</sup> A number of explanations have been proposed to explain this fatigue, including irreversible side-reactions between the POM and the organic species,<sup>58, 93</sup> as well as the production of deep, highly-stable coloured defects, however there is no general consensus within the field of study. Therefore, further work is warranted addressing the mechanism(s) of POM-hybrid photochromism.

It should be noted that recently, significantly fatigue-resistant photochromic POM-hybrid compounds have been produced.<sup>96</sup> These materials include covalently attached functionalized organic groups to the anion (diarylethenes), whereby the irradiation of a specific wavelength induces a change in the organic molecules conformation resulting in

absorption within the visible spectrum. Irradiation with another wavelength induces the back reaction, reversing the organic molecules conformation and the changed absorbance.

Work presented in this thesis aims to address this incomplete understanding by investigating the chemical and structural changes that accompany surfactant-POM photochromic function.

In this work, the photochromic properties of a simple class II surfactant-POM hybrid is presented. The rate of colouration and bleaching, as well as changes to CTA-W<sub>12</sub> upon photochromism and their relation to photochromic fatigue will also be presented.

### **1.6 Photochromic quality and the photochromic cycle**

As explained in the previous section, photochromism is the change in a material's absorption spectrum in response to the absorption of electromagnetic radiation. This absorption-instigated colouration can be reversed in the absence of incident electromagnetic radiation, a process termed bleaching. A material's colouration and subsequent bleaching is termed its photochromic cycle. A number of parameters can be used to describe the quality of a photochromic material.

A material that exhibits a large  $\Delta\text{Abs.}$  (or analogously a large change in reflectance,  $\Delta R$  or transmittance,  $\Delta T$ ) upon colouration is desired. An ideal photochromic material possesses the following properties:

- (i) The  $\Delta\text{Abs.}$  should occur quickly in response to the appropriate incident electromagnetic radiation. In the absence of the appropriate incident electromagnetic radiation, the coloured material should bleach quickly back to its original, pre-coloured state.
- (ii) The absorption spectrum of the bleached material should match that of the as-prepared, pre-coloured material. The bleached material should then be able to recolour back to the coloured state when the radiation is reapplied at the same rate as the initial colouration, and the recoloured absorption spectrum should match that of the initially coloured material.
- (iii) Once bleached, all subsequent colourations should occur at the same rate and degree as the first, and the coloured material should always bleach back to the pristine, as-prepared state at the end of every cycle.

Of course, all real photochromic materials are a compromise between these attributes. Photochromic materials undergo fatigue with each iteration of the photochromic cycle and

this detrimentally affects the performance of these materials. The result can include incomplete colouration (colouring to a lesser extent as compared to the initial colouration) or incomplete bleaching (retainment of colour at the end of a photochromic cycle), which results in decreased  $\Delta Abs.$  in future cycles. The rate of colouration or bleaching may also decrease with increasing photochromic cycles. The extent to which a photochromic material retains its initial colouration-bleaching properties is termed the material's reversibility. The number of cycles that a material can undergo before it is deemed unfit for photochromic purposes is deemed the photochromic lifetime.

In this work the photochromic properties of a surfactant-POM hybrid will be investigated, including the material's kinetics of initial colouration and bleaching and the extent to which the cycle is reversible.

### **1.7 In situ photoreduction of TMO-hybrids during X-ray-based measurements**

The use of x-rays to characterize the chemical and structural properties of materials and molecular architectures is very common. The proliferation of techniques such as x-ray photoelectron spectroscopy (XPS), small angle x-ray scattering (SAXS), x-ray adsorption spectroscopy (XAS) and x-ray diffraction (XRD) has undoubtedly greatly contributed to the fields of modern science. However, x-rays have sufficient energy to instigate the ionization of atoms.<sup>70, 97-99</sup> Such events create highly reactive free-radicals in organic molecules, and secondary and Auger electron cascades which reduce or oxidize neighbouring atoms and instigate further ionization events.<sup>100-102</sup> Depending upon the type of sample, these events can drastically alter the chemical, and therefore structural, composition of a sample.<sup>101, 103</sup>

The determination of the oxidation states of metallic cations by techniques such as XPS is useful in the many fields that study these materials. This is especially true for materials containing group V and VI transition metal-oxides. For example, the determination of the  $M^{n+}/M^{(n-1)+}$  ratio (where  $M = W, Mo$  or  $V$  and  $n =$  oxidation state) post UV photoreduction in group V and VI metal-oxide based photochromic<sup>60, 73, 95, 104</sup> and photocatalytic<sup>56, 105</sup> materials is a determinant of efficiency. XPS-derived determination of this ratio may return inflated erroneous results, due to the inevitable coincidental photoreduction by x-rays. Of course, the realisation that measurements involving x-ray incidence can change the chemical bonds and oxidation states in these materials is not new.<sup>73,</sup>

<sup>95, 104, 106</sup> However, to the best of our knowledge no quantitative investigation has been carried out thus far examining these inevitable processes in group V and VI transition-metal-oxide inorganic-organic hybrid materials.

Within this work the photoreduction kinetics of a surfactant-POM hybrid is investigated as a function of XPS scan-time. It is hoped that this work will enable researchers studying group V and VI transition metal-oxide hybrid materials in the fields of photochromism and photocatalysis to better understand x-ray derived data of their samples.

### **1.8 Chapter overviews**

In this work, the synthesis, as well as the thermo- and photo-stability of a Class I surfactant-polyoxometalate structure containing the isopolytungstate metatungstate,  $[\text{H}_2\text{W}_{12}\text{O}_{40}]^{6-}$ , and the cationic organic surfactant cetyltrimethylammonium,  $\text{C}_{19}\text{H}_{42}\text{N}^+$  ( $\text{CTA}^+$ ) will be presented in detail. This compound will be designated ‘CTA- $\text{W}_{12}$ ’.

In Chapter 2, the production of the material will be described, including the chemical reactants, synthesis methods and purification techniques used. Imaging, spectroscopic, gravimetric and other techniques used to characterize the studied material’s structural, thermal, optical, and chemical properties will also be described. A description of how the photochromic cycle of CTA- $\text{W}_{12}$  was assessed will also be included.

In Chapter 3, the synthesis of CTA- $\text{W}_{12}$  will be presented, including the  $\text{CTA}^+$ -isopolytungstate pH-dependent solution equilibria that governed its synthesis. The structural characterization of CTA- $\text{W}_{12}$  will also be discussed in detail in this chapter, including the surfactant-packing dependent dynamics that lead to the observed meso- and nano-structure.

In Chapter 4, the thermal-stability of CTA- $\text{W}_{12}$  will be presented, including all observed phase-transformations and thermal decomposition intermediates. The fifth temperature-dependent phase transformation of CTA- $\text{W}_{12}$  will be studied in detail, due to the interesting phase-transformation and highly crystalline lattice that this phase exhibited. The thermal decomposition and crystal-phase transformation profile of the POM containing CTA- $\text{W}_{12}$  will then be compared against a bulk tungsten-trioxide analogue, CTA- $\text{WO}_3$ .

In Chapter 5, the photochromic properties of CTA- $\text{W}_{12}$  will be explored, including the kinetics of the material’s colouration  $\leftrightarrow$  bleaching cycle (as described above) and the maintenance of the measured  $\Delta R$  with each iteration of the photochromic cycle, i.e. the

material's irreversibility/switchability/photochromic-lifetime. The chemical and structural changes that occur during CTA-W<sub>12</sub> photochromism will also be presented, which will form the basis of a discussion on CTA-W<sub>12</sub> photochromic irreversibility.

In Chapter 6, the interaction of soft x-rays with CTA-W<sub>12</sub> will be presented. This includes analyzing the effect of successive XPS scans on the W4f core-electron spectrum in CTA-W<sub>12</sub> and determining the degree of photoreduction of the tungsten centres due to this successive interaction.

In Chapter 7, conclusions will be drawn from the results of my work, with an emphasis on the thermal- and photo-stability of the metatungstate anion within a CTA<sup>+</sup> surfactant matrix. Possible avenues for future work will also be discussed.

## Chapter 2. Methods and Materials

The compounds studied in this thesis were produced by aqueous chemistry, followed in some cases by calcination. In this chapter the methods used to produce the compounds, and the techniques used to characterize them, are described

### 2.1 Chemical synthesis

#### 2.1.1 Synthesis of CTA-W<sub>12</sub>

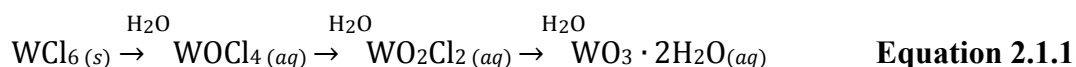
The following chemicals were purchased from Sigma-Aldrich® and used as received: tungsten hexachloride (WCl<sub>6</sub>), cetyltrimethylammonium bromide (C<sub>19</sub>H<sub>42</sub>NBr), ammonium hydroxide (NH<sub>4</sub>OH, 30% in H<sub>2</sub>O), methanol (CH<sub>3</sub>OH), ethanol (C<sub>2</sub>H<sub>7</sub>OH), ammonium metatungstate ((NH<sub>4</sub>)<sub>6</sub>[H<sub>2</sub>W<sub>12</sub>O<sub>40</sub>].4H<sub>2</sub>O), ammonium paratungstate ((NH<sub>4</sub>)<sub>10</sub>[H<sub>2</sub>W<sub>12</sub>O<sub>42</sub>].4H<sub>2</sub>O), chloroform (CHCl<sub>3</sub>) and deuterated chloroform (CDCl<sub>3</sub>). Deionized H<sub>2</sub>O was used in all reactions unless otherwise stated.

Although a range of substances were produced by wet chemical synthesis, most of the work described in this chapter focuses on the preparation and properties of the hybrid surfactant-polyoxometalate compound (C<sub>19</sub>H<sub>42</sub>N)<sub>7</sub>[H<sub>2</sub>W<sub>12</sub>O<sub>40</sub>]Cl·2H<sub>2</sub>O. For convenience, this compound will be designated as CTA-W<sub>12</sub> in the discussion that follows.

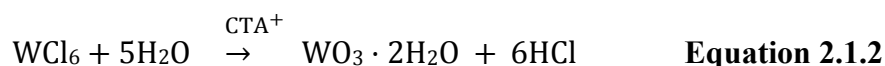
Calcination of the compounds produced by wet chemistry caused further changes. For example, CTA-W<sub>12</sub> underwent a series of sequential phase transformations and chemical changes when heated to 800°C. The particular crystalline compounds in this sequence will be designated as Phase I (equals CTA-W<sub>12</sub>), Phase II, Phase III *etc* through to Phase VIII.

The method used to synthesize the studied compound employs a ‘one-pot’ synthesis approach, in which the POMs and resulting SEP array is formed in the one reaction vessel.

A typical method to synthesize CTA-W<sub>12</sub> was as follows: 0.62 g (0.0017 mol) of CTA-Br was placed in a 1 L beaker and dissolved in 100 ml of de-ionized H<sub>2</sub>O, with the aid of a stirrer-bar at 70°C to promote dissolution. Once the solution turned clear the temperature was reduced to the ambient and 3.05 g of WCl<sub>6</sub> (0.0077 mol) was added, turning the solution black. This solution was then allowed to react overnight (~16 hrs), which then turned yellow due to the hydrolysis of WCl<sub>6</sub> to WO<sub>3</sub>·2H<sub>2</sub>O within the CTA<sup>+</sup> micelles. The process of WCl<sub>6</sub> hydrolysis is described in in Equation 2.1.1.



The complete equation that describes the hydrolysis of WCl<sub>6</sub> within the CTA<sup>+</sup> micelles is given in Equation 2.1.2.



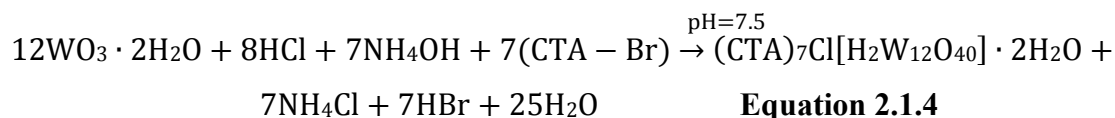
As can be predicted, the pH of the resulting WO<sub>3</sub>·2H<sub>2</sub>O, HCl and CTA<sup>+</sup> suspension is quite acidic, and was measured to be 0.5 with pH-paper. Interestingly, pH measurements differed between pH-meters and pH-paper, with pH-meters routinely returning readings that were below that measured by the paper. Three different pH meters were used to investigate this discrepancy initially, with all meters returning similar readings. It is possible that this is due to the fact that the reaction would likely be occurring within micelles of CTA<sup>+</sup>, considering the relative hydrophobicity of WCl<sub>6</sub> and WO<sub>3</sub>. This would cause the pH within the micelles containing WCl<sub>6</sub>, WO<sub>3</sub> and HCl to be quite different from the wider, outside solution. It is possible that the meter was more sensitive to the solution within the CTA<sup>+</sup> micelles and returned lower readings than that of the pH paper. Because of this, and to maintain consistency, pH paper was used throughout my research to measure the pH of solutions. All pH measurements described within this work are based on 14-tier coloured pH paper, which allowed accurate pH readings to the nearest 0.5 units.

30% NH<sub>4</sub>OH was then added to the yellow CTA-WO<sub>3</sub>·2H<sub>2</sub>O suspension until pH = 7.5 (usually around 4.5 ml, 0.0385 mol), instigating a colour-change from yellow to white as

WO<sub>3</sub>·2H<sub>2</sub>O was transformed to [H<sub>2</sub>W<sub>12</sub>O<sub>42</sub>]<sup>6-</sup>. The net equation that gives [H<sub>2</sub>W<sub>12</sub>O<sub>42</sub>]<sup>6-</sup> from WO<sub>3</sub>·2H<sub>2</sub>O is presented in Equation 2.1.3.



The full chemical equation that describes what is occurring both within the CTA<sup>+</sup> micelles containing the hydrophobic WO<sub>3</sub>·2H<sub>2</sub>O and the outside wider solution when CTA-W<sub>12</sub> is formed is given in Equation 2.1.4.



This reaction was allowed to proceed for a further 16 hours (overnight), after which the product was filtered with the aid of double filter-paper and a Büchner funnel before being washed with de-ionized water five times. The wet CTA-W<sub>12</sub> was then placed upon a watch-glass and allowed to dry in the dark environment of a draw slightly ajar, under an upturned beaker for two days, before being ground into a fine powder with a mortar and pestle.

### 2.1.2 Synthesis of CTA-WO<sub>3</sub>

An analogue of CTA-W<sub>12</sub> was also investigated, designated as CTA-WO<sub>3</sub>. This compound is similar to CTA-W<sub>12</sub>, in that it also composed of alternating layers of tungsten oxide and the surfactant CTA<sup>+</sup>. However, the tungsten oxide in CTA-WO<sub>3</sub> is in the form of the dihydrate trioxide, WO<sub>3</sub>·2H<sub>2</sub>O, rather than the [H<sub>2</sub>W<sub>12</sub>O<sub>42</sub>]<sup>6-</sup> isopolytungstate present in CTA-W<sub>12</sub>.

CTA-WO<sub>3</sub> synthesis closely followed that of CTA-W<sub>12</sub>, differing only in that NH<sub>4</sub>OH was not added; once the 0.62 g CTA-Br (0.0017 mol) had completely dissolved in 100 ml of de-ionized H<sub>2</sub>O 3.05 g (0.0077 mol) of WCl<sub>6</sub> was added, which turned the clear solution black. The resultant suspension was then allowed to hydrolyze overnight (16 hours) at room-temperature, which turned from black to yellow, before being filtered, washed and dried as detailed previously.

### 2.1.3 Soxhlet extraction

The product yielded from the fifth temperature-dependent phase-transition of CTA-W<sub>12</sub>, phase V (stable between 230 and 320°C), showed a well-developed X-ray diffraction pattern reminiscent of a highly crystalline hexagonally-close-packed phase. Such a material may have potential applications as a catalyst-bed or proton-conductor if it could be made more porous by removing the remaining organic CTA<sup>+</sup> thermal decomposition intermediates, and therefore this phase was investigated in more detail. Soxhlet extraction was used to remove the remaining organically-soluble material as described below:

Soxhlet extraction<sup>107</sup> is a separation technique that takes advantage of the differential solubility of a mixture of compounds in a particular solvent, and works well when the target compound is insoluble in a specific solvent and the other components are very soluble. The solvent, held in a round-bottom-flask (RBF), is heated to instigate boiling. The resulting vapours rise into a distillation arm and comes into contact with the sample which is held in a thick filter-paper thimble. The soluble fraction of the sample is then dissolved and consequently washes through into the base of the apparatus. The solvent is recycled by evaporation because it rises into a condenser column, resulting in condensation before the liquid falls back into the distillation arm. A siphon attached to the distillation arm allows for emptying back into the RBF once it has become full. The solvent and dissolved fraction then continues within the above process until heat is removed from the apparatus. The insoluble fraction can then be collected from the filter-paper thimble. With this method, it was possible to remove the organically soluble fraction from mixtures containing Phase V and CTA<sup>+</sup> decomposition products. After Soxhlet extraction, the organically soluble fraction that had been dissolved out of the sample was purified by washing three times with water to remove excess solvent (CHCl<sub>3</sub>), and left to dry in a draw. A diagram of a Soxhlet apparatus is depicted in Fig. 2.1.1.

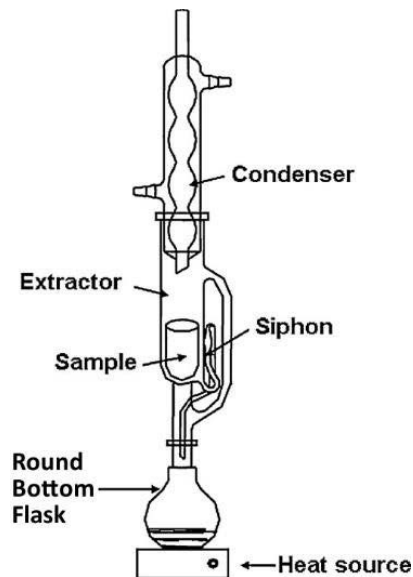


**Figure 2.1.1.** Soxhlet apparatus for the purpose of Soxhlet extraction.<sup>107</sup>

## **2.2 Characterization techniques**

### **2.2.1 Powder X-ray diffraction**

Hard X-rays ( $> 10$  KeV), with very short wavelengths compared to the size of atoms, typically interact with them primarily with their electrons, due their relative abundance and effective cross-sectional area. This interaction is largely elastic, meaning that for the vast majority of instances the energy of the X-ray before the interaction is the same as the scattered X-ray after the interaction. In crystals where the atoms (and associated electrons) are located at regular intervals, the interaction of a beam of monochromatic X-rays with the crystal produces regular array of spherical waves. These spherical waves will interfere with each other either constructively resulting in an increase in amplitude, or destructively resulting in a decrease in amplitude, dependent upon the phase of the interfering waves. This interference is predicted by *Bragg's Law*, Equation 2.2.1.

$$2d \sin\theta = n\lambda \qquad \text{Equation 2.2.1}$$

Where  $d$  is the distance between planes of atoms in a crystal,  $\theta$  is the incident angle of the interacting X-ray,  $n$  is any integer and  $\lambda$  is the wavelength of the interacting X-ray. The

destructive and constructive interference of scattered waves will therefore produce a pattern of dark and bright regions on a detector's surface. This pattern is termed a *diffraction pattern*.

In single crystal X-ray diffraction (XRD) a crystal is mounted on a goniometer that positions the sample relative to an incident beam of X-rays at selected orientations to produce 2D diffraction patterns from particular atomic planes. Because each spot in the pattern arises from constructive interference, as described by Bragg's Law (Equation 2.2.1), each spot corresponds to a particular variation in electron density, and by correlation, distance between atomic positions. The intensity of the spot is dependent on the number of X-ray interactions with the particular atom, which in turn is dependent on the electron density around the atom and therefore the type of atom (element). This information can be combined to yield the total electron density within the diffracted plane. The crystal in the goniometer can be rotated to produce a series of 2D diffraction patterns which can then be analysed and combined to form a 3D model of the atoms within the crystal. This allows for the calculation of the degree of symmetry within the crystal, and therefore the determination of the crystal's space group (type of symmetry) and unit cell (the smallest unit of atomic positions that can be repeated indefinitely to construct the entire crystal).

The structure of sufficiently crystalline powders can also be determined by XRD measurement and analysis. Because powders are randomly orientated, every possible atomic plane within the sample is incident to the X-ray beam at each instance. Some planes will be at the correct orientation to be diffracted by the X-rays and will produce a diffraction pattern. Rotating the sample relative to the X-ray incidence can increase the randomness of the sample and mitigate any possible anisotropy. A flat, circular detector is placed at a specific distance from the sample to collect the diffraction patterns scattered from the powder. Due to the randomness of the scattering, these patterns manifest as a series of circular rings around the beam axis (rather than the pattern of bright spots collected in single crystal XRD). The angle between the beam and the ring, termed the scattering angle and denoted as  $2\theta$ , can then be analysed to determine atomic spacings in accordance with Bragg's Law (Equation 2.2.1). The information gathered in powder X-ray diffraction (P-XRD) is usually displayed as a plot of diffracted intensity versus  $2\theta$ , termed a *diffractogram*.

In this work P-XRD was performed on two instruments, the X-ray diffractometer available at UTS (Bruker® D8 Discover XRD), and the P-XRD beamline at the Australian

Synchrotron, Melbourne. The latter was used when more accurate patterns (resolution of  $0.01^\circ$  or better) were required or when the effect of *in situ* heating or irradiation was studied. The Bruker<sup>®</sup> D8 Discover employs a Cu-K $\alpha$  radiation source with an emitted photon-energy of 8.05keV (1.54184 Å). Measurements were typically made from  $2-80^\circ 2\theta$ , with a typical scan rate of  $3^\circ 2\theta/\text{min}$  on a rotating stage.

Synchrotrons are a type of particle accelerator that traps travelling electrons in a circular ring (termed a storage ring) via the use of strong magnets. Because the storage ring is circular, the particles are always accelerating (due to the constant change of velocity), and resultantly constantly emitting radiation (in accordance to the laws of electromagnetism). To take advantage of this, most synchrotrons are fitted with beam-lines, sections of the synchrotron that syphon off this radiation for use in experimental procedures. Because of the usual accelerating voltages employed by synchrotrons (GeV), and the relativistic effects resultant from this velocity, the radiation emitted by the accelerating particles typically falls within the hard X-ray to infrared range. Modern synchrotrons are much more intense than more conventional X-ray (such as X-ray tubes) sources used in traditional X-ray diffractometers (such as that described above), and is one of the reasons why such facilities are highly sought after among researchers. Because intensity of the diffracted light in P-XRD, and therefore the quality of the diffractogram, is also dependent on the intensity of the X-ray source, Synchrotron X-ray beam-lines are able to produce high-quality diffractograms in much less time compared to traditional P-XRD instruments employing X-ray tube sources. Such speed in data collection is very useful when studying changing systems, such as using heating ramps to monitor temperature-dependent phase transitions, and the monitoring of radiation dose-dependent crystallographic changes. Both of these cases are studied within the work covered in this thesis.

Within my PhD I travelled to the Australian Synchrotron on two occasions (February and November of 2015). On both occasions I used the P-XRD beam-line to gather patterns of the different crystallographic phases that were produced when CTA-W<sub>12</sub> was heated from  $30^\circ\text{C}$  to  $800^\circ\text{C}$ , (first visit) and when it was subjected to UV radiation (second visit). Samples were mounted in a 0.5 mm silica capillary which was then mounted in the P-XRD beamline. Complete patterns ( $3-100^\circ 2\theta$ ) were collected every 2 min. Each set of two progressive patterns were averaged, thereby producing a pattern every 4 min. The photon energy that was

employed in my first visit (thermal work) was 18.00 keV ( $\lambda = 0.6888 \text{ \AA}$ ) and 12.032 keV ( $\lambda = 0.8254 \text{ \AA}$ ) for my second visit (UV irradiation work). At each visit a reference pattern of the as-prepared sample was recorded by collecting a diffractogram a fresh (not irradiated or heated) sample of CTA-W<sub>12</sub> in the beam-line.

During my first visit, the Eurotherm<sup>®</sup> hot air blower was employed to heat samples between room-temperature ( $\sim 23^\circ\text{C}$ ) to  $800^\circ\text{C}$ . The UV radiation source employed during my second visit was the Dynamax<sup>®</sup> BlueWave<sup>™</sup> 50 with a spectral output of  $1 \text{ W/cm}^2$  within 280-320nm. The source originated from an optical fibre which was then aimed at the mounted capillary. A remote foot-pedal outside the beam-line housing allowed the source to be turned on and off at will.

### 2.2.2 UV-visible spectroscopy

Photons interact with the electrons of atoms. Valence electrons are at sufficient energy positions within the atom such that absorption of ultra-violet and visible-light photons promote said electrons to higher energy positions (i.e.  $e_{\text{HOMO}} \xrightarrow{\gamma} e_{\text{LUMO}}$ ). When these promoted electrons relax back to original positions, radiation is emitted equal to the difference between these energy levels, as per the conservation of energy. However, in some cases this energy may be converted to heat within the sample upon electron relaxation.

The photons transmitted through or scattered by a sample can be detected and analysed to provide a transmission, or reflection spectrum from the sample, with the difference between light in and light out equal to the amount absorbed. Exposing a sample to a range of wavelengths of light, and measuring the transmitted or reflected photons, will therefore produce a spectrum of transmitted or reflected light. These spectra provide empirical information on how the target material interacts with UV and visible light and can be analysed to yield information on the valence electrons within the sample.

Two types of UV-vis spectroscopy were employed during the course of this work; UV-vis absorbance spectrometry and UV-vis reflectance spectrophotometry. UV-vis absorbance spectrometry was used for aqueous samples and employs the Beer-Lambert Law to provide a spectrum of absorbance versus incident wavelength. This spectrum provides explanation of the colour of the sample, as well as the energetic location of electron transitions (described earlier), and therefore rudimentary chemical information.

UV-vis reflectance spectrophotometry measures reflected photons from a solid surface, producing a spectrum of excitation energy versus intensity of detected reflected photons. The collected spectrum, with intensity  $I$ , is then compared against the spectrum of a known standard (such as an aluminium mirror) with intensity  $I_0$ . The quantity  $I/I_0$ , also known as reflectance, is then plotted against the incident light energy, producing a UV-vis reflectance spectrophotometry spectrum. This spectrum provides angular dependent information on the sample's optical transitions and colour.

In this work, UV-vis absorbance spectrometry was performed on the Shimadzu<sup>®</sup> UVmini-1240V<sup>™</sup>, within a quartz-cuvette using methanol as the solvent and baseline. UV-vis reflectance spectrophotometry was performed on the Agilent<sup>®</sup> Cary<sup>™</sup> 7000 UV/VIS/NIR UMS, using an aluminium mirror as a reference.

### **2.2.3 Scanning electron microscopy**

A scanning electron microscope (SEM) injects a beam of electrons onto the surface of a sample. These electrons interact elastically and inelastically with the atoms of the sample, instigating an array of radiative processes which can then be detected and consequently analysed by the instrument's software. If an electron from the electron beam imparts a sufficient amount of energy to the electrons of the imaged sample, the electron can become ejected from the sample. These inelastically ejected electrons are termed secondary electrons (SEs), and can be detected by the instrument and analysed by software to determine the origin of ejection, thus forming topological images of the sample's surface. Because electrons are massive compared to photons, their wavelength when travelling is quite small (dependent upon the de Broglie wavelength). This allows for much greater resolution of the sample surface, when compared to conventional light-microscopy, and hence much higher magnification images are possible with SEMs.

Concurrent with the process of sample ionization and SE generation is the production of X-rays from the imaged sample. If a beam of electrons imparts a sufficient amount of energy to a core-level (deeper than the valance-band) electron in the sample and causes ionization, a more energetic electron will relax to fill this vacancy, consequently releasing radiation. Due to the energy levels involved with this process the radiation released from these relaxation processes are X-ray photons. Because the electron levels within an atom are

unique to the specific element, these X-rays can be detected and analysed to determine the elemental make-up of the sample surface. This technique is called Energy-Dispersive X-ray Spectroscopy (EDX).

A SEM was used in this work to produce high-magnification images of the topology of samples and determine surface elemental morphology with EDX. Two SEMs were employed to achieve this; the Zeiss<sup>®</sup> Supra 55VP SEM and the Zeiss<sup>®</sup> Evo SEM. EDX was carried out with the Bruker<sup>®</sup> EDX Detector.

#### **2.2.4 Transmission electron microscopy**

A transmission electron microscope (TEM) employs a beam of electrons which is transmitted through a thin sample. These electrons interact elastically or in elastically with the atoms of the sample, with the degree of interaction proportional to the local electron density. Once transmitted the electrons arrive at the detector (usually a charge-coupled device), after which the instrument software analyses the direction and energy of the transmitted electrons which is used to produce a 2D image.

Due to the direct method of detection, TEMs are able to produce images with much higher resolution/magnification than SEMs (which detect scattered secondary electrons). Since these interactions are heavily dependent upon local electron density, TEM images provide useful structural information about a sample. Assuming sufficient resolution, nanoscopic features such as crystallographic planes, atomic lattices and organic/inorganic regions can easily be seen within a TEM image.

Within this work TEM images were used to calculate the lamellar spacing of selected samples, which complemented P-XRD data. The TEM used within my PhD was JEOL<sup>®</sup> JEM-2200FS Field Emission Microscope at the University of Sydney, operated by UTS staff-member Dr Annette Dowd.

#### **2.2.5 X-ray photoelectron spectroscopy**

X-ray photoelectron spectroscopy (XPS) involves projecting a beam of X-rays upon a sample and detecting and analysing the liberated electrons resultant from ionization events. All ground-state electrons are bound to the parent atom at particular bond strength, or binding energy. If this binding energy is overcome, such as via X-ray photon absorption, the electron

will become ionized and hence travel away from the nucleus. This liberated electron is then analysed, once it reaches the detector, to determine the incident kinetic energy resultant from ionization. Because electron binding energies are specific to particular electron orbitals and respective elements, the electron's ionization is completely dependent upon incident X-ray energy. In this way, the energy of incident X-rays can be tuned to the binding energies between specific electron orbitals to determine the type and degree of chemical bonding in a compound. With these methods, XPS spectra of binding-energy versus ionization counts can be produced, proving valuable depth and spatially dependent elemental information.

In this work, XPS was used to elementally characterize samples, mapping chemical bonding, and to measure the changes in binding energy of  $W_{4f}$  orbitals prior to and directly after photo-colouration. The XPS instrument used in this work was the Thermo Scientific® ESCALAB250Xi, operated by Dr Bin Gong at the University of New South Wales. The instrument utilized monochromated Al K- $\alpha$  (1486.68 keV) radiation at 120 W. The spectrometer was calibrated using  $Au_{4f7}$ ,  $Ag_{3d5}$  and  $Cu_{2p3}$  lines at 83.96, 368.21 and 932.62 eV respectively, at a  $C_{1s}$  binding-energy reference (284.8 eV for adventitious hydrocarbon)

Scans presented in Chapter 5 were analysed with the XPS fitting software CasaXPS, whilst the scan presented in Chapter 6 were analysed with fitting software Fityk (<http://fityk.nieto.pl>). The separation between all presented  $W(4f_{7/2})$  and  $W(4f_{7/2})$  doublets was fixed at 2.2 eV, and the ratio between their areas and full-width-half-maximum (FWHM) set at 4:3 and 1:1, respectively. Peaks were fitted using a Nelder-Mead<sup>108</sup> fitting method after performing a Shirley-type background subtraction when using Fityk (Chapter 6). The  $W_{5p_{3/2}}$  satellite peak was not considered within the fitting parameters when using Fityk, due to its non-contribution to the  $W_{4f}$  spectrum, and hence influence on the determination of tungsten oxidation states.

### **2.2.6 Infrared and Fourier transform infrared spectroscopy**

Mid-infrared radiation ( $400-400\text{ cm}^{-1}$ ) is within the appropriate frequency range to excite resonant vibrations of molecular bonds. The energy of the vibration is directly related to the structure of the bond, i.e. the geometry and strength/length of the bond and the masses of the atoms associated with the bond as well as the degree to which the incident light couples with the excited mode. Such vibrations include symmetric stretching, asymmetric stretching,

rocking, wagging and twisting of molecular bonds. Because the resonance of the vibration is directly related to the frequency of incident infrared (IR) light, IR spectroscopy can be used to identify the frequency/energy locations of molecular vibrations. This information can then be used to decipher the bond type, and hence, chemical composition of the excited groups.

Only bonds that exhibit a change in dipole moment, a difference of electric charge across the bond, are able to be excited by mid-infrared radiation in this way. Because of this, symmetrical bonds that possess the same atom at both sides of the bond (such as diatomic gases) are not observed in IR spectroscopy. However, such molecules may be polarizable, and hence, are visible with Raman spectroscopy (described in the proceeding section). In this way, Raman and IR spectroscopies are complementary, and both should be used to form a more complete analysis of the sample being investigated.

Typically, lattice vibrations, also called phonons, of solid compounds also fall within this energy window, and hence, are visible to both IR and Raman spectroscopies. As such, these spectroscopic techniques can also be used to identify the energetic position, and hence type, of the phonon excited, contributing to the characterization of the investigated sample.

IR spectra show the intensity of the excited vibration (number of photons absorbed by the mode) plotted against the energy location of the vibration (typically in wavenumbers,  $\text{cm}^{-1}$ ). The resulting peaks can thus be assigned to specific molecular bonds within the investigated sample.

Bulk samples are typically too opaque for IR spectroscopy. To account for this samples are usually prepared for IR spectroscopy by diluting the target compound in an IR-translucent material (such a simple salt, e.g. KBr). The mixture is then pressed into a pellet before being analysed by the instrument.

Most modern IR-spectrophotometers are Fourier transform infrared (FT-IR) spectrophotometers. This is due to the large increases to both the speed of measurement, and improvement in the produced spectrum's signal-to-noise ratio (when compared to conventional scanning IR spectroscopy). This is possible due the employment of a wide-range excitation source (as opposed to a monochromatic source used in conventional IR). The sample's absorption of this source is then analysed with an algorithm, the Fourier transform, to determine the energy location of the absorbed light.

In this work (FT-)IR spectroscopy was used to identify molecular bonds within prepared samples, contributing to the characterization of target compounds. A Nicolet® 6700 FT-IR Spectrometer was used to do this.

### **2.2.7 Raman spectroscopy**

The adsorption of visible and IR light causes the molecular bonds to vibrate and rotate, as described in the previous section. This adsorption causes the molecule to be excited to a short-lived virtual energy state, with the energy increase equal to the energy of the absorbed photon. Most of this light is quickly emitted, with the energy of the emitted photon equalling its energy at incidence, a type of elastic scattering termed *Rayleigh scattering*. However, if the energy of the final state (after scattering/emission) of the molecule is higher or lower than the initial state (before scattering/emission), then the difference between these states is imparted on the emitted photon. If the difference is positive, then the emitted photon will be lower in energy compared to its energy before interaction. This inelastic scattering mechanism is termed a *Stokes shift*. If the difference is negative, then the photon will have a higher energy, which is termed in *anti-Stokes shift*. The intensity of Stokes/anti-Stokes shifted photons (collectively termed *Raman shifted*) is proportional to the polarizability of the excited vibrational mode. The energy required to excite a particular vibrational mode is dependent upon the strength/length of the bond, and hence bond-type, as described previously. Therefore, spectra of inelastic scattering intensity plotted against the energy location of observed shifts will yield information on the type of molecular bonds within an investigated sample surface.

Because many symmetrical molecules are polarizable, they can be analysed with Raman spectroscopy, unlike in IR spectroscopy. However, molecular bonds that are not polarizable are not visible to Raman spectroscopy, although they may still vibrate in response to incident IR light and therefore visible with IR spectroscopy. In this way, Raman spectroscopy is said to provide complementary information when used in conjunction with IR spectroscopy. In this work a Renishaw® inVia™ confocal Raman microscope employing a 633 nm laser was used to excite and observe Raman modes in investigated samples.

### 2.2.8 Thermogravimetric analysis and differential thermal analysis

Thermogravimetric analysis (TGA) involves the continual recording of a sample's weight as it is heated. When sufficiently heated, compounds will progressively change in mass as the sample decomposes into volatile components (lose mass) or reacts with the atmosphere (e.g. oxidation with O<sub>2</sub>) to form new bonds (gain mass). This change in mass can be plotted against temperature to form a mass vs temperature plot, or more commonly an initial mass % vs temperature plot. This information can be used to derive a number of fundamental properties of the sample, such as thermal stability, hydration and organic content.

The first-derivative of this curve can also be plotted against temperature, commonly termed a DTG plot, consequently highlighting the temperature ranges of mass-changes and the relative magnitude of mass-change events. This data also makes it easier to identify the physical component ratios within an analysed sample, e.g. organic:inorganic ratio within a metal-organic framework, as well as the thermal stability of the decomposing sample and the possible decomposition products at particular temperatures.

Similar to TGA, differential thermal analysis (DTA) involves the progressive heating of a sample while recording the temperature of the sample and an inert reference. The temperature difference between the sample and the inert reference is then plotted against the temperature of the instrument to form a DTA plot. This plot highlights points where the sample was at a higher temperature than the reference (exothermic), or lower than the reference (endothermic). This information can be used to decipher heat-instigated changes within a sample, such as melting, crystallographic phase changes, liquid-crystal clearing points and combustions.

The type of atmosphere that a sample is heated in will affect the TGA and DTA profile of the analysed sample. Oxidative atmospheres (such as air and O<sub>2</sub>) will promote oxidative reactions as the sample is heated. Inversely, reducing atmospheres (such as H<sub>2</sub> and propene) will promote reductive reactions, and inert atmospheres (such as N<sub>2</sub> and Ar) will not interact chemically with the sample (at the measured temperatures). Therefore, a number of different atmospheres can be used when carrying out TGA-DTA to investigate the thermal properties and transitions of a compound as it is subjected to different chemical environments.

Within this work, the SDT Q600<sup>®</sup> V20.9 was used to produce TGA and DTA plots, typically operating at a heating rate of 5°C/min, from 30°C to 800-950°C employing either air or N<sub>2</sub> with a gas flow-rate of 100 ml/min.

### **2.2.9 Nuclear magnetic resonance spectroscopy**

Atomic nuclei that possess an unequal number of protons and neutrons, or an odd number of protons inherently have a non-zero spin, and therefore the nucleus has angular momentum and a corresponding magnetic moment. Under a magnetic field, these nuclei will absorb and re-emit photons equal to the energy differences in the nuclei's spin-levels, which in turn are dependent on the strength of the applied magnetic field. This absorption and re-emission of photons by nuclei is a resonant process, hence the name nuclear magnetic resonance (NMR), and can be described with a characteristic frequency (measured in Hz).

Electron shells around these nuclei, due to their own inherent charge and spin, produce a magnetic field in the opposite direction to the nucleus. This has a 'shielding' effect on the parent nucleus and reduces the magnitude of the applied magnetic field affecting the resonating nuclei. Accordingly, the spin energy-levels are reduced, as well as the corresponding resonant frequency. This shifting of the resonant frequency in response to the local electron-density is termed a 'chemical shift'. As such, nuclei within a larger local electron-density as compared to the isolated elementary atom, due to electron donation (reduction) or proximity to electronegative species (such as O and halides) will resonate at a lower frequency. This chemical shift to lower frequency is termed 'upfield'. Inversely, atoms that are within a lower electron-density, due to oxidation or proximity to cations, will resonate at a higher frequency. Accordingly, this chemical shift is termed 'downfield'. Upfield and downfield chemical-shifts are quite small, and usual deviations are on the order of millionths. NMR instrument software takes advantage of this and most NMR spectra are recorded in intensity vs parts-per-million (ppm).

Because the intensity of an NMR signal is proportional to the number of nuclei resonating at a particular frequency, the intensity of the peaks in an NMR spectrum can be used to determine the number of nuclei within a specific chemical environment. Along with the knowledge of how particular nuclei can be shielded, and to what degree, NMR spectra can be used to build an accurate representation of the studied molecule.

Within this study proton NMR ( $^1\text{H}$ -NMR) spectroscopy was employed to characterize prepared compounds, and to investigate the chemical changes that occurred due to thermal decomposition. This was achieved with an Agilent Technologies<sup>®</sup> NMR spectrometer, operating at a magnetic field strength of 500.3 MHz. The spectra displayed are an average of 16 scans, collected with a relaxation delay of 1.00 s and a pulse angle of 60°.

#### **2.2.10 Microanalysis/combustion analysis**

Combustion analysis (a form of microanalysis) can be used to determine an organic or organic-hybrid sample's elemental composition, thereby allowing the calculation of a sample's empirical formula. Within this technique, small amounts of sample are combusted (into  $\text{CO}_2$ ,  $\text{H}_2\text{O}$  and  $\text{N}_2\text{O}$ ) which are then quantitatively analysed to determine the molar ratio of the original C, H and N components. Combined with other techniques, such as TGA, and knowledge of synthesis parameters, the empirical formula an organic or organic-hybrid compound can be determined.

Within this work, several combustion analyses (also termed C,H&N analyses) was performed by the University of Otago, New Zealand.

#### **2.2.11 CTA-W<sub>12</sub> photochromism investigation**

Photochromism can be described as the reversible colouration of a material by the material's interaction with an applied electromagnetic field, as will be described in detail in Chapter 5. Colouration is typically instigated by the absorption of electromagnetic radiation by the material, which culminates in the emergence of an excited state that absorbs light in differing spectral regions as compared to the original un-excited, or as-prepared state. The loss of this colour, a process termed bleaching, is the reverse reaction of this excitation.

In this work the photochromic properties of the sample CTA-W<sub>12</sub> was investigated. To achieve this CTA-W<sub>12</sub> was subjected to the same UV source as described above in the Synchrotron section, Section 2.2.1, to instigate photo-colouring (Dynamax<sup>®</sup> BlueWave<sup>™</sup> 50). Samples were typically mounted on an aluminium stub and irradiated for a specified time, usually 1 or 3 hours, depending on the experiment (further detail will be given in figure captions). The photo-coloured samples were then quickly placed in the appropriate

instrument for the desired measurement to be carried out (UV-vis reflectance, FT-IR, Raman or XPS).

To determine the degree of the colour change (change diffuse reflectance,  $\Delta R$ ) due to photo-colouration/reduction, UV-vis reflectance spectroscopy was used to collect the reflective UV-vis spectrum of the as-prepared samples and immediately after UV exposure. Photo-coloured samples were then left in the dark under an upturned container for 24 hours or more to allow for complete bleaching before proceeding exposures. Chemical changes that may have occurred due to UV irradiation and consequent photochromic cycling were investigated by FT-IR, Raman and XPS.

### **2.2.12 Hysteresis study**

A hysteresis study was conducted on the photochromism of CTA-W<sub>12</sub> in order to determine the reversibility of the material's colouration-bleaching cycle, an important performance parameter of all photochromic materials. To achieve this, a small enclosed plastic rectangular box was 3D printed using a XYZprinting<sup>®</sup> Da Vinci Pro 3D printer. Two small openings were made in the box; one on the side so that the DYNAMAX<sup>®</sup> BlueWave 50 UV lamp could penetrate the interior, and another at the top so that a white-light source could be shone through. A thin layer of CTA-W<sub>12</sub> particulates was placed at the bottom of the box which was lined with reflective aluminium foil to maximize the incidence of the UV lamp's light upon the sample. Visible light spectra of the sample were recorded by an Ocean Optics<sup>®</sup> visible light spectrometer which was connected to the white light source on top of the box. The entire experimental set-up was fixed to the laboratory bench in order to restrict sample movement and maintain constant irradiance from the lamp across the entirety of the experiment. A diagram of the experimental set-up is depicted below, Figure 2.2.1:

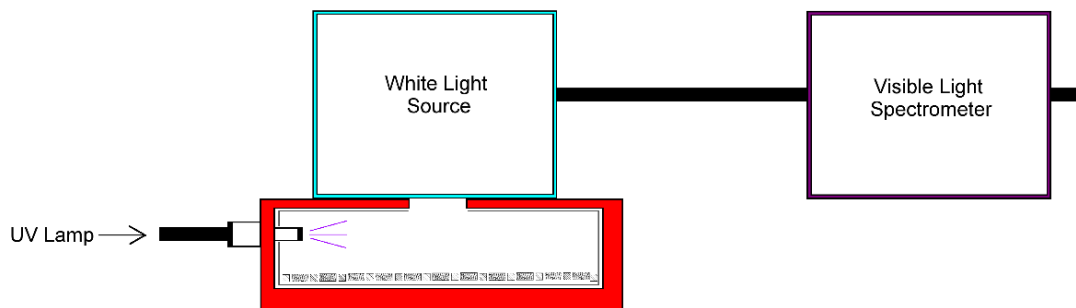


**Figure 2.2.1.** Experimental set-up for CTA- $W_{12}$  hysteresis study.

Each photochromic cycle consisted of 2 hours of UV irradiation followed by 48 hours of bleaching. Visible light spectra of CTA- $W_{12}$  were collected for the as-prepared/as-deposited sample, after each period of 2 hours UV irradiation (coloured state) and after each 48 hour bleaching period (bleached state). Spectra were also collected every 15 min during the first irradiation period in order to determine the colouration kinetics of CTA- $W_{12}$ . A total of 18 cycles were performed for the hysteresis experiment.

### 2.2.13 Gas chromatography-mass spectrometry

Gas chromatography-mass spectrometry (GC-MS) was used in this work to identify products of photo-redox reactions between  $[H_2W_{12}O_{40}]^{6-}$  and  $CTA^+$  during CTA- $W_{12}$  photochromism. GC-MS is a common analytical technique used to identify differing molecules within a tested sample. This is achieved through the mutual application of gas chromatography (GC) and mass spectrometry (MS).

The GC within GC-MS involves analysis of a sample that has been previously dissolved in an appropriate volatile solvent. Within this study, chloroform,  $CHCl_3$  was used. This mixture is mixed with an unreactive carrier gas, such as helium or  $N_2$ , and thus becomes vaporized. This gaseous mixture, termed the *mobile phase* in GC experimentation, is fed through a narrow tube, typically referred to as a *column*, which contains an appropriate polymer-based *stationary phase*. The molecules within the mobile phase to be analyzed interact with stationary phase to different degrees, depending on the molecules physical and

chemical properties. This separates the molecules in the column and causes them to exit the column at differing times.

The separated molecules are then subject to MS, which involves ionization of the molecules which are then further analyzed in terms of their mass-to-charge ratio. Based upon the detected molecules mass and charge the elements within a molecule, and thus the molecules empirical formula, can be determined. This can then be compared against other known properties of the analyzed sample in order to determine the individual molecules present.

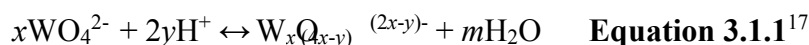
In this work a Thermo Scientific<sup>®</sup> GC-MS was used, employing a TSQ-8120504 stationary phase, scanning for masses between 25 and 300 amu with a 0.2014s scan time. The method employed a heating profile of initially holding the instrument at 50°C for 5min, followed by a heating rate of 5°C/min to 250°C, followed by a heating rate of 10°C/min to 280°C and finally held at 280°C for 10min. The MS transfer line temperature was held at 280°C and the ion source at 290°C.

## Chapter 3. Synthesis of CTA-W<sub>12</sub>

### 3.1 Background Theory

#### 3.1.1 Aqueous tungstate equilibria

Tungstates (tungsten bound to oxygen) form a variety of structures in aqueous media dependent upon solution concentration, pH and temperature.<sup>109-118</sup> This is a common behaviour for oxides of many Group V and VI transition metals. At high pH > 8 tungstates adopt the pyramidal structure of the anion orthotungstate, [WO<sub>4</sub>]<sup>2-</sup>.<sup>109</sup> As solution pH is lowered, orthotungstate condenses to form a myriad of structures, following Equation 3.1.1 below:



Tungstates will condense and precipitate to bulk, hydrophobic WO<sub>3</sub> at pH < 2. Between pH 2 and 8, tungstates exist as hydrophilic, multi-nuclear cyclic arrangements of WO<sub>6</sub> octahedra termed *isopolyanions*, or more specifically *isopolytungstates*. Typically, paratungstates A and B, [H<sub>2</sub>W<sub>12</sub>O<sub>42</sub>]<sup>10-</sup> and [W<sub>7</sub>O<sub>24</sub>]<sup>7-</sup> respectively, form between pH 6 and 8, metatungstates, [H<sub>2</sub>W<sub>12</sub>O<sub>40</sub>]<sup>7-</sup>, form between pH 6 to 4, and decatungstates, [W<sub>10</sub>O<sub>32</sub>]<sup>6-</sup>, and other smaller isopolytungstates exist at pH 5 to 2. The structure of the [H<sub>2</sub>W<sub>12</sub>O<sub>40</sub>]<sup>7-</sup> anion is commonly referred to as the *Keggin* anion, due to the determination of its structure by J. F. Keggin in 1933.<sup>119</sup> Anion derivatives of the Keggin structure are by far the most studied polyoxometalate in history, as will be discussed in Chapter 5.<sup>9, 71, 120, 121</sup>

Tungstate solutions are slow to equilibrate upon changes in pH between these structures, and complete equilibrium is only achieved after weeks or even months in some systems.<sup>112, 113, 116-118</sup> It is for this reason that most aqueous tungstate solutions in slightly basic to acidic (pH 2 to 8) aqueous solutions usually exist as equilibrating mixtures. Figure 3.1.1 highlights this fact.

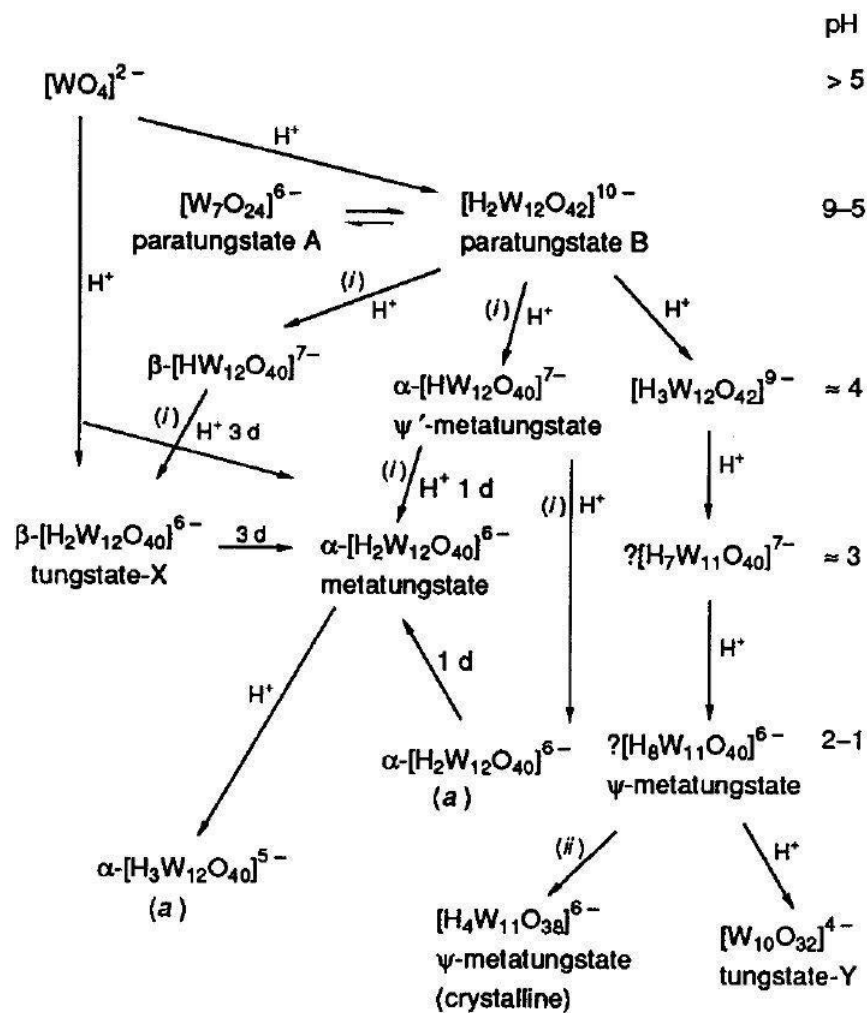


**Figure 3.1.1.** Tungstate equilibrium scheme devised by J. Hastings and O. Howarth (1992).

The scheme highlights the complexity of equilibrating tungstate solutions, and the time required to achieve equilibration.<sup>112</sup>

Counter-cations can be used to shift and accelerate equilibrium points towards favoured isopolyanions in tungstate solutions, with cation charge, hydrophobicity, size and shape affecting the equilibrium position.<sup>122</sup>

Due to their size and hydrophilicity, POM solutions containing small alkali cations, such as  $\text{Li}^+$ ,  $\text{Na}^+$ ,  $\text{K}^+$  and  $\text{NH}_4^+$ , are known to precipitate crystals containing high degrees of hydration, and favour lesser charged, lower nuclearity anions.<sup>9, 121, 123</sup> Larger metallic cations, such as  $\text{Cs}^+$ ,  $\text{Ca}^+$  and  $\text{Mg}^+$ , are known to form crystals with a lower degree of hydration due to crystal packing considerations, and favour higher charged, larger anions. Large organic-

cations are known to isolate assembled POMs via hydrophobic-hydrophilic separation. However, in the interests of yield, product purity and time, POM research is usually conducted using readily-made POMs in salt form. With these purchased precursors researchers are able to combine selected POMs with cations in chosen solvents under appropriate conditions to produce desired clusters and architectures.<sup>124, 125</sup> Furthermore, by combining differing oxoanions clusters, with specific geometries, a near infinite number of unique polyoxometalate clusters are synthesizable.<sup>110, 115, 122</sup> For example, by combining the pentagonal star-like  $M(\text{MO}_6)$  cluster (where  $M = \text{W}, \text{Mo}$  or  $\text{Nb}$ ) with the edge-sharing dimer  $\text{M}_2\text{O}_{10}$  and other small oxoanions, large curved and open-pore structures are accessible, giving rise to the ‘Celtic ring’ macro-cycles and large fullerene-type spheres.<sup>110, 122</sup> With this approach, many researchers have been able to design and isolate desired POM clusters and crystal-structures upon precipitation.<sup>122</sup>

### 3.1.2 Tungstate-quaternary ammonium equilibria and Keggin cluster formation

Tungstates,  $\text{WO}_4^{2-}$ , (and molybdates) are known to form a variety of hydrated,  $\text{WO}_3 \cdot 2\text{H}_2\text{O}$ , layered monoclinic and orthorhombic crystallographic phases when precipitated from aqueous solutions, dependent upon reaction temperature, pH and tungstate and cation concentration.<sup>120, 126-129</sup> The layered structure arises due to double-layers of octahedra which are separated by W-OH groups, and water.<sup>126</sup> W-OH protons are acidic and can be exchanged with other cations in aqueous solutions to form more porous structures such as pyrochlore ( $\text{Na}^+$ ) and hexagonal ( $\text{Ag}^+$ ,  $\text{Li}^+$  and  $\text{NH}_4^+$ ) phases.<sup>127</sup> The ease of proton/cation exchange in tungstate and molybdates porous oxides has led these materials to be considered in a number of ionic-conductor applications.<sup>128, 130, 131</sup>

Large organic-cations, however, such as methyl-substituted ammoniums, are unable to be accommodated within the interstitial-layer sites of the continuous layered and bulk crystal-phases. Because of this, higher nuclearity  $\text{WO}_6$  isopolytungstate structures are favoured that allow for more condensed, isolated tungstate phases. For example, tungstates are known to form layered  $\text{WO}_6$  monoclinic, hexagonal or pyrochlore structures when precipitated in the presence of relatively small ammonium ( $\text{NH}_4^+$ ) or methyl-ammonium ( $\text{NH}_3(\text{CH}_3)^+$ ) cations (i.e.  $(\text{NH}_4)_x(\text{WO}_3)_{x/2} \cdot n\text{H}_2\text{O}$  or  $(\text{NH}_3(\text{CH}_3))_x(\text{WO}_3)_{x/2} \cdot n\text{H}_2\text{O}$ , respectively).<sup>120</sup> Conversely, orthorhombically arranged Keggin anions are favoured when

the protons of the ammonium cation are substituted by more than one methyl (or larger organic) group, such as dimethyl-ammonium ( $\text{NH}_2(\text{CH}_3)_2^+$ ), trimethyl-ammonium ( $\text{N}(\text{CH}_3)_3^+$ ) or tetramethyl-ammonium,  $\text{TMA}^+$  ( $\text{N}(\text{CH}_3)_4^+$ ) (i.e.  $((\text{NH}_x(\text{CH}_3)_{4-x})_6[\text{H}_2\text{W}_{12}\text{O}_{40}].n\text{H}_2\text{O})$ , where  $x = 0 - 2$ ).<sup>120, 127, 129, 132</sup> The selection between the Keggin anion or a layered-tungstate upon precipitation is dependent upon tungstate and cation concentration, with stoichiometric ratios favouring Keggin anions ( $((\text{NH}_x(\text{CH}_3)_{4-x})_6[\text{H}_2\text{W}_{12}\text{O}_{40}].n\text{H}_2\text{O})$ ) and higher cation ratios favouring encapsulated tungstate colloids ( $((\text{NH}_x(\text{CH}_3)_{4-x})_2[\text{W}_2\text{O}_4].n\text{H}_2\text{O})$ ).<sup>129</sup>

If the ratio between cations and tungstate anions is too low (less than 0.5), then there will be an insufficient number of large cations to force the equilibrium away from layered-oxide structures. This leads to protons now ‘substituting’ the methylated ammonium cations, resulting in typical  $\text{WO}_6$  layered structures. This Keggin-anion/bulk-oxide cation-mediated equilibrium is illustrated in Figure 3.1.2.<sup>129</sup>

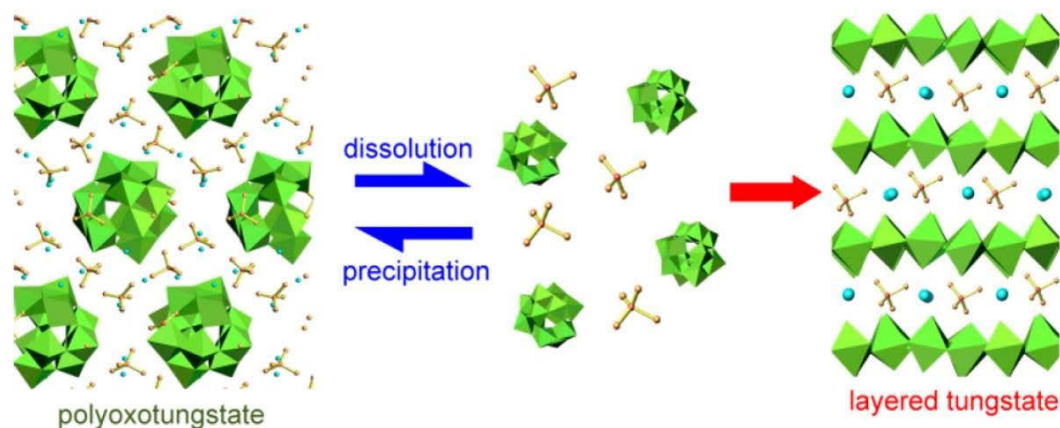
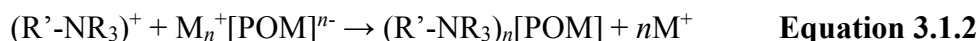


**Figure 3.1.2.** Tungsten octahedra (green) precipitate from aqueous solution to form layered structures (right) or orthorhombically arranged polyoxotungstates/Keggin units (left) dependent upon methyl-ammonium (red and orange) concentration.<sup>129</sup>

Keggin-anion formation by the presence of methyl-substituted ammonium has also been found to be true for larger organic-cations, such as the surfactant dodecyltrimethyl-ammonium ( $\text{CH}_3(\text{CH}_2)_{11}\text{N}(\text{CH}_3)_3^+$ ).<sup>120</sup> In these cases the cationic head-groups are situated within the orthorhombic arrangement housing the Keggin anions, and the lipophilic tails point towards each other resulting lamellar structures.

### 3.1.3 Surfactant-polyoxometalate chemistry

The vast majority of the POM-hybrids mentioned in Section 1.2 are examples of class I hybrids, i.e. the hybrid component is linked to the POM by a covalent bond. However, class II hybrid materials are derived from favourable synthesis methods that take advantage of predictable and manipulable self-assembly dynamics, directed by attractive coulombic anion-cation and repulsive hydrophobic-hydrophilic forces. These materials are fairly straightforward to synthesize since the small-cations ( $\text{Na}^+$ ,  $\text{K}^+$ ,  $\text{NH}_4^+$ , etc.) of a POM salt are easily displaced by larger organic-cations, such as surfactants, through cation-exchange reactions. Once a POM has exchanged its metallic counter-cations and consequently become encapsulated by the surfactant via cation-exchange, it is referred to as a surfactant-encapsulated POM (SEP). This process is described for a reaction involving simple monovalent alkali-metal and organic cations by Equation 3.1.2.



Where  $\text{M}^+$  represents a small-cation,  $\text{R}'$  represents the hydrophobic alkyl-tail of a surfactant (if present) and  $\text{R}$  represents the smaller alkyl groups (typically  $-\text{CH}_3$  or  $-\text{C}_2\text{H}_5$ ) of the hydrophilic cationic head-group. The magnitude of  $n$ , or the POM:surfactant ratio of an SEP, which is resultant from charge-density-matching between the inorganic anions and organic cations, has a profound effect on the nano- and meso-structure of SEP materials.<sup>64, 66, 133-137</sup> The more surfactants that are incorporated into an SEP material (per POM), the greater fraction of the organic and therefore hydrophobicity of the material. This tunable parameter has obvious influences on SEP packing and solubility which can be further manipulated via selection of appropriate solvent and capping-agents.<sup>64, 136</sup> A larger value of  $n$ , or otherwise greater surfactant volume fraction, also increases anion-anion distance, both within the hydrophilic spaces containing the POMs, which are separated by the surfactant head-groups, and across the hydrophobic spaces containing the lyophilic alkyl-chains.<sup>134, 135, 138-140</sup>

Most commonly, singly charged cationic-surfactants are used in SEP synthesis, and therefore POM anionic charge usually determines the POM:surfactant ratio ( $n$ ). Apart from the size of the cluster and degree of reduction, POM anionic charge is dependent upon the

type of heteroatom included, for example;  $P^{5+}$  in  $[PW_{12}O_{20}]^{3-}$ ,  $Si^{4+}$  in  $[SiW_{12}O_{40}]^{4-}$ ,  $Al^{3+}$  in  $[AlW_{12}O_{40}]^{5-}$  and  $2H^+$  in  $[H_2W_{12}O_{40}]^{6-}$  in typical Keggin clusters. Once the POMs are stable in a solution/solvent, the compounds are easily synthesizable via cation-exchange processes, with the larger organic-cations displacing smaller cations such as alkali-metals and ammonia.

Within any inorganic-organic hydrophobic-hydrophilic system, the charge density at the hydrophobic-hydrophilic interface resultant from anion:cation matching directs the geometry of the interface, and consequently influences the mesostructure of the material. Due to geometric considerations, splayed, curved surfaces/interfaces are not able to accommodate as high charge-densities as flatter, more regular surfaces.<sup>133</sup> Because the interface is comprised of larger multi-charged anionic POMs, and smaller singly-charged cationic surfactants, the charge-density at the POM:surfactant interface is quite high. As will be discussed in the following section, such high interface charge densities usually result in the flat bi-layer structures typically found in SEP materials.<sup>64, 136</sup> However, due to the labile nature of ionic bonding, surfactants on the surface of the POM clusters are quite mobile and able to migrate in response to changing nano-/meso-structures, driven by the greater forces of charge-density-matching and hydrophobic-hydrophilic repulsion. Such mobility can be harnessed via solvent effects, as will also be discussed later, resulting in numerous other nano- and meso-structures.

Larger POMs ( $> W_{20}$ ) that have a much higher anionic charge and surface area, such as Celtic-ring and fullerene ball-like structures, tend to form surfactant-encapsulated clusters (SECs) that, due to their bulky size, large volume of hydrophobic space and consequently large molecular weight, prohibit organization into continuous crystals in solution. In the dry-state, such SECs typically form hexagonal structures where columns of the large hydrophilic POMs are separated by large numbers of hydrophobic organic chains.<sup>31, 141</sup>

### 3.1.4 Surfactant-polyoxometalate packing

The repulsive hydrophobic-hydrophilic and attractive hydrophobic-hydrophobic and hydrophilic-hydrophilic forces within SEP materials give rise to phase-separated hydrophobic and hydrophilic domains. These separated domains form bi-layers, where layers of hydrophilic inorganic compounds and ionic surfactant head-groups are separated by layers of hydrophobic surfactant alkyl-chains. These bi-layers form continuous structures which

typically fall within the categories of cubically arranged spheres (similar to micelles), hexagonally arranged rods (or ‘elongated spheres’) or flat lamellar planes (or ‘infinitely stretched rods’). The selection between these structures is largely dependent upon the manner in which the surfactant tails and head-groups pack within the hydrophobic space and hydrophilic interface, respectively.<sup>133</sup>

Along with the number of surfactants per POM ( $n$ ), the morphology of the surfactant influences the packing of surfactants within SEP materials, and the corresponding mesostructure. Spatial properties such as volume of the hydrophobic portion of the amphiphile,  $V$ , and the effective head-group cross-sectional area at the interface,  $A_0$ , directly relate to the packing of the surfactant within the bi-layer.<sup>133, 142-144</sup> The curvature elastic energy formed at the interface by the interaction of the surfactant head groups with each other,  $l$ , further contributes to surfactant packing.<sup>144</sup>

In materials which are comprised of only one type of surfactant (i.e. homogenous surfactant tail length and head-group size) and no co-surfactants (such as short-chain alcohols), and where the tail-length used is sufficiently long ( $> \sim C_{10}$ ), the value of  $l$  is minimized. This is due to the uniform head-groups forming regular arrangements at the interface, rather than the arrangement of differing sizes that naturally give rise to curvature, as seen in Fig. 3.1.3.<sup>144</sup> Larger tail-lengths mutually increase amphiphile conformity (isotropy) due to the increased asymmetry of the amphiphile, which further inhibits interface curvature.

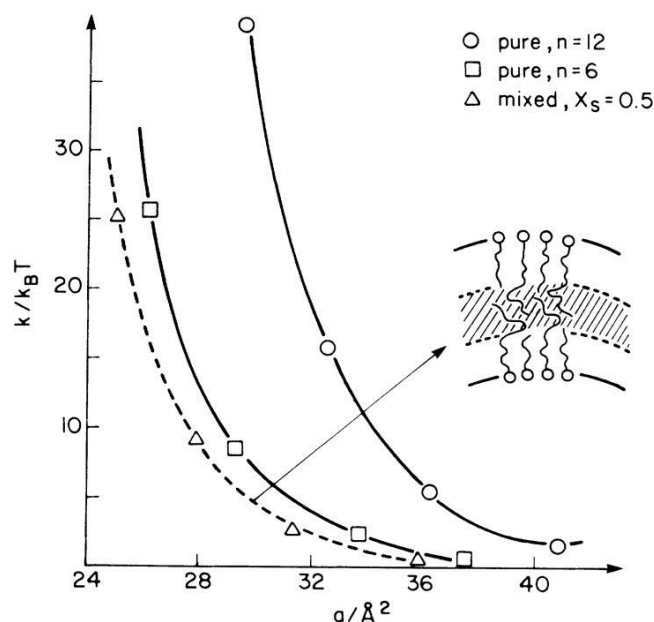


**Figure 3.1.3.** Curvature elastic energy versus surfactant-tail volume of different length surfactants ( $n = 12, 6$  where  $n$  represent the length of the alkyl-chain,  $C_n$ ) and a mixture of surfactants ( $X_s = 50\%$  mixture of  $C_{12}$  and  $C_{16}$ ). Here  $k \propto 1/l$  and  $a \propto 1/V$ . It is seen that curvature of the hydrophobic-hydrophilic interface increases as tail-length decreases, and if differing tail lengths are present.<sup>144</sup>

Larger values of  $V$ , which is dependent on surfactant tail number and length, further increase the attractive Van der Waals forces between the chains which leads to greater lateral packing of the hydrophobic tails. Tighter packing of the alkyl-tails favours flatter bi-layers as curved interfaces require increased separation of tail-ends. Smaller effective head-group cross-sectional areas ( $A_0$ ), which increases with head-group size, and decreases with increasing surfactant concentration and inorganic counter-anion charge, allow for denser packing of the surfactant head-groups across the hydrophobic-hydrophilic interface. By considering these packing variables, the surfactant packing parameter,  $g$ , can be used to predict the curvature of the hydrophobic-hydrophilic interface, and hence, the bi-layer mesostructured, Equation 3.1.3.

$$g = V/A_0 l \quad \text{Equation 3.1.3}^{107, 118, 119}$$

Equation 3.1.3 shows that  $g$  increases as the volume,  $V$ , (i.e. tail number or tail length) of the hydrophobic alkyl-chain increases, and as the head-group size,  $A_0$ , and curvature elastic energy,  $l$ , decreases. Bi-layers with a high surfactant packing parameter, or large  $g$ , are found to form flatter interfaces, whereas smaller values of  $g$  tend to give rise to more curved interfaces. Typically, surfactant micelles arranged in a simple-cubic ( $Pm3n$ ) conformation form at low ( $0 - 0.33$ ) values of  $g$ , followed by hexagonally arranged tubes at higher ( $0.33 - 0.5$ ) values, then body-centred-cubic arrangements of micelles ( $Ia3d$ ) ( $0.5 - 0.67$ ) and finally lamellar stacking of surfactants at very high values of  $g$  ( $0.67 - 1.0$ ). This trend is summarized in Table 3.1.1 is observed.<sup>142, 143</sup>

**Table 3.1.1.** Value of  $g$  within curved and flat mesophases.

$g$	Mesosophase
0 - 1/3	cubic ( $Pm3n$ )
1/3 - 1/2	hexagonal ( $p6m$ )
1/2 - 2/3	cubic ( $Ia3d$ )
2/3 - 1	lamellar

The large differences between anion to cation charge and surface area of the macromolecular POMs compared to (typically) monovalent surfactant species (such as cetyltrimethylammonium) leads to dense surfactant packing and the effective value of  $A_0$  to be small in SEP materials. Dense packing predictably leads to a high surfactant packing parameter within SEP bi-layers, and is the reason why the vast majority of mid-sized ( $< W_{20}$ ) SEP materials form lamellar structures in and from aqueous media, provided the surfactant is of sufficient length ( $> C_{10}$ ) and co-surfactants (such as alcohols) are absent.<sup>31, 32, 64, 66, 93, 134, 135, 145, 146</sup>

As will be discussed in detail in the following section, POMs form pseudo-hexagonal arrangements within the hydrophilic space.<sup>134, 135, 138, 147</sup> Therefore, SEP materials that contain shorter tailed organic cations, such as TMA<sup>+</sup> (N(CH<sub>3</sub>)<sub>4</sub><sup>+</sup>) and tetrabutyl-ammonium, TBA<sup>+</sup> (N(C<sub>2</sub>H<sub>5</sub>)<sub>4</sub><sup>+</sup>), form more condensed versions of these hexagonal structures, where the

lamellar-supporting alkyl-tail is ‘removed’, and the hexagonal layers of POMs approach each other.<sup>120, 127, 132</sup> Of course, surfactants incorporating rigid groups such as aromatic rings and carbon double-bonds can be used to force particular cluster and nano/meso-structures.<sup>64</sup> Such methods are routinely employed in order to produce desired structures, and functionalities.<sup>39,</sup>  
148

### 3.1.5 The SEP lamellar phase and the 1:4 ratio

As described in the previous sections, sufficiently long ( $> \sim C_{10}$ ) linear tailed surfactants, such as cetyltrimethylammonium, ( $C_{16}H_{33}N(CH_3)_3^+$ , CTA<sup>+</sup>) and dimethyldioctadecylammonium ( $(C_{18}H_{37})_2N(CH_3)_2^+$ , DODA<sup>+</sup>), and small to medium sized POMs, such as the Keggin, Dawson, Linqvist and decatungstate structures, tend to form lamellar structures due to the high charge density at the hydrophobic-hydrophilic interface. The high charge density results from anion-cation digitation (or “charge-density-matching”) between large multi-valent macromolecular POMs and smaller mono-valent surfactants.<sup>133, 149, 150</sup> The tendency for highly-charged hydrophobic-hydrophilic interfaces to form lamellar bi-layer structures can be rationalized by considering the surfactant packing parameter,  $g$ , used to describe liquid-crystal arrays formed within water;  $g = V/LA_0$ .<sup>133, 142, 143</sup> However, as was also mentioned earlier, very large POMs ( $>W_{20}$ ) such as Celtic-ring and fullerene-type structures do not form lamellar, or other continuous bi-layer structures, due to the very large amount of surfactants per anion that prohibit such condensation and organization. Therefore, there must be a limit to the formation of lamellar bi-layers by high  $g$  materials, and the applicability of the surfactant packing parameter. The transition between these two phases is driven by disorder, within the bi-layer interface and the corresponding effects on the hydrophobic space.<sup>134, 135</sup>

Within the hydrophilic space of the lamellar bi-layer, the POMs are arranged in a 2D pseudo-hexagonal pattern, separated by the surfactant cationic quaternary-ammonium head-groups and water.<sup>134, 135, 138, 147</sup> In this manner, each anion is surrounded by six other anions, as seen in Figure 3.1.4(a). The cationic head-groups also adopt this 2D pseudo-hexagonal arrangement and are situated between the POM anions at the interface, Figure 3.1.4(a) and (b). Nyman *et al* found in their study of  $(CTA)_4[SiW_{12}O_{40}]$ <sup>134, 135</sup> that the head-groups tend to form dimers in between the anions, resulting in each Keggin anion being surrounded by 12 surfactants, Figure 3.1.4.

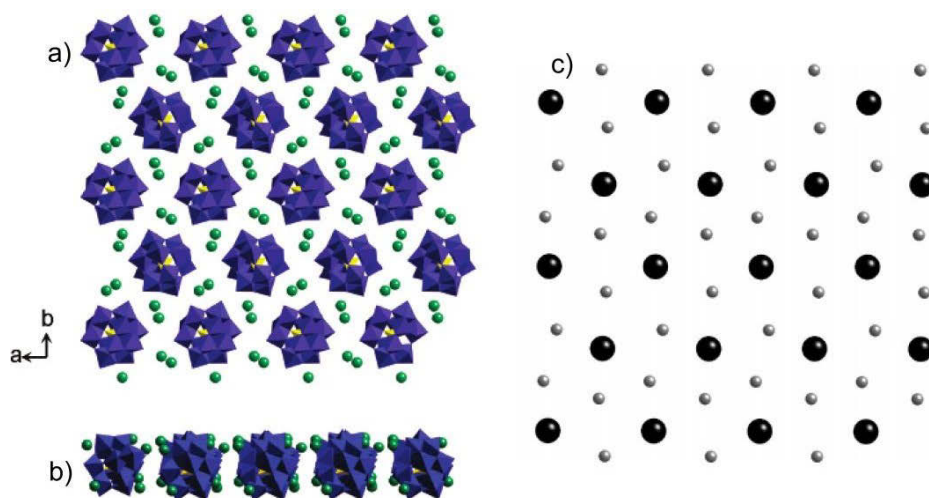


**Figure 3.1.4.** View down the  $c$ -axis of the Keggin anions within the hydrophilic layer of  $(\text{CTA})_4[\text{SiW}_{12}\text{O}_{40}]$ . (a) It is seen that the Keggin anions (blue and yellow clusters) form a pseudo hexagonal pattern within the layer, separated by the mutually pseudo-hexagonally arranged dimers of cations quaternary-ammonium head-groups (green). (b) View of the same layer parallel to the  $b$ -axis. (c) Simplified diagram of the pseudo-hexagonally arranged species where large black spheres represent the Keggin anions and smaller grey spheres represent quaternary-ammonium dimers. The more irregular arrangement of the dimers is more easily realised.<sup>134</sup>

Typically, due to the difference in cross-sectional-area of the larger cationic quaternary-ammonium head-groups compared to the thinner alkyl-chains of the surfactants, the amphiphiles are tilted within the hydrophobic layer, with respect to the hydrophobic-hydrophilic interface. This is due to space filling requirements between the differing cross-sectional-areas and the maximization of the attractive hydrophobic-hydrophobic forces between the alkyl-chains. In instances where the cross-sectional-areas are more similar, such as the case of ammonium head-group surfactants ( $\text{R-NH}_3^+$ , where  $\text{R}$  = alkyl-chain), chain tilting is not observed.<sup>138, 151</sup> Further maximization of the attractive hydrophobic-hydrophobic forces and space-filling requirements causes the alkyl-chains across the hydrophobic width to not meet each other end-to-end but interdigitate with the amphiphiles from the opposite side of the layer.<sup>134, 135, 139, 147</sup> Nyman *et al* found in their study of

(CTA)<sub>4</sub>[SiW<sub>12</sub>O<sub>40</sub>] that the chains are interdigitated by up to 14 carbons from the end of the amphiphile (meaning the two carbons closest to the cationic-nitrogen are not interdigitated).<sup>134</sup>

The 1:4 POM:surfactant ratio, as depicted in Figure 3.1.4(a) and (c), presents a highly ordered, highly symmetrical pseudo-hexagonal arrangement of head-group dimers and POM anions. Further inclusion of surfactants beyond the 1:4 ratio breaks this symmetry, such as in the 1:5 case of (CTA)<sub>5</sub>(CH<sub>3</sub>CN)<sub>4</sub>[H<sub>x</sub>SiMo<sub>12</sub>O<sub>40</sub>], and result in a departure from the pseudo-hexagonal organization of ions towards more disordered arrangements, Figure 3.1.5.<sup>135</sup>

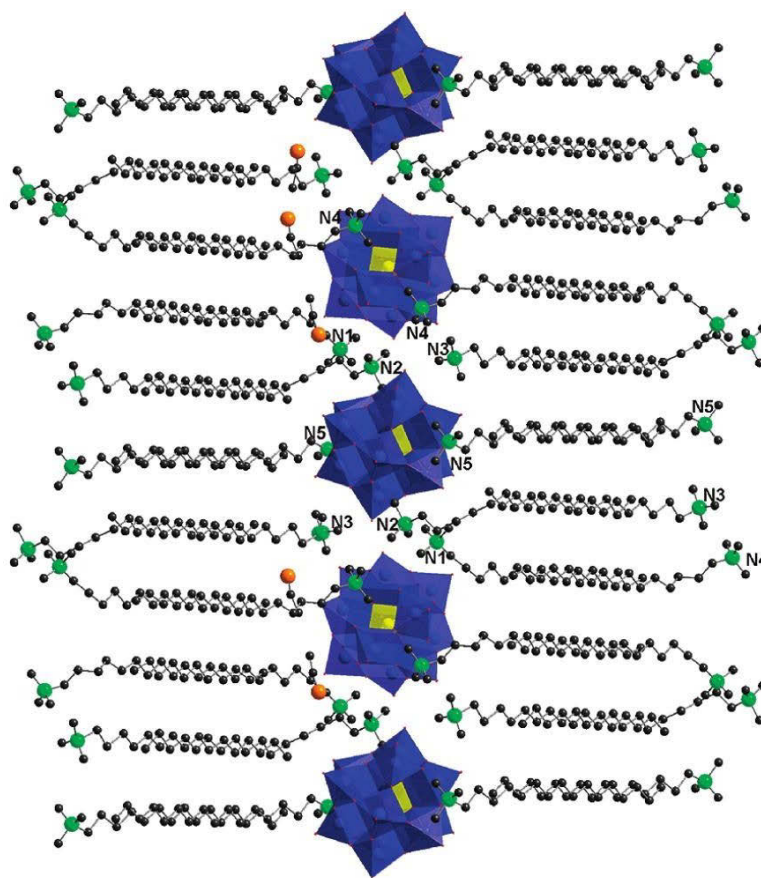


**Figure 3.1.5.** View of the SEP (CTA)<sub>5</sub>(CH<sub>3</sub>CN)<sub>4</sub>[H<sub>x</sub>SiMo<sub>12</sub>O<sub>40</sub>] down the *a*-axis highlighting the interdigitation, tilting and individuality of the hydrophobic alkyl-chains due to the differing degrees to which the head-groups (green) penetrate the hydrophilic layer. Keggin anions appear blue with a yellow silicon hetero-atom core, CTA<sup>+</sup> surfactants are represented with green nitrogen cations and black carbon atoms and acetonitrile groups are orange.<sup>135</sup>

Due to columbic charge separation mechanisms between the cationic head-groups of the surfactants, asymmetrical arrangement causes un-equivalence between the sites where the surfactant becomes affixed to the anion. This difference between these sites on the surface of the spherical POM results in differing degrees to which the head-groups penetrate the hydrophobic-hydrophilic interface, and therefore the amount of the alkyl-chain that resides within the hydrophobic layer. Differing available lengths correspond to differing degrees of interdigitation with the opposing surfactant tails. This leads to conformational uniqueness among the surfactants within a unit cell, due to the differing number of carbons interdigitated and the hydrophobic forces between the chains. This uniqueness is depicted within Figure 3.1.5, where all five surfactants are found to be orientated uniquely within the SEP compound  $(\text{CTA})_5(\text{CH}_3\text{CN})_4[\text{H}_x\text{SiMo}_{12}\text{O}_{40}]$ , each interdigitated to different degrees, resulting in unique conformations of the undigitated carbons, Figure 3.1.5.<sup>134, 135</sup>

Increasing orientational uniqueness among surfactants within SEP materials predictably results in increased bi-layer disorder. Figure 3.1.4(b) depicts the calculated sites where the cationic head-groups (green spheres) electrostatically affix to the Keggin anions (blue clusters) within the 1:4 compound  $(\text{CTA})_4[\text{SiW}_{12}\text{O}_{40}]$ .<sup>134</sup> It can be seen that these sites form a plane when viewed down the *c*-axis, just above and below the tops of the POMs. From this direction it can be easily realised that further inclusion of surfactants would require adherence to the POM either at the very bottom of the cluster or further within the hydrophilic space as inclusion closer to the populated interface would increase repulsive cation-cation electrostatic forces. Inclusion of surfactant head-groups at shallower positions on the base (or apex) of POMs causes a greater length of the surfactant tail to penetrate into the hydrophobic space.<sup>134</sup> This extended length places pressure on the opposing hydrophilic layer, causing the hydrophobic space to widen in order to accommodate an increased lamellar distance, as depicted in Figure 3.1.6(b).

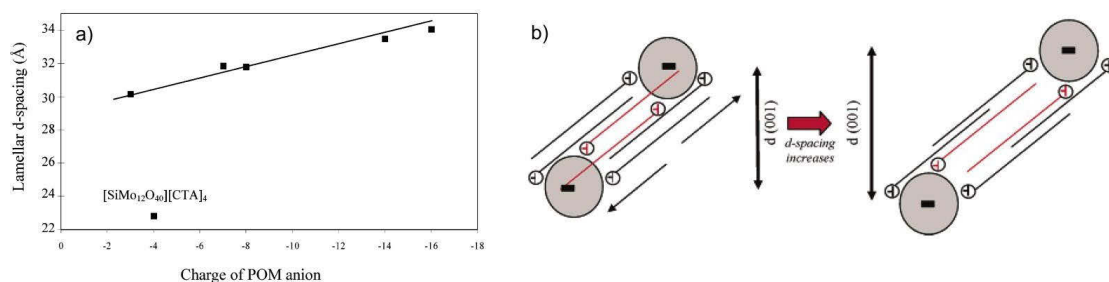


**Figure 3.1.6.** (a) Lamellar d-spacing, or hydrophobic space width, as a function of the POM anionic charge. (b) Additional surfactants beyond a 1:4 POM:alkyl-chain ratio increases lamellar d-spacing due to surfactant inclusion at the base/apex of POMs.<sup>134</sup>

The unique order found in 1:4 SEP materials is due to the maximized symmetry of the 2D hexagonally arranged cations (surfactant head-groups) and anions (POMs) at the bi-layer interface, and the resulting conformity of the surfactant tails within the inter-lamellar space. This regularity in turn results in the maximum number of carbons interdigitated per chain, hence maximising the attractive Van der Waals forces between them. All these attributes result in the minimization of the interlamellar distance (hydrophobic width) as is depicted in Figure 3.1.6(a), due to the contractive attractive forces. Increases in lamellar SEP disorder coincides with a departure from the 1:4 surfactant ratio, a reduction in hexagonal symmetry of the ions at the bi-layer interface and an increase in interlamellar distance.

Increasing the length of the surfactant tail, and in turn the hydrophobic portion of the amphiphile, also predictably increases the width of the hydrophobic layer.<sup>138-140</sup> Surfactants with an alkyl-chain length of up to  $\sim\text{C}_{20}$  are regularly used to form lamellar structures. Larger surfactants, due to their high molecular weight, have low solubility in most solvents and therefore are not commonly used.<sup>140</sup>

Increasing disorder within a SEP material comprising of a POM:surfactant ratio of greater than 1:4 is likely to result in interface curvature resultant from disordered lamellar planes. The existence of neighbouring areas of different interlamellar distances would cause the interface between them to bend to accommodate the connection. Therefore, the inclusion of a surfactant head-group to the base or apex of a POM, and the resulting disorder in the lamellar structure, represents the transition from an ordered SEP bi-layer to a disordered SEC stack and the limit of the surfactant packing parameter,  $g$ , applicability (Equation 3.1.3). As

surfactants increasingly surround the entirety of the anion, dependent on anion charge, the process of ‘surfactant-encapsulation’ progresses until continuous bi-layer structures are no longer possible, resulting in the hexagonally-arranged columnar SEC stacks referred to earlier.

### 3.1.6 Solvent effects

Due to the ionic nature of the bond between the POM and surfactant, surfactant species are quite mobile on the surface of these macromolecules. Because of this and the high hydrophobicity of the surfactant-tails, intermolecular solvent forces are able to easily influence the outwards-facing hydrophobic alkyl-chains of SEPs. Effects of these solvent forces can cause anisotropy of the connection sites between the POMs and cationic head-groups at the surface of the anions, leading to uneven coverage, Figure 3.1.7. Anisotropic coverage of the surfactants has dramatic effects on SEP packing, and can induce curvature within the bi-layer, resulting in a myriad of meso- and micro-structures.

An example of this solvent-dependent architecture is found within the commonly studied compounds containing the double-tail dioctadecyldimethyl ammonium (DODA<sup>+</sup>) cation and Keggin [PW<sub>12</sub>O<sub>40</sub>]<sup>3-</sup> and [SiW<sub>12</sub>O<sub>40</sub>]<sup>4-</sup> anions. Changing the polarity of the solvent within this system is seen to drive reversible transitions between disk, cone, tubular and flower-like structures.<sup>30, 68, 69</sup> A 3:1 chloroform/butanol (CHCl<sub>3</sub>/C<sub>4</sub>H<sub>9</sub>OH) solvent ratio was observed by A. Nisar *et al* (2009) to form layered disk structures separated by the hydrophobic alkyl-chains of the DODA amphiphile. When a higher polarity 2:1 ratio was used, the original disk structure became bent at the centre, eventually forming a hole around which cone-shaped structures grew. After 10 h of aging in the 2:1 chloroform/butanol solvent, the cone formations dissolved and were replaced by tubular structures.<sup>69</sup>

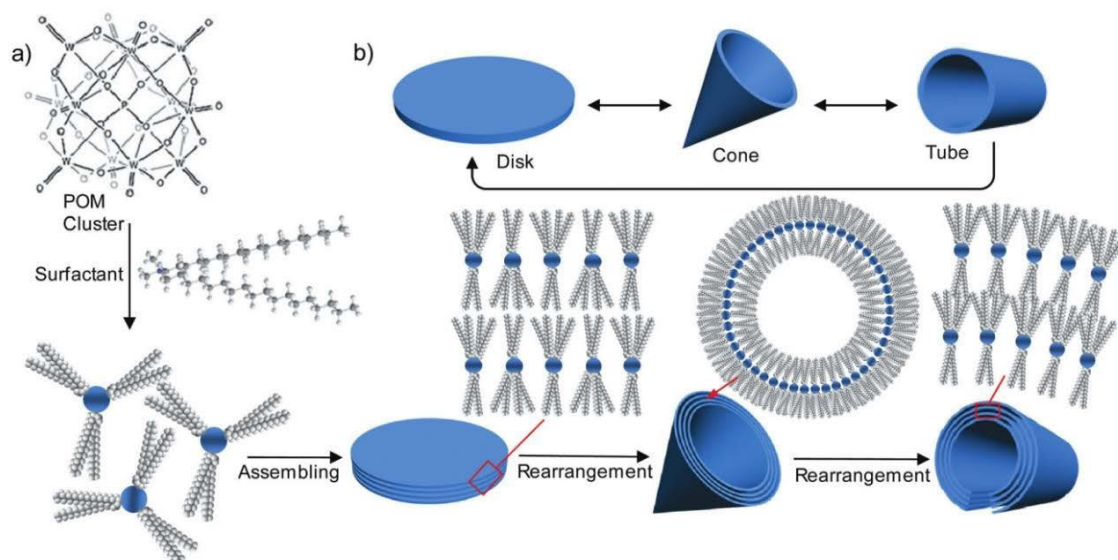


**Figure 3.1.7.** Solvent-dependent reversible transformations of  $(\text{DODA})_3[\text{PW}_{12}\text{O}_{40}]$  structures in butanol/chloroform mixtures.<sup>69</sup>

The reversible behaviour of this system is highlighted within Figure 3.1.7. Initially, it is thought the DODA amphiphiles are arranged symmetrically on the surface of the POMs (lower left, Figure 3.1.7), due to charge separation mechanisms. However, upon assembling in the 3:1 chloroform/butanol solvent, one of the amphiphiles migrates leaving two amphiphiles on one side and one on the opposite side (middle, Figure 3.1.7). This results in the hybrid moieties condensing in an alternative arrangement with respect to each other (one ‘up’ next to two ‘up’), forming flat disk-like structures. This arrangement presents the densest possible packing of the DODA chains in the SEP bi-layer structure, due to the minimized curvature. When the polarity of the solvent is increased to 2:1, the alternative arrangement is thought to be broken and the monomers are instead isotropically aligned, forcing the formation of curved cone structures when assembling. In time (>10 h) the growth of these cones in the direction of the apex becomes too great, forcing dissolution of the cone and eventual appearance of tubular structures. Changing the chloroform in the 3:1 solution for tetrahydrofuran ( $\text{C}_4\text{H}_8\text{O}$ ), acetone ( $\text{C}_3\text{H}_6\text{O}$ ) or butanone ( $\text{C}_4\text{H}_8\text{O}$ ) is seen to form ‘rose’, ‘snow’ and ‘ice-ball’ like structures respectively. These more complex structures are the result of the growth of multiple disks around a central point, or seed.<sup>30</sup>

The reversible nature of the solvent dependent (DODA)-[PW<sub>12</sub>O<sub>40</sub>] system highlights the manipulability of surfactant-POM architectures. Other such examples are found within the (DODA)-[Mo<sub>6</sub>O<sub>19</sub>] system forming planar-strips in nonpolar dichloromethane (CH<sub>2</sub>Cl<sub>2</sub>) and helical strips when polar propanol (C<sub>3</sub>H<sub>8</sub>O) is added.<sup>67</sup>

### **3.2 Synthesis of CTA-W<sub>12</sub>**

For a complete description of the synthesis of CTA-W<sub>12</sub> see Section 2.1.1.

It is useful to mention here that the synthesis of CTA-W<sub>12</sub> does not follow the typical synthetic method of surfactant-POM hybrids. As mentioned in Section 3.1.1, POMs are usually purchased as pre-formed anions, typically in the form of a simple salt with simple cations such as NH<sub>4</sub><sup>+</sup> and Na<sup>+</sup>, before they undergo cation-exchange with the chosen surfactant to produce the desired hybrid compound.<sup>152</sup> The method used in this work instead follows the process described in Section 3.1.2, where larger organic-cations are used to precipitate isopolyanions from tungstate solutions. Ammonium metatungstate hydrate, (NH<sub>4</sub>)<sub>6</sub>[H<sub>2</sub>W<sub>12</sub>O<sub>42</sub>]·xH<sub>2</sub>O, was purchased to compare the product that resulted from its cation-exchange with CTA<sup>+</sup> with CTA-W<sub>12</sub>, however, it was found that this product was not photochromic, nor did it exhibit a similar P-XRD pattern. It is unsure why this is case, however, further investigation into this matter falls outside the scope of this PhD. Such investigation is possibly a topic for future work.

#### **3.2.1 Characterization of CTA-W<sub>12</sub>**

The presence of the Keggin anion in CTA-W<sub>12</sub> was determined via Raman (Fig. 3.2.1.) and ATR FT-IR (Fig. 3.2.2.) spectroscopies, from the location of the characteristic  $\nu_{ss/as}(W=O)$  vibration, and its ratio to the neighbouring  $\nu(-O-W-O-)$ ,  $\delta(-W-OH_2)$  and  $\nu(-W-O-W-)$  peaks.<sup>84, 153-157</sup> The presence of CTA<sup>+</sup> is also visible due to the presence of  $\sigma(-CH_3)$ ,  $\sigma_s(-N^+(CH_3))$ ,  $\nu_{as}(-N^+-CH_3)$  and  $\nu_{as}(-CH_3)$  vibrations and  $\delta(-CH_2-)$ ,  $\nu_{ss}(-CH_2-)$ ,  $\nu_{as}(-CH_2-)$  vibrations ascribable to the cationic head-group and alkyl-tail of CTA<sup>+</sup>, respectively.<sup>156, 159-</sup>

161

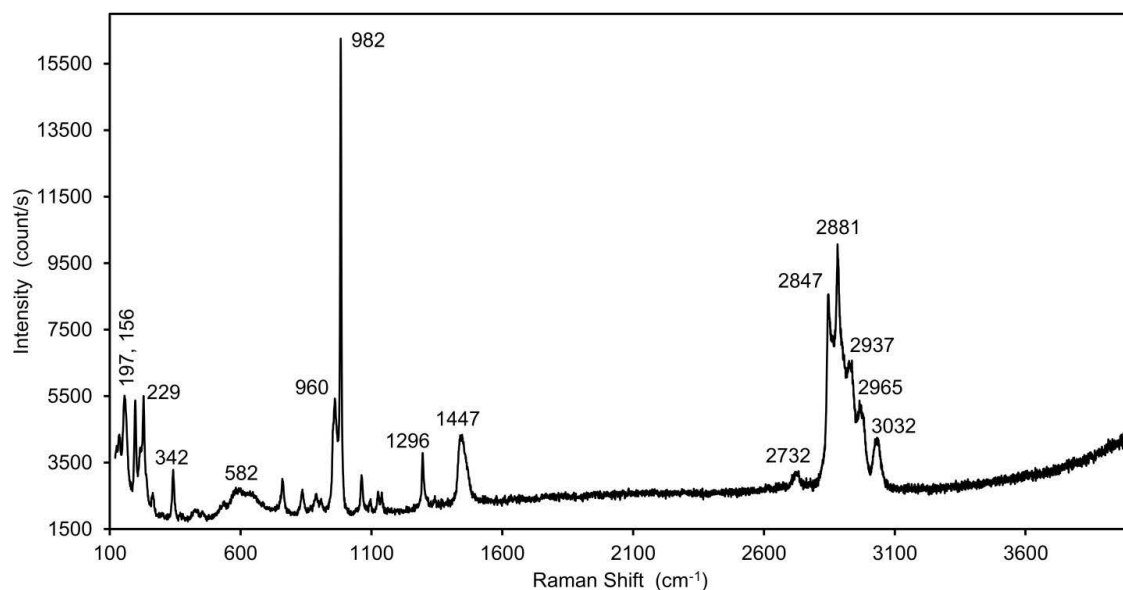


**Figure 3.2.1.** Raman spectrum of CTA- $W_{12}$ .  $\nu(-N^+(CH_3))$ ,  $\nu(-CH_3)$ ,  $\nu_{as}(-CH_2-)$ ,  $\nu_{ss}(-CH_2-)$ ,  $\nu(CH_3 \cdots N^+)$ ,  $\delta(-CH_3)$  and  $\sigma(N-R_4^+)$  vibrations appear at 3032, 2965, 2937–2847, 2732, 1447 and 1296  $cm^{-1}$  respectively, belonging to aliphatic CTA $^+$ .  $\nu_{ss}(W=O)$  and  $\nu_{as}(W=O)$  vibrations appear at 982 and 960  $cm^{-1}$ .<sup>153-155</sup> The broad peak with a maximum at 582  $cm^{-1}$  and peaks at 342 and 229  $cm^{-1}$  correspond to  $\nu(-O-W-O-)$ ,  $\delta(-W-OH_2)$  and  $\nu(-W-O-W-)$  vibrations of the Keggin anion, respectively. Raman-active lattice-modes of surfactant-tungstate hybrids appear at 197 and 156  $cm^{-1}$ .<sup>158</sup>

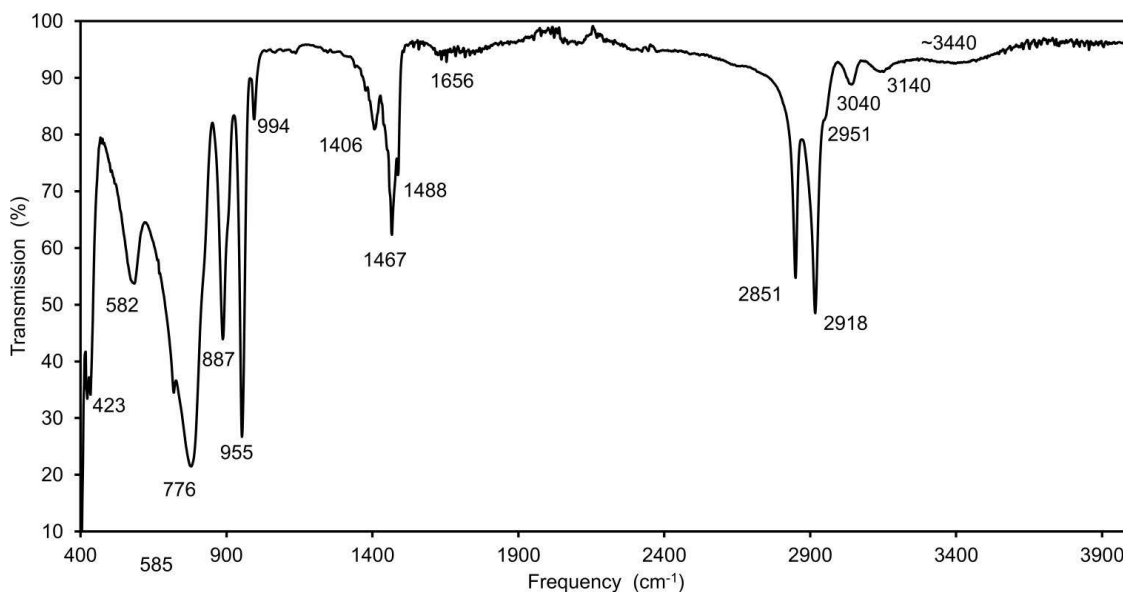


**Figure 3.2.2.** ATR FT-IR spectra of CTA- $W_{12}$ . Bands at 423, 582, 776, 887, 955 and 994  $\text{cm}^{-1}$  can be assigned to  $\delta(\text{O}_b\text{-W}=\text{O}_d)$ ,  $\nu(\text{O-W-O})$ ,  $\nu(\text{W-O}_c\text{-W})$ ,  $\nu(\text{W-O}_b\text{-W})$ ,  $\nu_{\text{as}}(\text{W}=\text{O})$  and  $\nu_{\text{ss}}(\text{W}=\text{O})$  stretching vibrations of the  $[\text{H}_2\text{W}_{12}\text{O}_{40}]^{6-}$  cage, respectively.<sup>84, 155-157</sup> Bands at 1406, 1467, 1488, 2851, 2918, 2951, 3040 and 3140 are assigned to  $\sigma(-\text{CH}_3)$ ,  $\delta(-\text{CH}_2-)$ ,  $\sigma_s(-\text{N}^+(\text{CH}_3))$ ,  $\nu_{\text{ss}}(-\text{CH}_2-)$ ,  $\nu_{\text{as}}(-\text{CH}_2-)$ ,  $\nu_{\text{as}}(-\text{CH}_3)$  and  $\nu_{\text{as}}(-\text{N}^+\text{-CH}_3)$  vibrations of  $\text{CTA}^+$ , respectively.<sup>158-161</sup> Broad peaks at 1656, 3240 and 3440 are assigned to  $\nu(-\text{OH})$  and unequivocal  $\delta(\text{H}_2\text{O})$ , respectively.

The relative amounts of  $[\text{H}_2\text{W}_{12}\text{O}_{40}]^{6-}$  and  $\text{CTA}^+$  in CTA- $W_{12}$  was determined via C,H&N micro-analysis, Table 3.2.1, and TGA techniques, Table 3.2.2 and Figure 4.3.1. A 1:7  $[\text{H}_2\text{W}_{12}\text{O}_{40}]^{6-}:\text{CTA}^+$  ratio best fit the data obtained from these techniques, however such a ratio based purely on the presence of  $\text{CTA}^+$  and  $[\text{H}_2\text{W}_{12}\text{O}_{40}]^{6-}$  would result in a total charge of +1. It was therefore concluded, after further study of the micro-analysis and TGA data, that the presence  $\text{Cl}^-$  (from the hydrolysis of  $\text{WCl}_6$ ) is likely, due to its relative abundance compared to the only other inorganic anion present,  $\text{Br}^-$  (0.0462 mol of  $\text{Cl}^-$  compared to 0.0017 mol of  $\text{Br}^-$ ) and its stronger association with  $\text{CTA}^+$ .<sup>162</sup> Furthermore, the small mass losses before 150°C in the TGA, Figure 4.3.1, are likely due to dehydration of the sample. Combining all the above data, the empirical formula  $(\text{CTA})_7[\text{H}_2\text{W}_{12}\text{O}_{40}]\text{Cl}\cdot 2\text{H}_2\text{O}$  was deduced.

Measured micro-analysis and theoretical C,H&N data based on the formula (CTA)<sub>7</sub>[H<sub>2</sub>W<sub>12</sub>O<sub>40</sub>]Cl.2H<sub>2</sub>O is compared in Table 3.2.1.

**Table 3.2.1.** Measured and theoretical C, H and N content in CTA-W<sub>12</sub> based on the empirical formula (CTA)<sub>7</sub>[H<sub>2</sub>W<sub>12</sub>O<sub>40</sub>]Cl.2H<sub>2</sub>O.

<b>ELEMENT</b>	<b>MEASURED (%)</b>	<b>THEORETICAL (%)</b>
<b>C</b>	32.22	32.53
<b>H</b>	6.24	6.16
<b>N</b>	2.03	2.00

TGA (Figure 4.3.1.) from 30°C to 800°C revealed the ratio of non-volatile content (WO<sub>3</sub> and Cl at 800°C) to volatile content (H<sub>2</sub>O and organics). Mass loss below 150°C is likely due to dehydration of the compound and is therefore ascribed to loss of H<sub>2</sub>O. Measured TGA is compared with theoretical data based on the probable empirical formula, (CTA)<sub>7</sub>[H<sub>2</sub>W<sub>12</sub>O<sub>40</sub>]Cl.2H<sub>2</sub>O, in Table 3.2.2.

**Table 3.2.2.** Measured and theoretical volatile (H<sub>2</sub>O and organics) and non-volatile (WO<sub>3</sub>) content in CTA-W<sub>12</sub> based on the empirical formula (CTA)<sub>7</sub>[H<sub>2</sub>W<sub>12</sub>O<sub>40</sub>]Cl.2H<sub>2</sub>O.

<b>FRACTION</b>	<b>MEASURED (%)</b>	<b>THEORETICAL (%)</b>
<b>WO<sub>3</sub></b>	53.93	59.32
<b>Organics and Cl</b>	44.47	40.68
<b>H<sub>2</sub>O</b>	1.59	1.10

The lamellar structure of CTA-W<sub>12</sub> was confirmed via P-XRD (Figure 3.2.3) and TEM (Figure 3.4.2(b) and (c)) analysis. Within the P-XRD pattern of Figure 3.2.3, the interlamellar distance appears at  $2\theta = 3.617^\circ = 24.5\text{\AA}$ , and the separation between the sheets of 2D pseudo-hexagonally arranged POMs appears at  $2\theta = 9.024^\circ = 9.75\text{\AA}$ .

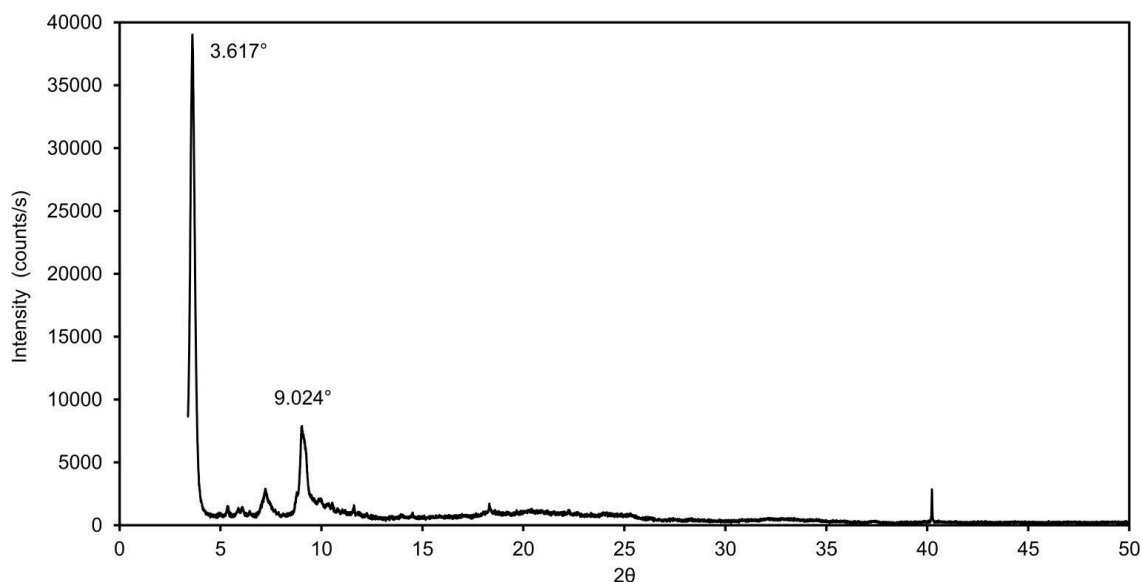


**Figure 3.2.3.** Background-subtracted P-XRD pattern of CTA-W<sub>12</sub>

The vast majority of work presented in this thesis focuses on the synthesis and performance of the SEP (CTA)<sub>7</sub>[H<sub>2</sub>W<sub>12</sub>O<sub>40</sub>]Cl·2H<sub>2</sub>O or CTA-W<sub>12</sub>. As will be discussed in detail in Chapter 5, CTA-W<sub>12</sub> is a photochromic material, as its absorption bands shift into the visible region when excited by above band-gap radiation. It also undergoes a number of phase transformations when heated, which will be discussed in detail in Chapter 4.

### 3.2.2 Synthesis and characterization of layered tungsten hydroxides

Samples produced by precipitation of the reactant solution without addition of NH<sub>4</sub>OH, which was at pH 0.5 after WCl<sub>6</sub> + 5H<sub>2</sub>O → WO<sub>3</sub>·2H<sub>2</sub>O + 6HCl hydrolization, yielded a product containing alternating layers of WO<sub>3</sub>·2H<sub>2</sub>O and CTA<sup>+</sup>. The synthesis for this compound is described in Section 2.1.2 and summarized in Equation 2.1.2. This result is similar to that found by Ingham *et al* in their study of layered alkyl-ammonium tungsten oxides.<sup>158</sup> The state of tungsten as the monoclinic di-hydrate oxide in CTA-WO<sub>3</sub> was confirmed by XRD, RAMAN and FT-IR, Figure 3.2.4-6.

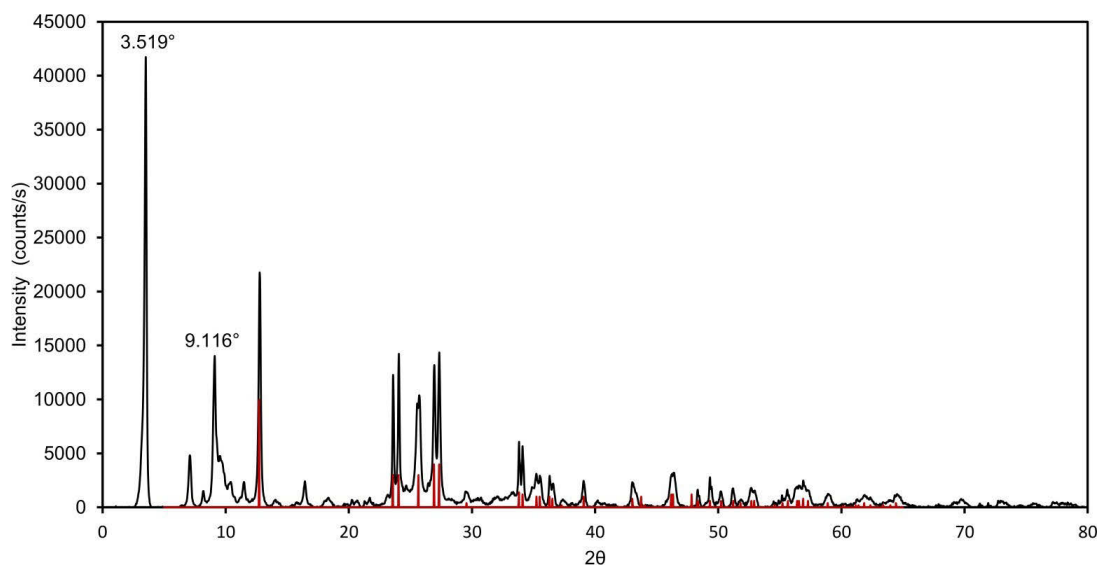


**Figure 3.2.4.** Background-subtracted P-XRD pattern ( $\lambda = \text{Cu K}\alpha$ ) of CTA- $\text{WO}_3$ , the product retrieved after one week of  $\text{WCl}_6$  hydrolysis in the presence of  $\text{CTA}^+$ .  $\text{WO}_3 \cdot 2\text{H}_2\text{O}$  (-) stick plot is from JCPDS 00-018-1420  $\text{WO}_3 \cdot 2\text{H}_2\text{O}$  (-). The lamellar-separation peak appears at  $3.519^\circ$  ( $d = 25.1 \text{ \AA}$ ).

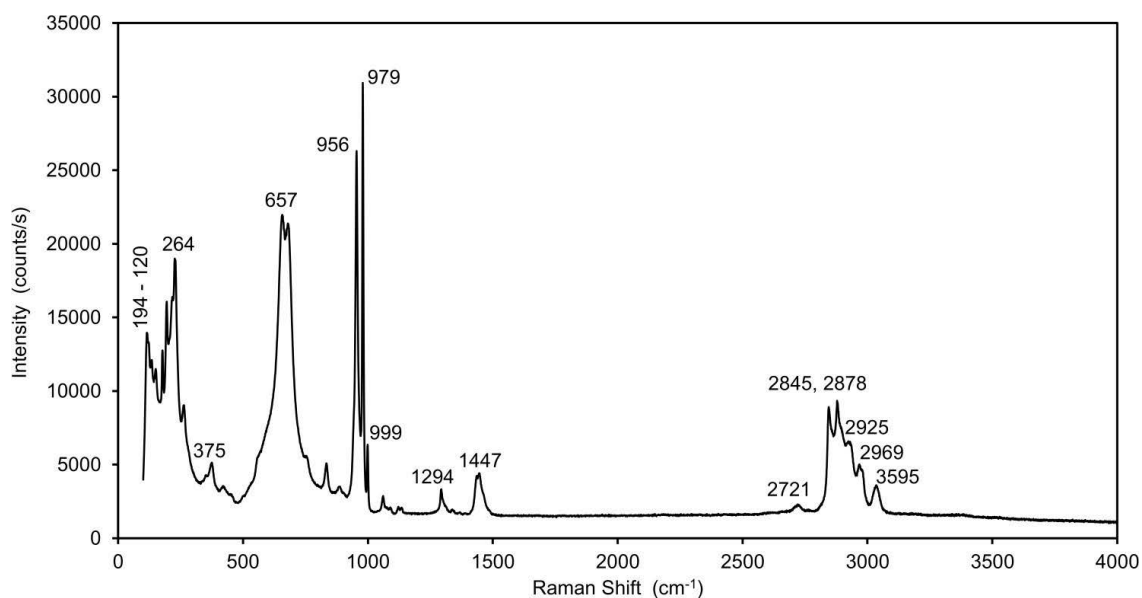


**Figure 3.2.5.** Raman spectrum of CTA-WO<sub>3</sub> collected with 633 nm excitation.  $\nu(\text{N-R}_4^+)$ ,  $\nu(-\text{CH}_3)$ ,  $\nu(-\text{CH}_2-)$ ,  $\nu(\text{CH}_3-\text{N}^+)$ ,  $\delta(-\text{CH}_3)$  and  $\sigma(\text{N-R}_4^+)$  vibrations appear at 3595, 2969, 2925–2845, 2721, 1447 and 1294  $\text{cm}^{-1}$  respectively, belonging to aliphatic CTA<sup>+</sup>. Three non-equivalent  $\nu(\text{W}=\text{O})$  vibrations, from differing W=O bond lengths,<sup>153, 154</sup> appear at 999, 979 and 956  $\text{cm}^{-1}$ . The double-peak with a maximum at 657  $\text{cm}^{-1}$  and the peaks at 375 and 264  $\text{cm}^{-1}$  are assigned to  $\nu(\text{O-W-O})$ ,  $\nu(\text{W-OH}_2)$  and  $\nu(\text{W-O-W})$  vibrations respectively. Raman-active lattice-modes of surfactant-tungstate hybrids appear from 194–120  $\text{cm}^{-1}$ .<sup>158</sup>

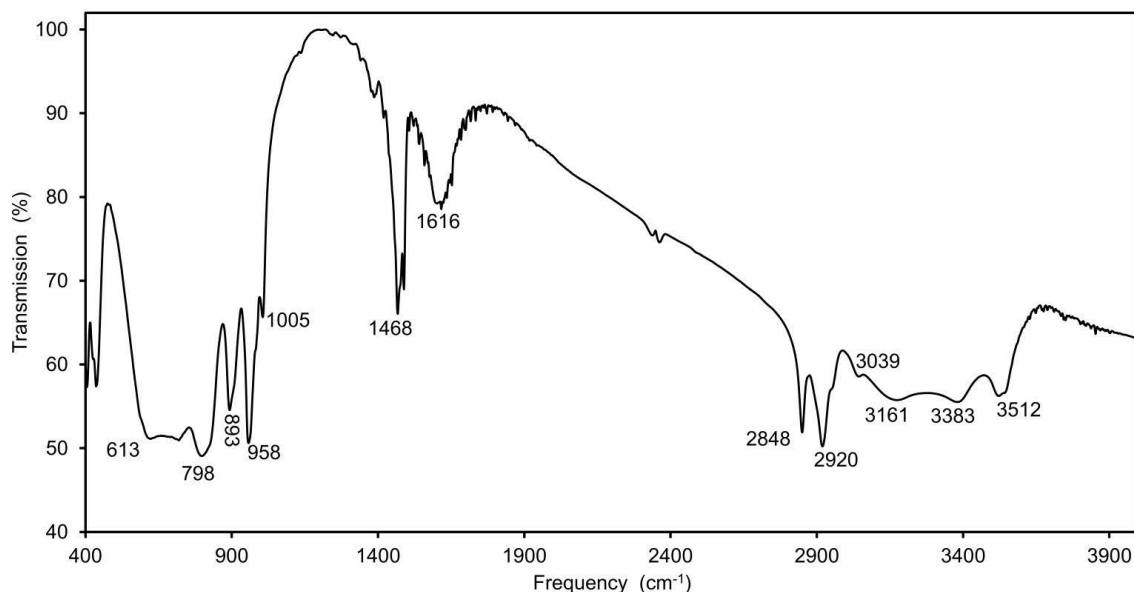


**Figure 3.2.6.** FT-IR Spectrum of CTA-WO<sub>3</sub> (KBr pellet). Broad peaks from 3512 to 3161 cm<sup>-1</sup> are assigned to non-equivalent  $\nu(-OH)$  species. Peaks at 3039, 2920 and 2848 cm<sup>-1</sup> arise from  $\nu(N^+-(CH_3))$ ,  $\nu_{as}(-CH_2-)$  and  $\nu_{ss}(-CH_2-)$  vibrations of CTA<sup>+</sup>, respectively.<sup>159, 160</sup> The broad peak centred on 1616 cm<sup>-1</sup> is assigned to intercalated  $\delta(H_2O)$ . The asymmetric double-peak with a maximum at 1468 cm<sup>-1</sup> corresponds to  $\omega(-CH_2-)$ ,  $\delta(-CH_2-)$  and  $\sigma(-CH_3)$  modes. Peaks at 1005 and 958 cm<sup>-1</sup> correspond to  $\nu_{ss}(W=O)$  and  $\nu_{as}(W=O)$  vibrations of surface and inter-layer W=O species. Peaks at 893 and 798-613 cm<sup>-1</sup> are assigned to multiple  $\nu(O-W-O)$  modes across the WO<sub>3</sub> sheets.<sup>155</sup>

CTA-WO<sub>3</sub> lost 22.3% mass by 800°C, implying a non-volatile WO<sub>3</sub> content of 77.7% (Figure 3.3.1). Approximately 4.5% mass was lost by 150°C, indicating the degree of hydration of CTA-WO<sub>3</sub>. This combined data combined with C,H&N microanalysis revealed a CTA:WO<sub>3</sub>:H<sub>2</sub>O ratio of 1:6:7 implying an empirical formula of (CTA).6[WO<sub>3</sub>].7H<sub>2</sub>O. Measured and theoretical C,H&N content is compared in Table 3.2.3.

**Table 3.2.3.** Measured and theoretical C,H&N content of CTA-WO<sub>3</sub> based on the empirical formula (CTA).6[WO<sub>3</sub>].7H<sub>2</sub>O.

<b>ELEMENT</b>	<b>MEASURED (%)</b>	<b>THEORETICAL (%)</b>
<b>C</b>	11.98	12.55
<b>H</b>	2.77	3.16
<b>N</b>	0.87	0.77

Measured and theoretical volatile organic (CTA<sup>+</sup>), non-volatile (WO<sub>3</sub>) and hydration (H<sub>2</sub>O) content based on the empirical formula (CTA).6[WO<sub>3</sub>].7H<sub>2</sub>O is summarized in Table 3.2.4.

**Table 3.2.4.** Measured and theoretical volatile organic (CTA<sup>+</sup>), non-volatile (WO<sub>3</sub>) and hydration (H<sub>2</sub>O) content based on the empirical formula (CTA).6[WO<sub>3</sub>].7H<sub>2</sub>O

<b>FRACTION</b>	<b>MEASURED (%)</b>	<b>THEORETICAL (%)</b>
<b>WO<sub>3</sub></b>	77.7	77.4
<b>CTA<sup>+</sup></b>	17.8	16.5
<b>H<sub>2</sub>O</b>	4.5	6.1

There would be 12 H<sub>2</sub>O molecules per 6 WO<sub>3</sub> in WO<sub>3</sub>.2H<sub>2</sub>O, therefore the presence of CTA<sup>+</sup> has displaced 5 H<sub>2</sub>O molecules per 6 WO<sub>3</sub> units in CTA-WO<sub>3</sub>. Similar cases of alkyl-ammonium surfactants displacing interlayer water have been reported in the literature.<sup>158</sup>

SEM images of CTA-WO<sub>3</sub> support this assignment, which displays a material consisting of large platelets from 1 to 5 μm in size. Such observations are typical of layered monoclinic tungsten oxide hydrates.<sup>163-166</sup>

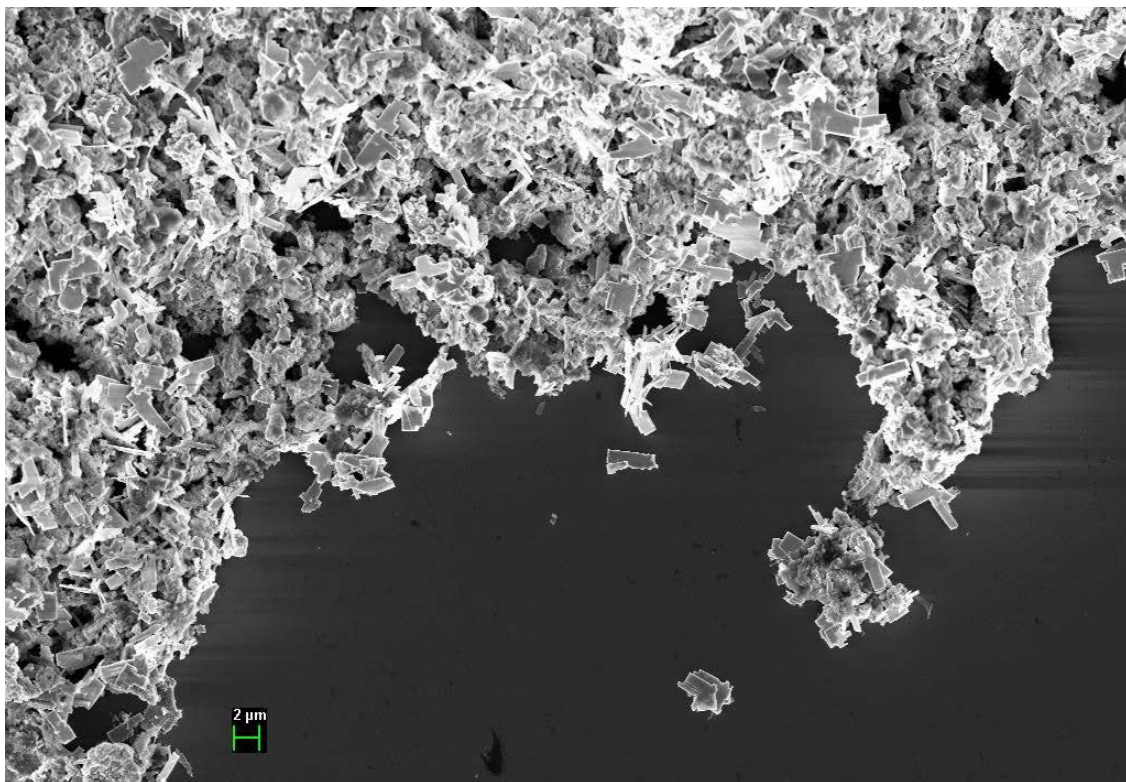


**Figure 3.2.7.** SEM image of CTA-WO<sub>3</sub>

Absence of both CTA<sup>+</sup> and NH<sub>4</sub>OH unsurprisingly yielded the hydrated monoclinic oxide, WO<sub>3</sub>·2H<sub>2</sub>O, as WCl<sub>6</sub> was hydrolyzed in the highly acidic environment. This determination was supported by XRD, Raman and FT-IR data:

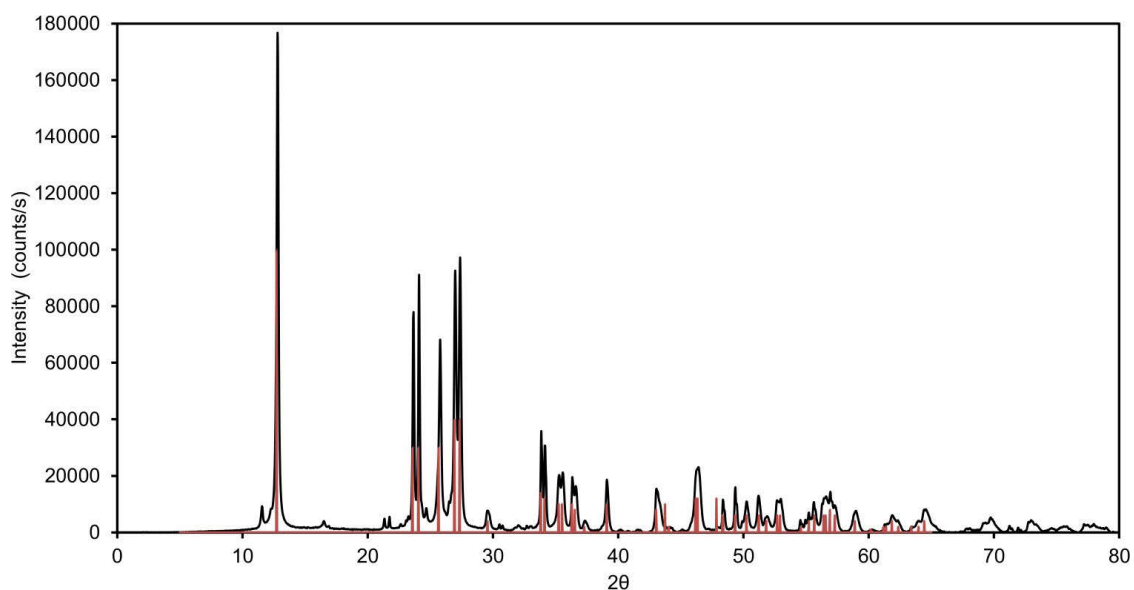


**Figure 3.2.8.** P-XRD pattern of the product of  $\text{WO}_3 \cdot 2\text{H}_2\text{O}$ . Stick plots are generated from the same JCPDS seen in Figure 3.2.4.

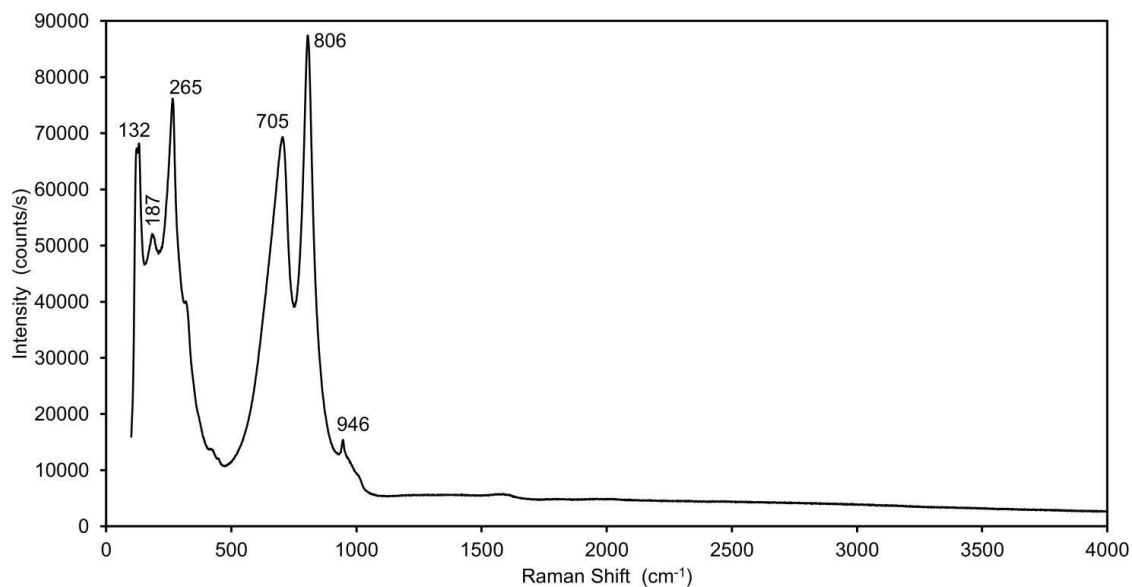


**Figure 3.2.9.** Raman spectrum of  $\text{WO}_3 \cdot 2\text{H}_2\text{O}$ . The small peak at  $946 \text{ cm}^{-1}$  is due to the  $\nu(\text{W}=\text{O})$  vibration from surface octahedra or defects. Peaks at  $806$  and  $705 \text{ cm}^{-1}$  correspond to non-equivalent  $\nu(\text{W}-\text{O}-\text{W})$  stretching. The asymmetric peak with a maximum at  $265 \text{ cm}^{-1}$  is comprised of  $\delta(\text{O}-\text{W}-\text{O})$  and  $\nu(\text{O}-\text{W}-\text{O})$  modes, and bulk trioxide lattice modes are seen at  $187$  and  $132 \text{ cm}^{-1}$ .<sup>158</sup>

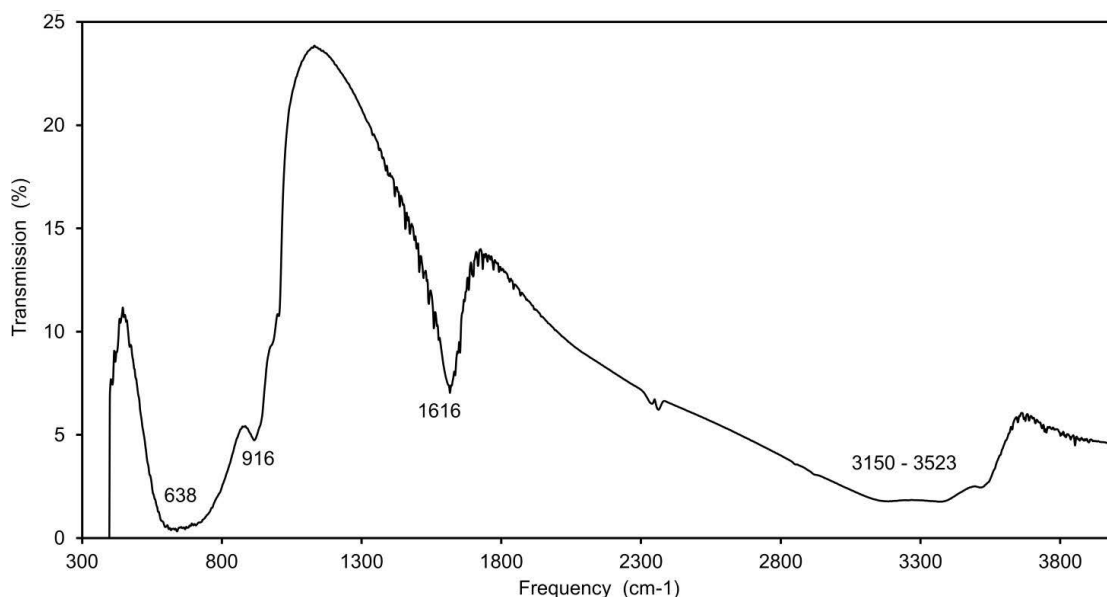


**Figure 3.2.10.** FT-IR spectrum of  $\text{WO}_3 \cdot 2\text{H}_2\text{O}$  collected in a KBr pellet. The broad peak from 3523 to 3150  $\text{cm}^{-1}$  and extending towards the lower-energy region is assigned to differing  $\nu(\text{H}_2\text{O})$  vibrations. The broad peak centred on 1616  $\text{cm}^{-1}$  is assigned to  $\delta(\text{H}_2\text{O})$  vibrations. The 916  $\text{cm}^{-1}$  peak is likely due to  $\nu(\text{W}=\text{O})$  vibrations from surface octahedra or defects, and the broad peak centred on 638  $\text{cm}^{-1}$  arises from  $\nu(\text{W}-\text{O}-\text{W})$  vibrations throughout the bulk-lattice.<sup>167</sup>

### 3.2.3 Synthesis of other tungstate-CTA compounds

As stated previously, CTA- $\text{W}_{12}$  was only produced after a CTA- $\text{WO}_3$  colloidal suspension was raised to pH 7.5, with  $\text{NH}_4\text{OH}$ . This is interesting as the metatungstate anion,  $[\text{H}_2\text{W}_{12}\text{O}_{40}]^{6-}$ , is typically formed at pH 3.5-6.<sup>109, 112, 113</sup> In order to investigate the formation of  $[\text{H}_2\text{W}_{12}\text{O}_{40}]^{6-}$  at more acidic pH, two CTA- $\text{WO}_3$  colloidal suspensions were prepared (as described in the previous section), and raised (from pH 0.5) to pH 4 and 7 with  $\text{NH}_4\text{OH}$ . The resulting suspensions were stirred for a further one week to accommodate any change in equilibria that may have occurred. After this, the suspensions were filtered and dried under an upturned beaker in an ajar drawer for 48 hours, before measurement by P-XRD (Fig. 3.2.11), FT-IR (Fig. 3.2.12) and Raman spectroscopy (Fig. 3.2.13).

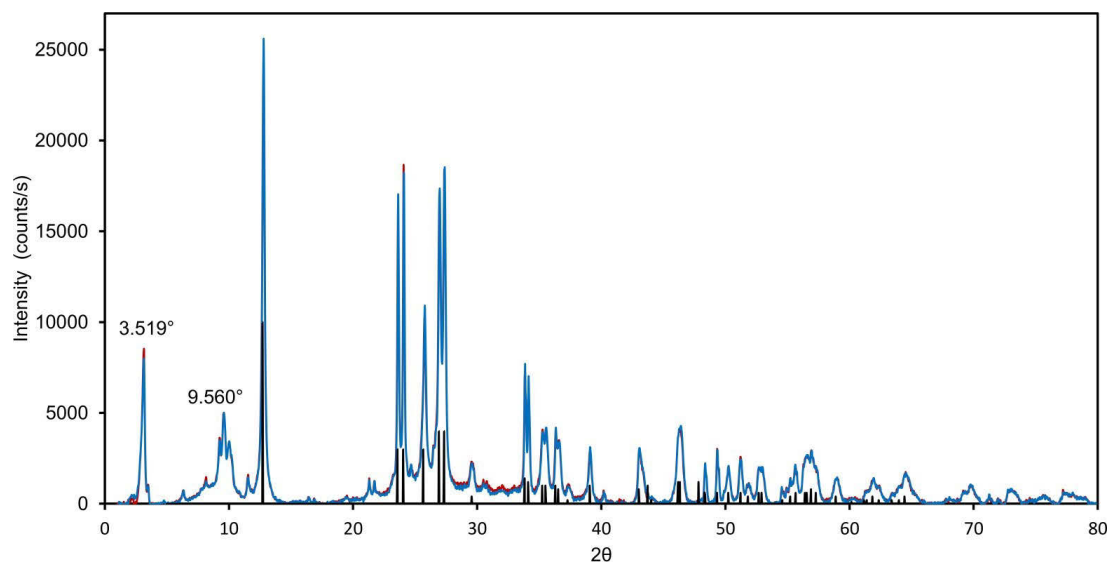


**Figure 3.2.11.** P-XRD patterns of the dried products produced from CTA-WO<sub>3</sub> colloidal suspensions raised to pH 4 (-) and pH 7 (-), followed by stirring for one week. Stick plot (-) is from JC-PDF 00-018-1420 for WO<sub>3</sub>·2H<sub>2</sub>O (as in Fig. 2.2.3).

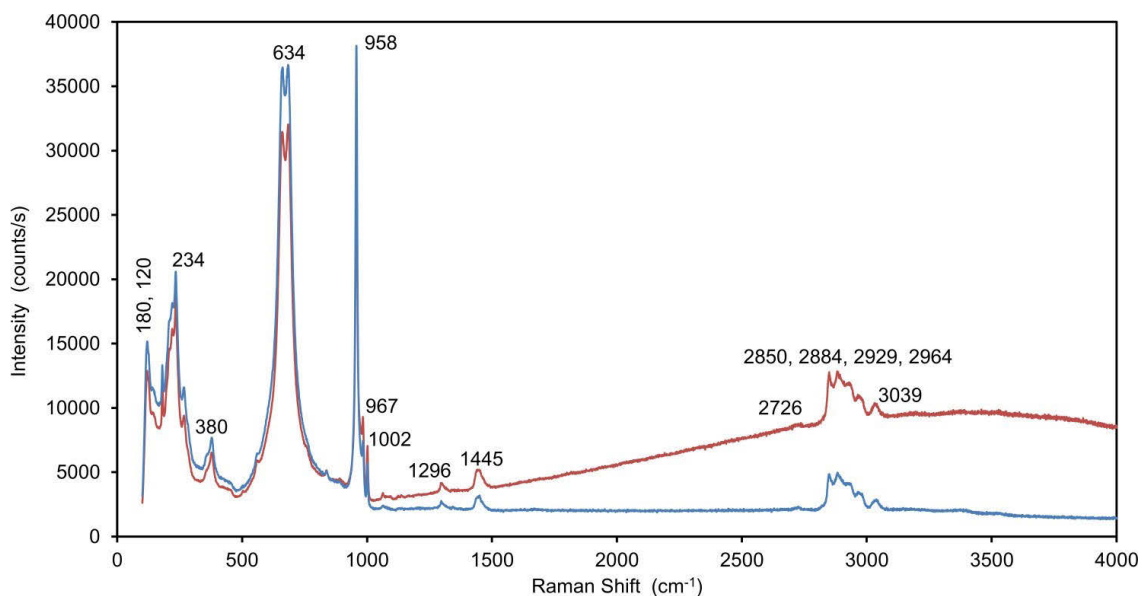


**Figure 3.2.12.** Raman spectra of samples as described in Figure 3.2.11.  $\nu(\text{N-R}_4^+)$ ,  $\nu(-\text{CH}_3)$ ,  $\nu(-\text{CH}_2-)$ ,  $\nu(\text{CH}_3\cdots\text{N}^+)$ ,  $\delta(-\text{CH}_3)$  and  $\sigma(\text{N-R}_4^+)$  vibrations appear at 3039, 2964, 2929–2850, 2726, 1445 and 1296  $\text{cm}^{-1}$  respectively, belonging to aliphatic  $\text{CTA}^+$ . Three non-equivalent  $\nu(\text{W}=\text{O})$  vibrations, from unequivocal POM species and/or  $\text{W}=\text{O}$  bond lengths,<sup>153, 154</sup> appear at 1002, 967 and 958  $\text{cm}^{-1}$ . The double-peak with a maximum at 634  $\text{cm}^{-1}$  and the peaks at 380 and 234  $\text{cm}^{-1}$  are assigned to  $\nu(\text{O-W-O})$ ,  $\nu(\text{W-OH}_2)$  and  $\nu(\text{W-O-W})$  vibrations respectively. Raman-active lattice-modes of surfactant-tungstate hybrids appear from 180–120  $\text{cm}^{-1}$ .<sup>158</sup>

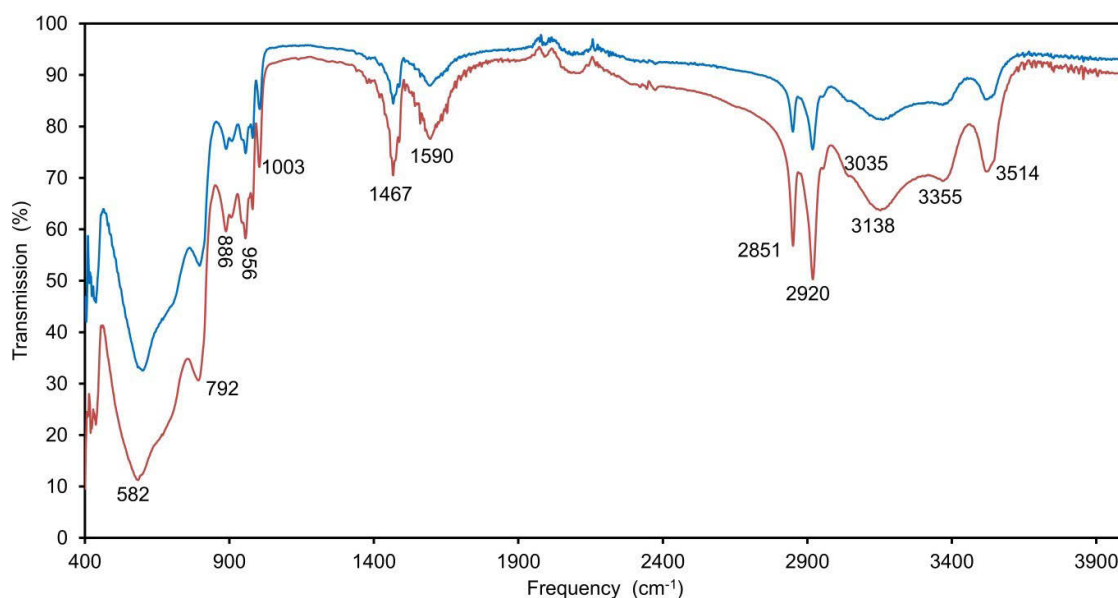


**Figure 3.2.13.** ATR FT-IR of samples as described in Figure 3.2.11. Broad peaks at 3514, 3355 and 3138  $\text{cm}^{-1}$  are due to non-equivalent  $\nu(-\text{OH})$  species. Peaks at 3035, 2920 and 2851  $\text{cm}^{-1}$  arise from  $\nu(\text{N}^+(\text{CH}_3))$ ,  $\nu_{as}(-\text{CH}_2)$  and  $\nu_{ss}(-\text{CH}_2-)$  vibrations of CTA, respectively. The broad peak centred on 1590  $\text{cm}^{-1}$  is assigned to intercalated  $\delta(\text{H}_2\text{O})$ . The asymmetric peak with a maximum at 1467  $\text{cm}^{-1}$  contains to  $\delta(-\text{CH}_2-)$  and  $\sigma(-\text{CH}_2-)$  modes. The small peak at 1003  $\text{cm}^{-1}$  is from to the  $\nu(-\text{N}-\text{C}-)$  vibration.<sup>3, 4</sup> Peaks at 956 and 886  $\text{cm}^{-1}$  correspond to  $\nu(\text{W}=\text{O})$  and  $\nu(\text{O}-\text{W}_b-\text{O})$  vibrations. The peak from 792 to 582  $\text{cm}^{-1}$  is due to  $\nu(\text{O}-\text{W}_c-\text{O})$  vibrations.<sup>156, 157</sup>

It is seen that the products of both alkalized and aged CTA- $\text{WO}_3$  suspensions yield compounds very similar to that of CTA- $\text{WO}_3$  prepared at pH 0.5 (Figures 3.2.4-6). It can be concluded then that CTA- $\text{W}_{12}$ , and more specifically the  $[\text{H}_2\text{W}_{12}\text{O}_{40}]^{6-}$  anion, was not produced at a pH lower than 7 (as compared to 7.5).

In light of this, a further attempt to synthesize CTA- $\text{W}_{12}$  at more acidic pH was carried out, this time by alkalizing suspensions of  $\text{WO}_3 \cdot 2\text{H}_2\text{O}$  with  $\text{NH}_4\text{OH}$  to pH 4 and stirring for a further one week to allow for equilibration to the metatungstate anion. Aqueous CTA-Br was then added to this solution just prior to filtration and drying for 48 hours.

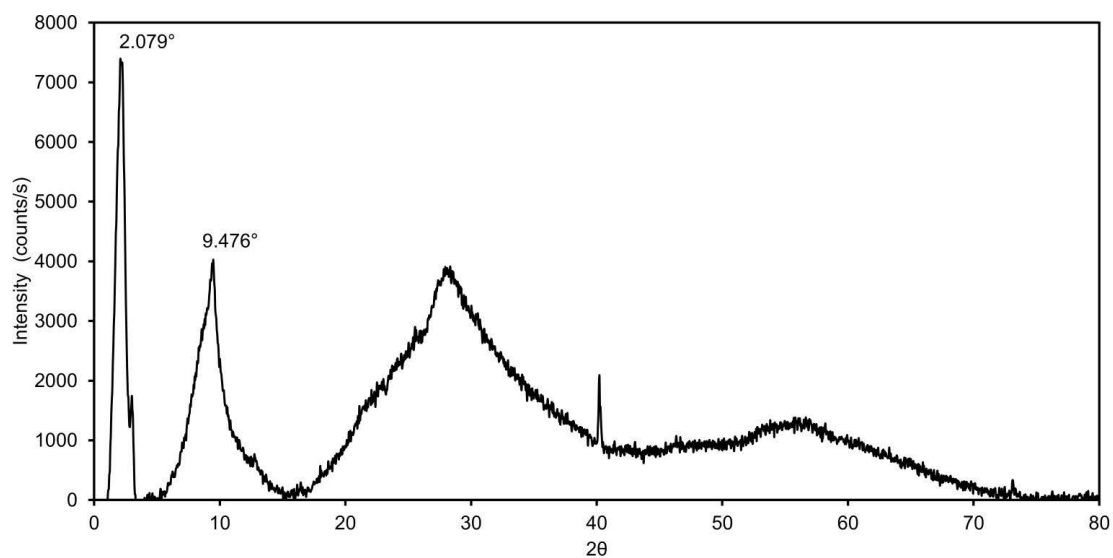


**Figure 3.2.14.** P-XRD pattern of the dried product produced from a  $\text{WO}_3 \cdot 2\text{H}_2\text{O}$  suspension alkalinized to pH 4 with  $\text{NH}_4\text{OH}$  and stirred for one week, followed by addition of CTA-Br.

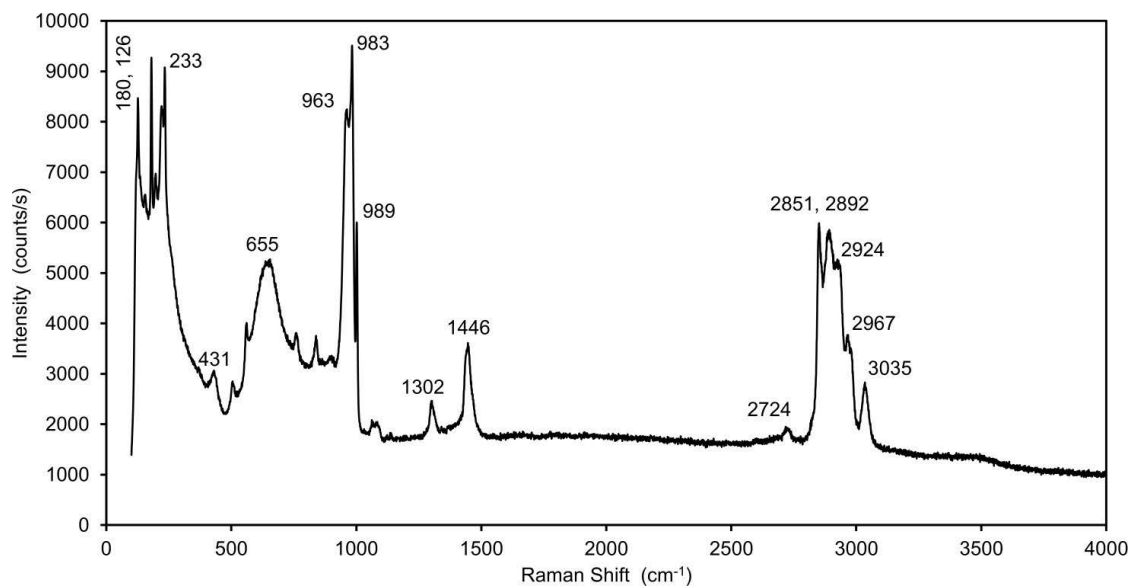


**Figure 3.2.15.** Raman spectra of sample as described in Figure 3.2.14.  $\nu(\text{N-R}_4^+)$ ,  $\nu(-\text{CH}_3)$ ,  $\nu(-\text{CH}_2-)$ ,  $\nu(\text{CH}_3 \cdots \text{N}^+)$ ,  $\delta(-\text{CH}_3)$  and  $\sigma(\text{N-R}_4^+)$  vibrations appear at 3035, 2967, 2924–2851, 2724, 1446 and 1302  $\text{cm}^{-1}$  respectively, belonging to aliphatic  $\text{CTA}^+$ . Three non-equivalent  $\nu(\text{W=O})$  vibrations, from three POM species and/or  $\text{W=O}$  bond lengths,<sup>153, 154</sup> appear at 989, 983 and 963  $\text{cm}^{-1}$ . The width and asymmetry of the peak at 963  $\text{cm}^{-1}$  is indicative of differing POM species.<sup>168</sup> The broad peak with a maximum at 655  $\text{cm}^{-1}$  and the peaks at 431 and 233  $\text{cm}^{-1}$  are assigned to  $\nu(\text{O-W-O})$ ,  $\nu(\text{W-OH}_2)$  and  $\nu(\text{W-O-W})$  vibrations respectively. Raman-active lattice-modes of surfactant-tungstate hybrids appear from 180–126  $\text{cm}^{-1}$ .<sup>158</sup>

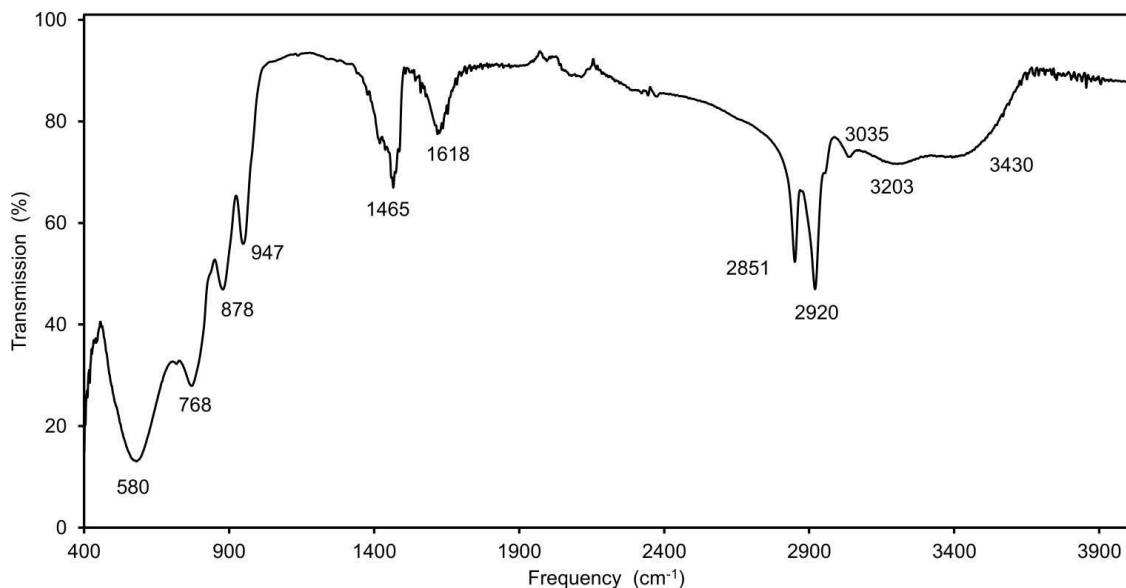


**Figure 3.2.16.** ATR FT-IR spectrum of sample as described in Figure 3.2.14. Broad peaks at 3430 and 3203  $\text{cm}^{-1}$  are assigned to non-equivalent  $\nu(-\text{OH})$  species. Peaks at 3035, 2920 and 2851  $\text{cm}^{-1}$  arise from  $\nu(\text{N}^+(\text{CH}_3))$ ,  $\nu_{as}(-\text{CH}_2-)$  and  $\nu_{ss}(-\text{CH}_2-)$  vibrations of  $\text{CTA}^+$ , respectively. The broad peak centred on 1618  $\text{cm}^{-1}$  is assigned to intercalated  $\delta(\text{H}_2\text{O})$ . The asymmetric peak with a maximum at 1465  $\text{cm}^{-1}$  contains  $\omega(-\text{CH}_2-)$ ,  $\delta(-\text{CH}_2-)$  and  $\sigma(-\text{CH}_2-)$  modes. Peaks at 947 and 878  $\text{cm}^{-1}$  correspond to  $\nu(\text{W}=\text{O})$  and  $\nu(\text{O}-\text{W}_b-\text{O})$  vibrations. The broad, asymmetric peaks at 768 and 580  $\text{cm}^{-1}$  are due to  $\nu(\text{O}-\text{W}_c-\text{O})$  vibrations that arise from the polymerized, differing, oxoanions.<sup>156, 157</sup>

From the combined P-XRD, Raman and FT-IR data, it can be determined that  $\text{WO}_3 \cdot 2\text{H}_2\text{O}$  suspensions alkalized to pH 4 with  $\text{NH}_4\text{OH}$  (from pH 0.5), followed by stirring for one week and then CTA-Br addition did not result in the production of CTA- $\text{W}_{12}$ . Observing the P-XRD of Figure 3.2.14, the peaks appear quite broad and ill-defined, especially within the higher  $2\theta$  range. The (001) reflection depicting the inter-lamellar distance ( $2.079^\circ$  or  $42.5\text{\AA}$ ) appears at lower  $2\theta$  than in CTA- $\text{W}_{12}$  ( $3.617^\circ$  or  $24.5\text{\AA}$ ), it is also more asymmetric, and appears to contain a double-apex and shoulder-peak. The peak centred at  $9.476\text{\AA}$ , indicative of the separation between the 2D pseudo-hexagonally arranged POMs in SEP materials, also appears much broader than that found within CTA- $\text{W}_{12}$  (Figure 3.2.3). Furthermore, the inorganic ( $< 1000 \text{ cm}^{-1}$ ) vibrational bands in the Raman (Fig. 2.2.15) and FT-IR (Figure 3.2.16) spectra are boarder and more asymmetric than CTA- $\text{W}_{12}$  (Fig. 2.2.1-2) and also

contain shoulders and double-apexes. This is most pronounced within the  $\nu(\text{W}=\text{O})$  vibrations around  $\sim 960\text{ cm}^{-1}$ , where a broad triple-peak is seen in the Raman spectrum, and a broad asymmetric shoulder-containing peak is seen in the FT-IR.

All these features are indicative of inhomogeneous SEP materials containing multiple differing tungstate anions. In such materials, the anions of differing charge and shape associate with differing numbers of surfactants which pack together to form disordered lamellar bi-layers containing differing interlamellar distances and irregular pseudo-hexagonal arrays, such as that depicted in Figure 3.2.14.<sup>134, 135</sup> The interlamellar distance is also much larger than CTA- $\text{W}_{12}$  ( $42.6\text{ \AA}$  compared to  $24.5\text{ \AA}$  in CTA- $\text{W}_{12}$ ), which likely a further result from disorder within the bi-layer, as described in Section 3.1.5 and Figure 3.1.6. Furthermore, the many different W-O bond lengths present vibrate at differing wavenumbers, which cumulatively contribute to form broad peaks in Raman and FT-IR spectroscopies.<sup>111, 168, 169</sup>

The most likely reason why multiple POM species are present within this sample, and not just the  $[\text{H}_2\text{W}_{12}\text{O}_{40}]^{6-}$  anion as in CTA- $\text{W}_{12}$ , is that very long times are needed for tungstate solutions to equilibrate.<sup>112, 113, 116-118</sup> This means that the alkalinized  $\text{WO}_3 \cdot 2\text{H}_2\text{O}$  colloid likely needed longer than the one week in this experiment to completely equilibrate to a homogeneous solution containing only the one anion.

To further explore tungsten equilibria in the CTA- $\text{W}_{12}$  reaction mechanism, a suspension of CTA- $\text{W}_{12}$  was produced, as described in Section 3.2.1, and alkalinized to pH 8 with  $\text{NH}_4\text{OH}$ . Upon reaching pH 8, the solution changed appearance from the turbid ('milky') white/colourless of CTA- $\text{W}_{12}$ , to quite transparent. This change is likely due to the appearance of another tungstate anion, which is likely to be the paratungstate-A,  $[\text{H}_2\text{W}_{12}\text{O}_{42}]^{10-}$ , at pH 8.<sup>116, 118</sup> This alkalinized CTA- $\text{W}_{12}$  solution was then separated into two solutions and acidified to pH 4 and 7 with HCl. Once acidified below pH 7.5, the solutions returned to the turbid white/colourless appearance of CTA- $\text{W}_{12}$  colloidal suspensions. After one week of stirring, the suspensions were then filtered and dried for 48 hours.

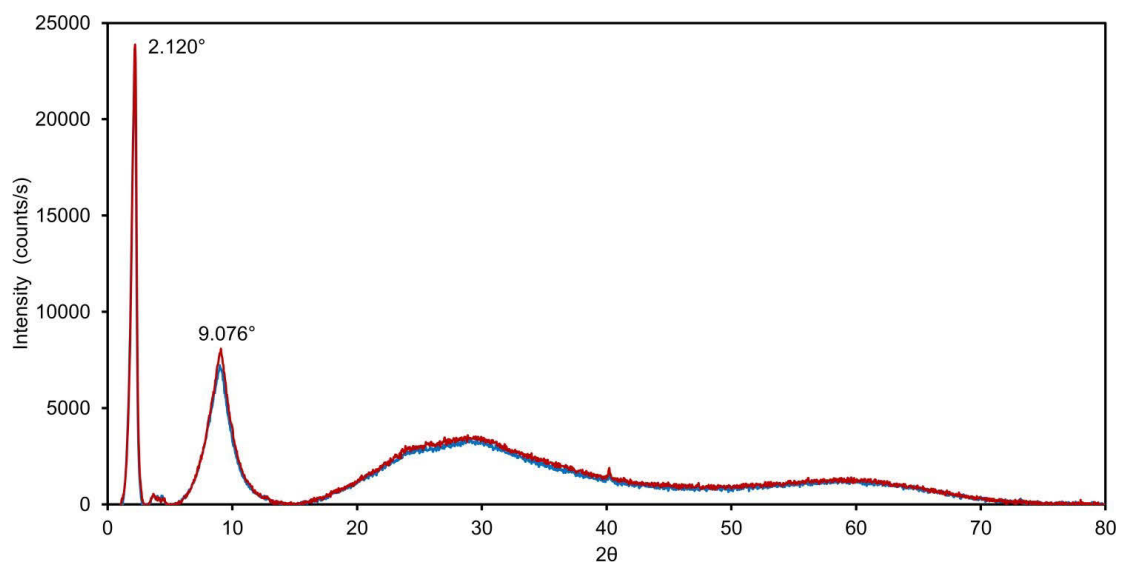


**Figure 3.2.17.** P-XRD of the dried product from a CTA- $W_{12}$  suspension alkalized to pH 8 (with  $NH_4OH$ ), followed by acidification to pH 4 (-) and pH 7 (-) (with HCl) and stirred for a further one week.

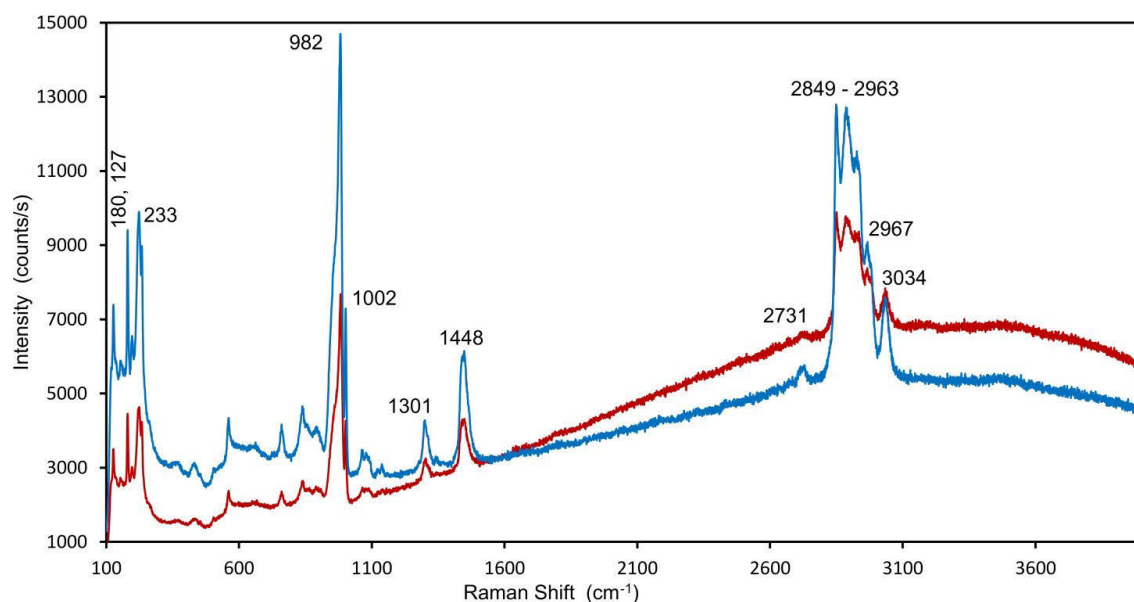


**Figure 3.2.18.** Raman spectra of the samples as described in Figure 3.2.17.  $\nu(\text{N-R}_4^+)$ ,  $\nu(-\text{CH}_3)$ ,  $\nu(-\text{CH}_2-)$ ,  $\nu(\text{CH}_3 \cdot \text{N}^+)$ ,  $\delta(-\text{CH}_3)$  and  $\sigma(\text{N-R}_4^+)$  vibrations appear at 3034, 2967, 2963–2849, 2731, 1448 and 1301  $\text{cm}^{-1}$  respectively, belonging to aliphatic  $\text{CTA}^+$ . A large, asymmetric double-peak attributable to  $\nu(\text{W}=\text{O})$  vibrations, (due to differing POM species and/or  $\text{W}=\text{O}$  bond lengths,<sup>153, 154</sup>) appear at 1002 and 982  $\text{cm}^{-1}$ . The width and asymmetry of the peak at 982  $\text{cm}^{-1}$  is indicative of differing POM species.<sup>168</sup> The peak at 233  $\text{cm}^{-1}$  is assigned to  $\nu(-\text{W}-\text{O}-\text{W}-)$ . Raman-active lattice-modes of surfactant-tungstate hybrids appear from 180–127  $\text{cm}^{-1}$ .<sup>158</sup>

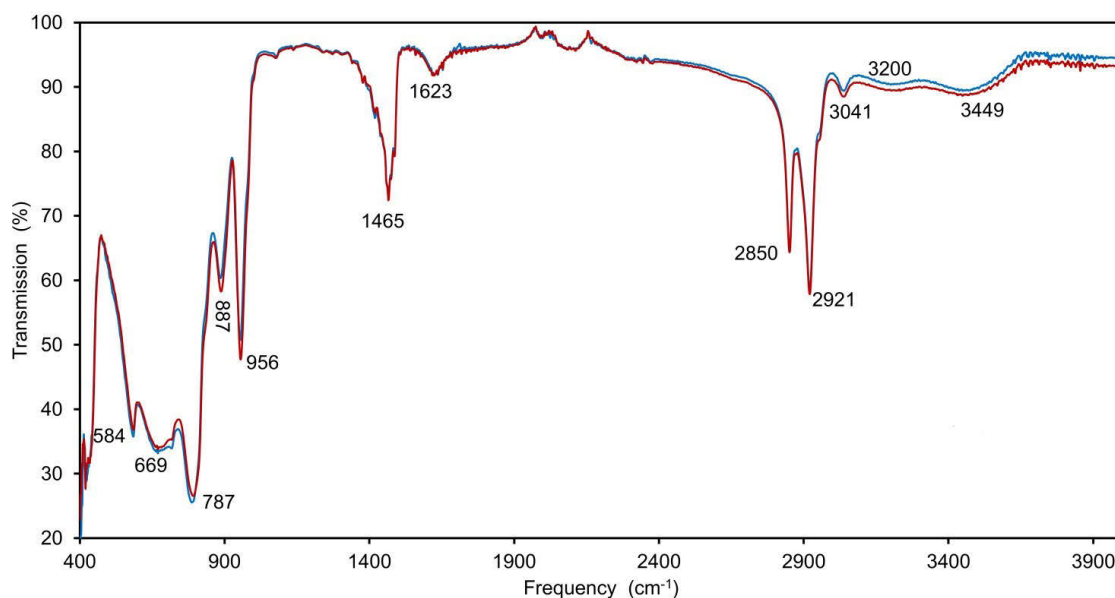


**Figure 3.2.19.** ATR FT-IR of the samples as described in Figure 3.2.17. Broad peaks at 3449 and 3200  $\text{cm}^{-1}$  are assigned to non-equivalent  $\nu(\text{H}_2\text{O})$  species. Peaks at 3041, 2921 and 2850  $\text{cm}^{-1}$  arise from  $\nu(-\text{N}^+(\text{CH}_3))$ ,  $\nu_{as}(-\text{CH}_2)$  and  $\nu_{ss}(-\text{CH}_2-)$  vibrations of  $\text{CTA}^+$ , respectively. The broad peak at 1623  $\text{cm}^{-1}$  is assigned to intercalated  $\delta(\text{H}_2\text{O})$ . The asymmetric peak with a maximum at 1465  $\text{cm}^{-1}$  contains  $\omega(-\text{CH}_2-)$ ,  $\delta(-\text{CH}_2-)$  and  $\sigma(-\text{CH}_2-)$  modes. Peaks at 956 and 887  $\text{cm}^{-1}$  correspond to  $\nu(\text{W}=\text{O})$  and  $\nu(\text{O}-\text{W}_b-\text{O})$  vibrations. The broad peaks at 787, 669 and 584  $\text{cm}^{-1}$  are due to  $\nu(\text{O}-\text{W}_c-\text{O})$  vibrations that arise from the polymerized, differing, oxoanions.<sup>156, 157</sup>

The P-XRD of the sample depicted in Figure 3.2.17 is similar to that of Figure 3.2.14, where very broad peaks are observed, unlike the sharp peaks indicative of more ordered crystal structures like that found in  $\text{CTA-W}_{12}$  (Fig. 2.2.3). Again, the (001) reflection appears at much lower  $2\theta$  than in  $\text{CTA-W}_{12}$  ( $2.120^\circ$  compared to  $3.617^\circ$ ), indicative of a larger, more distorted bi-layer. Additionally, the Raman and FT-IR spectra of Figures 3.2.18 and 3.2.19 contain broad, asymmetric peaks within the inorganic region ( $< 1000 \text{ cm}^{-1}$ ). This is again likely due to slow transformation of the tungstates in solution, this time from  $[\text{H}_2\text{W}_{12}\text{O}_{42}]^{10-}$  to  $[\text{H}_2\text{W}_{12}\text{O}_{40}]^{6-}$ , resulting an inhomogeneous SEP containing multiple POM species.

It can be said however, that the above sample is likely less inhomogeneous than that presented within Figures 3.14-16 (sample **S1**). Not only are the P-XRD more symmetrical (although still quite broad), but the inorganic vibrations in the FT-IR and Raman spectra are

also much sharper and more defined. Figure 2.2.15 contains a broad triple-peak  $\nu(\text{W}=\text{O})$  vibration, compared to two in Figure 3.2.18 (sample **S2**), and seems to contain large broad peak in the  $400 - 900 \text{ cm}^{-1}$  region, the region attributable to  $\nu(\text{O}-\text{W}_b-\text{O})$  and  $\nu(\text{O}-\text{W}_c-\text{O})$  vibrations, whereas Fig. 2.2.18 contains many sharper peaks within this region. The same greater inhomogeneity is represented within the FT-IR spectra, where large broad peaks attributable to  $\nu(\text{O}-\text{W}_b-\text{O})$  and  $\nu(\text{O}-\text{W}_c-\text{O})$  vibrations are found within the spectrum of Figure 3.2.16, contrasting to the sharper peaks of Figure 3.2.19.

This is likely due to the fact that **S1** underwent a greater range of pH change in the absence of  $\text{CTA}^+$  (0.5 to 4) as compared to **S2**, which contained  $\text{CTA}^+$  from the beginning of synthesis. Within the pH range of 0.5 to 4, tungstates are known to adopt a number of isopolyanion forms (Section. 3.1.1), including decatungstate,  $[\text{W}_{10}\text{O}_{32}]^{6-}$ , and metatungstate. These isopolytungstates likely persisted in solution until  $\text{CTA}^+$  addition one week later. Conversely, **S2** underwent a pH from 7.5 to 8 (and back again), likely resulting a mixture of just metatungstates and paratungstates.

### 3.2.4 CTA-tungstate products from high pH solutions

Products obtained from the synthesis method described in Section 3.2.1 at pH 8 resembled an SEP compound containing the paratungstate-B anion,  $[\text{H}_2\text{W}_{12}\text{O}_{42}]^{10-}$ , and  $\text{CTA}^+$  (CTA-Para). This assignment is confirmed by XRD and Raman spectroscopy by comparing CTA-Para to the decahydrate of ammonium paratungstate,  $(\text{NH}_4)_{10}[\text{H}_2\text{W}_{12}\text{O}_{42}]\cdot 10\text{H}_2\text{O}$ .

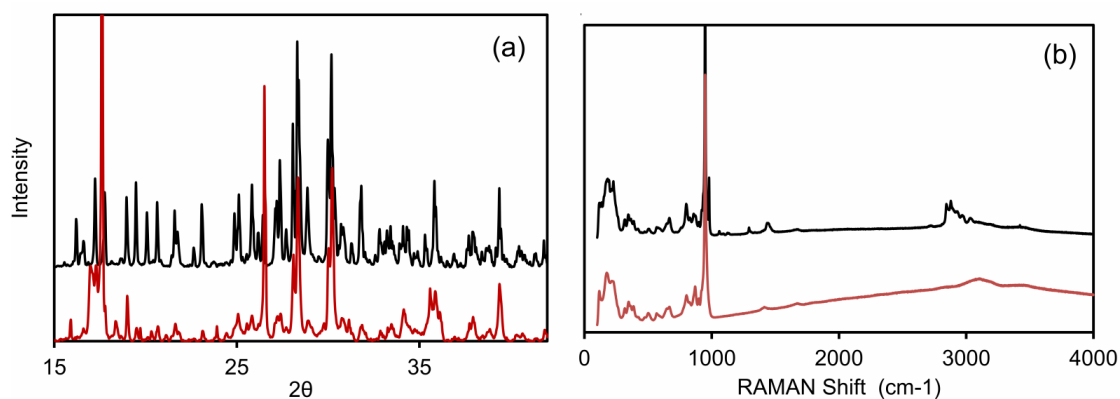


**Figure 3.2.20.** (a) XRD patterns of (-) CTA-Para and (-)  $(\text{NH}_4)_{10}[\text{H}_2\text{W}_{12}\text{O}_{42}]\cdot 10\text{H}_2\text{O}$  (b) Raman spectra of (-) CTA-Para and (-)  $(\text{NH}_4)_{10}[\text{H}_2\text{W}_{12}\text{O}_{42}]\cdot 10\text{H}_2\text{O}$

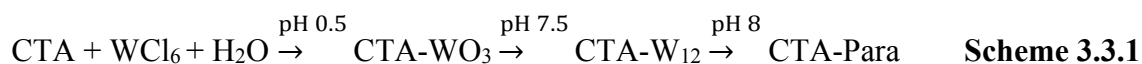
Differences in the Raman spectra of Figure 3.2.20(b) in the regions of 1060 – 1300 cm<sup>-1</sup> and 2700 – 3050 cm<sup>-1</sup> are attributable -CH<sub>2</sub>- and -CH<sub>3</sub> vibrations of CTA<sup>+</sup> in CTA-Para. Further evidence for the assignment of [H<sub>2</sub>W<sub>12</sub>O<sub>42</sub>]<sup>10-</sup> to the anion present in CTA-Para is the materials lack of photochromicity. As will be discussed in Chapter 5, unlike metatungstates and all other isopolytungstates, the [H<sub>2</sub>W<sub>12</sub>O<sub>42</sub>]<sup>10-</sup> anion does not form an adsorption band in the visible-region upon reduction.<sup>170</sup>

The CTA-Para samples depicted in Figure 3.2.20 were at pH 8 for only 1 day. This makes metatungstate to paratungstate-B conversion within CTA<sup>+</sup> micelles a much faster process than paratungstate-B to metatungstates conversion, considering the products depicted in Figures 3.2.17-19. A similar slow reaction rate from paratungstate-B to metatungstates was observed by H. Ortner in his study of isopolytungstate equilibria.<sup>171</sup>

### **3.3 Tungstate-CTA<sup>+</sup> solution dynamics**

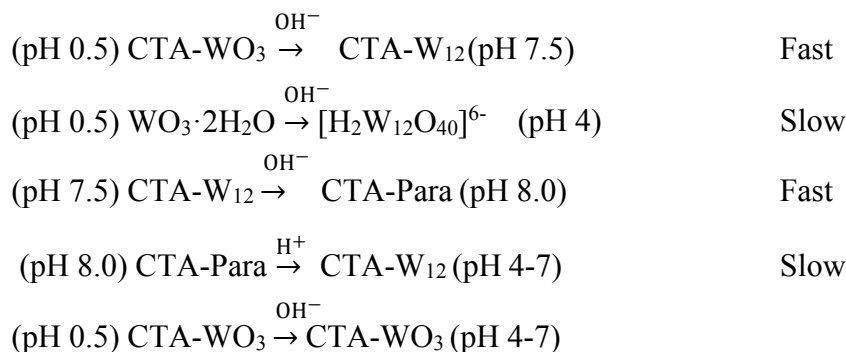
#### **3.3.1 Tungstate-CTA equilibria**

Summarizing the above findings, CTA-W<sub>12</sub> was only synthesized when suspensions of CTA-WO<sub>3</sub> (at pH 0.5) were alkalized to 7.5 with NH<sub>4</sub>OH. Precipitates collected at pH 8 contained the inert paratungstate-A anion. This reaction sequence is depicted in reaction Scheme 3.3.1.



Attempts to synthesize CTA-W<sub>12</sub> by synthesizing metatungstate first, followed by CTA<sup>+</sup> addition (Figures 3.2.14-16), resulted in inhomogeneous SEP samples that were comprised of multiple polyanion species. This most likely occurred due to the tungstate solutions requiring longer than one week to equilibrate from WO<sub>3</sub>·H<sub>2</sub>O to [H<sub>2</sub>W<sub>12</sub>O<sub>40</sub>]<sup>6-</sup>. Inhomogeneous samples were also produced when suspensions of CTA-W<sub>12</sub> that exceeded pH 7.5 were acidified (Figures 3.2.17-19). Interestingly, no change occurred to CTA-WO<sub>3</sub> suspensions that were alkalized from pH 0.5 up to 7, as can be seen by comparing Figures 3.2.4-6 and Figures 3.2.11-13. The above findings can be summarized within Scheme 3.3.2.

### Scheme 3.3.2.

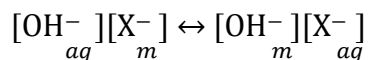


### 3.3.2 Conversion of CTA-WO<sub>3</sub> to CTA-W<sub>12</sub>

This last equation in Scheme 3.3.2 is quite interesting as tungstate solutions are known to adopt a variety of structures in aqueous solutions from pH ~2 to pH 7 (Section 3.1.1). The resistance to chemical change by CTA-WO<sub>3</sub> suspensions indicates an insulating role of CTA<sup>+</sup> to external pH change. CTA<sup>+</sup> cations form micelles in aqueous solution, which would contain hydrophobic WO<sub>3</sub>·2H<sub>2</sub>O particles and the CTA<sup>+</sup> alkyl-tails in the present case. Within the CTA<sup>+</sup> micelle the reaction to form [H<sub>2</sub>W<sub>12</sub>O<sub>40</sub>]<sup>6-</sup> from WO<sub>3</sub> and OH<sup>-</sup> (from NH<sub>4</sub>OH) would be as follows;



The outer surface of the micelles is terminated by the CTA<sup>+</sup> cationic head-groups and counter-anions, forming a *Stern* or electric double-layer.<sup>172, 173</sup> These counter-anions would most likely be Cl<sup>-</sup> or Br<sup>-</sup>, considering the ionic-binding strengths of the charged halides as compared to OH<sup>-</sup>.<sup>173, 174</sup> Due to the halide terminated surface, and the hydrophobicity of the interior, diffusion of hydrophilic OH<sup>-</sup> from the solution across the Stern layer and into the micelles to react with WO<sub>3</sub>·2H<sub>2</sub>O to produce [H<sub>2</sub>W<sub>12</sub>O<sub>40</sub>]<sup>6-</sup> would be hindered. The equilibrium and transfer of OH<sup>-</sup>/anionic-halide across CTA<sup>+</sup> micelles is described in Equation 3.3.2 and derived from work presented in<sup>173</sup>:



$$K_{\text{OH}}^{\text{X}} = \frac{[\text{OH}^-]_m[\text{X}^-]_{aq}}{[\text{OH}^-]_{aq}[\text{X}^-]_m} \quad \text{Equation 3.3.2}$$

where  $[\text{OH}^-]_{aq}$  is the concentration of  $\text{OH}^-$  in solution,  $[\text{OH}^-]_m$  is the concentration of  $\text{OH}^-$  within the micelles,  $[\text{X}^-]_{aq}$  is the concentration of  $\text{Cl}^-$  or  $\text{Br}^-$  in solution,  $[\text{X}^-]_m$  is the concentration of  $\text{Cl}^-$  or  $\text{Br}^-$  within micelles, and  $K_{\text{OH}}^{\text{X}}$  is the rate of exchange between  $\text{Cl}^-$  or  $\text{Br}^-$  and  $\text{OH}^-$  across the Stern layer. From Equation 3.3.2 it is possible to see that the barrier to  $[\text{H}_2\text{W}_{12}\text{O}_{40}]^{6-}$  is only overcome at  $\text{pH} > 7$ , when  $\text{OH}^-$  becomes much more freely abundant in solution, as was observed in the present work, Schemes 2.1-2.

TGA was performed on the samples presented in Figures 3.2.11-13, which contained CTA- $\text{WO}_3$  alkalyzed to  $\text{pH} 4$  (**B4**) and  $\text{pH} 7$  (**B7**) to further investigate the shielding role of  $\text{CTA}^+$  in polyoxotungstate synthesis, Figure 3.3.1(b) and (c). This was compared to TGA of CTA- $\text{WO}_3$ , Figure 3.3.1(a), synthesized at  $\text{pH} 0.5$ , to determine if **B4** and **B7** contained a larger organic fraction, Figure 3.3.1(d). A larger organic fraction, i.e. more  $\text{CTA}^+$  cations, would mean that species containing a larger anionic charge would be present in the sample, most likely due to  $\text{WO}_3 \cdot 2\text{H}_2\text{O}$  reacting with  $\text{OH}^-$  and  $\text{H}_2\text{O}$  to form polytungstates.

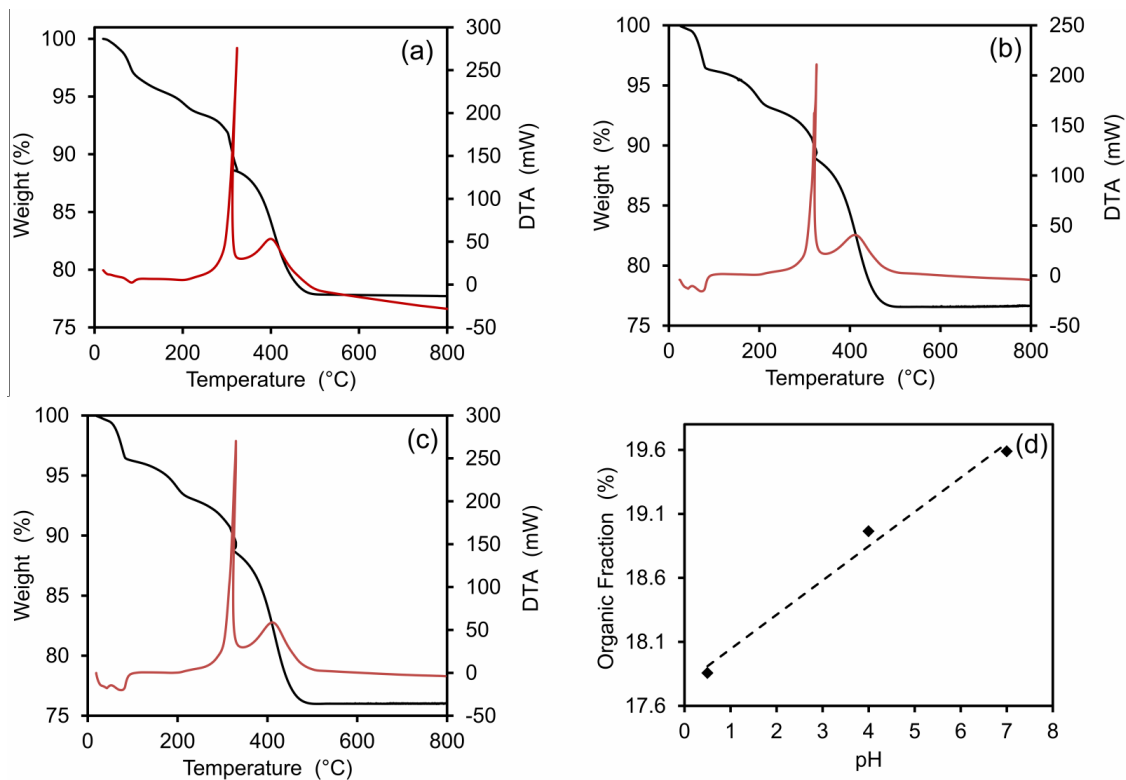


**Figure 3.3.1.** (a) TGA and DTA of CTA-WO<sub>3</sub> (b) TGA and DTA of **B4** (c) TGA and DTA of **B7** (d) Organic (CTA<sup>+</sup>) fraction of sample versus synthesis pH

The shape of all three decomposition curves look similar, with all containing two stages of endothermic dehydration below 200°C, and two stages of exothermic CTA<sup>+</sup> decomposition from 200 to 500°C (this will be further investigated in detail in the following chapter). The two dehydration events likely arise from loss crystal water at ~60°C, and loss of tighter bound interlayer W-OH species at ~80°C. In light of this, all mass loss from temperatures lower than 150°C is ascribed to dehydration of the sample. Considering this, the TGA experiments depicted in Figure 3.3.1 reveals that CTA-WO<sub>3</sub> is comprised of 17.9% CTA<sup>+</sup>, **B4** is comprised of 18.9% CTA<sup>+</sup>, and **B7** is comprised of 19.6% CTA<sup>+</sup>. These values are quite similar to each other, with only 1.7% organic mass difference between pH 0.5 (CTA-WO<sub>3</sub>) and pH7 (**B7**). If it is agreed that these measured values fall outside the error of the instrument, and all mass loss above 150°C is indeed ascribable to the decomposition of CTA<sup>+</sup>, a slight trend of increasing CTA<sup>+</sup> content with increasing pH is seen, Figure 3.3.1(d).

This would suggest that some of the  $\text{WO}_3$  from the CTA- $\text{WO}_3$  particles is reacting with available  $\text{OH}^-$  to produce higher anionic charged polyanions. However, this value of 19.6%  $\text{CTA}^+$  is much less than that of the 40.7% found within CTA- $\text{W}_{12}$  (Section 3.2.1). This suggests that although the production of polyanions from CTA-tungstate suspensions might occur in acidic solutions (pH 0.5-7) at low levels, however, a large shift in equilibrium occurs at pH 7.5.

It is therefore concluded that significant diffusion of  $\text{OH}^-$  into  $\text{CTA}^+$  micelles is only possible when the basic hydrophilic species becomes much more abundant in the solution, i.e.  $> \text{pH } 7$ . Similar  $\text{OH}^-$  (and  $\text{H}^+$ ) concentration dependent reactions have been found to occur in  $\text{CTA}^+$  micelles for reactions between hydrophilic and hydrophobic reactants.<sup>172-174</sup> Considering that there is 15 times more  $\text{Cl}^-$  anions than  $\text{Br}^-$  anions in CTA- $\text{W}_{12}$  synthesis (Section 3.2.1), and that  $\text{Cl}^-$  was detected in the material and  $\text{Br}^-$  was not, (as confirmed by XPS, Figure 5.3.3) it is much more likely  $\text{Cl}^-$  is the predominant counter-anion to  $\text{CTA}^+$  in solution. Rearranging Equation 3.3.2 and formulas in<sup>173</sup> for  $k_m$ , the rate constant for Equation 3.3.1 within  $\text{CTA}^+$  micelles for the present yields Equation 3.3.3.

$$k_m = k_{aq} \text{CTA}_m \cdot K_{\text{OH}}^{\text{Cl}} \frac{[\text{OH}^-]_{dq}}{[\text{OH}^-]_m} \quad \text{Equation 3.3.3}$$

where  $k_{aq}$  is the rate of the reaction outside the micelle,  $\text{CTA}_m$  is the fraction of micellized  $\text{CTA}^+$  and  $K_{\text{OH}}^{\text{Cl}}$  is the rate of exchange between  $\text{Cl}^-$  and  $\text{OH}^-$  across the micelle interface. Intuitively, the  $k_m$  increases as the total micelle volume increases ( $\text{CTA}_m$ ), the concentration of available  $\text{OH}^-$  increases,  $[\text{OH}^-]_{dq}$  and as the rate at which  $\text{OH}^-$  is transferred into the micelle,  $K_{\text{OH}}^{\text{Cl}}$

### **3.4 Structural characterization of CTA- $\text{W}_{12}$**

As was described in section 2.1, anionic POMs and cationic surfactants can combine to form an array of structurally diverse SEP materials. Such combinations typically form lamellar structures, as described in Sections 3.1.4-5, however this is not always the case. Therefore, effort was made to further characterize the meso- and nano-structure of CTA- $\text{W}_{12}$ .

### 3.4.1 P-XRD, SEM and TEM of CTA-W<sub>12</sub>

As can be seen within Figure 3.2.3 of Section 3.2.1, CTA-W<sub>12</sub> appears to be a lamellar-structured SEP material, as revealed by P-XRD. In these materials the interlamellar distance is comprised of hydrophobic surfactant-tails, separated by hydrophilic layers of pseudo-hexagonally arranged POMs and water, as is described in Sections 3.1.4-5. Visual representation of CTA-W<sub>12</sub>, based on the P-XRD pattern of Figure 3.2.3, is depicted in Figure 3.4.1:

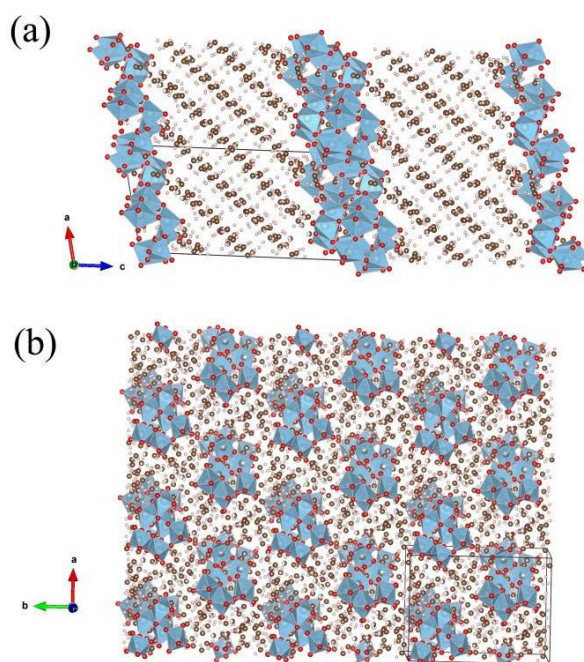


**Figure 3.4.1.** Visual representation based on pattern presented in Figure 3.2.3. (a) Lamellar structure of CTA-W<sub>12</sub> depicting the [H<sub>2</sub>W<sub>12</sub>O<sub>40</sub>]<sup>6-</sup> clusters (blue octahedra and red spheres), separated by the interdigitated surfactant tails of CTA<sup>+</sup> (brown and grey spheres). (b) 2D pseudo-hexagonal arrangement of the POMs within the hydrophilic layer. The positions of the light elements are notional only, and are taken from the closely related compound studied by Nyman *et al.*<sup>135</sup>.

Within this representation, the two main structural features of SEP bi-layers are highlighted. Figure 3.4.1(a) depicts the bi-layered structure of CTA-W<sub>12</sub>, where the layers of hydrophilic inorganic POMs (blue octahedra and red spheres) are separated by the hydrophobic alkyl-

chains of the organic surfactants (brown and grey spheres). As is described in Sections 3.1.4-5, the surfactant-tails are tilted with respect to the bi-layer interface and interdigitated with the surfactant-tails originating from the opposite of the layer. The separation between the sheets of POMs, i.e. the interlamellar spacing, is measured to be  $24.90 \pm 0.20$  Å by P-XRD and Rietveld refinement.

The lamellar structure of CTA- $W_{12}$ , with an interlamellar spacing of  $\sim 24.5$  Å is further confirmed by TEM imaging. Within the TEM images of Figure 3.4.2(b) and (c), the dark regions containing the inorganic POMs and water which are separated by the light regions containing the surfactant tails, are clearly visible. Measurement of the interlamellar distance by TEM was made more accurate by considering the average interlamellar distance over a 35 nm length, perpendicular to the (001) plane. This was made easier by using image software that measured the contrast across the selected length, Figure 3.4.2(d). Figure 3.4.2(a) depicts an SEM image of CTA- $W_{12}$ , illustrating that the sample is made of flat, irregular shape particulates approximately 200 nm in size.

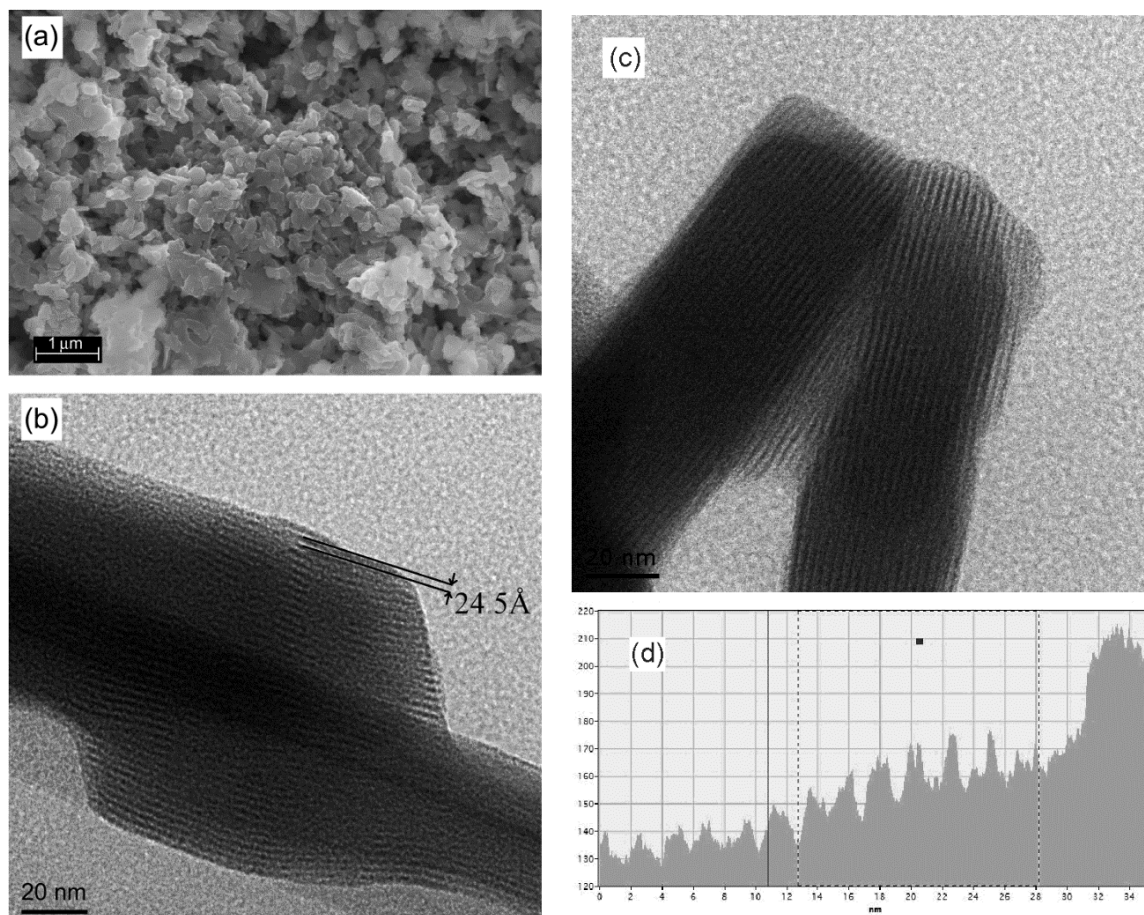


**Figure 3.4.2.** (a) SEM image of CTA-W<sub>12</sub>. (b) and (c) TEM images of CTA-W<sub>12</sub>. (d) Typical 35nm contrast-dependent length section used to calculate interlamellar distance of CTA-W<sub>12</sub>.

The presence of  $\nu_{ss}(-CH_2-)$  and  $\nu_{as}(-CH_2-)$  vibrational bands (Figure 3.2.2) located below 2924 and 2854  $cm^{-1}$ , respectively, means that the alkyl-chains are linearly aligned and are not bent due to *gauche* disorder.<sup>64, 159, 160</sup> Considering this, and that the interlamellar distance is 24.5 Å in width, a CTA<sup>+</sup> surfactant is 24 Å in length<sup>84</sup> and a metatungstate anion is 10 Å in diameter,<sup>175</sup> this would mean that each surfactant is tilted at an angle of approximately 53° and 37° with respect to the two interfaces of the hydrophobic space. This interlamellar distance is very similar to the 24.44 Å found by Nyman *et al* in their study of  $(CTA)_5(CH_3CN)_4[H_xSiMo_{12}O_{40}]$ ,<sup>135</sup> and similar to 21.46 Å found by Asami *et al* in their study of  $[(CH_3)_4N]_6[H_2W_{12}O_{40}] \cdot 9H_2O$ .<sup>48</sup> Nyman *et al* found that in  $(CTA)_5(CH_3CN)_4[H_xSiMo_{12}O_{40}]$ , the CTA<sup>+</sup> surfactants are interdigitated by an average of

13.3 carbons per chain, and it is likely, considering the similar interlamellar distance of CTA- $W_{12}$ , that the CTA<sup>+</sup> tails are interdigitated to a similar degree within the current sample. However, Nyman *et al* also found that most of the surfactants per unit cell adopt unique orientations and interdigitation degrees, as described in Section 3.1.5, and observed some CTA<sup>+</sup> surfactants being completely interdigitated (16 carbons) and others only by nine carbons. It is likely a similar case applies to CTA- $W_{12}$ , considering it also exceeds the 1:4 POM:surfactant ratio required for completely ordered SEP materials.

The microstructure of CTA- $W_{12}$  is revealed in the SEM image of Figure 3.4.2(a), where it is seen that CTA- $W_{12}$  forms irregularly shaped particles on the order of 100-500 nm.

### 3.4.2 Hyper-digitation of CTA- $W_{12}$

The 1:7 POM:surfactant ratio of CTA- $W_{12}$  is greater than the 1:4 required for ordered lamellar SEP structures, and therefore it is likely that the bi-layers of the sample are distorted. As detailed within Section 3.1.5, POM:surfactant ratios beyond 1:4 break the symmetry of the 2D pseudo-hexagonal arrangement of the POMs and surfactant head-groups across the (01) plane (Figure 3.1.4). Evidence of this increased asymmetry can be found within the P-XRD pattern of Figure 3.2.3. Here, the as-measured (110) reflection, indicative of the separation between the hexagonally organized POMs, appears much more asymmetric than the calculated pattern, to the degree that it contains a shoulder on the larger  $2\theta$  side. The calculated pattern is based on a ‘perfect’ hexagonal arrangement, and therefore does not contain this feature. The asymmetry of the as-measured (110) reflection is due the differing degrees of separation between the anions, arising from CTA<sup>+</sup> head-groups protruding into the hydrophilic space to different extents. This tendency towards disorder by lamellar SEP materials with POM:surfactant ratios is highlighted in by Nyman *et al* in Figure 3.4.3.

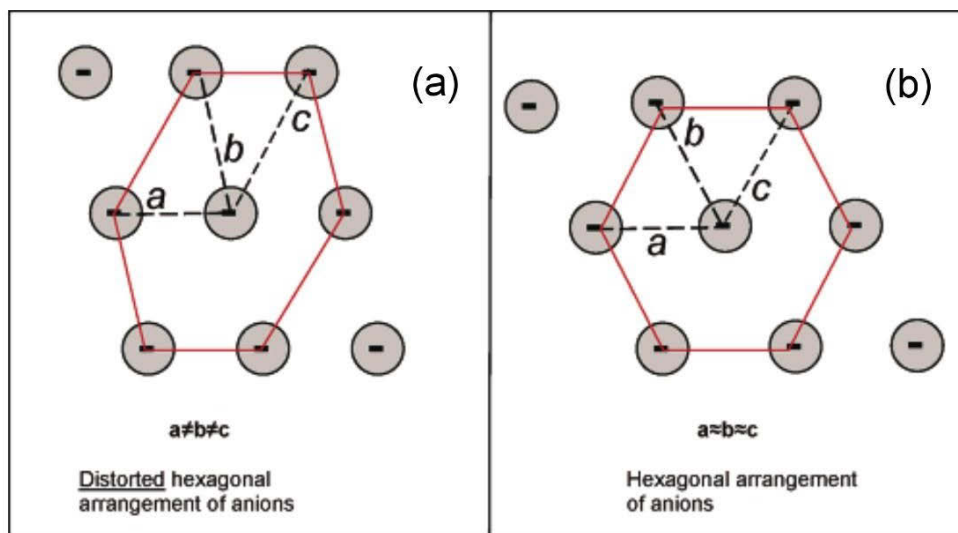


**Figure 3.4.3.** Distortion within the 2D pseudo-hexagonal arrangement of anionic POMs across the (001) plane (bi-layer interface) due to the POM:surfactant ratio exceeding 1:4 (a), as compared to the more symmetrical arrangement within a 1:4 SEP (b).<sup>134</sup>

The degree of bi-layer and interface distortion in CTA- $W_{12}$ , however, would be much less than the samples presented within Figures 3.2.14 and 3.2.17. These samples contain mutually present differing polyanions associated with greatly varied amounts of surfactants. These pack together to form highly-disordered SEP arrays, as is evident from the largely amorphous P-XRD patterns.

### 3.5 Conclusions: surfactant-mediated aqueous synthesis of Keggin polytungstates

The SEP material CTA- $W_{12}$  was synthesized and characterized. It was synthesized from  $WCl_6$ ,  $CTA^+$  and  $NH_4OH$  in an aqueous solution where by  $WCl_6$  was dissolved in  $CTA^+$  micelles which hydrolysed to produce  $WO_3 \cdot 2H_2O$  before  $NH_4OH$  was added to adjust the suspension from pH 0.5 to pH 7.5 which instigated the polymerization of  $[H_2W_{12}O_{40}]^{6-}$ . Only this method produced CTA- $W_{12}$ ,  $WCl_6$  hydrolysed without the presence of  $CTA^+$ , or surfactant-tungstate suspensions that were acidified from solutions with pH > 7.5 resulted in the production of multiple species of polytungstates. It was concluded that this was due the slow kinetics of equilibrating tungstate solutions.  $CTA^+$  micelles insulated  $WO_3 \cdot 2H_2O$  from external pH change as  $CTA^+/WO_3 \cdot 2H_2O$  suspensions that were alkalized up to pH 7

displayed little change from suspensions collected at pH 0.5. With the above method,  $\text{CTA}^+$  was used to direct the production of Keggin isopolytungstates from a tungstate suspension.

The empirical formula of  $\text{CTA-W}_{12}$  was deduced to be  $(\text{CTA})_7[\text{H}_2\text{W}_{12}\text{O}_{40}]\text{Cl}\cdot 2\text{H}_2\text{O}$  from C, H & N microanalysis and TGA data.  $[\text{H}_2\text{W}_{12}\text{O}_{40}]$  was determined as the isopolytungstate synthesized by Raman and FT-IR spectroscopies. The material has a lamellar bi-layer structure, as evidenced by P-XRD and TEM, which is slightly disordered due to the POM:surfactant ratio exceeding 1:4 resulting in hyper-digitization.

The work presented in this Chapter contributes to the growing knowledge of POM synthesis. This work highlights the slow equilibrium kinetics of aqueous isopolyanion solutions, and that the use of additional cations is necessary if desired compounds are to be made within reasonable time limits and yields.

## **Chapter 4. Thermal Stability and Decomposition of Surfactant-Polyoxometalate Frameworks**

This chapter presents an investigation into the thermal stability of the surfactant-POM CTA-W<sub>12</sub>. This includes the temperature dependent structural and chemical changes of the compound across its thermal decomposition. The thermal decomposition of CTA-W<sub>12</sub> is then compared to an analogue containing alternating layers of WO<sub>3</sub>·2H<sub>2</sub>O and CTA<sup>+</sup>. A decomposition intermediate of CTA-W<sub>12</sub> is further studied due to its potential as a porous WO<sub>x</sub> material. For justification for this work, see Section 1.4.

### **4.1 Background Theory**

#### **4.1.1 Calcination of surfactant-metal-oxide precursors**

Using surfactants as a templating agent to design porous catalytic substrates was first carried out using silica and alkyl-ammonium amphiphiles in order to produce the Mobil Composition of Matter (MCM) series of mesoporous materials.<sup>72, 79, 176</sup> This work was initially carried out by the Mobil company in order to produce high surface-area catalytic beds for use in cracking of crude oil to produce desired lighter hydrocarbons. By incorporating cationic-surfactants into silica frameworks via wet-chemistry methods, silica-hybrids with large pore-sizes could be produced.<sup>72, 79, 133, 176</sup> Calcination of the silica-hybrid precursors removed the labile organic surfactant, leaving the structure of the porous inorganic silica network largely unchanged, Figure 4.1.1. The intensive research in this field by Mobil and others greatly benefited the petroleum refinement industry as well as the knowledge of mesoporous material design and production.

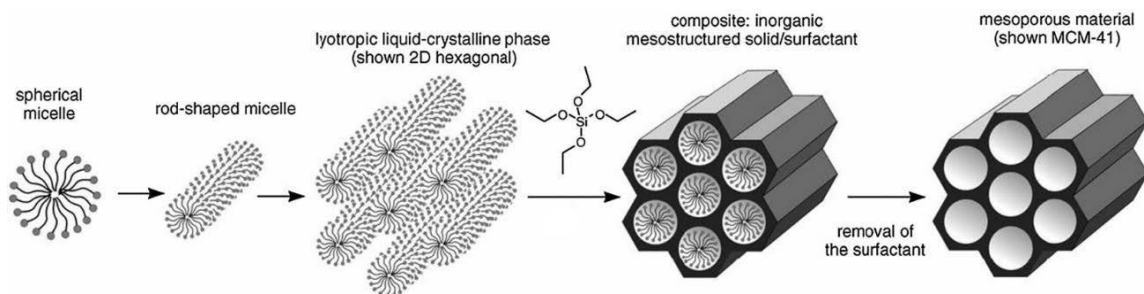


**Figure 4.1.1.** Production of MCM-41 catalytic substrate.<sup>176</sup>

Synthesis of the hybrid precursors is governed by self-assembly mechanisms such as charge-compensation and phase-separation of the hydrophobic cationic-surfactants and hydrophilic anionic silicates. By controlling the rate of condensation of the silicates, the anionic charge of the inorganic species can be controlled, thereby mutually controlling the amount of cationic surfactants that are introduced into the material.<sup>72, 79, 133</sup> The relative volume fraction of the surfactants in the material dictates the surfactant-packing-parameter,  $g$ , at the pore-interface which directly governs the mesophase that results, as described in Section 3.1.4. With this method an array of porous silicates can be produced including those with hexagonal channels (MCM-41), cubically arranged spherical pores (MCM-48) or stacked lamellar sheets (MCM-50), Figure 4.1.2.

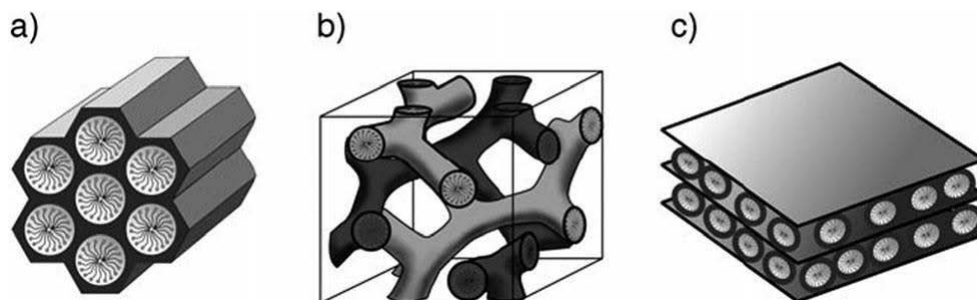
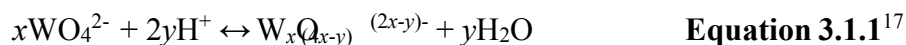


**Figure 4.1.2.** Mesostructural representations of (a) hexagonally arranged silicates (MCM-41), (b) cubically arranged silicates (MCM-48) and (c) meso-lamellar arranged silicates (MCM-50).<sup>176</sup>

Depending on solution pH and reactant concentration, Group 5 and 6 transition metals condense in aqueous solutions to form clusters of differing anionic charge (as described in Section 3.1.1) in a mechanism similar to that of silicate condensation. It was therefore

envisaged that similar porous networks of transition metal-oxides could also be produced in a similar process.<sup>133</sup> The condensation reactions for silicates and the analogous tungstate reaction are described in Equations 3.1.1 and 4.1.1.



Tungsten oxides in particular are employed in large number of catalytic reactions, making the production of highly-porous high-surface area catalytic beds very desirable. However, all attempts to produce such crystalline mesoporous materials from the calcination of surfactant-incorporated precursors have resulted in the collapse of the initial structure and the formation of non-porous bulk oxides.<sup>72, 79, 80, 84</sup> A number of explanations have been offered: U. Ciesla *et al* and A. Stein *et al* both cite likely incomplete condensation of the inorganic monomeric species which would result in unstable pore walls after surfactant-template removal,<sup>79, 80, 84</sup> while G. Soler-Illia *et al* and U. Ciesla *et al* additionally state changing oxidation states of the reactive multi-valence metal centres during calcination causes changes in bond order and resulting oxygen-coordination which leads to instability and collapse of the porous structure.<sup>72, 79, 80</sup> The multiple phase transformations of group 5 and 6 metal oxides over the calcination temperature range, which would strain the thin walls of precursor considerably, has also been cited as a contributing factor.<sup>72</sup> Additionally, attempts to remove templating organic species via solvent or electrochemical methods have also resulted in collapse of the porous structure into non-porous bulk oxides.<sup>80</sup>

However, porous networks of tungsten and other transition-metal oxides via calcination of organic-inorganic precursors is successful if weakly-bonding organic-templating agents and non-aqueous inorganic species are used, such as block copolymers and metal-chlorides in organic solvents, such as those produced by P. Yang *et al*.<sup>178</sup> This fabrication method limits the interaction between the organic-templating agent and the porous inorganic-phase in an effort to minimize redox reactions between the two phases during calcination. Redox reactions between the organic and inorganic phases are likely responsible for the changing oxidation states of metal-centres during calcination, which cause changes in octahedral bond order and contribute to the collapse of porosity.<sup>72, 178</sup> Calcination

of the above weakly-associating organic-inorganic hybrids only leads to the formation of amorphous phases however, and the adoption of crystallinity is seen to coincide with the loss of porosity.<sup>178, 179</sup>

By studying the thermal transformations and decomposition of an alkyl-ammonium isopolytungstate hybrid, the work presented in this chapter aims to further clarify the reasons as to why the production of highly porous crystalline tungsten oxides seems to be a current impossibility.

#### **4.1.2 Thermal stability of organic spacers including alkyl-ammonium surfactants**

The thermal stability of the organic templating molecule is of obvious importance when designing mesoporous oxides, as it must evacuate the sample below the thermal stability of the porous oxide in order for the desired mesoporous structure to result. Considering this, the ideal case for mesoporous oxide design would include an organic templating agent that boiled off or completely oxidized to produce gaseous  $\text{CO}_x$ ,  $\text{NO}_x$  and  $\text{H}_2\text{O}$  at the calcination temperature. However, due to the difference in bond energies between the atoms that make up typical organic precursors, these molecules tend to decompose into various volatile and non-volatile components with elevating temperature rather than boiling off or combusting within a small temperature range. Reactions promoted by the anionic inorganic precursor can also contribute to the variety of decomposition products produced. Decomposition products may be volatile and evacuate the sample as desired or remain in the sample due to thermal stability or association with inorganic sites. For example, cationic organic decomposition products of surfactants, such as methyl-ammoniums, are likely to remain within the sample if  $\text{OH}^-$ , metal-hydroxide or other basic species/sites are mutually present.<sup>180-183</sup> In line with this work, the thermal decomposition of the alkyl-ammonium surfactant  $\text{CTA}^+$  will be studied in detail. Below is a table listing bond energies within alkyl-ammonium surfactants.

**Table 4.1.1.** Bond energies within alkyl-ammonium molecules:<sup>180, 184</sup>

<b>Bond</b>	<b>Energy (kJ/mol)</b>
C-H	402 – 414
N-H	389
C-C	347 – 356
C-N	289 – 314

As can be seen in Table 4.1.1, C-N and C-C bonds are considerably weaker than N-H and C-H bonds. This difference governs alkyl-ammonium thermal decomposition via the two dominant decomposition mechanisms of *Hoffman degradation* (also known as Hoffman elimination) and hydrocarbon ‘cracking’.<sup>180-183</sup> Hoffman degradation is the lower temperature/energy decomposition mechanism which involves cleavage of the C-N bond between the cationic-nitrogen and the alkyl-chain. Depending on the atmospheric environment and morphology of the precursor, Hoffman degradation can occur from ~180°C during calcination and is usually observed up to ~250°C after which other decomposition mechanisms become more prominent.<sup>180-182</sup> The mechanism occurs with the mutual presence of basic sites, such as OH<sup>-</sup> and M<sub>x</sub>[OH]<sub>x</sub> species typically found within inorganic precursors. The mechanism occurs via transfer of a proton from the β-carbon site, Figure 4.2.1, to the basic site resulting in the formation of trimethyl-ammonia and a long chain alkene, 1-hexadecene in the case of CTA<sup>+</sup> degeneration.<sup>180</sup> Cleavage around other C-N bonds is also seen to a lesser extent, such as the between N<sup>+</sup> and the CH<sub>3</sub> species which make up the head-group.<sup>180, 182, 183</sup> Cleavage of head-group methyl species results in the formation of bulky N,N-dimethylhexadecylamine ((C<sub>16</sub>H<sub>33</sub>)N(CH<sub>3</sub>)<sub>2</sub>) and volatile CH<sub>3</sub>OH (due to reaction with OH<sup>-</sup>) minor products.

The temperature at which Hoffman degradation occurs at is too low to instigate combustion of the evacuating organic species in oxidizing atmospheres, rendering the mechanism endothermic as the degraded products evaporate from the sample. The Hoffman degradation mechanism of the long-chain quaternary alkyl-ammonium surfactant CTA<sup>+</sup> is displayed in Figure 4.1.3.

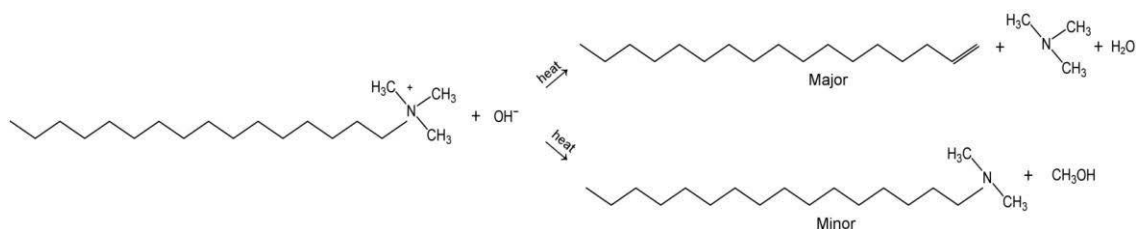


**Figure 4.1.3.** Hoffman degradation mechanism of CTA<sup>+</sup>.

Trimethylamine produced via Hoffman degradation can remain in the calcining sample up to ~400°C, due to the molecule's strong adsorption to numerous Lewis or Brønsted acid sites (OH<sup>-</sup> and -M-OH, where M = metallic cation) within the calcining precursor.<sup>182, 183, 185, 186</sup>

The other main decomposition mechanism of alkyl-ammonium surfactants is cracking of the long alkyl-chains into smaller, more volatile components via cleavage of C-C bonds. This is the same process that is employed in petro-chemistry to refine crude oil into more useful molecules such as octane and propane. Depending on the atmospheric environment and morphology of the precursor, cracking is usually observed from ~250°C onwards during calcination. The chemical make-up of the calcining inorganic precursor is known to affect the products of cracking reactions. For example, aluminium doped in silica is known to promote isomerism of the cracking products, leading to branched alkanes and alkenes.<sup>182</sup> Cracking reactions proceed until complete volatilization of the organic under inert (e.g. N<sub>2</sub>, He and Ar) or reducing (e.g. H<sub>2</sub>) atmospheres. Under oxidizing atmospheres, organic precursors and their decomposition intermediates begin to combust by ~300°C leading to the production of gaseous CO<sub>x</sub>, NO<sub>x</sub> and H<sub>2</sub>O. Both cracking and combustion degradation mechanisms are exothermic, due to the breaking of C-C bonds and the formation of C/N/H-O bonds, respectively. However, due to the magnitude of evaporation in some precursors, these events can be observed as slightly endothermic in inert or reducing atmospheres. Combustion of CTA<sup>+</sup> and its degradation products is regularly observed to be incomplete, which results in 'soft-coke' residues within the pores of the calcining precursor.<sup>180, 181</sup> The degree of incompleteness seems to be larger in transition-metal-oxides as compared to silicates.<sup>181</sup> Soft-coke is described as a carbonaceous residue largely consisting of amorphous carbon with some C-H groups present.<sup>181</sup> By ~400°C soft-coke begins to combust with the oxidizing atmosphere to produce gaseous oxides, which can be catalysed by the newly

formed oxide resulting in large exotherms. Kleitz *et al* summarize the thermal degradation process of CTA<sup>+</sup> in their study of alumina silicates, Figure 4.1.4.<sup>181</sup>

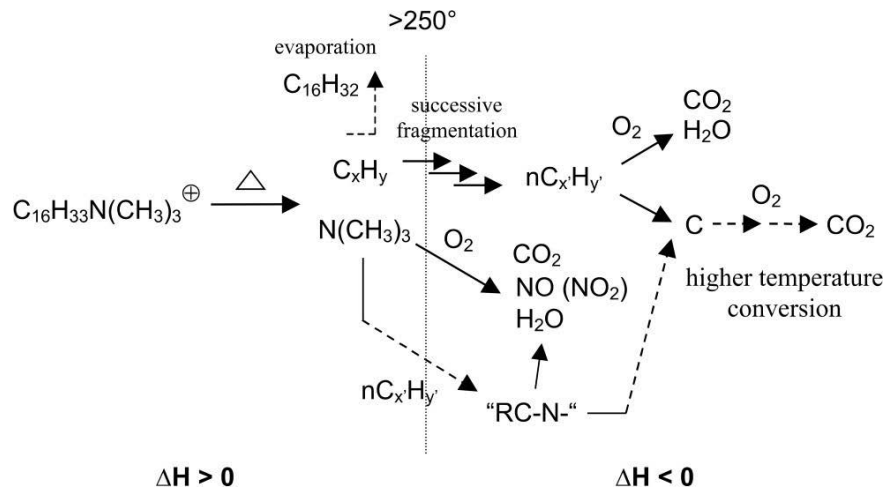


**Figure 4.1.4.** Thermodynamics of CTA<sup>+</sup> decomposition, as described by Kleitz, F., Schmidt, W., Schüth, F., Evolution of mesoporous materials during the calcination process: structural and chemical behaviour. *Microporous and Mesoporous Materials* **2001**, 44-45, 95-109.<sup>181</sup>

The final temperature of complete organic-precursor removal is highly dependent on the inorganic material being calcined; for un-doped silica and transition-metal oxides complete removal is observed at ~550°C in air,<sup>182</sup> however montomillites containing various metallic cations have been recorded losing mass up to ~900°C.<sup>180</sup>

### 4.1.3 Keggin fragmentation

POMs are not stable at high temperatures. Heat-treatment of polyoxometalate-containing materials and the associated loss of hydration is known to fragment the large oxoanions into smaller, more condensed units until final reorganization to bulk trioxides at even higher temperatures, Figure 4.1.5. POM properties such as the degree of initial hydration, presence and type of counter-cations, addenda metal-octahedra substitution as well as the treatment method used, including the heating rate and atmosphere, are all known to affect the rate of thermal decomposition and fragmentation.

In the case of Keggin anion decomposition, the process begins with the ejection of an octahedral unit resulting in the formation of the defective lacunary structure which is preceded by complete sample dehydration.<sup>71, 74, 75, 187</sup> In Keggin anions that contain an addenda-substituted metal centre, such as  $\text{VO}^{2+}$  in  $\text{H}_4[\text{PVMo}_{11}\text{O}_{40}]$ ,<sup>71</sup> this is the octahedral unit that is expelled. Reduction of the metal-centers accompanies this initial decomposition step, due to the movement of  $\text{O}^{2-}$  and  $e^-$ .<sup>74, 187</sup> Continued heating causes the defective anion to fragment, supposedly by the cleavage of corner-sharing bonds which results in the formation of free edge-sharing  $\text{M}_3\text{O}_{13}$  trimers (where  $\text{M} = \text{Mo}, \text{W}, \text{V}$  or  $\text{Nb}$ ). If the Keggin anion is not substituted, this fragmentation occurs at a lower temperature.<sup>71</sup> These trimers then condense into more stable, larger edge-sharing polyanions, such as hepta- and octo-polyanions. At higher temperatures, the condensed polyanion intermediates further reorganize to form the corner-sharing octahedral networks of bulk trioxides.<sup>71, 75, 187</sup> The initially formed trioxide lattices are defective and contain many oxygen-vacancies and edge-sharing defects and require continual treatment under oxidizing atmospheres to produce crystalline stoichiometric transition-metal trioxides.<sup>71</sup>

## Model: Structural Reorganization

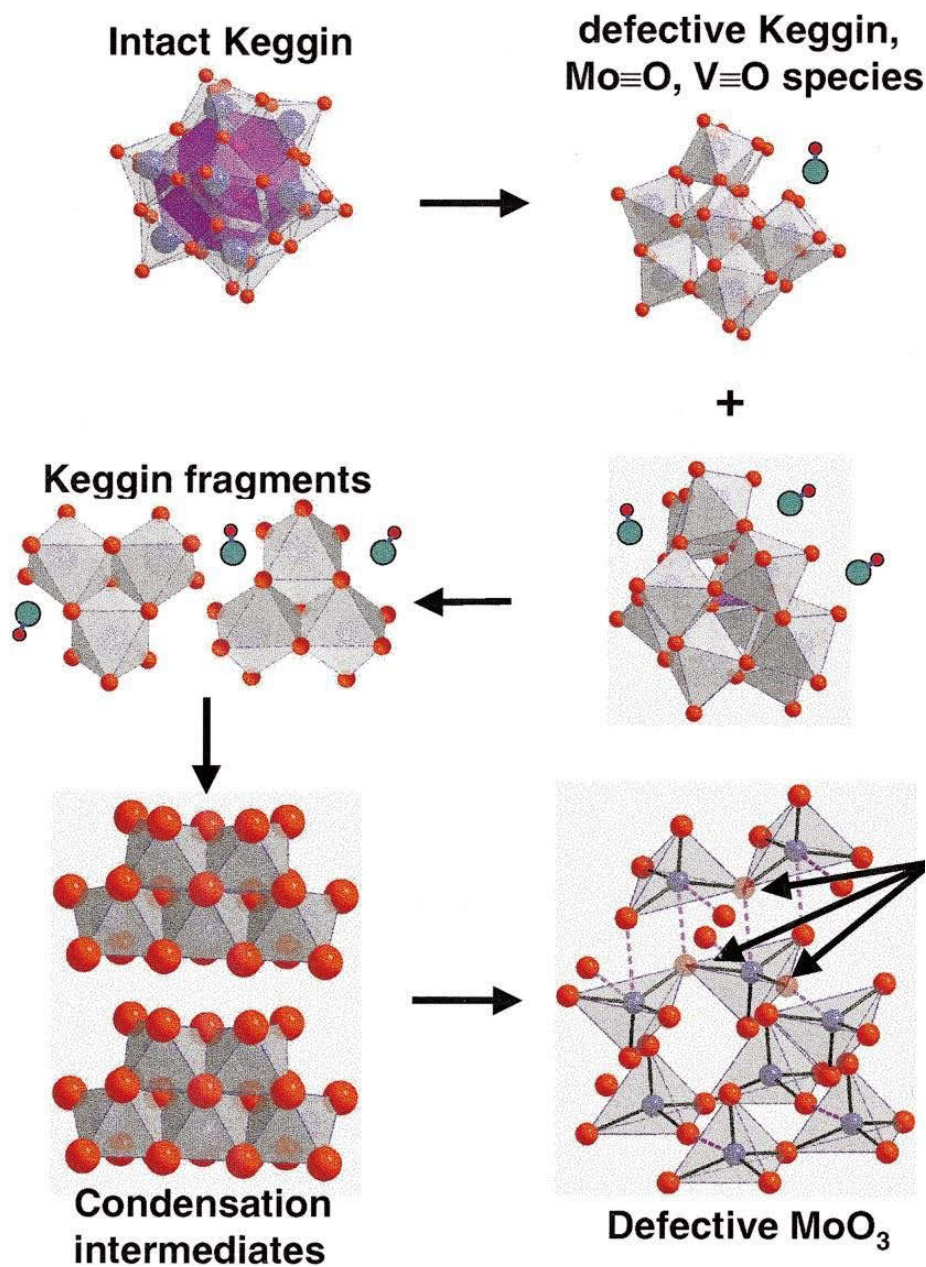


**Figure 4.1.5.** Model of Keggin anion fragmentation and condensation as proposed by G. Mestl *et al.*<sup>71</sup> Mestl, G. Ilkenhans, T. Spielbauer, D. Dieterle, M. Timpe, O. Kröhnerta, J. Jentoft, F. Knözinger, H. Schlögl, R., Thermally and Chemically Induced Structural Transformations of Keggin-type Heteropoly Acid Catalysts. *Appl. Catal. A* **2001**, 210, 13–

34.

It was observed by G. Mestl *et al*<sup>71</sup> and J. Wienold *et al*<sup>187</sup> in their respective studies of the thermal transformations of  $\text{Cs}_{4-x}\text{H}_x[\text{PVMo}_{11}\text{O}_{40}]\cdot y\text{H}_2\text{O}$  that the presence of water strongly affects the kinetics of the fragmentation and condensation process. Slower heating rates that allowed for complete sample dehydration before the onset of instability ( $\leq 0.2$  K/min) were observed to delay both the onset of fragmentation and the emergence of the bulk trioxide from the oxoanion fragments.<sup>71</sup> The inclusion of  $\text{Cs}^+$  cations in the initial sample, which are known to displace  $\text{H}_2\text{O}$  upon sample precipitation, had the same Keggin-anion stabilizing effect.<sup>187</sup>

The destabilizing role of  $\text{H}_2\text{O}$  in POM decomposition may stem from the mobility it affords to the protons on the surface of Keggin and other (condensed) polyanions. M. Janik *et al* found in their computational study of the decomposition of Keggin anions that the movement of two acidic protons onto a bridging-oxygen site necessarily preceded the formation of the lacunary structure.<sup>75</sup> The mutual presence of water greatly reduced the activation-energy of this step by  $\sim 50\%$  (40.0 kJ/mol in the anhydrous case compared to 19.6 kJ/mol) via the formation of mobile  $\text{H}_3\text{O}^+$ . Therefore, the presence of water at high-temperatures would increase the rate of POM decomposition.

The presence of  $\text{O}_2$  is observed to stabilize the intact Keggin anion and polyanions fragments, delaying the formation of the bulk trioxide relative to treatment in inert atmospheres (He).<sup>71, 187</sup> G. Mestl *et al* observed that heating  $\text{H}_4[\text{PVMo}_{11}\text{O}_{40}]$  under  $\text{O}_2$  results in a mixture of isopolyanion fragments by 700K, whereas treatment under propene ( $\text{C}_3\text{H}_6$ ) in a stream of He (mimicking catalytic conditions) resulted in complete transformation to defective  $\text{MoO}_3$  by the same temperature. Similar results were observed by J. Wienold *et al*.<sup>187</sup> It is suggested that  $\text{O}_2$  is able to re-oxidize the uncoordinated metal-centres that form during the initial fragmentation of the Keggin anion and when the fragments condense into  $\text{MoO}_3$ , thus prohibiting bulk-oxide formation from the reorganizing octahedra. Additionally,  $\text{O}_2$  is likely able to oxidize reduced Keggin anions and fragments that form during decomposition, prohibiting the progress of decomposition towards the bulk trioxide.<sup>187</sup>

Understanding the mechanisms of polyoxometalate thermal decomposition and fragmentation is essential if porous inorganic oxide networks are to be produced from calcined SE-POM precursors. In this work, by studying the calcination of the SE-POM precursor CTA- $\text{W}_{12}$  the fragmentation and otherwise decomposition of the metatungstate

Keggin anions will be investigated in detail. It is hoped that this endeavour will help answer questions as to why the production of neutral mesoporous tungsten oxide materials from surfactant-templated precursors seems to be a current impossibility.

#### 4.1.4 Crystallographic phases of $\text{WO}_x$

Stoichiometric  $\text{WO}_3$  is formed by corner-sharing octahedra,  $\text{WO}_6$ , which consists of a  $\text{W}^{6+}$  cation at the centre connected to six  $\text{O}^{2-}$  ligands. The octahedra are connected via sharing of the  $\text{O}^{2-}$  ligands which results in a network of corner-corner sharing octahedra. The relative orientations of the  $\text{WO}_6$  octahedra are dependent on temperature, and as such,  $\text{WO}_3$  undergoes a number of crystallographic phase transitions when cooling and heating, Figure 4.1.6.<sup>163, 188, 189</sup>

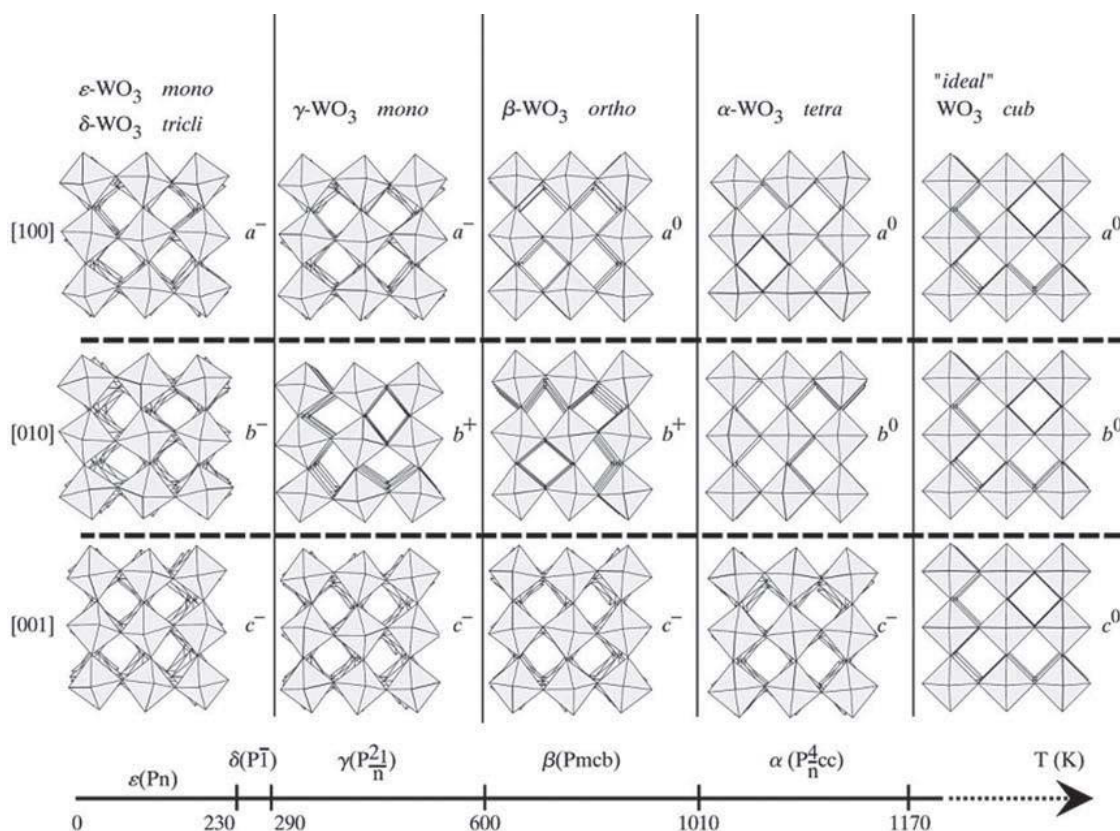


**Figure 4.1.6.** Temperature dependent phases of  $\text{WO}_3$ .<sup>190</sup> Roussel, P.; Labbe, P.; Groult, D., Symmetry and twins in the monophosphate tungsten bronze series  $(\text{PO}_2)_4(\text{WO}_3)_{2m}$  ( $2 < m < 14$ ). *Acta Crystallogr. B* **1999**, B56, 377-391.

A number of other crystallographic phases are also possible by deviating from the  $\text{WO}_3$  stoichiometry. As will be discussed in detail in the following chapter, removal of  $\text{O}^{2-}$  ligands results in edge-sharing between the neighbouring octahedra. At low levels of oxygen loss these edge-sharing octahedra are dispersed within the tungsten oxide network and can be classified as defects. At higher concentrations, where  $x < 2.87$  in  $\text{WO}_x$ , the edge-sharing octahedra begin to accumulate and organise into regular arrays which results in a variety of other crystallographic phases dependent upon  $x$ .<sup>126, 188, 189, 191</sup>

The Lewis-base characteristics of  $-\text{W}-\text{O}$  bonds within  $\text{WO}_6$  octahedra makes the acceptance of acidic protons favourable. Due to this,  $\text{WO}_3$  is able to form a number of hydrates via acceptance of protons and the formation of  $-\text{W}-\text{OH}_2$  sites and corresponding  $\text{WO}_5(\text{OH}_2)$  octahedra.<sup>126, 188</sup> The inclusion of  $-\text{W}-\text{OH}_2$  groups prohibits the formation of a continuous network of  $\text{WO}_6$  octahedra and instead distorted layers of  $\text{WO}_5(\text{OH}_2)$  octahedra form. The case of continuous  $\text{WO}_5(\text{OH}_2)$  layers represents the monohydrate of tungsten oxide,  $\text{WO}_3 \cdot \text{H}_2\text{O}$ , commonly referred to as tungstite, which forms a highly distorted orthorhombic phase due to the hydrogen bonding between neighbouring  $-\text{W}-\text{OH}_2$  sites.<sup>163, 192</sup>  $\text{WO}_5(\text{OH}_2)$  units in  $\text{WO}_3 \cdot \text{H}_2\text{O}$  form alternating rows of octahedra where one  $\text{WO}_5(\text{OH}_2)$  octahedral unit with the  $-\text{W}-\text{OH}_2$  group facing 'up' is connected to a  $\text{WO}_5(\text{OH}_2)$  octahedral unit with the  $-\text{W}-\text{OH}_2$  group facing 'down', Figure 4.1.7.

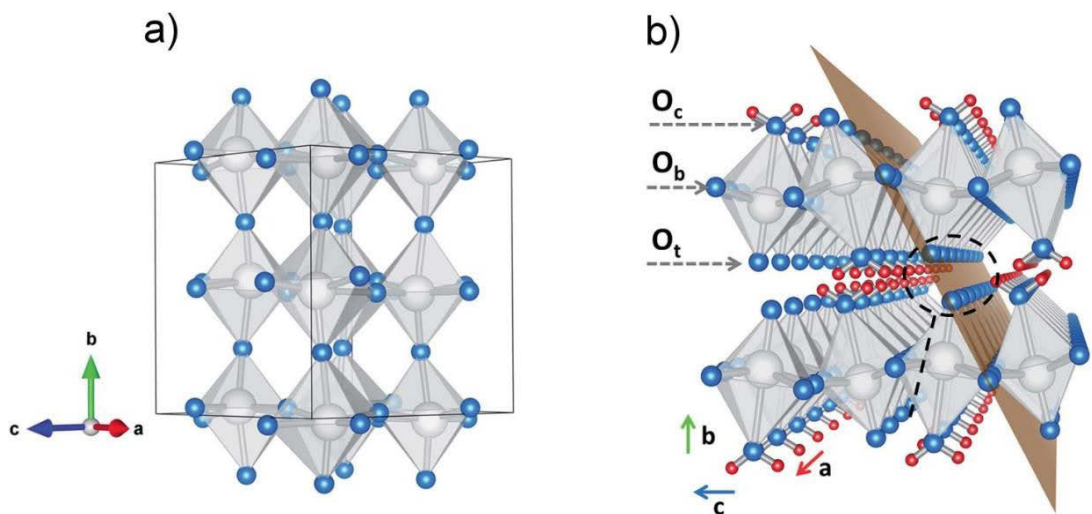


**Figure 4.1.7.** (a)  $\text{WO}_6$  octahedral network of monoclinic  $\gamma\text{-WO}_3$ , and (b) distorted  $\text{WO}_5(\text{OH}_2)$  alternating octahedral network. Large grey spheres = W, smaller blue spheres = O and smallest red spheres = H.  $\text{O}_c$  = Oxygen coordinated with H,  $\text{O}_b$  = corner-sharing oxygen and  $\text{O}_t$  = terminal oxygen.<sup>192</sup>

Tungsten trioxide is able to further accommodate water via intercalation of  $\text{H}_2\text{O}$  between the sheets of alternating  $\text{WO}_5(\text{OH}_2)$ . These intercalated  $\text{H}_2\text{O}$  molecules are hydrogen-bonded to the  $-\text{W}-\text{OH}_2$  sites, Figure 4.1.8(a), and form a continuous monolayer between the sheets of octahedra, Figure 4.1.8(b), with one intercalated  $\text{H}_2\text{O}$  associated with every  $\text{WO}_5(\text{OH}_2)$  octahedra. Thus, this structure represents the dihydrate,  $\text{WO}_3 \cdot 2\text{H}_2\text{O}$ , of tungsten trioxide and can be crystallographically characterised as sheets of monoclinic  $\text{WO}_3$  (similar to  $\gamma\text{-WO}_3$ , Figure 4.1.6) separated by  $\text{H}_2\text{O}$  monolayers.

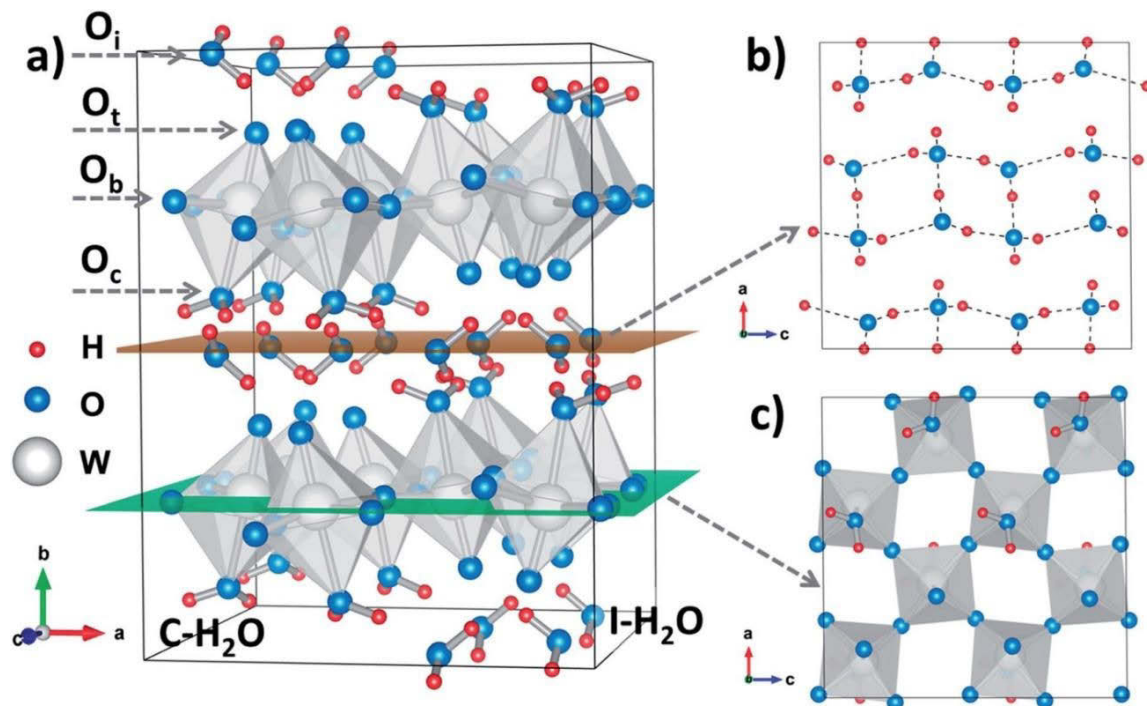


**Figure 4.1.8.** (a) Structural representation of  $\text{WO}_3 \cdot 2\text{H}_2\text{O}$ , depicting sheets of alternating  $\text{WO}_5(\text{OH}_2)$  octahedra and intercalated  $\text{H}_2\text{O}$  (I- $\text{H}_2\text{O}$ ). (b) Hydrogen-bonded network of intercalated  $\text{H}_2\text{O}$  monolayer. (c) Sheet of  $\text{WO}_5(\text{OH}_2)$  octahedra highlighting the alternating positions of the coordinated water (C- $\text{H}_2\text{O}$ ). Colour representations are same as Fig.

3.1.7.<sup>192</sup>

Including the monohydrate and dehydrate, two other tungsten trioxide hydrates are known to be stable:  $\text{WO}_3 \cdot 0.5\text{H}_2\text{O}$  (hemihydrate) and  $\text{WO}_3 \cdot 0.33\text{H}_2\text{O}$  (or  $\text{WO}_3 \cdot 1/3\text{H}_2\text{O}$ ).<sup>126, 163, 188, 193</sup>  $\text{WO}_3 \cdot 0.5\text{H}_2\text{O}$  has a cubic pyrochlore structure where six-member  $\text{WO}_6$  corner-sharing octahedra form tunnels in which the  $\text{H}_2\text{O}$  resides.  $\text{WO}_3 \cdot 0.33\text{H}_2\text{O}$  is observed to form orthorhombic crystals and consists of both  $\text{WO}_5(\text{OH}_2)$  and  $\text{WO}_6$  octahedra in a stoichiometric ratio that results in  $\text{WO}_3 \cdot 0.33\text{H}_2\text{O}$ .<sup>126, 188</sup>

Tungsten oxide hydrates are widely used as precursors to more novel tungsten-oxide-based nanostructures, especially via the use of hydrothermal reactions.<sup>188, 194</sup> The acidity of the protons in  $\text{WO}_5(\text{OH}_2)$  octahedra allow them to be exchanged with a wide variety of cationic species, such as alkyl-ammonium surfactants as described in Section 3.1.2, allowing for greater functionalization. The lability of acidic interlayer W-OH sites affords the layered networks a considerable degree of proton and cation conductivity, and has led to the research

of  $\text{WO}_3 \cdot x\text{H}_2\text{O}$  in battery applications.<sup>131, 192, 194</sup> Furthermore, the lability of -W-OH sites, along with tungsten's multi-valent properties, has seen the chemical sensing ability of  $\text{WO}_3 \cdot x\text{H}_2\text{O}$  widely researched, especially towards  $\text{NO}_x$  detection.<sup>166, 195</sup> The layered formation of  $\text{WO}_3 \cdot x\text{H}_2\text{O}$  allows for further fabrication to expose preferred crystal faces, such as the high-energy (002) plane widely used in (photo-)catalysis, or the (111) plane which exposes the acidic W-OH sites.<sup>189</sup>

In this work, an alkyl-ammonium intercalated  $\text{WO}_3 \cdot x\text{H}_2\text{O}$  layered material was synthesized (as described in Section 3.2.2) and its thermal stability studied. The thermal profile of this material was then compared against a POM-containing analogue in order to understand the thermal decomposition of organic-templated tungsten-oxide precursors more completely.

#### **4.1.5 Hexagonal tungsten oxides**

More porous crystallographic structures of  $\text{WO}_3$ , as compared to those covered in the previous section, are attainable with the use of additional preparation methods, such as solvo-thermal reactions and calcination of precursors. One such phase is the hexagonal phase, h- $\text{WO}_3$ , which has seen greatly increased attention in the recent decades due to the focus on porous oxide materials for applications such as (photo-)catalysis, gas-sensing and electro- and/or photo-chromism where high surface-areas are paramount.<sup>77, 196</sup> The structure of h- $\text{WO}_3$  is comprised of six-membered rings of corner-sharing  $\text{WO}_6$  octahedra which stack together to form large hexagonal tunnels within the rings and smaller triangular ones between the rings, Figure 4.1.9:

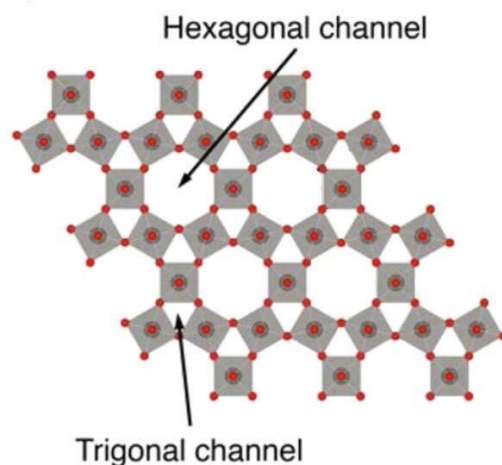


**Figure 4.1.9.** Crystallographic structure of the h-WO<sub>3</sub> phase, large grey spheres = W, smaller red spheres = O.<sup>197</sup>

Solvo-thermal methods to produce h-WO<sub>3</sub> involve heating the previously mentioned tungsten oxide hydrates under pressure in anhydrous solvents for extended periods of time (days).<sup>123, 163, 198</sup> However, the hexagonal phases that result from such methods tend to be metastable and can collapse after extended aging (weeks) or heating beyond 400°C.<sup>123, 193, 198, 199</sup>

The addition of small cations, such as H<sup>+</sup>, alkali-metals (Li<sup>+</sup>, Na<sup>+</sup>, K<sup>+</sup> and Cs<sup>+</sup>) and NH<sub>4</sub><sup>+</sup>, can stabilize the porous hexagonal network indefinitely. The doped hexagonal networks can be synthesized by hydrothermal methods using an aqueous tungsten precursor (e.g. Na<sub>2</sub>WO<sub>4</sub>) and desired guest cation,<sup>123</sup> by thermal decomposition of ammonium meta- or para-tungstate ((NH<sub>4</sub>)<sub>6</sub>[H<sub>2</sub>W<sub>12</sub>O<sub>40</sub>] or ((NH<sub>4</sub>)<sub>10</sub>[H<sub>2</sub>W<sub>12</sub>O<sub>42</sub>]),<sup>198, 200, 201</sup> or electrochemically via intercalation into an existing h-WO<sub>3</sub> structure.<sup>202, 203</sup> These stable M<sub>x</sub>WO<sub>3-x</sub> hexagonal oxides (where M = H<sup>+</sup>, NH<sub>4</sub><sup>+</sup>, Na<sup>+</sup>, Li<sup>+</sup>, etc) are collectively termed hexagonal tungsten bronzes (HTBs). HTBs exhibit interesting properties additional to WO<sub>3</sub>, such as strong visible-light absorption and metal-like conductivity, due to the partial population the W 5d band by the oxidation of the guest cation (M → M<sup>+</sup> + e<sup>-</sup>).<sup>197,202</sup>

However, occupation of the porous tunnels and catalytic -W-O- basic sites by the guest cations make their presence in the oxide undesirable for applications such as (photo-)catalysis and gas-sensing. Because of this, attempts have been made to completely evacuate h-WO<sub>3</sub> of guest cations, although all cases have resulted in the collapse of the porous structure into the condensed m-WO<sub>3</sub> phase, Fig. 3.1.6, which is the thermodynamically stable

phase of  $\text{WO}_3$  within the studied temperature range (17 – 400°C).<sup>198, 200, 204, 205</sup> C. Balázsi and J. Pfeifer found in their study of sodium HTBs that the porous hexagonal phase was only synthesized when a critical concentration of  $\text{Na}^+$  was present in the reaction, and that higher initial concentrations of  $\text{Na}^+$  increased the  $\text{h-WO}_3 \rightarrow \text{m-WO}_3$  transition temperature.<sup>204, 205</sup> Furthermore, V. Potin *et al* discovered that  $\text{WO}_3$  nano-rods deposited onto a cleaved mica substrate exposing a monolayer of potassium grew into hexagonal  $\text{K}_x\text{WO}_3$  bronze when annealed, and that when the K atoms were depleted only  $\text{m-WO}_3$  formed.<sup>199</sup> Similarly, I. Szilágyi *et al* found in their study of hexagonal ammonium tungsten bronzes (HATBs) that the collapse of the  $\text{h-WO}_3$  structure coincided with the complete removal of  $\text{NH}_4^+$  and  $\text{NH}_3$  from the lattice, Figure 4.1.10.<sup>198, 200</sup>

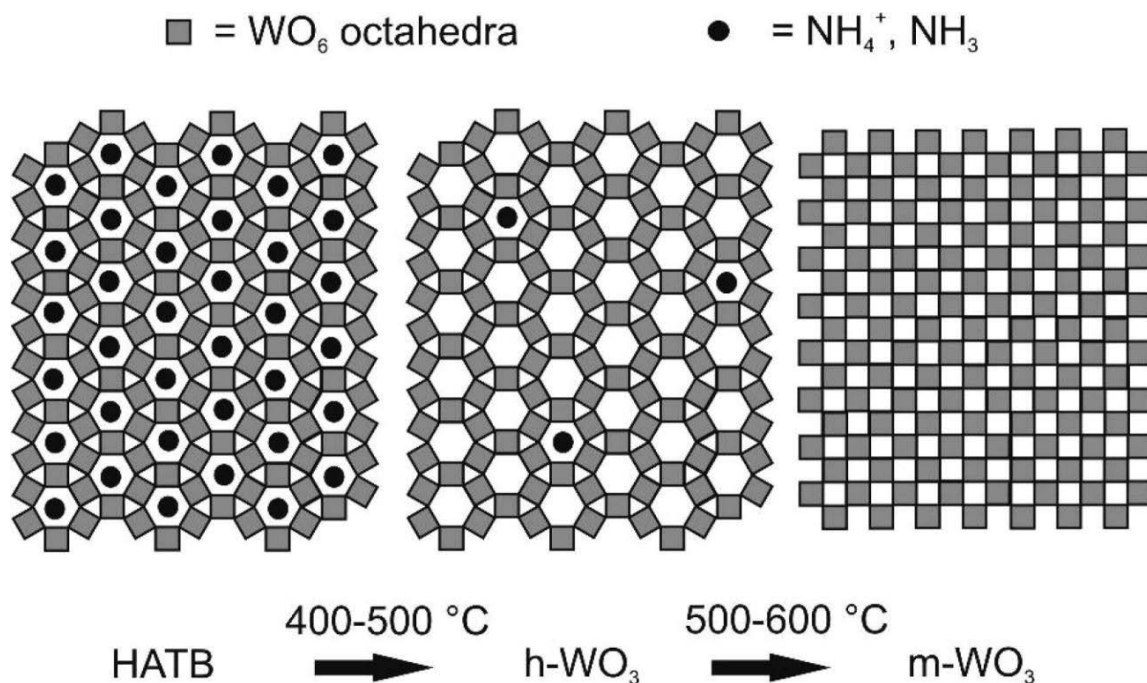


**Figure 4.1.10.**  $\text{h-WO}_3$  requires small concentrations of guest cations in order to remain stable. Removal of these cations results in the collapse of the porous hexagonal structure into the condensed  $\text{m-WO}_3$  phase.<sup>200</sup>

However, the concentration of guest cations required to keep  $\text{h-WO}_3$  stable was observed to be quite low; 0.15 wt% in the case of  $\text{NH}_4^+$  and  $\text{NH}_3$ , and 160 ppm of  $\text{Na}^+$  in the respective studies.<sup>200, 205</sup> I. Szilágyi *et al* propose that the presence of guest cations increases the activation energy of the  $\text{h-WO}_3 \rightarrow \text{m-WO}_3$  transition, such that it is unfavorable at room

temperature.<sup>200</sup> It was also argued that the presence of cations within the pores of h-WO<sub>3</sub> would inhibit WO<sub>6</sub> octahedra reorganization from the six-membered-ring structure into the corner-sharing checker-board structure of m-WO<sub>3</sub>, Figures 4.1.6 and 4.1.10.

The instability of h-WO<sub>3</sub> to complete cation removal is an example of the overall instability of neutral highly-porous tungsten-oxide materials. Studying cation removal in a similar system such as the removal of templating organic species from an SE-POM precursor by calcination will contribute to the understanding of why such methods do not result in the production of highly-porous tungsten-oxides.

#### **4.2 Thermal decomposition of CTA-Br**

Before the thermal decompositions of CTA-W<sub>12</sub> and CTA-WO<sub>3</sub> are discussed, it is instructive to describe the thermal decomposition of the volatile CTA<sup>+</sup> portion of these compounds, as represented by pure CTA-Br. As described in Section 3.1.3, CTA<sup>+</sup> is a long-chain surfactant comprised of a 16 carbon long saturated alkyl chain connected to a cationic quaternary-ammonium head group consisting of three methyl species, Figure 4.2.1:

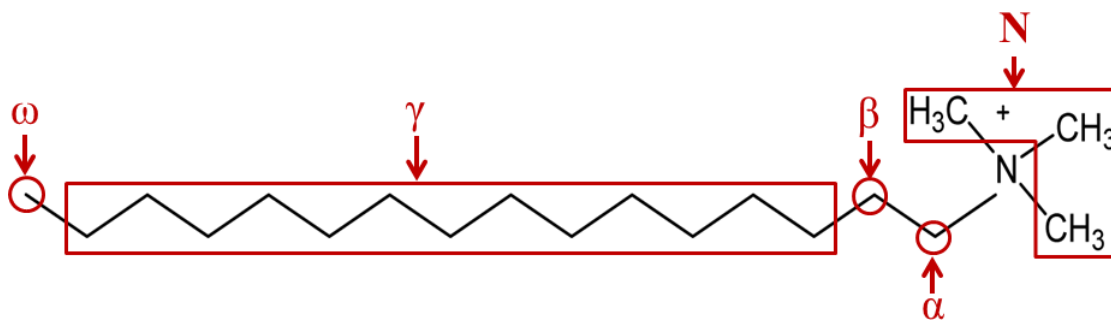


**Figure 4.2.1.** Molecular structure of the surfactant CTA-Br, indicating all non-equivalent chemical environments of the C and H atoms.

The TGA, DTG and DTA of CTA-Br is presented in Figure 4.2.2. CTA<sup>+</sup> decomposition in air proceeds over one large exothermic peak from 180 to 320°C and a smaller exothermic peak from ~350 to 500°C, although largely centred between 400 to 500°C. The larger exothermic peak contains three maxima at 231, 246 and 281°C.

As described in Section 4.1.2, alkyl-ammonium decomposition occurs due to two mechanisms; Hoffman degradation which occurs at lower temperatures ( $\sim 180 - 250^\circ\text{C}$ ) via cleavage of C-N bonds around the cationic head-group, and hydrocarbon cracking which occurs at higher temperatures ( $\sim 250 - 350^\circ\text{C}$ ) via cleavage of C-C bonds.<sup>181-183</sup> Considering this, the predominant products of CTA<sup>+</sup> decomposition due to Hoffman degradation would include; cracking between the  $\alpha$ -C (carbon closest to cationic nitrogen) and N<sup>+</sup> to form 1-hexadecene (C<sub>16</sub>H<sub>32</sub>, b.p. = 280°C) and trimethyl-ammonium (HN(CH<sub>3</sub>)<sup>+</sup>, b.p. = 3°C), or, cracking between N<sup>+</sup> and the N-C atoms (carbons which form the methyl-groups of the cationic head-group) to form N,N-dimethylhexadecylamine (C<sub>18</sub>H<sub>39</sub>N, b.p. = 150°C) and reactive CH<sub>3</sub><sup>•</sup> species which would quickly react with H<sup>+</sup> or H<sub>2</sub>O to form volatile methane (CH<sub>4</sub>) or methanol (CH<sub>3</sub>OH).<sup>181-183</sup> The products of hydrocarbon cracking would produce a wide variety of alkanes and alkenes, some of which would be sufficiently volatile to boil off when produced. Heavier alkanes and alkenes could be further cracked into lighter molecules or combust with O<sub>2</sub> (in an oxidizing environment) to produce gaseous CO<sub>x</sub>. However, it is known that the combustion of alkyl-ammonium decomposition products is usually an incomplete process which leads to the build-up of 'soft coke', a mostly carbonaceous soot-like residue with some attached hydrogen.<sup>181, 182, 206</sup> Carbonaceous soft-coke would eventually oxidize to gaseous CO<sub>x</sub> given sufficient time and temperature increase. Of course, diatomic bromine, Br<sub>2</sub> (b.p. = 59°C) would also be produced and evaporated over this temperature range.

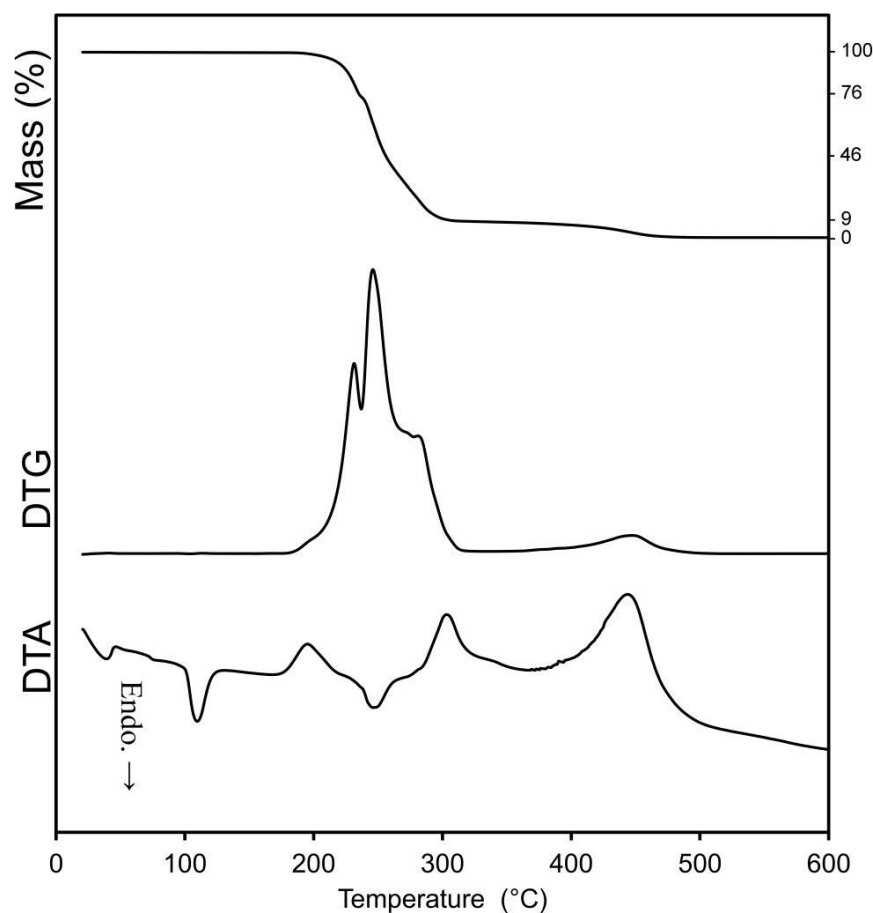


**Figure 4.2.2.** TGA (top curve), DTG (middle curve) and DTA (bottom curve) of CTA-Br heated in air.

DTA in the region coinciding with the larger exothermic peak, between 180 and 320°C, is quite interesting as it contains both exotherms and endotherms. This behaviour is likely due to CTA<sup>+</sup> cracking into volatile components, which combust with O<sub>2</sub> to initially produce an exotherm (180 - 220°C). From 220 to 275°C evaporation of the volatile decomposition products predominates, resulting in a more endothermic event. By 275°C and until 320°C, the rate of evaporation decreases and the combustion of the volatile organic compounds is once again dominant such that it is sufficient to produce an exotherm.

Cracking and evaporation of decomposition products is not complete by 320°C as approximately 9% mass still remains at this temperature. This mass is thought to be soft-coke, which was also observed by Kleitz *et al.*,<sup>181</sup> in their study of CTA<sup>+</sup> decomposition in porous silica materials. By 350°C the temperature is sufficient to oxidize the carbonaceous

material into volatile components (CO or CO<sub>2</sub>). This process is completed by 500°C whereby no mass remains in the TGA instrument.

#### **4.3 Thermal decomposition of CTA-W<sub>12</sub>**

The thermal decomposition of CTA-W<sub>12</sub> occurs over three main stages: dehydration and expansion, Keggin anion fragmentation and the adoption of a condensed hexagonal phase, and finally reorganization into a bulk oxide. In air, these three stages are accompanied by three endothermic and three major exothermic events (Figure 4.3.1). Eight crystallographically distinct phase transformations were measured across the samples' decomposition (Figure 4.3.2), which have been labelled phase I to VIII (with CTA-W<sub>12</sub> = phase I) for clarity.

##### **4.3.1 Dehydration and expansion – phases I - III**

Decomposition of CTA-W<sub>12</sub> begins with a small mass loss occurs at ~80°C which coincides with a small endothermic event and can be attributed to dehydration via loss of 2 H<sub>2</sub>O, Figure 4.3.1.

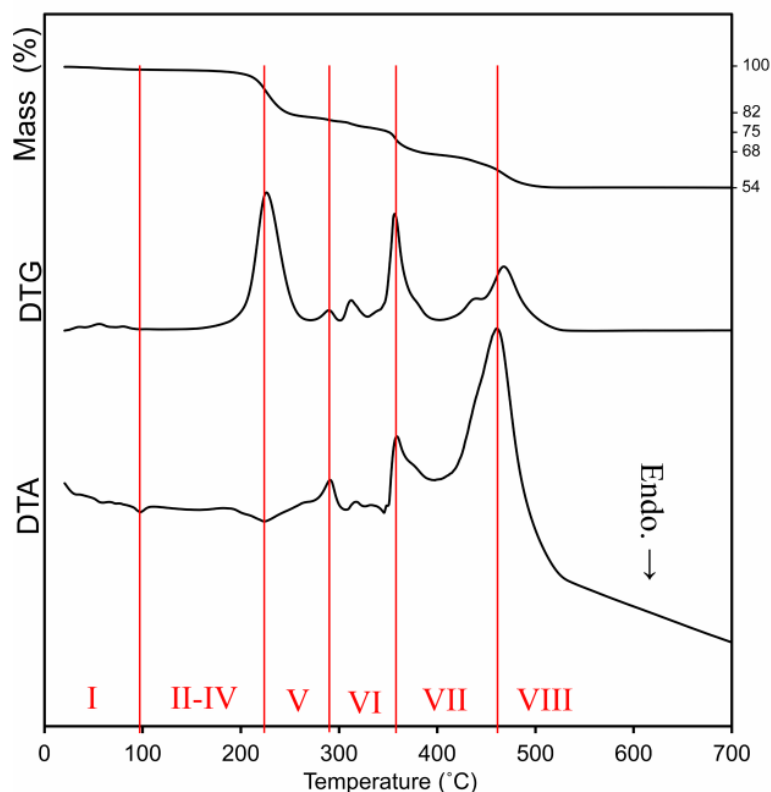


**Figure 4.3.1.** TGA, DTG and DTA of CTA- $W_{12}$  in air. Red lines and Roman numerals mark the domain of distinct phases.

At 98°C the (001) and (002) peaks intensify and shift to lower  $2\theta$  indicating expansion of the inter-lamellar distance, which again coincides with an endothermic event. This change marks the adoption of phase II. The endothermic transformation and shifting of the peaks to lower  $2\theta$  is assigned to the tilted digitated alkyl-tails adopting a less digitated, more normal orientation relative to the bi-layer interface (smectic A), causing expansion of the interlamellar distance.<sup>145</sup> This expansion continues monotonically until 185°C when it accelerates, which marks the samples' transformation to phase III. Phase III is characterised by the emergence of two new peaks at  $d = 17.00$  and  $14.86$  Å. Calculation of the interlamellar distance (001) from the (002) peak returns a distance of 28 to 31 Å, which indicates the CTA<sup>+</sup> are still interdigitated to considerable degree at this temperature, considering the length of two CTA<sup>+</sup> molecules end-to-end is 48 Å.<sup>84</sup>

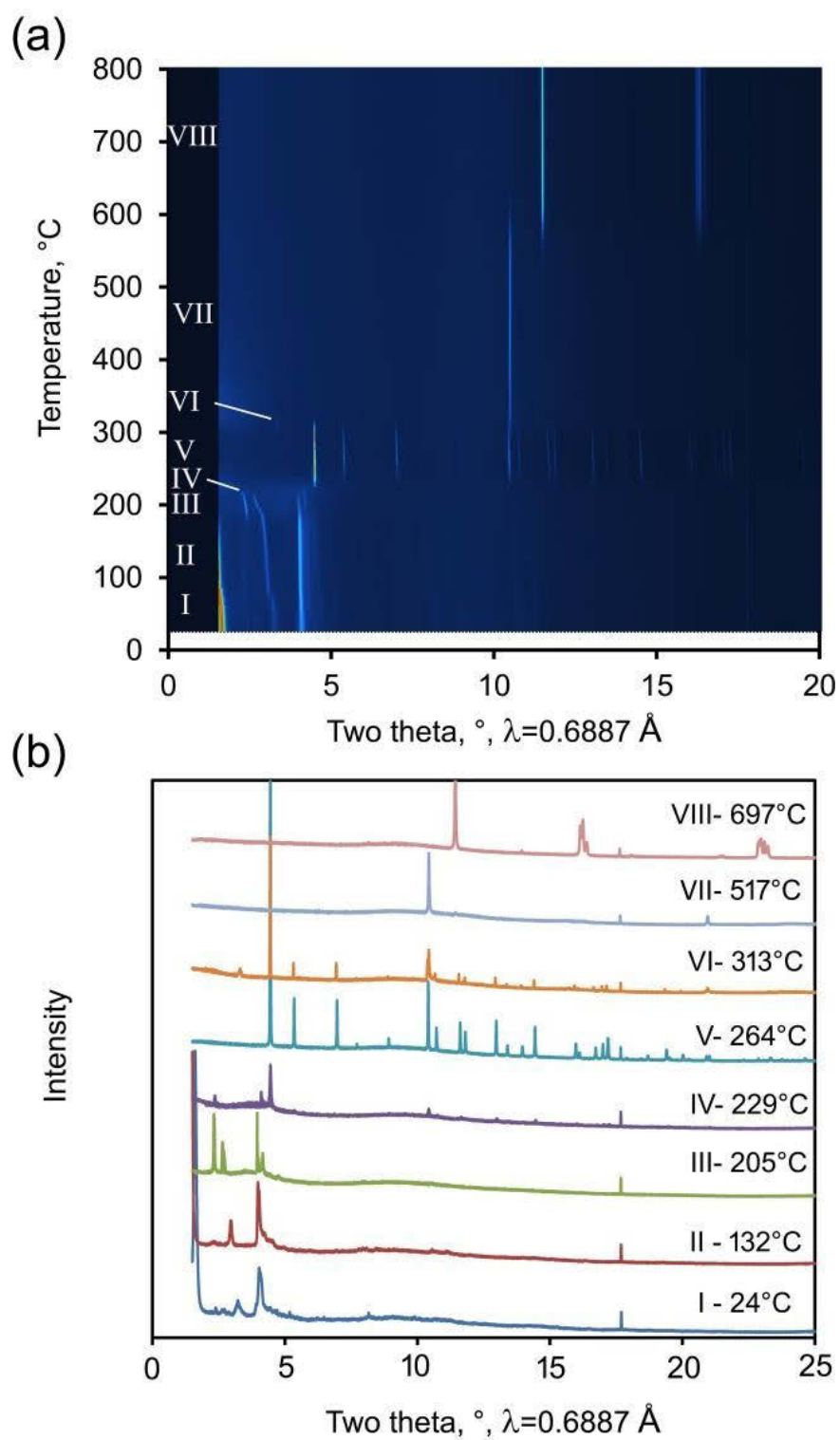


**Figure 4.3.2.** (a) Heat map of CTA-W<sub>12</sub> thermal decomposition consisting of *in situ* synchrotron P-XRD patterns recorded from 30 to 800°C (b) Stacked P-XRD plot of CTA-W<sub>12</sub> thermal decomposition containing the distinct phases.

It is worth noting here that none of the phases I-III displayed an XRD pattern the same as that of the similar  $(\text{CTA})_6\text{W}_{12}$  compounds synthesized by Stein *et al*<sup>84</sup> by prolonged hydrothermal treatment at 100 to 150°C (but measured at room temperature). This suggests that at least four different metallotropic structures are possible in this system with the outcome of the synthesis depending on temperature and synthesis conditions.

XRD patterns, Figure 4.3.2, show that the progression from phases I  $\rightarrow$  II  $\rightarrow$  III is continuous as demonstrated by the smooth, unbroken movement of the lamellar-ascribed peak. Therefore, these phases only differ from each other by the size of their interlamellar distance, and not from new crystal nucleation or growth. Such a continuous transition can be described as a first-order. FT-IR data, Fig. 4.3.3, of phases I-III supports this conclusion as the spectra of these phases are very similar to each other, signifying that no significant new molecular/ionic bonds or other significant chemical change has occurred to the sample over this temperature range. It is therefore evident that, up to 220°C, interdigitation of the  $\text{CTA}^+$  tails, and the resultant lamellar distance in  $\text{CTA-W}_{12}$  is temperature dependent, with interdigitation greatest at low temperatures, resulting in high tilt-angles and shortened interlamellar distances. As the temperature increases, up to 220°C, the  $\text{CTA}^+$  tails become less interdigitated, resulting in smaller tilt-angles and larger interlamellar distances.

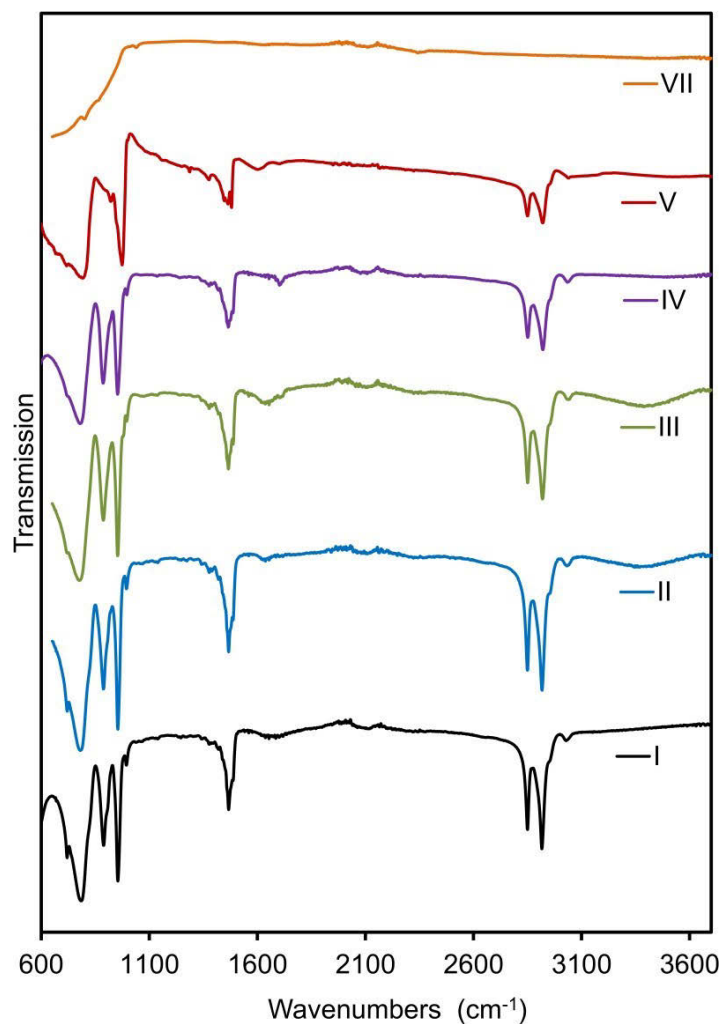


**Figure 4.3.3.** *Ex-situ* ATR FT-IR spectra of the phases present across CTA- $W_{12}$  thermal decomposition.

The only significant difference between the spectra of phases I to III is the appearance of a small band at  $1705\text{ cm}^{-1}$  in the spectrum of phase III. This peak is ascribable to oxidised carbon (C=O or C-OH), and suggests that by  $\sim 200^\circ\text{C}$ , the temperature is sufficiently elevated to oxidise organic CTA<sup>+</sup>.

#### 4.3.2 Lamellar decomposition – phase IV

The adoption of phase IV at  $220^\circ\text{C}$  marks the first first-order transition within the thermal decomposition of CTA- $W_{12}$ , signalling the destruction of the lamellar structure. The discontinuity of the first-order transition is depicted in Figure 4.3.4, where the adoption of

phase IV presents a marked difference from the previously continuous phase I  $\rightarrow$  III transitions (as represented by the position of the (002) peak). The transition coincides with the first significant mass loss from the sample, Figure 4.3.1, and due to the temperature and magnitude of the event, it can be attributed to Hoffman elimination of CTA<sup>+</sup> as described in Sections 4.1.2. and 4.2.

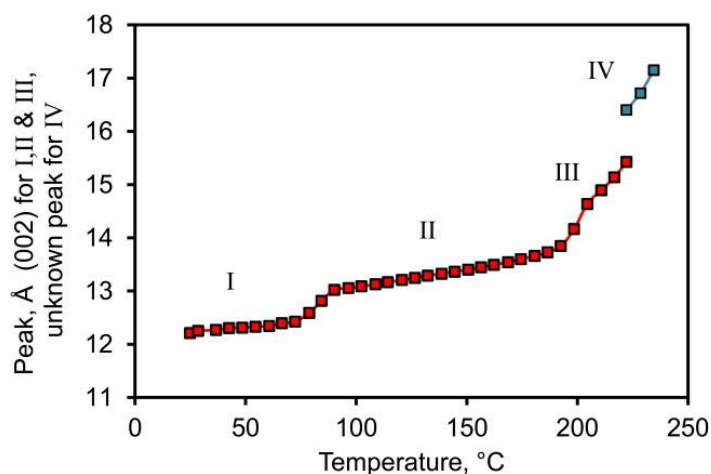


**Figure 4.3.4.** (002) Peak position, in Å, as a function of temperature illustrating interlamellar expansion from 30 to 220°C. Phase transitions from I  $\rightarrow$  II  $\rightarrow$  III are continuous whereas the transition from III  $\rightarrow$  IV is not.

The first-order transition between phases III and IV is therefore due to the decomposition and loss of CTA<sup>+</sup> and associated lamellar-supporting hydrophobic tails which instigates a collapse in the lamellar order of the sample. As expected, significant amount of amorphization accompanies the presence of phase IV, as indicated by the increased intensity of the P-XRD background signal, Figure 4.3.8.

Phase IV exists within the small temperature range of 220 to 235°C, and can be seen as a transitional phase between the much stable lamellar-phases (I $\rightarrow$ III) and the hexagonal phase (phase V). This assignment is further supported by XRD, Figure 4.3.2, where the pattern of phase IV is seen to contain similar peaks to phase III at low  $2\theta$ , and similar peaks to phase V at high  $2\theta$  (although at much lower intensities).

From phase IV, and until the onset of phase VII ( $\sim 500^\circ\text{C}$ ), the FT-IR bands associated with the vibrations of organic  $\text{CTA}^+$  ( $> 1050\text{ cm}^{-1}$ ) start to significantly decrease in intensity (Figure 4.3.3), concurrent with mass loss evident in the TGA over this temperature range. The oxidised-carbon peak at  $1705\text{ cm}^{-1}$  also increases in intensity, suggesting progressed oxidation to  $\text{CTA}^+$ .

### 4.3.3 Keggin fragmentation and adoption of HCP structure – phase V

The onset of phase V at  $235^\circ\text{C}$  is marked by the appearance of well-formed diffraction peaks (Figure 4.3.2), indicating a high degree of crystallinity. The phase persists until  $310^\circ\text{C}$  where it undergoes another first-order phase transition into a bulk-oxide. The phase V pattern of Figure 4.3.2 fits the case of a hexagonally organised isopolytungstate network (Figure 4.3.5) and is very similar to Au atoms arranged within a hexagonally-close-packed (HCP) crystal.

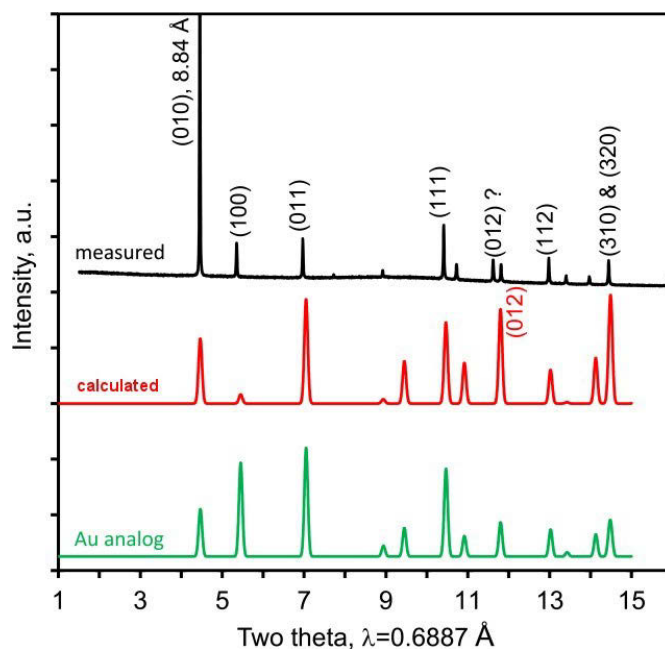


**Figure 4.3.5.** Measured (-) and calculated (-) XRD patterns of phase V. Both patterns are similar to a HCP array of Au atoms (-).

The adoption of the HCP phase is likely due to the loss of lamellar-supporting amphiphiles which instigates the collapse of the inorganic phase. The hexagonal crystal structure of phase

V can therefore be described as sheets of pseudo-hexagonally arranged anions, similar to that which appears in Figure 3.1.4, that are no longer separated by interdigitated hydrophobic alkyl-chains and instead are stacked on top of each other to produce the HCP structure apparent in Figure 4.3.5.

The low-frequency region ( $< 1050 \text{ cm}^{-1}$ ) within the FT-IR spectrum (Fig. 3.3.3) of phase V is markedly different from all previous spectra, (which are very similar to each other,) due to the absence of the corner-sharing-oxygen stretching band,  $\nu(\text{W-O}_b\text{-W})$ , previously located at  $885 \text{ cm}^{-1}$ . Corner-oxygen species,  $\text{O}_b$ , bind the four trimers of the Keggin anion together (Figure 4.3.7), and the disappearance of this peak marks the destruction, or otherwise fragmentation, of the Keggin unit (as described in Section 4.1.3). To further investigate the fragmentation process, *ex-situ* ATR FT-IR was performed on samples of phase V from 270 to  $310^\circ\text{C}$ , Figure 4.3.6.

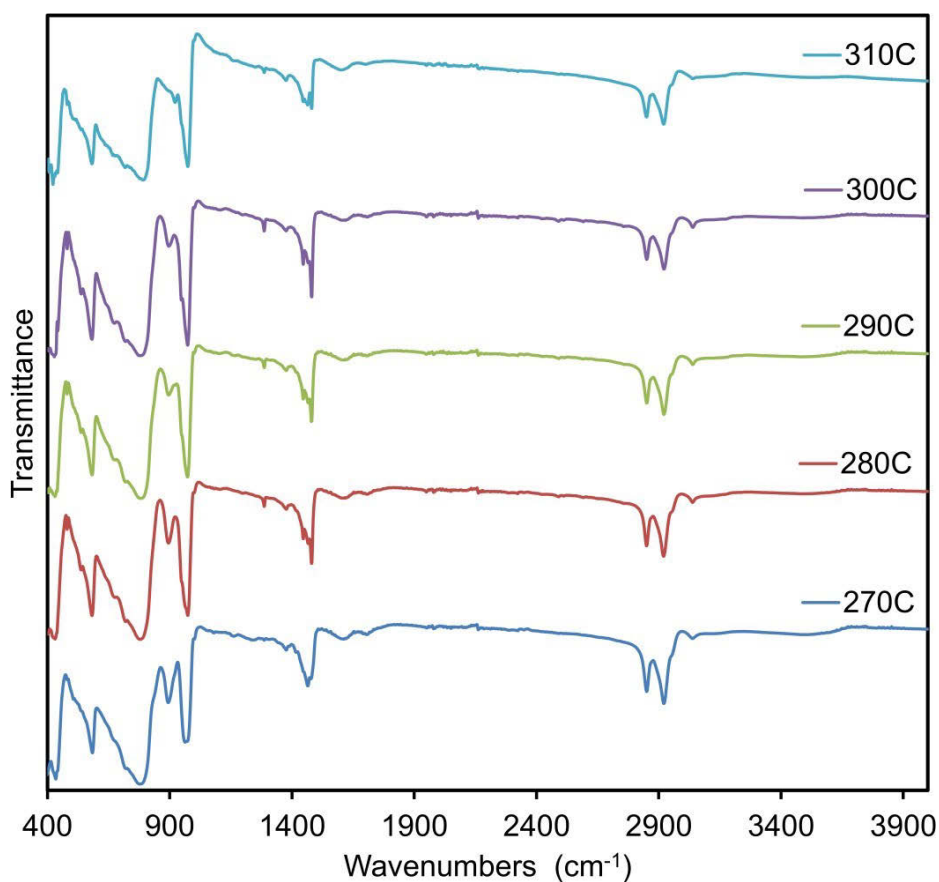


**Figure 4.3.6.** *ex-situ* ATR FT-IR spectra of phase V from 270 to  $310^\circ\text{C}$ .

The  $\nu(\text{W-O}_b\text{-W})$  peak is seen to progressively decrease in intensity and blue-shift, from 885 to 919  $\text{cm}^{-1}$ , over from 270 to 310°C. Similar observations were made by A. Bielanski *et al* in their infrared study of the thermally-induced transformations of  $\text{H}_{3-x}\text{PMo}_{12-x}\text{V}_x\text{O}_{40}$  type Keggin anions.<sup>207</sup> Such changes in the IR spectra are not only assignable to a decreasing number of  $\text{O}_b$  bonds in the sample, but also to shortening of the  $\text{W-O}_b\text{-W}$  bonds as well. Concurrently, the  $\nu(\text{W=O}_d)$  peak at 973  $\text{cm}^{-1}$  is seen to increase in intensity and develop a shoulder around 946  $\text{cm}^{-1}$ . This suggests an increase in the number and type (length) of  $\text{W=O}_d$  bonds, likely due to the presence of new  $\text{WO}_6$  octahedral environments.

These changes in the FT-IR spectra suggest that the Keggin structure of the tungstate anions is destroyed over the course of phase V, via the separation of the corner-shared trimers. The presence of edge-sharing,  $\nu(\text{W-O}_c\text{-W})$ , from 500 – 800  $\text{cm}^{-1}$ , and a strong  $\text{W=O}_d$  band suggests that some form of tungsten isopolyanion persists at 310°C. The decreasing intensity and blue-shifting  $\nu(\text{W-O}_b\text{-W})$  band can be attributed to the trimers are ‘folding-up’ on themselves, likely forming more condensed isopolyanions that only contain edge-sharing between octahedra. All of these observations are indicative of Keggin fragmentation, Figure 4.3.7, as the edge-sharing trimers, previously connected to each other via corner-sharing, disconnect and condense into smaller, more condensed edge-sharing isopolyanions such as hepta- and octa-tungstates, as described in Section 4.1.3.<sup>71</sup> These condensed polyanions would then reorganize into bulk tungsten oxides at higher temperatures.

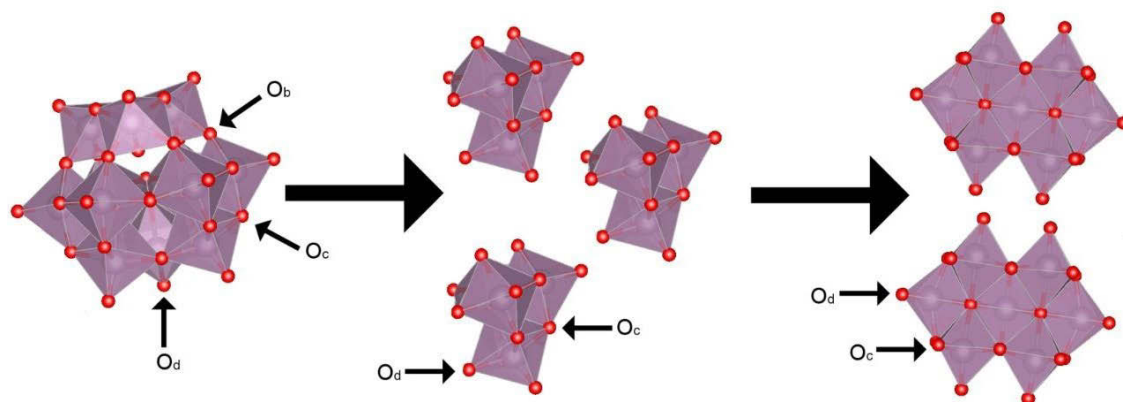


**Figure 4.3.7.** Keggin anion (left) decomposition occurs over the course of phase V in a multi-step process, involving separation into edge-sharing trimers (middle) before condensing into larger edge-sharing isopolytungstates such as heptatungstates (right) and octatungstates.

A number of changes are also seen to occur within the higher-frequency side ( $> 1050 \text{ cm}^{-1}$ ) of Figure 4.3.6. The  $\nu_{ss}(\text{CH}_2)$  and  $\nu_{as}(\text{CH}_2)$  vibrations at  $2919$  and  $2950 \text{ cm}^{-1}$ , respectively, are seen to progressively decrease in intensity from  $270$  to  $310^\circ\text{C}$ , concurrent with  $\text{CTA}^+$  cracking and consequent evaporation/combustion of volatile products over this temperature range, Figure 4.3.1. Furthermore, the broad asymmetric band located around  $\sim 1460 \text{ cm}^{-1}$ , containing bands assignable to bonds around the cationic-nitrogen, is seen to sharpen, revealing a number of previously un-resolved peaks. This is due to the  $\delta(\text{CH}_2)$  band at  $1465 \text{ cm}^{-1}$  decreasing in intensity, whilst the  $\sigma_s(\text{N}^+-\text{CH}_3)$ ,  $\sigma(\text{CH}_3)$ ,  $\omega(\text{CH}_3/\text{CH}_2)$  and  $\rho(\text{N}^+-\text{CH}_3)$  bands at  $1488$ ,  $1446$ ,  $1376$  and  $186 \text{ cm}^{-1}$ , respectively, are all seen to increase in intensity. Mutually, the  $\nu_{as}(\text{N}^+-\text{CH}_3)$  band at  $3039 \text{ cm}^{-1}$  also increases in intensity. All these observations are attributable to a decreasing  $\text{CH}_2$  content (*i.e.* alkyl chains) and a relative increasing  $\text{CH}_3$  content.

This behaviour is indicative of Hoffman elimination of the  $\text{C}_\beta\text{-N}^+$  bond within  $\text{CTA}^+$  producing 1-hexadecane ( $\text{C}_{16}\text{H}_{32}$ ) and trimethyl-ammonium ( $\text{HN}(\text{CH}_3)^+$ ), as opposed to cracking around  $\text{C}_\text{N}$  to produce volatile N,N-dimethylhexadecylamine ( $\text{C}_{18}\text{H}_{39}\text{N}$ ) and reactive  $\text{CH}_3^\bullet$ , as described in Sections 4.1.2 and 4.2.<sup>182</sup> Cationic methyl-ammonium species would remain in the sample, bound to the isopolyanion fragments until their decomposition and subsequent transition to bulk oxide from  $335^\circ\text{C}$ .

Interestingly, H<sub>2</sub>O attributable peaks,  $\delta(\text{H}_2\text{O})$  and  $\nu(\text{H}_2\text{O})$  at 1600 and 3400 cm<sup>-1</sup>, respectively, increase from phase IV to V, Figure 4.3.3. These peaks remain over the course of phase V, Figure 4.3.7, albeit gradually decreasing in intensity. The origins of this H<sub>2</sub>O is unlikely to be crystallographic or hydrated water at such elevated temperatures, and are more likely attributed to protons more strongly attached to O<sub>c</sub> and O<sub>t</sub> sites at the surface of the isopolytungstates. Mestl *et al*<sup>71</sup> and Damyanova *et al*<sup>208</sup> observed in their studies of the thermal decompositions of H<sub>4</sub>(PVMo<sub>11</sub>O<sub>40</sub>) and H<sub>3</sub>(PMo<sub>12</sub>O<sub>40</sub>), respectively, that heating rates of over 0.2°C/min are too fast to allow for complete dehydration at high temperatures and that, above such rates, acidic protons remain attached to the polyanions (or polyanions fragments) up until the formation of bulk oxides. The increase in concentration of W-OH sites from phase IV to V is a direct result of Keggin anion fragmentation into more numerous smaller isopolytungstates, thereby increasing the total number of W-OH sites within the material.

#### 4.3.4 Bulk-oxide formation

Phase VI is a short lived transient phase which appears from 300°C and persists until 335°C. Phase VI is quite similar to phase V, and only differs by the relative intensity of peaks, and the appearance of a strong, broad reflection at  $d = 11.93 \text{ \AA}$ , Figure 4.3.2. The adoption of phase VI is accompanied by an increase in the amorphous content of the sample, as indicated by the increase in the background signal over this temperature range, Figure 4.3.8(b). Phase V or VI does not decrease in intensity at the expense of the growth phase VII, and therefore likely nucleates from the amorphous portion of the sample. It can therefore be concluded that, like phase IV, phase VI is a ‘transition phase’, between the ordered HCP arrangement of phase V, and the ordered bulk oxide of phase VII.

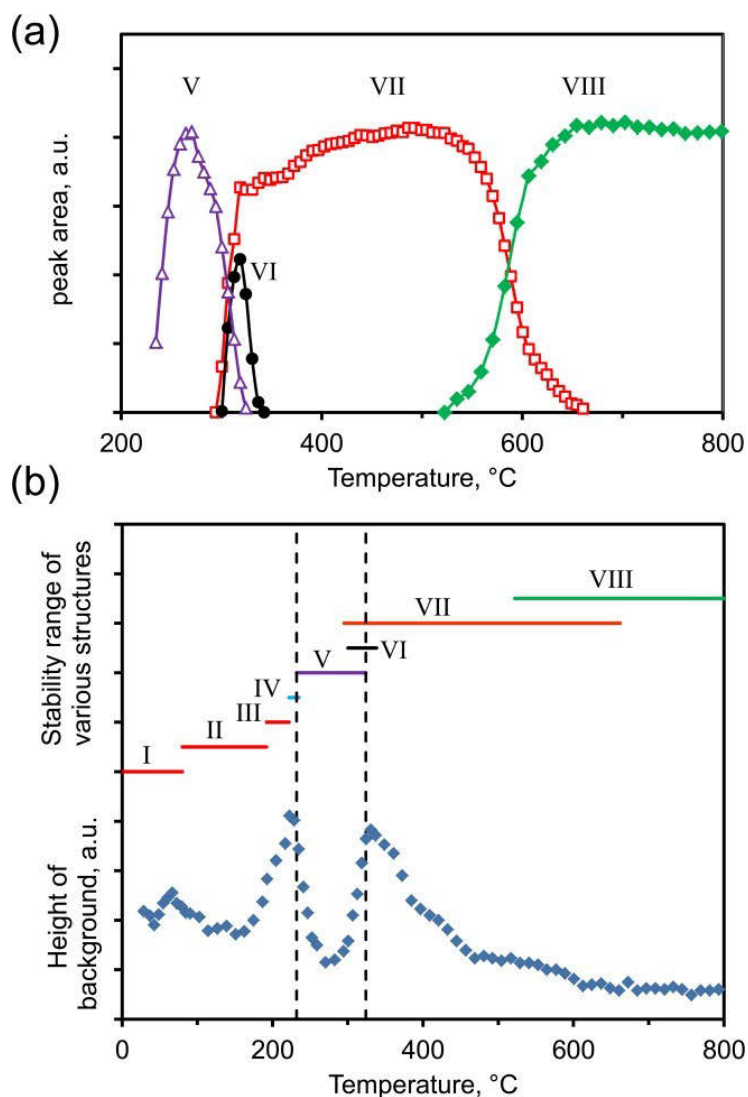


**Figure 4.3.8.** Conversion of phase V to VI to VII to VIII during thermal decomposition,(a) followed using the area under a characteristic peak for each phase (phase V; peak at  $d = 8.87 \text{ \AA}$  , phase VI; peak at  $d = 11.94 \text{ \AA}$  , phase VII; peak at  $d = 3.79 \text{ \AA}$  , phase VIII; peak at  $d = 3.46 \text{ \AA}$ ), (b) increase in amorphous background (represented by intensity of pattern at  $d = 19.7 \text{ \AA}$ ) with stability ranges of various phases superimposed. Note that the highly crystalline phase V forms from a relatively disordered precursor, and then decomposes to produce an initially relatively disordered product.

Mass loss continues over the course of phases VI and VII, Figure 4.3.1, up until  $\sim 500^\circ\text{C}$ , concentrated within two significant events ( $330 - 400^\circ\text{C}$  and  $400 - 520^\circ\text{C}$ ) which are

accompanied by relatively large exotherms. The first mass loss event and exotherm (accounting for 7% mass loss) from 330 – 400°C can be attributed to the loss of previously mentioned acidic protons as water, and the combustion of trimethyl-ammonium counter-cations, as the edge-sharing isopolyanions (phase VI) decompose into the corner-sharing network of bulk tungsten oxide (phase VII).

Phase VII, which is the dominant phase by 350°C, can be matched to the tungsten sub-oxide  $W_{17}O_{47}$  (COD: 96-210-7066). The final exothermic mass loss event from 400 – 520°C can be attributed to the combustion of ‘soft-coke’, the product resultant from incomplete  $CTA^+$  cracking and volatilization.<sup>181, 206</sup> The combustion of this carbonaceous material predictably coincides with the largest exothermic event of the thermal decomposition, as C is oxidized to CO and CO<sub>2</sub>. ATR FT-IR of phase VII collected at 550°C, Figure 4.3.3, displays a strong, broad peak from 600 to 1000  $cm^{-1}$ , attributable to  $\nu(W-O_b-W)$  modes within the bulk lattice, whilst the rest of the spectrum (1000 – 4000  $cm^{-1}$ ) is relatively featureless, supporting the assignment of a bulk oxide.

By 550°C the temperature is sufficient to instigate the transition to phase VIII, which can be matched to monoclinic tungsten dioxide,  $m-WO_2$  (JCPDF: 01-086-0134). This transition follows typical first-order rate kinetics, with the portion of phase VIII slowly increasing at the expense of phase VII, with both phases coexisting between 535 to 650°C, Figure 4.3.8.

#### **4.3.5 Effect of environment on $CTA-W_{12}$ thermal decomposition**

The end point of  $CTA-W_{12}$  thermal decomposition being  $WO_2$  (as opposed to  $WO_3$ ) signifies that the environment within the glass capillary during thermal decomposition must have been significantly reducing. This is not surprising considering the confined, sealed environment of the capillary, and the reactive products of  $CTA^+$  decomposition. To further investigate the role of the atmospheric environment, decomposition was carried out in a TGA instrument under the flow of  $N_2$  gas, Figure 4.3.9. This produced a product consisting of a mixture of  $WO_3$  and  $WO_2$  by 950°C. Decomposition of  $CTA-W_{12}$  under air, Figure 4.3.1, unsurprisingly yielded stoichiometric monoclinic tungsten trioxide,  $m-WO_3$ , which was matched to JCPDF: 01-083-0950, Figure 4.3.10. In light of the above results, it can be said

that some O<sub>2</sub> must have been presented in the TGA instrument even when N<sub>2</sub> was utilized as the flow gas.

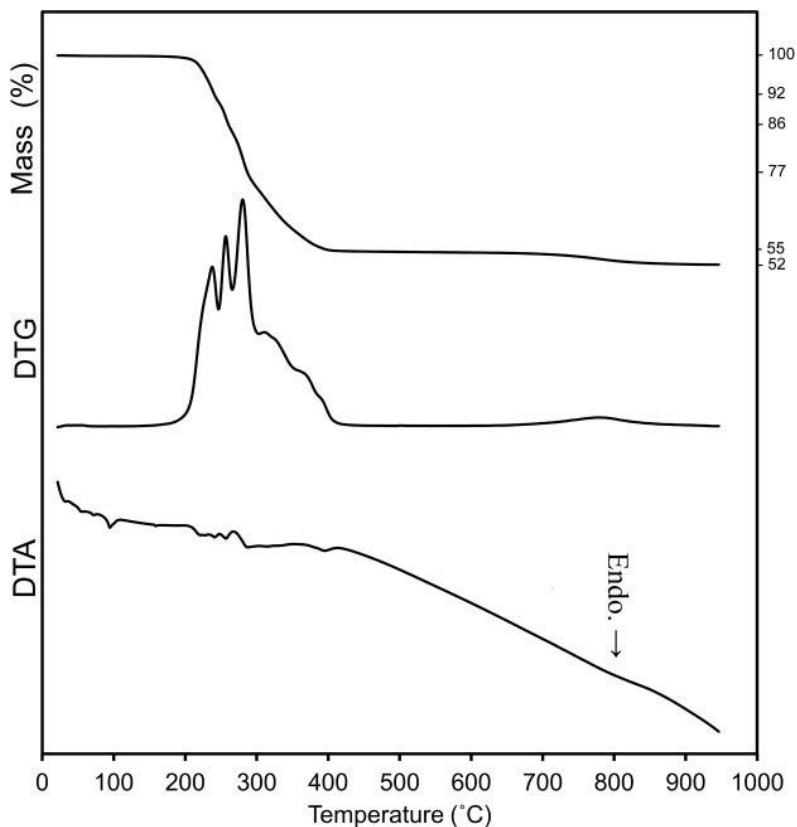


**Figure 4.3.9.** TGA, DTG and DTA of CTA-W<sub>12</sub> in N<sub>2</sub>.

Across the decomposition profile in N<sub>2</sub>, CTA-W<sub>12</sub> undergoes three major, narrowly separated mass loss events under nitrogen, without any significant heat exchanges with the environment. The first major mass loss event begins at ~210°C with the release of CTA<sup>+</sup> and dehydration, coinciding with a small endothermic signal. This is closely followed at 240°C with a similar event (release of organic CTA<sup>+</sup>), in the range 260 to 280°C. Decomposition and associated mass loss continues from 300°C to ~410°C, although at a much more steady rate as compared to the initial mass losses at lower temperatures, as any remaining organic CTA<sup>+</sup> (or CTA<sup>+</sup> decomposition products) evacuate the sample. From ~650°C, temperatures are sufficiently elevated to drive oxygen-vacancy generation within the lattice, and hence sub-stoichiometry, in the inert atmosphere,<sup>209</sup> which is attributed to the small mass loss of

3% at  $\sim 800^\circ\text{C}$ . This loss of oxygen results in a sub-stoichiometric oxide of  $\text{WO}_{2.65}$  at  $950^\circ\text{C}$  (89:11  $\text{WO}_3:\text{WO}_2$ ).

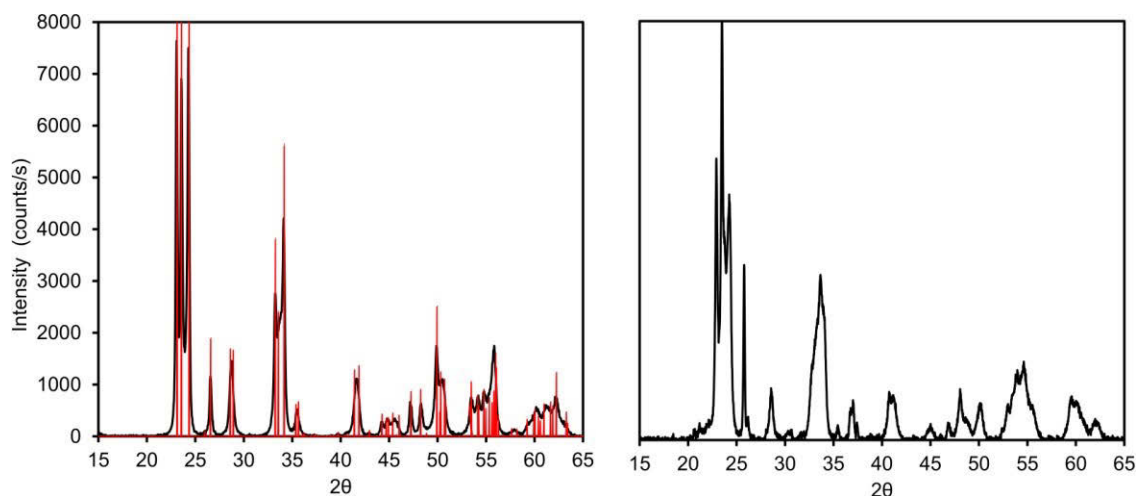


**Figure 4.3.10.** P-XRD of the product produced from (a) TGA under air (Figure 3.3.1) and (b) TGA under  $\text{N}_2$  (Figure 3.3.9). Red stick-plot in (a) is from JCPDF: 01-083-0950.

Comparing Figure 4.3.1 (air) to Figure 4.3.9 ( $\text{N}_2$ ), it is seen that the rate of decomposition is accelerated in inert-atmospheres ( $\text{N}_2$ ) as compared to more oxidizing ones (air). In air, Figure 4.3.1, CTA- $\text{W}_{12}$  undergoes all mass loss events by  $\sim 520^\circ\text{C}$ . Under  $\text{N}_2$ , all mass loss events are completed by  $\sim 420^\circ\text{C}$ , approximately  $100^\circ\text{C}$  cooler than in air. This acceleration by  $\text{N}_2$  relative to air can also be seen by observing the temperatures at which the main mass loss events take place. The events are spread across a wider range of temperatures ( $\sim 300^\circ\text{C}$ ) in air, whereas the events are barely separated in  $\text{N}_2$  ( $\sim 200^\circ\text{C}$ ). Furthermore, the mass losses under  $\text{N}_2$  do not accompany large exotherms, unlike in air at high temperatures, obviously due to  $\text{CTA}^+$  decomposition products being unable to combust with the inert environment.

#### **4.4 Thermal Decomposition of CTA- $\text{WO}_3$**

The thermal decomposition of CTA- $\text{WO}_3$  (Figures 3.2.4–7) was also studied in order to compare it to that of CTA- $\text{W}_{12}$ .

#### **4.4.1 Lamellar phases of CTA-WO<sub>3</sub>, phases I – III**

The thermal decomposition of CTA-WO<sub>3</sub> comprises of three main regions; dehydration and expansion, CTA<sup>+</sup> decomposition and evaporation and finally formation of monoclinic tungsten trioxide. These three regions are accompanied by six crystallographic phases changes, as displayed in Figure 4.4.1(a) and (b). Three major and one minor mass loss events were detected across the decomposition in air, Figure 4.4.2, whilst one major and three minor were detected in N<sub>2</sub>, Figure 4.4.3.

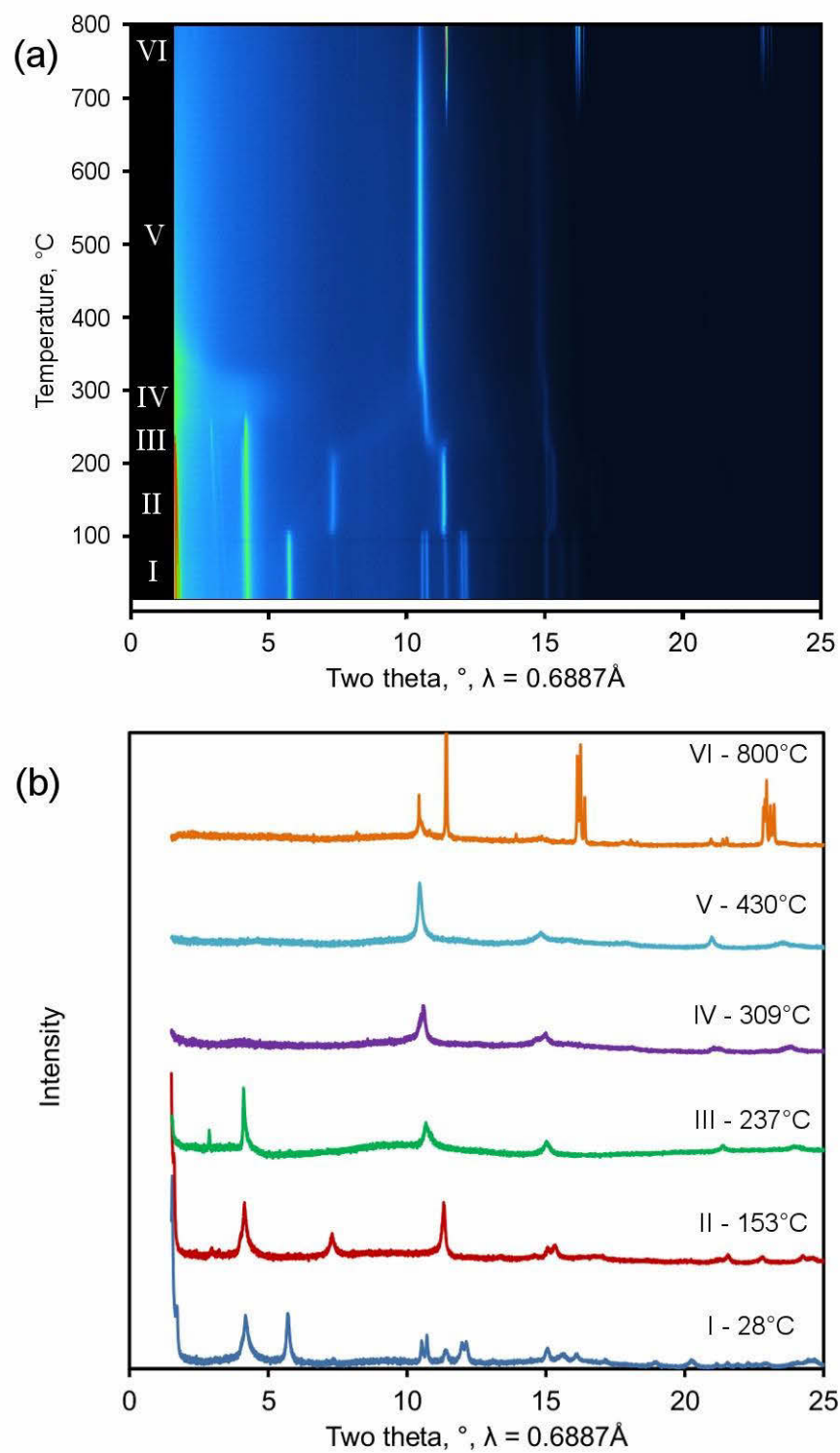


**Figure 4.4.1.** (a) Heat map of CTA-WO<sub>3</sub> thermal decomposition consisting of *in situ* synchrotron P-XRD patterns recorded from 30 to 800°C (b) Stacked P-XRD plot of CTA-WO<sub>3</sub> thermal decomposition containing the distinct phases.

Similar to CTA-W<sub>12</sub>, CTA-WO<sub>3</sub> begins thermally decomposition by dehydration and expansion of the lattice. This is measured by TGA as an endothermic mass loss from 30 to 90°C, Figure 4.4.2, and accounts for 3% of total mass. By 100°C dehydration is sufficient to cause a phase change from tungsten dihydrate, WO<sub>3</sub>·2H<sub>2</sub>O (phase I, ICDD: 00-018-1420), to the monohydrate WO<sub>3</sub>·H<sub>2</sub>O (phase II, ICDD: 00-043-0679). Dehydration of the hydrated tungstate continues over the course of phase II, accounting for a further 2% mass loss.

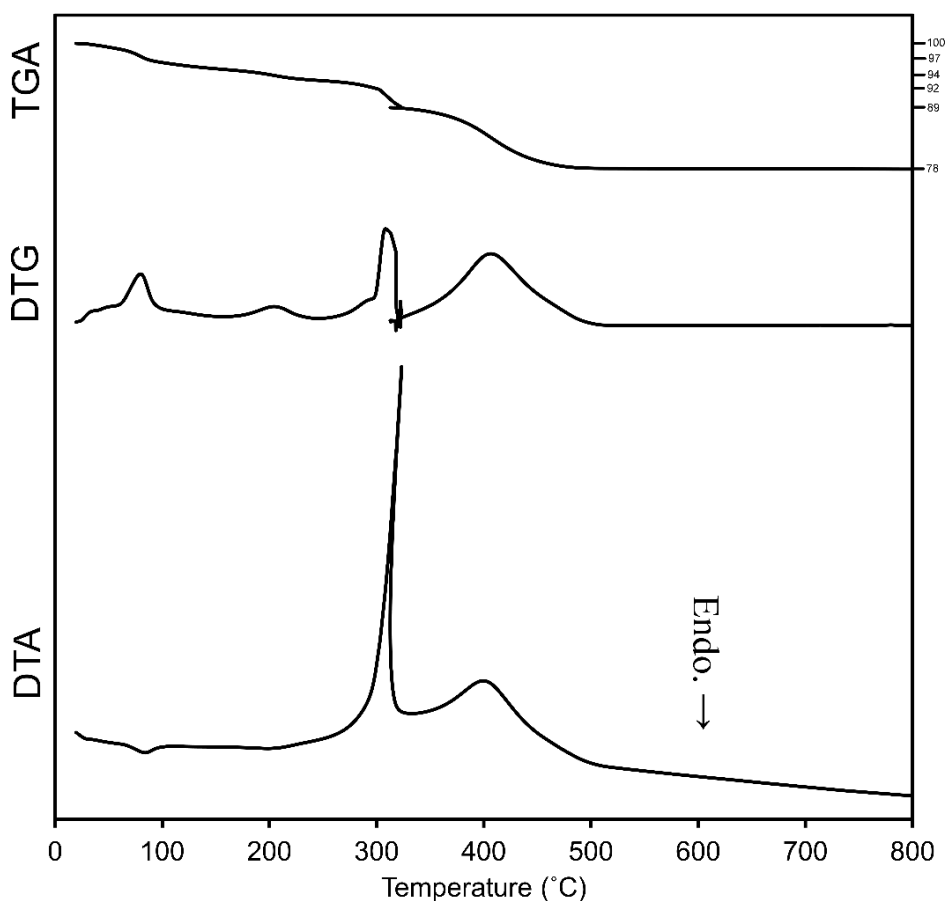


**Figure 4.4.2.** TGA, DTG and DTA of CTA-WO<sub>3</sub> in air.

CTA<sup>+</sup> begins to decompose and evaporate by ~180°C, similar to the case of CTA-W<sub>12</sub>. This low-temperature event is attributed to Hoffman degradation/elimination of the C<sub>β</sub>-N<sup>+</sup> bond within CTA<sup>+</sup>, resulting in volatile trimethyl-ammonium and 1-hexadecene. Due to the loss of the lamellar supporting amphiphiles, this mass loss instigates the transition to phase III by 225°C. Phase III still contains a peak at low 2θ, due almost certainly to the presence of

lamellae, although the maximum of this peak has moved beyond the beam-stop by this stage. Phase III is further characterized by a sharp reflection located at 13.74Å.

#### 4.4.2 Lamellar decomposition and bulk-oxide formation

The XRD pattern of phase III persists until 274°C, whereby a quick transition to phase IV is observed. The adoption of phase IV marks the destruction of lamellar structure, as evidenced by the absence of previously present low  $2\theta$  peaks. CTA<sup>+</sup> cracking and volatilization within the TGA depicted in Figure 4.4.2 begins at 250°C and steadily continues until 300°C, at which an abrupt large mass loss occurs. This loss is equal to 3% of the total mass of CTA-WO<sub>3</sub> and is accompanied by a very large exotherm, which is seen to disrupt the TGA instrument, Figure 4.4.2, causing the TGA curve to temporarily progress backwards. Considering the temperature of this event, it is likely caused by products of CTA<sup>+</sup> cracking quickly forming and combusting with the oxidizing environment, which is catalysed by the transition-metal-oxide substrate.<sup>180</sup>

Considering that thermal decomposition is accelerated in less oxidising environments, such as that found within the silica capillary used to mount the sample depicted in Figure 4.4.1, the temperature of the phase III to IV transition is likely delayed in the TGA (air) depicted in Figure 4.4.2 as compared to Figure 4.4.1. This dramatic mass loss event at 300°C in the TGA is therefore attributed to the phase III to IV transition, detected at 274°C within the *in situ* XRD (capillary), Figure 4.4.1. The abruptness of this event is therefore likely related to the destruction of the confining lamellar structure and resultant exposure of CTA<sup>+</sup> to the oxidizing environment. The exposed CTA<sup>+</sup> surfactants then quickly crack into volatile components, catalysed by the newly formed transition-metal-oxide, and subsequently combusted resulting in the observed large exotherm.

Like the phase IV of CTA-W<sub>12</sub> thermal decomposition, this phase IV can also be considered as a ‘transition phase’, between the lamellar separated arrangements of phases I to III, and the more continuous bulk-oxide arrangements of phases V and VI. Exothermic mass loss continues over the course of phase IV, although at a much steadier rate relative to the previous mass loss event. All mass loss from the thermal decomposition of CTA-WO<sub>3</sub> is complete by ~500°C. This steadier mass loss from 320°C to 500°C is attributed to combustion of carbonaceous soft-coke, similar to the case of CTA-W<sub>12</sub>, Section 4.3.4.<sup>181, 182,</sup>

<sup>206</sup> The P-XRD pattern of phase IV, Fig. 4.4.1, is quite similar to that of phase VII within the thermal decomposition of CTA-W<sub>12</sub> (Fig. 3.3.2), which was matched to the tungsten sub-oxide W<sub>17</sub>O<sub>47</sub> (COD: 96-210-7066). However, the peaks of the CTA-WO<sub>3</sub> variant (phase IV) are at a much lower intensity, indicating a greater degree of amorphization. It can be said then, that formation of W<sub>17</sub>O<sub>47</sub> from a hexagonal network of isopolyanions is more crystalline than that formed from sheets of monoclinic WO<sub>3</sub>.

As was the case for CTA-W<sub>12</sub> (phase VIII), the final phase (phase VI) within CTA-WO<sub>3</sub> thermal decomposition is m-WO<sub>2</sub>, which begins to appear from ~650°C. However, the pattern of m-WO<sub>2</sub> from CTA-WO<sub>3</sub> differs to that from CTA-W<sub>12</sub> due to the presence of a large peak at  $d = 3.79 \text{ \AA}$ . This peak persists from the same peak that is found within phases IV and V, and is still apparent up to 800°C. It is uncertain what this peak is due to, although considering the chemical morphology of the sample, it is likely to be due to a feature of the W-O lattice as all other components of CTA-WO<sub>3</sub> would be decomposed and removed from the sample by this temperature.

#### 4.4.3 Effect of environment

Thermal decomposition of CTA-WO<sub>3</sub> under inert-atmosphere (N<sub>2</sub>), Figure 4.3.3, is seen to accelerate mass loss processes, similar to the case of CTA-W<sub>12</sub>, with all CTA<sup>+</sup> (and cracking products) released from the sample by 420°C, as opposed to 500°C in air. Under N<sub>2</sub>, dehydration of CTA-WO<sub>3</sub> still occurs at ~90°C (3% total mass), Hoffman degeneration occurs from ~180°C (4% total mass), and the largest mass loss event involving cracking and volatilization of CTA<sup>+</sup> occurs at 300°C (15% total mass). However, due the volatile CTA<sup>+</sup> cracking products not being able to combust with the inert-atmosphere, there is no dramatic exotherm, or disturbance to the TGA instrument, and instead the event coincides with a moderate endotherm (due to evaporation).

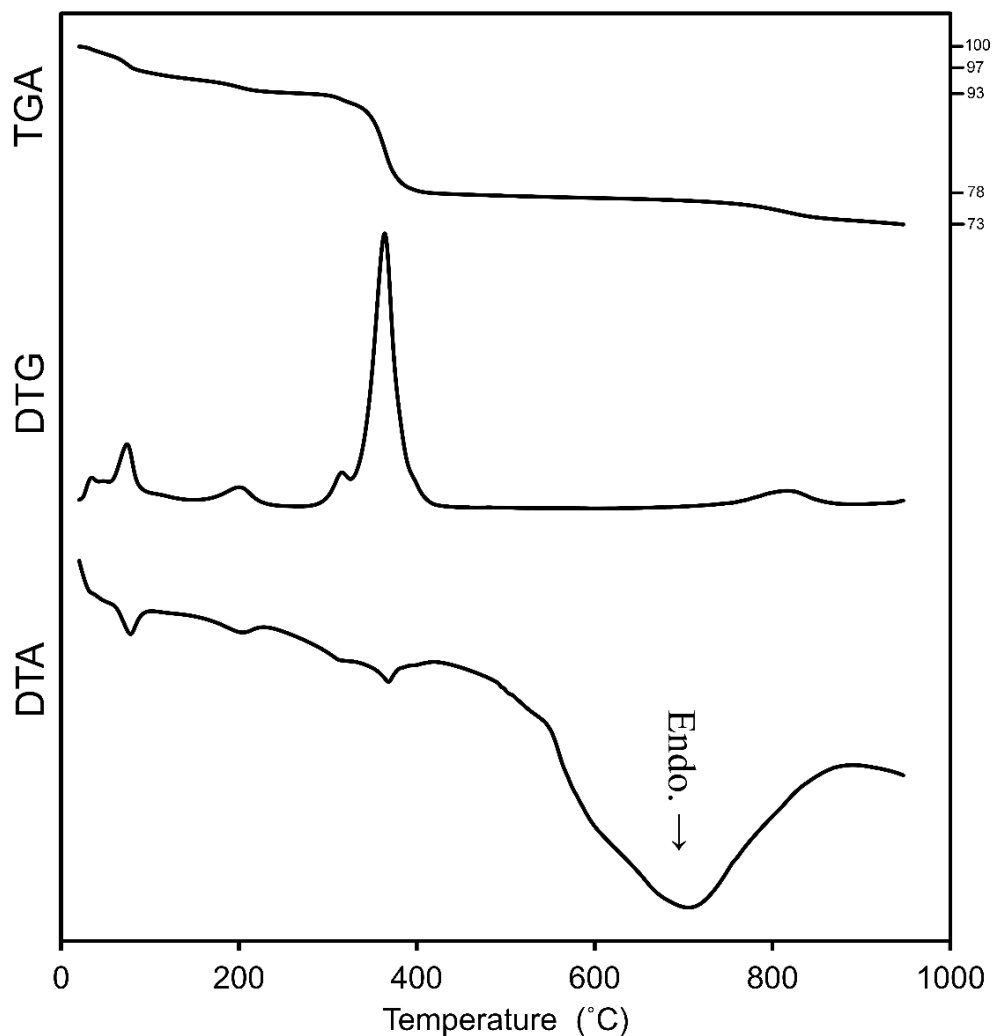


**Figure 4.4.3.** TGA, DTG and DTA of CTA-WO<sub>3</sub> in N<sub>2</sub>.

By ~750°C the temperature is sufficiently elevated to cause oxygen loss from the tungsten oxide, which causes a large endotherm. This oxygen loss accounts for 4.15% of total mass of CTA-WO<sub>3</sub>. If it is assumed that only WO<sub>3</sub> is present at 550°C, than this loss of oxygen renders the stoichiometry at 950°C to be WO<sub>2.22</sub>.

#### 4.4.4 Comparison to CTA-W<sub>12</sub> thermal decomposition

CTA<sup>+</sup> decomposition and consequent volatilization/combustion occurs differently in CTA-WO<sub>3</sub>, Figures 4.4.2-3, and CTA-W<sub>12</sub>, Figures 4.3.1 and 4.3.9. CTA<sup>+</sup> within CTA-W<sub>12</sub> is decomposed and released across two minor and three major events in air, labelled 1 to 4 in Figure 4.4.4 (with the two minor events collectively labelled 2). These events have maxima

at 225, 312, 356 and 467°C. In comparison, CTA<sup>+</sup> is decomposed and released over one minor and two major events within CTA-WO<sub>3</sub>, labelled 1 to 3 in Figure 4.4.4, centring on 203, 308°C and 406°C. Comparing these events between the two samples, it is seen that the mass loss 1 is the largest mass loss event in CTA-W<sub>12</sub>, which occurs from ~180°C, which coincides with a minor mass loss event in CTA-WO<sub>3</sub> (also labelled 1). In contrast, the largest mass loss event during CTA-WO<sub>3</sub> thermal decomposition is mass loss 2 at 308°C, which coincides with a minor mass loss event within CTA-W<sub>12</sub> decomposition (also labelled 2). Considering the low temperature of mass loss 1 in both samples, the event can be attributed to Hoffman degeneration, and consequent production of trimethyl-ammonium and 1-hexadecene.<sup>180-182, 206</sup> Additionally, mass loss 2 at around 310°C in both samples is attributed to the higher temperature cracking reaction of CTA<sup>+</sup> decomposition, which produces various alkane, alkenes and other organic fragments.

The difference between the magnitude of Hoffman degeneration and CTA<sup>+</sup> cracking in these two samples suggests that the rates of these mechanisms are dependent upon the environment surrounding CTA<sup>+</sup>. Hoffman degeneration requires OH<sup>-</sup>, and the mutual presence of Lewis base sites, such as those found at O<sub>c</sub> and O<sub>t</sub> sites on the surface of isopolyanions, is known to reduce the activation energy of the mechanism.<sup>180, 184, 210</sup> It is therefore not surprising that Hoffman degeneration of CTA<sup>+</sup> in CTA-W<sub>12</sub> is greatly favoured, as compared to CTA-WO<sub>3</sub> thermal decomposition, which does not contain Lewis base sites. The predominant CTA<sup>+</sup> decomposition mechanism in CTA-WO<sub>3</sub> is therefore the higher temperature cracking mechanism, which likely involves oxidation of the volatile products by the catalytic transition-metal-oxide substrate, and is responsible for the dramatic exotherm, Figure 4.4.2, coincident with this event. This difference in decomposition processes is also reflected under N<sub>2</sub> decomposition within Figures 4.4.3 and 4.3.9.

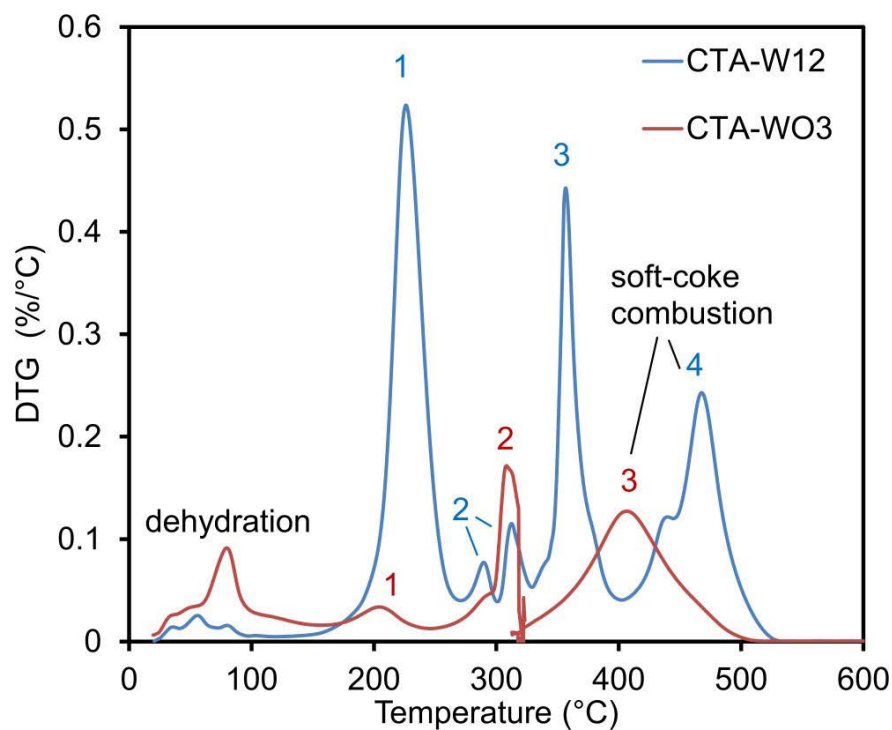


**Figure 4.4.4.** Comparison of DTG curves of CTA-W<sub>12</sub> and CTA-WO<sub>3</sub> in air.

The trimethyl-ammonium retained in CTA-W<sub>12</sub> is released within mass loss 3, collectively with H<sub>2</sub>O resultant from decomposition of the isopolyanions. This explains why mass loss 3 in CTA-W<sub>12</sub> decomposition does not coincide with any mass loss event in CTA-WO<sub>3</sub>.

Ammonia/ammonium retention by an anionic inorganic phase during CTA<sup>+</sup> thermal decomposition was also observed by F. Kleitz *et al* in their study of mesoporous silicates.<sup>181</sup>

Oxidation of soft-coke residue from incomplete CTA degeneration/cracking is likely the cause of mass loss 3 and mass loss 4 in the CTA-WO<sub>3</sub> decomposition profiles. This process is seen to occur from 318°C in CTA-WO<sub>3</sub> decomposition, and from 400°C in CTA-W<sub>12</sub>, a difference of 80°C. Explanation for this difference can be found within the recorded *in situ* XRD patterns of the decomposing samples. Combustion of soft-coke residues is seen to occur within both samples once the bulk sub-oxide phase has formed, which is 320°C in CTA-WO<sub>3</sub> (in air) and 400°C in CTA-W<sub>12</sub>. These bulk transition-metal-oxides likely catalyze the oxidation of the carbonaceous residue, dramatically reducing the energy requirement of the reaction as soon as they are formed. The above differences in the thermal decomposition profiles between CTA-W<sub>12</sub> and CTA-WO<sub>3</sub> are summarized in Table 4.4.1.

**Table 4.4.1.** Comparison of CTA-W<sub>12</sub> and CTA-WO<sub>3</sub> thermal decomposition events in air.

<b>Decomposition Event</b>	<b>CTA-W<sub>12</sub></b>		<b>CTA-WO<sub>3</sub></b>	
	Temperature (°C)	Volatile fraction (%)	Temperature (°C)	Volatile fraction (%)
<b>Dehydration</b>	RT – 180	3.7	RT – 180	22.5
<b>Hoffman degeneration</b>	180 – 270	37.7	180 – 245	6.92
<b>CTA<sup>+</sup> cracking</b>	245 – 320	7.3	270 – 330	22.6
<b>Ammonium combustion</b>	320 – 400	23.6	N/A	N/A
<b>Soft-coke combustion</b>	400 – 535	27.7	320 – 520	48.0

RT = Room temperature, Volatile fraction (%) = fraction of total mass loss across samples thermal decomposition as measured by TGA in air

Further effects of the anionic properties of metatungstates are reflected within the organic fraction of the two samples, where CTA-WO<sub>3</sub> has an organic content of 16.3%, which is much lower when compared to CTA-W<sub>12</sub> at 41.5%.

#### **4.5 Phase V (CTA-W<sub>12</sub> thermal decomposition intermediate)**

The phase V formed within the course of CTA-W<sub>12</sub> thermal decomposition sparked interest as it appeared to be a porous network of hexagonally arranged isopolytungstates. Such a material could be applicable for use as a proton-conductor<sup>211, 212</sup> or catalytic substrate,<sup>213</sup> due to the possible high surface-area and concentration of O<sub>c</sub> and O<sub>t</sub> Lewis base sites. Because of this, effort was made to further characterize this phase, and remove impurities. An SEM image of phase V is presented in Figure 4.5.1.

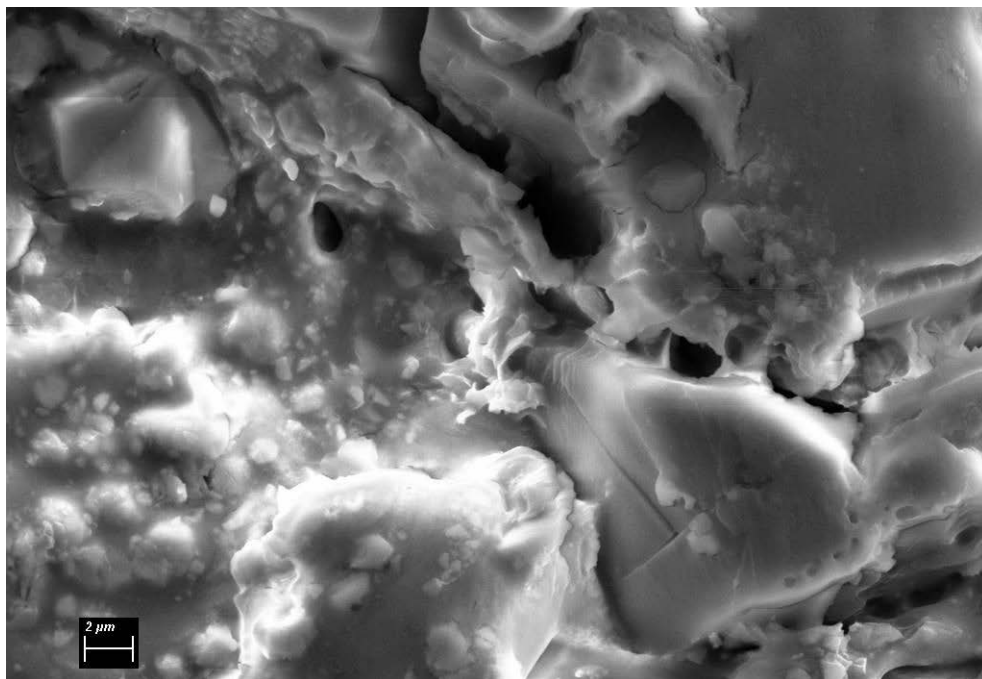


**Figure 4.5.1.** SEM image of phase V.

SEM of phase V reveals a microstructure of crystalline particulates that are dispersed in an almost featureless, much less crystalline matrix that is easily charged. Considering the TGA, Figure 4.3.1, and XRD, Figure 4.3.2, data at this decomposition temperature (300°C), the image likely reflects crystalline, hexagonally-arranged tungsten POMs that exist within a matrix of organic CTA<sup>+</sup> decomposition products, likely comprising of multiple alkane, alkene and methylated ammonium species.

#### 4.5.1 Soxhlet extraction

TGA reveals that phase V still contains a sizable organic fraction, 38.5% of the beginning (CTA- $W_{12}$ ) total organic weight by 275°C, Fig. 3.3.1. Furthermore, cracking of CTA<sup>+</sup> in CTA- $W_{12}$  occurs across the near entirety of phase V's range of stability (245 to 320°C), Table 3.4. Therefore, in order to remove non-contributing components from this material, effort was made to remove any unbound organic fraction. A Soxhlet apparatus, as described in Section 2.1, was used to do this, employing chloroform (CHCl<sub>3</sub>) as the solvent to remove any soluble organic material. By doing this, it was intended that neutral, large alkyl species soluble in CHCl<sub>3</sub>, such as hexadecene and N,N-dimethylhexdecylamine, would be removed from the sample, leaving behind only insoluble isopolytungstates and cationic methyl-ammonium. Figure 4.5.2 displays FT-IR spectra of phase V as-prepared, the insoluble portion after Soxhlet extraction and the soluble fraction that was removed in CHCl<sub>3</sub> (after CHCl<sub>3</sub> was evaporated).

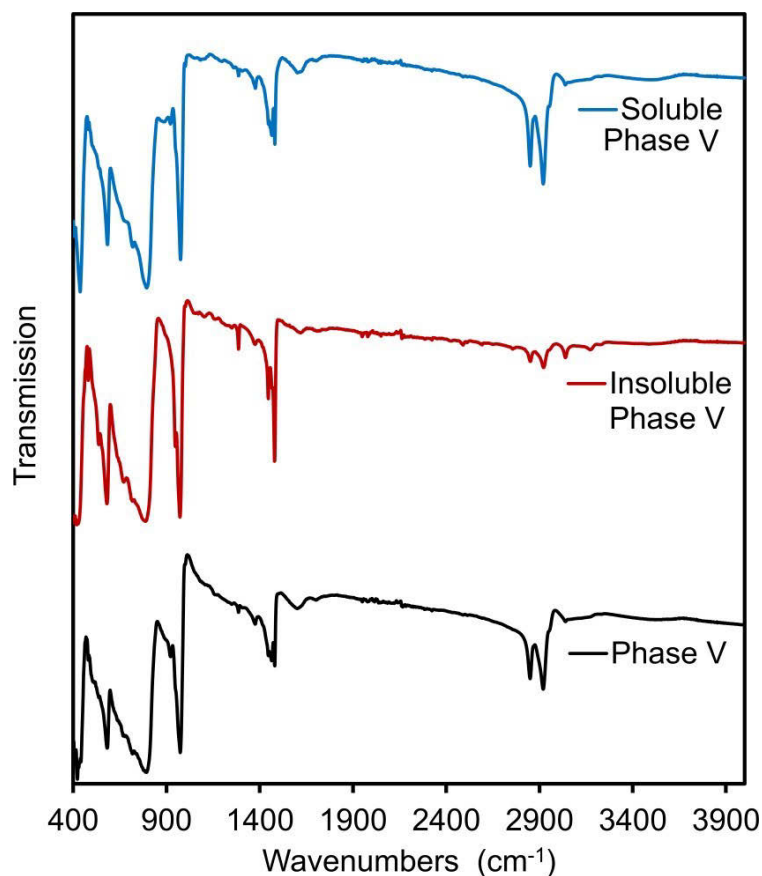


**Figure 4.5.2.** FT-IR spectra of phase V (310°C) as-prepared (-), after Soxhlet extraction (-) and the soluble fraction that was removed in CHCl<sub>3</sub> (after CHCl<sub>3</sub> was evaporated) (-).

CH<sub>2</sub> ascribable bands, such as  $\delta(\text{CH}_2)$ ,  $\nu_{\text{as}}(\text{CH}_2)$  and  $\nu_{\text{ss}}(\text{CH}_2)$  at 1464, 2850 and 2920 cm<sup>-1</sup>, respectively, are significantly diminished in the CHCl<sub>3</sub> insoluble portion after Soxhlet extraction, but increased in intensity in the portion that was soluble in CHCl<sub>3</sub>, relative to the parent phase V sample. This suggests that predominantly alkyl species, such as hexadecene and N,N-dimethylhexadecyl-amine, were removed from as-prepared phase V during Soxhlet extraction and became concentrated in the organic solvent, as intended. Furthermore, CH<sub>3</sub> and N<sup>+</sup>-CH<sub>3</sub> ascribable bands including  $\sigma_{\text{as}}(\text{N}^+-\text{CH}_3)$ ,  $\sigma(\text{CH}_3)$ ,  $\sigma_{\text{ss}}(\text{N}^+-\text{CH}_3)$  and  $\nu_{\text{as}}(\text{N}^+-\text{CH}_3)$  at 1286, 1406, 1480 and 3039 cm<sup>-1</sup>, respectively, are seen to increase in intensity within the CHCl<sub>3</sub> insoluble fraction after Soxhlet extraction, and remain within CHCl<sub>3</sub> soluble fraction. This suggests that cationic methyl-ammonium groups were not removed by CHCl<sub>3</sub>, and the concentration of such molecules increased in the CHCl<sub>3</sub> insoluble fraction as compared to the parent phase V.

<sup>1</sup>H-NMR of the CHCl<sub>3</sub> soluble fraction was collected and compared against as-prepared CTA-W<sub>12</sub> to determine what the products of thermal decomposition were by the time phase V had formed at 300°C, Figure 4.5.3.

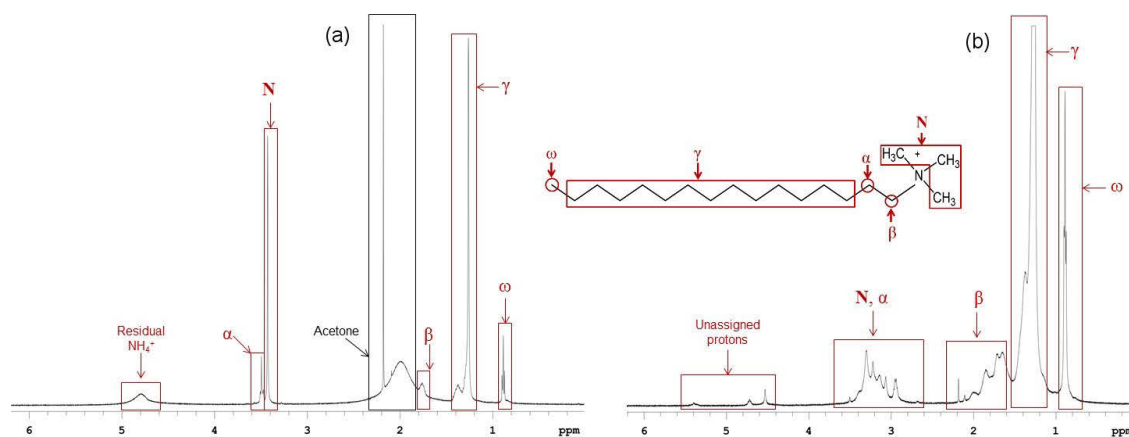


**Figure 4.5.3.** Labeled <sup>1</sup>H-NMR of (a) CTA-W<sub>12</sub> as prepared and (b) CHCl<sub>3</sub> soluble fraction of phase V (after evaporation of CHCl<sub>3</sub>) in CDCl<sub>3</sub>. **Inset:** Labeled CTA<sup>+</sup> surfactant (same as Fig. 4.2.1).

The individual chemical environments surrounding the C atoms in CTA<sup>+</sup> are easily identifiable within the <sup>1</sup>H-NMR spectrum of CTA<sup>+</sup>, Figure 4.5.3(a). Many more peaks appear

within the  $^1\text{H-NMR}$  spectrum of the  $\text{CHCl}_3$  soluble fraction of phase V, indicating significant amount of change has occurred by  $300^\circ\text{C}$ . Peaks are seen to broaden, as compared to CTA- $\text{W}_{12}$ , and become more numerous, indicating new chemical species resultant from Hoffman degeneration and cracking of  $\text{CTA}^+$ . In particular, the broadening of the  $\text{C}_\gamma$  ascribed peak indicates many differing alkyl species, and the many new  $\text{C}_\alpha$ ,  $\text{C}_\beta$  and  $\text{C}_\text{N}$  environments observed indicates significant alteration around the surfactant head-groups.

However, inorganic vibrations ( $< 1100 \text{ cm}^{-1}$ ) belonging to isopolytungstates are still predominant in the soluble fraction's spectrum, Figure 4.5.1. This suggests that a large proportion of what was dissolved in  $\text{CHCl}_3$  still contained inorganic tungstates, and did not only constitute of alkyl components.

#### **4.5.2 Analysis of fractions**

TGA was conducted on both fractions resulting from Soxhlet extraction, Figure 4.5.4, in order to determine the organic and  $\text{WO}_3$  compositions of the two fractions of phase V and further characterize structural compositions. Comparisons of the respective TGA, DTA and DTG curves were compared with CTA- $\text{W}_{12}$ , because CTA- $\text{W}_{12}$  is the precursor that transitions to the phase V compound across the sample's thermal decomposition.

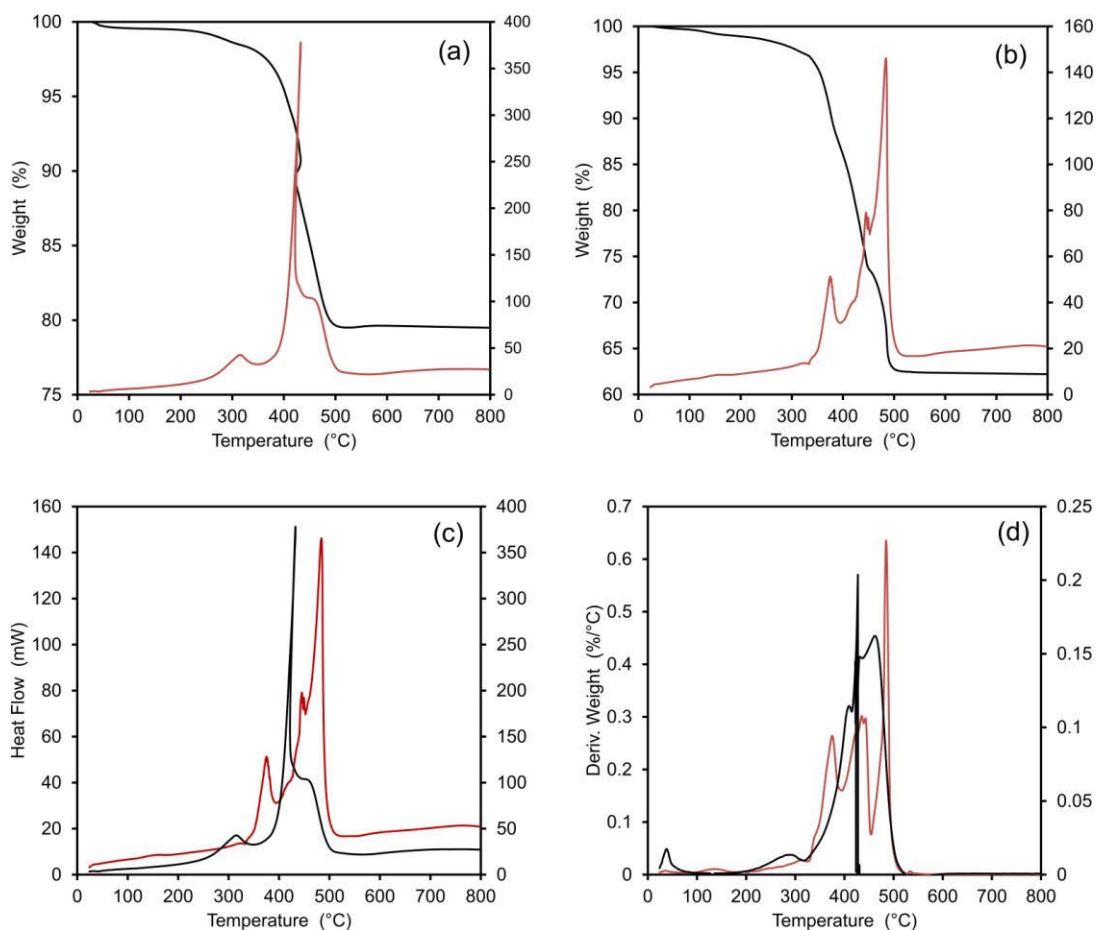


**Figure 4.5.4.** All measurements performed at a 5°C/min heating rate. TGA (-) and DTA (-) of the CHCl<sub>3</sub> insoluble (a) and soluble (b) fractions of phase V, (c) comparative DTA of insoluble (-) and soluble (-) fractions, and (d) comparative DTG of insoluble (-) and soluble (-) fractions.

All remaining mass at 800°C is ascribed to non-volatile WO<sub>3</sub> content. Mass loss at lower temperatures is ascribed to dehydration and loss of volatile organic compounds. With this in mind, TGA data of both fractions is summarized in Table 4.5.1:

**Table 4.5.1.** Comparison between volatile (organic and water) and non-volatile ( $\text{WO}_3$ ) content of  $\text{CHCl}_3$  insoluble and  $\text{CHCl}_3$  soluble fractions of phase V as measured by TGA.

<b>Fraction of Phase V</b>	<b>Volatile Content (%) (<math>\text{H}_2\text{O}</math> and Organics)</b>	<b>Non-Volatile Content (%) (<math>\text{WO}_3</math>)</b>
<b><math>\text{CHCl}_3</math> Insoluble</b>	20.6	79.4
<b><math>\text{CHCl}_3</math> Soluble</b>	37.8	62.2

Surprisingly, both fractions contain a majority weight percentage of  $\text{WO}_3$ , with a composition of 62.2 and 79.4 weight % for the  $\text{CHCl}_3$  soluble and insoluble fractions, respectively. The substantial  $\text{WO}_3$  content in both fractions likely points to presence of two separate isopolytungstate-based phases in phase V, rather than the presence of one condensed HCP phase and excluded/exterior organic decomposition products. To further clarify the chemical composition of the  $\text{CHCl}_3$  insoluble fraction, C,H&N microanalysis was conducted which revealed an organic composition of 14.84 weight% C, 2.25 weight% H and 1.68 weight% N. Combined with the TGA data, this analysis suggests an empirical formula of  $(\text{TMA})_{2.5}\text{H}_{3.5}[\text{W}_7\text{O}_{24}]$ , (where TMA = trimethyl-ammonium cation,  $\text{HN}(\text{CH}_3)_3^+$ ) combined with soft-coke residues (equivalent of  $\text{C}_{18}\text{H}_{16}$ ). Comparison between experimental microanalysis and theoretical calculations based on the formula  $(\text{TMA})_{2.5}\text{H}_{3.5}[\text{W}_7\text{O}_{24}]$  is presented in Table 4.5.2:

**Table 4.5.2.** Comparison between experimental C,H&N micro-analysis and theoretical calculations based on the empirical formula  $(\text{TMA})_{2.5}\text{H}_{3.5}[\text{W}_7\text{O}_{24}]$ .

<b>Element</b>	<b>Measured (%)</b>	<b>Theoretical (%)</b>
<b>C</b>	14.84	14.89
<b>H</b>	2.25	2.18
<b>N</b>	1.68	1.70

The inclusion of  $\text{TMA}^+$  is based upon the likely decomposition products of  $\text{CTA}^+$ , as described in Sections 4.1.3, 4.2 and 4.3.2. Justification for the assignment of acidic protons can be found within the FT-IR of phase V, Figures 4.3.3, 4.3.6 and 4.5.2, where they are attributed to the peak at  $1601\text{ cm}^{-1}$ . The C,H&N microanalysis reveals an increase in the N:H

and N:C ratios with respect to as-prepared CTA-W<sub>12</sub>, from 0.33 to 0.75 and from 0.06 to 0.11, respectively. This increase in relative N content supports the FT-IR spectra of Figure 4.5.1, and the hypothesis that [H<sub>2</sub>W<sub>12</sub>O<sub>40</sub>]<sup>6-</sup> catalyses Hoffman degeneration within CTA-W<sub>12</sub> which results in a material predominantly comprised of methyl-ammonium cations and isopolytungstates anions by 300°C (phase V). It should be stressed that assignment of the empirical formula (TMA)<sub>2.5</sub>H<sub>3.5</sub>[W<sub>7</sub>O<sub>24</sub>] is an estimate only, which provided the best fit to the combination of the TGA, microanalysis, FT-IR and NMR measurement techniques, and deviation from this stoichiometry is quite possible.

Similar to the case of CTA-WO<sub>3</sub> TGA, the insoluble fraction undergoes a dramatic mass loss event, which is centred at 427°C, and results in a large exotherm that disrupts the instrument, Figure 4.5.4(a) and (d). In order to avoid this extreme event, TGA, DTA and DTG analysis was redone on both samples at the reduced heating rate of 1°C/min (as opposed to 5°C/min), Figure 4.5.5.

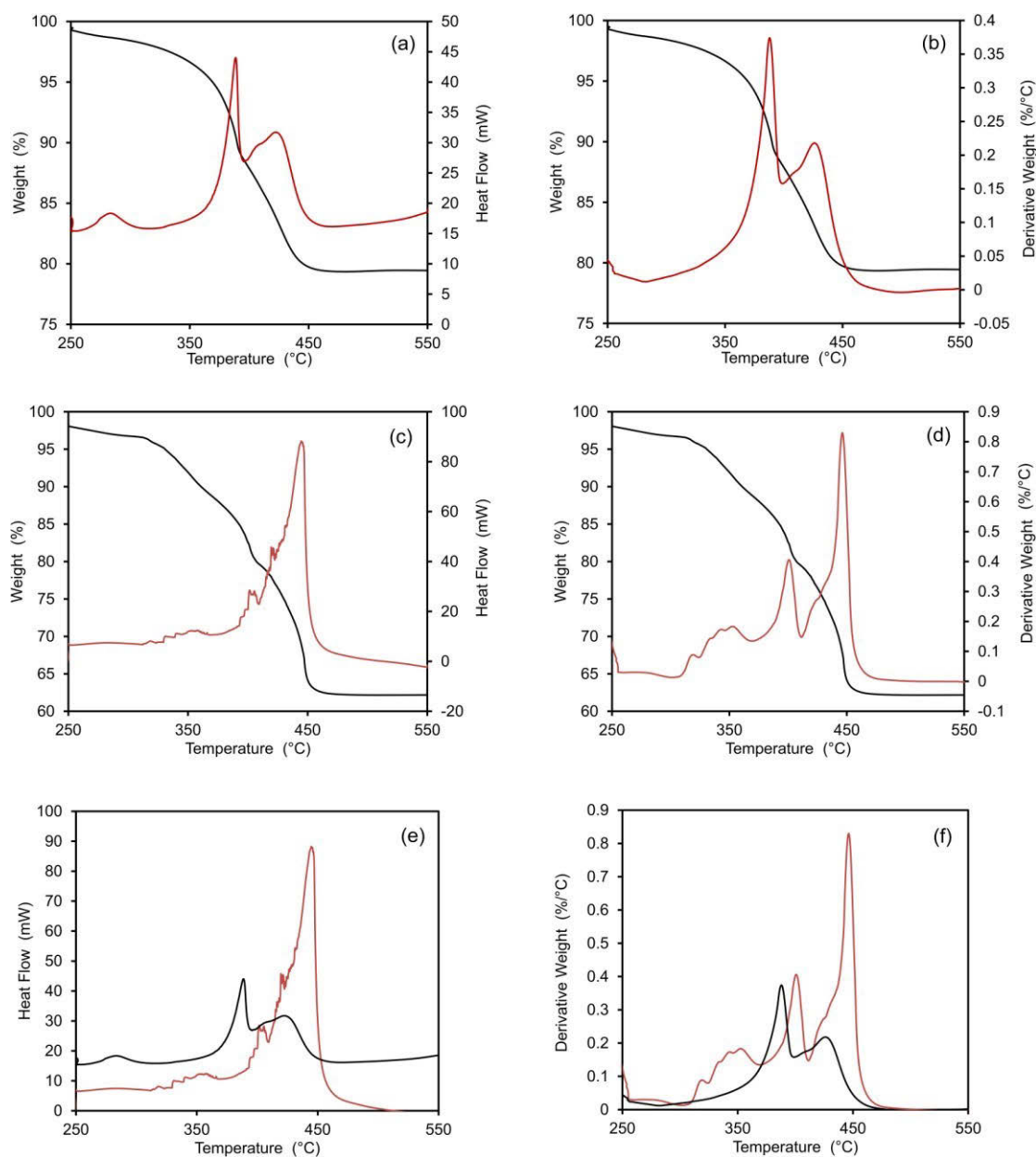


**Figure 4.5.5.** All measurements performed at a 1 °C/min heating rate. (a) TGA (-) and DTA (-) of the CHCl<sub>3</sub> insoluble fraction, (b) TGA (-) and DTG (-) of CHCl<sub>3</sub> insoluble fraction, (c) TGA (-) and DTA (-) of the CHCl<sub>3</sub> soluble fraction, (d) TGA (-) and DTG (-) of CHCl<sub>3</sub> soluble fraction, (e) DTA of the insoluble (-) and soluble (-) fractions and (f) DTG of the insoluble (-) and soluble (-) fractions.

The insoluble sample undergoes dehydration at 39 °C, which, due to the low temperature of this event, is ascribed to physisorbed water within the sample. Apart from this minor event,

no mass loss is detected within both samples until  $\sim 300^\circ\text{C}$ , which is not surprising considering the thermal histories of the samples and suggests the absence of Hoffman degeneration processes across the decomposition profile. The small exothermic mass loss centred at  $314^\circ\text{C}$ , Figure 4.5.4, within the insoluble fraction's TGA profile is attributed to cracking reactions of  $\text{CTA}^+$  decomposition products. The low amount of the cracking attributed to this event suggests a scarcity of alkyl species within the  $\text{CHCl}_3$  insoluble fraction and complements the FT-IR and C,H&N data. The sharp exotherm and associated peak in the DTG of the insoluble fraction in Figure 4.5.5 at  $388^\circ\text{C}$  (heating rate of  $1^\circ\text{C}/\text{min}$ ) corresponds to the instrument-disturbing event evident on Figure 4.5.4(a), (c) and (d) at  $427^\circ\text{C}$  (heating rate of  $5^\circ\text{C}/\text{min}$ ). Considering the derived empirical formula of the insoluble fraction,  $(\text{TMA})_{2.5}\text{H}_{3.5}[\text{W}_7\text{O}_{24}]$ , and the absence of alkyl-containing species, this large exothermic mass loss likely corresponds to the destruction of the fragmented isopolytungstates, release of constitutional  $\text{H}_2\text{O}$  and the combustion of the TMA counter-cations, similar to event 3 in  $\text{CTA-W}_{12}$  thermal decomposition at  $356^\circ\text{C}$ , Figure 4.4.4. The much steadier exothermic mass loss from  $425$  to  $520^\circ\text{C}$  at  $5^\circ\text{C}/\text{min}$ , Figure 4.5.4, and from  $397$  to  $500^\circ\text{C}$  at  $1^\circ\text{C}/\text{min}$ , Figure 4.5.5, and is therefore ascribed to oxidization of the residual carbonaceous soft-coke, similar to event 4 at  $467^\circ\text{C}$  in  $\text{CTA-W}_{12}$  thermal decomposition, Figure 4.4.4.

The  $\text{CHCl}_3$  soluble fraction undergoes dehydration from  $30$  to  $320^\circ\text{C}$ , which also likely includes loss of volatile  $\text{CTA}^+$  decomposition products. The first significant mass loss and exotherm within the  $\text{CHCl}_3$  soluble fraction is a relatively steady event and occurs from  $333^\circ\text{C}$  to  $398^\circ\text{C}$  at  $5^\circ\text{C}/\text{min}$ , Figure 4.5.4, and from  $300$  to  $372^\circ\text{C}$  at  $1^\circ\text{C}/\text{min}$ , Figure 4.5.5. Similar to the  $\text{CHCl}_3$  insoluble fraction, this first event corresponds to cracking reactions of the alkyl  $\text{CTA}^+$  thermal decomposition products. In line with the fraction's organic solubility, this event is much larger in the  $\text{CHCl}_3$  soluble fraction than the  $\text{CHCl}_3$  insoluble fraction, accounting for  $8.0\%$  mass in the soluble fraction as opposed to  $1.1\%$  in the insoluble fraction. A much sharper exothermic mass-loss then occurs at  $442^\circ\text{C}$  at  $5^\circ/\text{min}$ , Figure 4.5.4, and at  $400^\circ\text{C}$  at  $1^\circ\text{C}/\text{min}$ , Figure 4.5.5. Considering the abruptness and temperature region of the exothermic mass-loss, the event most likely corresponds to the destruction of the isopolytungstates and the combustion of the methyl-ammonium counter cations. Interestingly, the event is similar in magnitude to analogous event within the insoluble

fractions combined TGA. This is most likely explained by combustion of larger molecule weight counter-cations from less progressed CTA<sup>+</sup> decomposition products. The final and steadier exothermic mass-loss from 454 to 525°C at 5°C/min, Figure 4.4.5, and from 411 to 490°C at 1°C/min, Figure 4.5.5, is ascribed to oxidization of residual carbonaceous soft-coke. This event is much larger in magnitude as compared to the analogous event of the insoluble CHCl<sub>3</sub> fraction which reflects the much higher organic solubility of the fraction due to the presence of hydrophobic organic compounds and residues. The thermal decomposition of the CHCl<sub>3</sub> soluble fraction, and the thermal and mass loss events therein, are delayed (occur at a higher temperature) as compared to the CHCl<sub>3</sub> insoluble fraction.

Considering the moderate WO<sub>3</sub> content of the CHCl<sub>3</sub> soluble fraction of phase V, comparative P-XRD was conducted on both fractions and as-prepared phase V (without and solvent extraction), Figure 4.5.6.

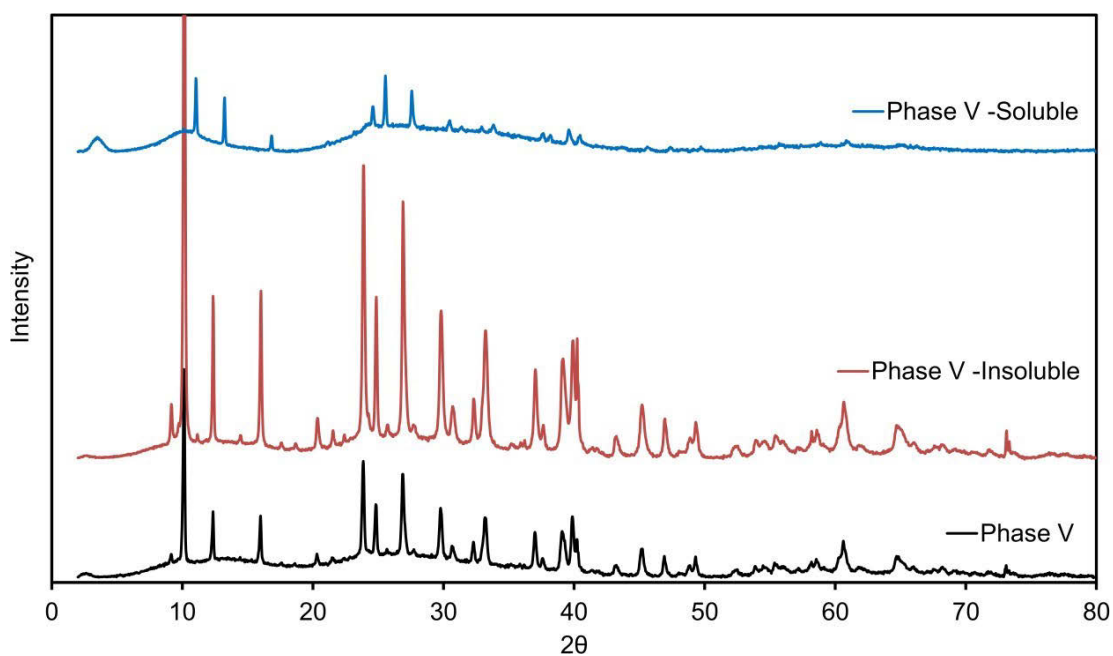


**Figure 4.5.6.** P-XRD patterns of phase V as prepared, after Soxhlet extraction with CHCl<sub>3</sub> (insoluble), and the extracted residue from the Soxhlet apparatus (after evaporation of CHCl<sub>3</sub>) (soluble).

The pattern of the CHCl<sub>3</sub> insoluble fraction closely resembles that of as-prepared phase V, although the peaks are significantly more intense suggesting the removal of portions within the parent phase V compound that do not contribute the P-XRD pattern. The pattern of the CHCl<sub>3</sub> soluble fraction is significantly different to that of phase V, however. Additionally, the pattern contains a large background signal and the peaks are significantly less intense and broader, indicating a much less crystalline material as compared to pristine phase V or the CHCl<sub>3</sub> insoluble fraction. The CHCl<sub>3</sub> soluble pattern also contains a relatively strong, broad peak centred at  $d = 25.52\text{\AA}$  which is largely absent in the insoluble fraction's pattern, although it appears as a small broad peak in the parent phase V pattern.

The above P-XRD patterns suggest that the pattern of phase V is largely formed from the more crystalline, CHCl<sub>3</sub> insoluble fraction within the material. The pattern of the CHCl<sub>3</sub> soluble fraction suggests that the extracted material, although soluble in organic solvents, is somewhat crystalline and contains a significant WO<sub>3</sub> content, supportive of FT-IR (Figure 4.5.2) and TGA (Figure 4.5.4) data. The strong, broad peak at  $d = 25.52\text{\AA}$  suggests the presence of large periodic spaces within the material, such as those created by the organization of long-chain alkyl groups, Figures 4.1.1-2. Their presence in the organically soluble fraction of phase V is not surprising considering the lipophilic properties of such molecules.

Raman spectroscopy was also conducted on the two fractions in order to further characterize the samples, Figure 4.5.7:

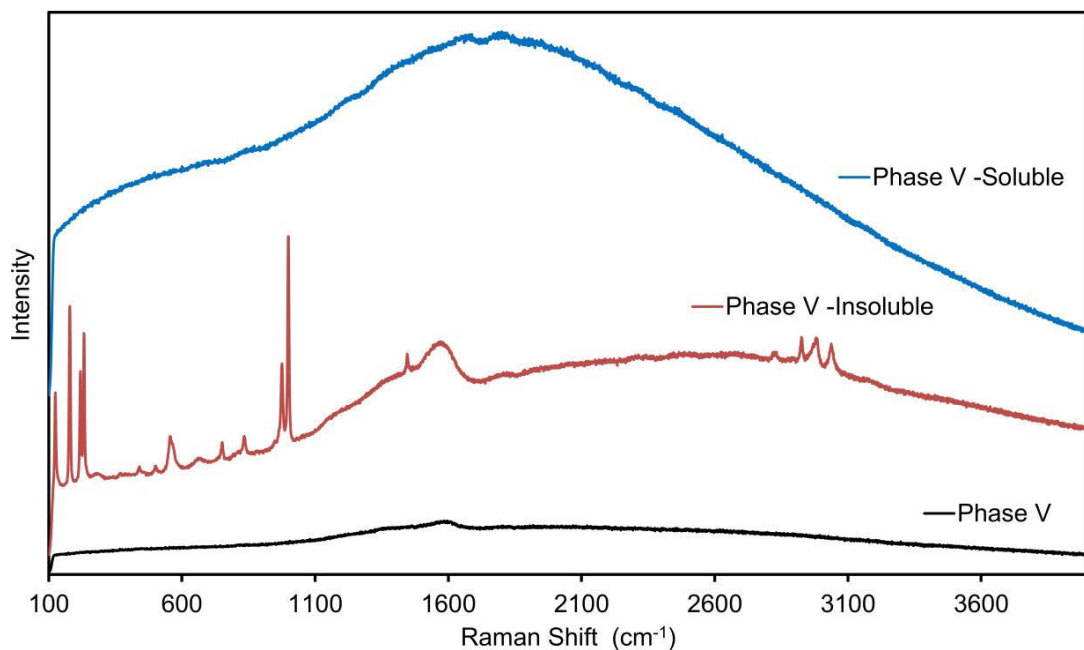


**Figure 4.5.7.** Raman spectra of phase V, phase V after Soxhlet extraction with  $\text{CHCl}_3$ , and the extracted residue (after evaporation of  $\text{CHCl}_3$ )

Broad photoluminescent (PL) signals with maxima at approximately  $1650 \text{ cm}^{-1}$  are measured by Raman spectroscopy of the parent phase V, and the  $\text{CHCl}_3$  soluble fraction. This broad emission corresponds to green - red light when adding  $1650 \text{ cm}^{-1}$ , the Raman shift, to  $633 \text{ nm}$ , the excitation energy ( $0.20 \text{ eV} + 1.96 \text{ eV} = 2.16 \text{ eV}$ ). Such strong, broad, featureless spectra are indicative of oxygen-vacancies in tungsten oxides, which inevitably contain reduced  $\text{W}^{5+}$  sites.<sup>214, 215</sup> Raman spectroscopy of the  $\text{CHCl}_3$  insoluble fraction reveals a spectrum consistent with a material consisting of isopolytungstates and methyl-ammonium cations. Bands ascribable to the vibrations of organic methyl-ammonium species appear at  $1446$ ,  $2827$ ,  $2926$ , and  $3037 \text{ cm}^{-1}$  and are assigned to  $\delta(\text{CH}_3)$ ,  $\nu_{\text{ss}}(\text{CH}_3)$ ,  $\nu_{\text{as}}(\text{CH}_3)$  and  $\nu(\text{N}^+(\text{CH}_3))$  modes, respectively. The absence of peaks that can be ascribed to  $\text{CH}_2$  suggests the removal of these species during Soxhlet extraction with  $\text{CHCl}_3$ . Interestingly, a strong broad peak is present centred at  $1569 \text{ cm}^{-1}$ . Bands within this region of Raman spectra are assigned to vibrations involving N bonded groups, namely  $\sigma(\text{N-R}_4^+)$  type deformation within quaternary amines ( $1490 - 1530 \text{ cm}^{-1}$ ) and  $\nu(\text{N-O})$  type vibrations on aliphatic nitrogen-containing compounds ( $1450 - 1575 \text{ cm}^{-1}$ ).<sup>216</sup> Clearly, due the broadness and strength of this

peak, considerable change has occurred around the cationic-nitrogens of CTA<sup>+</sup> (and its decomposition products) by 300°C.

Inorganic vibrations ascribable to W-O vibrations appear from 200 – 1000 cm<sup>-1</sup>. The  $\nu_{\text{ss/as}}(\text{W}=\text{O})$  band appears at 976 and 1000 cm<sup>-1</sup>, which is blue-shifted relative to as-prepared CTA-W<sub>12</sub> where the peak appears at 960 and 982 cm<sup>-1</sup>, Figure 3.2.1. This blue-shifting suggests a decrease in W=O bond length caused by heating to 300°C.<sup>217</sup> Such blue shifting is usually indicative of dehydration of the terminal oxygens whereby W-O<sub>t</sub>-H sites are converted to the shorter W=O<sub>t</sub> groups, via movement of the proton onto the more basic O<sub>c</sub> groups.<sup>71, 76, 208, 218-220</sup> G. Mestl *et al*<sup>71</sup> and K. Lee *et al*<sup>220</sup> also observed this dehydration and proton movement via Raman and FT-IR spectroscopy in their respective studies on the thermal transformations of Keggin anions.

#### 4.5.3 Characterization of fractions

In summary, the above FT-IR, combined TGA, XRD and Raman data suggests that phase V consists of two distinct fractions; one that contains hydrophobic alkyl groups and is consequently soluble in organic solvents (CHCl<sub>3</sub>), and another that does not contain hydrophobic alkyl groups and therefore insoluble in organic solvents. Both contain methylammonium cations and are mostly comprised of isopolytungstates, although the insoluble fraction consists of a greater WO<sub>3</sub> content. The insoluble fraction is observed to be a condensed, highly crystalline structure that is formed from hexagonally arranged isopolytungstates and is the main contributor to the XRD pattern of the parent phase V compound. The organically soluble fraction is a much less crystalline structure where the present isopolytungstates form a different arrangement, containing varied sizes of periodic spacings approximately ~25Å in size. The isopolytungstates within the soluble fraction appear to contain reduced W<sup>5+</sup> centres, whereas the insoluble fraction does not.

Further characterization of the two phases can be made by comparison of the respective FT-IR spectra, particularly in the regions containing vibrations of the isopolytungstates (400 – 1050 cm<sup>-1</sup>), Figure 4.5.8:

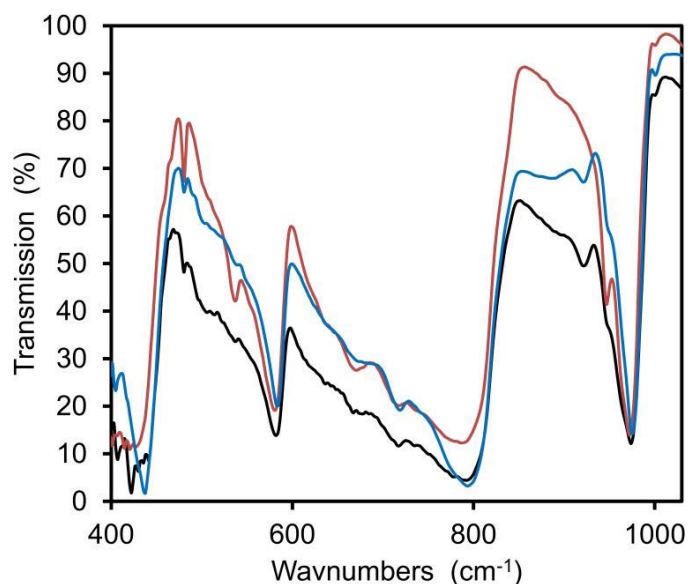


**Figure 4.5.8.** FT-IR spectra of phase V (-), and its respective  $\text{CHCl}_3$  soluble (-) and  $\text{CHCl}_3$  insoluble (-) fractions focusing on the vibrations of the inorganic isopolytungstates ( $400 - 1100 \text{ cm}^{-1}$ ).

A shoulder at  $949 \text{ cm}^{-1}$  within the  $\nu(\text{W}=\text{O})$  vibration ( $974 \text{ cm}^{-1}$ ) and a neighbouring peak at  $923 \text{ cm}^{-1}$  can be found within the FT-IR spectra of phase V and the  $\text{CHCl}_3$  soluble fraction. The neighbouring peak at  $923 \text{ cm}^{-1}$  is absent in the  $\text{CHCl}_3$  insoluble fraction's spectrum, and the shoulder at  $949 \text{ cm}^{-1}$  in the parent phase V presents as a more resolved peak. Considering the region where these vibrations manifest, the peaks and shoulders can all be ascribed to differing  $\nu(\text{W}=\text{O})$  vibrations, and hence W=O bond lengths. Differing W=O bond lengths would suggest differing isopolytungstates between the two samples. However, the peak at  $974 \text{ cm}^{-1}$  is dominant in all spectra, and therefore it can be assumed that this vibration is produced from the most abundant isopolytungstates within all of the samples. The smaller shoulder and neighbouring peaks therefore represent a minor fraction of the total isopolytungstates in both fractions.

Sparse literature exists that comments on the spectroscopies of hepta- and octa-tungstate compounds. This fact, together with the knowledge that Keggin anion fragmentation and decomposition is a statistical process, makes assignment of the individual peaks to specific isopolytungstates difficult. The  $\nu(\text{W}=\text{O})$  vibration at  $974 \text{ cm}^{-1}$  likely corresponds to either hepta- or octa-tungstate, and the smaller shoulder and neighbouring

peaks correspond to a similarly condensed (edge-sharing only) isopolytungstate with longer W=O bonds. Therefore, the CHCl<sub>3</sub> soluble fraction contains a minority portion of isopolytungstates with slightly longer W=O bonds than that of the minority portion in the CHCl<sub>3</sub> insoluble fraction. There is no proportional relationship between the size of an isopolytungstate cluster and the length of W=O<sub>t</sub> bonds, so assignment of the differing  $\nu(\text{W}=\text{O})$  vibrations to specific isopolytungstates by comparison of the band locations is not possible.<sup>221</sup> What can be concluded though is that the CHCl<sub>3</sub> insoluble fraction is at a more advanced stage of thermal decomposition than the CHCl<sub>3</sub> soluble fraction. The presence of long alkyl-chains, Figure 4.5.6, which are remnants of (or even unperturbed) CTA<sup>+</sup>, and reduced W<sup>5+</sup> centres, Figure 4.5.7, which are formed during the process of fragmentation itself,<sup>74, 222</sup> indicate that this fraction has not yet adopted the complete set of phase V characteristics as described in Section 4.3.3; a highly crystalline HCP structure formed by fragmented isopolytungstates which are charge-balanced by methyl-ammonium groups formed from CTA<sup>+</sup> degradation and cracking. The delayed combined TGA profile of the CHCl<sub>3</sub> soluble fraction as compared to the insoluble fraction further supports this. The CHCl<sub>3</sub> insoluble fraction is therefore comprised of reduced fragmenting isopolytungstates, which are ionically attached to long-chain alkyl-ammonium molecules. These anions and long-chain organic-cations pack imperfectly with hepta- or octa-tungstates and smaller methyl-ammonium molecules which form a somewhat crystalline phase, Figure 4.5.6.

#### **4.6 Conclusion: Formation of WO<sub>x</sub> from the thermal decomposition of CTA-W<sub>12</sub>**

It can be concluded from the above data and analysis of the thermal decomposition of CTA-W<sub>12</sub> that decomposition is controlled by both kinetics and thermodynamic stability. It is likely that, from the onset of CTA<sup>+</sup> degradation (~180°C), the decomposing precursor is heterogeneous, containing regions of more progressed and less progressed decomposition products. By the onset of Keggin anion fragmentation (~250°C, phase V) this inhomogeneity is so great that the decomposing precursor can be separated into two fractions based upon solubility in organic solvents (CHCl<sub>3</sub>). Perhaps this should not be surprising, since CTA<sup>+</sup> degradation and cracking, and Keggin anion thermal fragmentation/decomposition, are both kinetic processes which are heavily affected by the local environment, heating rate, heating atmosphere and degree of hydration. Differing local redox reactions at the molecular scale

between individual Keggin anions (and fragments), H<sub>2</sub>O (and H<sub>3</sub>O<sup>+</sup>) and CTA<sup>+</sup> (and CTA<sup>+</sup> degradation/cracking products) across wide temperature ranges likely result in the inhomogeneous decomposition intermediates observed in the previous section. This was directly observed in the *ex-situ* FT-IR data presented in Figure 4.3.6 where Keggin anion fragmentation to hepta- or octa-tungstates was observed to occur across a temperature range of ~60°C, as measured by the disappearing  $\nu(\text{W-O}_b\text{-W})$  peak. Further evidence of inhomogeneity within the decomposition products can be found within Figure 4.3.8, where phases V – VII are mutually present within the precursor from 300°C to ~360°C. The mutual presence of phase VII, which is the bulk sub-oxide W<sub>17</sub>O<sub>49</sub>, with phase V confirms that the non-porous bulk-oxide forms before complete organic removal. Complete removal of organic species from the precursor is only complete by ~530°C, Figure 4.3.1, a temperature at which the vast majority of the inorganic phase has already collapsed into the non-porous phases VII and VIII, Figure 4.3.8.

These findings help form a clearer picture as to why the production of highly-porous tungsten-oxides from POM-surfactant precursors seems to be a current impossibility. The kinetic nature of POM-surfactant precursor thermal decomposition processes results in the formation of an inhomogeneous material across its decomposition profile, due to differing decomposition rates and products throughout the volume of the precursor. A porous tungsten-oxide material formed from an organic-evacuated phase V would be ideal for purposes such as (photo-)catalysis. However, the temperature at which this porous phase forms is too low to allow for complete organic removal, and not sufficiently stable at higher temperatures when the organic species have completely evacuated. The reason for incomplete organic removal by the onset of phase V is obvious; the thermal stability of CTA<sup>+</sup> in CTA-W<sub>12</sub> is too high for complete degradation and volatilization by ~250°C, largely due to the strength of C-C bonds. The reasons for the instability of phase V before complete removal of the organic is more nuanced.

The transition to non-porous phase VII, W<sub>17</sub>O<sub>49</sub>, via the transient phase VI is likely related to the case of thermal and chemical instability of h-WO<sub>3</sub>. As covered in section 3.1.5, porous h-WO<sub>3</sub> collapses upon complete evacuation of cations, Figure 4.1.10, and/or at temperatures above 400°C.<sup>188, 198, 200</sup> This cation concentration-dependent stability is further evidenced in the production of WO<sub>x</sub> from the thermal decompositions of AMT and APT

where thermo-gravimetric signals of  $\text{NH}_3$ ,  $\text{NH}_4^+$  and  $\text{NO}_x$  accompany the collapse of the intermediate hexagonal phase into non-porous amorphous phases, from which bulk orthorhombic or monoclinic trioxides later crystallize.<sup>223, 224</sup> Considering the TGA, Figure 4.3.1, and XRD data, Figures 4.3.2 and 4.3.8, a similar case of cation-concentration dependent stability is likely true for phase V, where the loss of counter-cations coincides with the loss of the porous inorganic-anion structure and the formation of bulk  $\text{W}_{17}\text{O}_{49}$  sub-oxide. Moreover, the relatively dense orthorhombic phase of tungsten trioxide,  $\beta\text{-WO}_3$ , is known to be the thermodynamically stable phase of  $\text{WO}_3$  between 330 to 740°C, Figure 4.1.6, the temperature range which coincides with complete alkyl-ammonium surfactant evacuation.<sup>188</sup> Therefore, it is perhaps not surprising that the porous networks of free  $\text{WO}_6$  collapse into the more stable phase (at calcination temperatures) upon counter-cation removal.

Furthermore, organic-templated transition-metal oxide precursors are known to change oxidation state during calcination, due to redox reactions between the organic and inorganic component.<sup>225</sup> This was mutually observed in this work where reduced  $\text{W}^{5+}$  centres in the  $\text{CHCl}_3$  soluble fraction of phase V produced a broad PL emission when illuminated with 633 nm light during Raman measurements, Figure 4.5.7. Such changes in oxidation state facilitate changes in metal-oxygen coordination and hence, octahedra-octahedra coordination, thus allowing  $\text{WO}_6$  networks to transform into the various thermodynamically favourable phases across calcination temperatures.<sup>72, 79, 80</sup> Producing porous Group 5 and 6 transition-metal oxides is therefore only likely to be possible if these redox reactions are avoided, such as the case of employing weakly-bonding block-copolymers that do not interact strongly with the inorganic species upon removal under calcination.<sup>178</sup> It can be concluded then, that porous networks of crystalline  $\text{WO}_x$  challenging.

## Chapter 5. Photochromism of Quaternary Alkyl-Ammonium Polyoxometalate Hybrids

In this chapter, the photochromic properties of the simple class II surfactant-POM hybrid CTA-W<sub>12</sub> is investigated. An introduction to the topic of photochromism and the photochromism of TMO-based materials is given in Section 1.5, whilst an introduction photochromic quality and the photochromic cycle is given in Section 1.6.

Special attention is paid the quaternary-ammonium environment of the CTA<sup>+</sup> surfactant, and the changes that occur within this environment due to photochromism. The structural changes that accompany the photochromic process of surfactant-POM hybrid are also investigated here for the first time (based on my review of the current literature). The changes to CTA-W<sub>12</sub> are then analysed in order to determine the cause(s) of the photochromic material's irreversibility.

### 5.1 Background Theory

#### 5.1.1 Structure of the Keggin anion

Tungsten is a group VI transition metal with an electron configuration of [Xe]4f<sup>14</sup>5d<sup>4</sup>6s<sup>2</sup>.<sup>226</sup> Accordingly, the valence shell of tungsten is comprised of the four 5d and two 6s electrons, and hence the highest oxidation state of tungsten is W<sup>6+</sup>. In the hexavalent state W<sup>6+</sup> can form six bonds with oxygen, thus forming the familiar MO<sub>6</sub> (where M = metallic cation) octahedral motif found in many metallic oxides. These octahedra can bond together via sharing of the O<sup>2-</sup> ligands, forming planar sheets which give rise to the many WO<sub>3</sub> crystallographic phases described in Section 4.1.4. Within continuous bulk 3D WO<sub>3</sub> oxides all W<sup>6+</sup>-O<sup>2+</sup> bonds are equidistant and therefore the octahedra can be described as having an idealised O<sub>h</sub> symmetry. However, surface WO<sub>6</sub> octahedra contain monodentate O<sup>2-</sup> ligands, and hence, contracted W=O bonds terminate the surface.<sup>62, 227</sup> The contraction of the W=O bond length induces a repulsive force on the O<sup>2-</sup> ligand in the *trans* configuration relative to the W=O bond, thus elongating this bond length resulting in Jahn-Teller type distortion, Figure 5.1.1.<sup>227</sup>

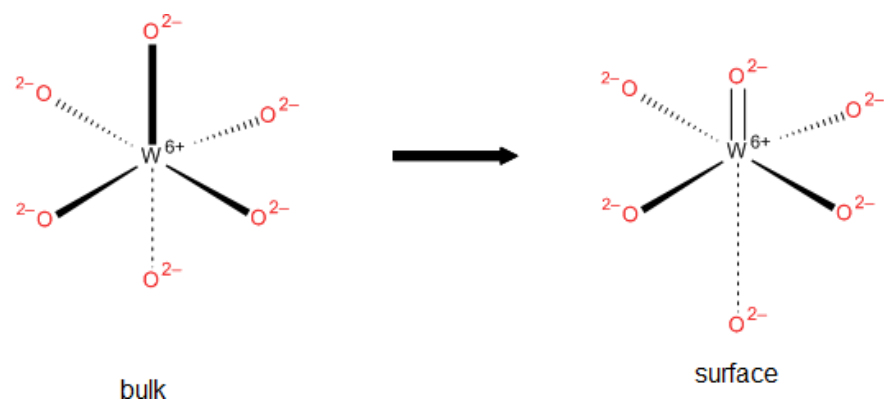


**Figure 5.1.1.** Octahedral representations of  $\text{WO}_6^{6-}$  in the bulk state with an idealised  $O_h$  symmetry (left) and at the surface with a distorted  $C_s$  symmetry (right).

These distorted surface octahedra are described as having  $C_s$  symmetry, and resemble those that which comprise polyoxometalates, which can be thought to be made out of cyclic arrangements of these distorted  $\text{WO}_6$  octahedra. However, the tight cyclic arrangements of polyoxometalates and the pseudo-spherical geometries which result require the edge-sharing of some octahedra to form the closed loops of  $-\text{W}-\text{O}-$  bonds, which is dissimilar to the case of  $\text{WO}_3$ .

By far the most studied polyoxometalate, and the one that has seen the most applications industry is the Keggin anion, which is discussed extensively in this work. This anion and its derivatives have seen numerous applications in catalytic organic oxidative reactions, medicine and chemical sensors.<sup>17, 26, 39, 71</sup> Previously discovered by J. Berzelius in 1826,<sup>228</sup> the macro-molecule is termed the ‘Keggin’ anion due to its structure being deciphered by J. Keggin in 1933.<sup>229</sup>

The anion can be thought of being comprised of comprised of four  $\text{W}_3\text{O}_{13}$  trimers, three  $\text{WO}_6$  octahedra that are intra-connected by edge-sharing oxygen bonds ( $\text{O}_c$ ) and inter-connected to other trimers by corner-sharing bonds ( $\text{O}_b$ ).<sup>227</sup> Alternatively, the anion can also described as three sets of four  $\text{W}_4\text{O}_{18}$  tetramers of corner-sharing octahedra connected to each other by edge-sharing bonds.<sup>227</sup> These four trimers or three tetramers pack together to form the familiar pseudo-spherical  $C_{4v}$  structure depicted in Figure 5.1.2.

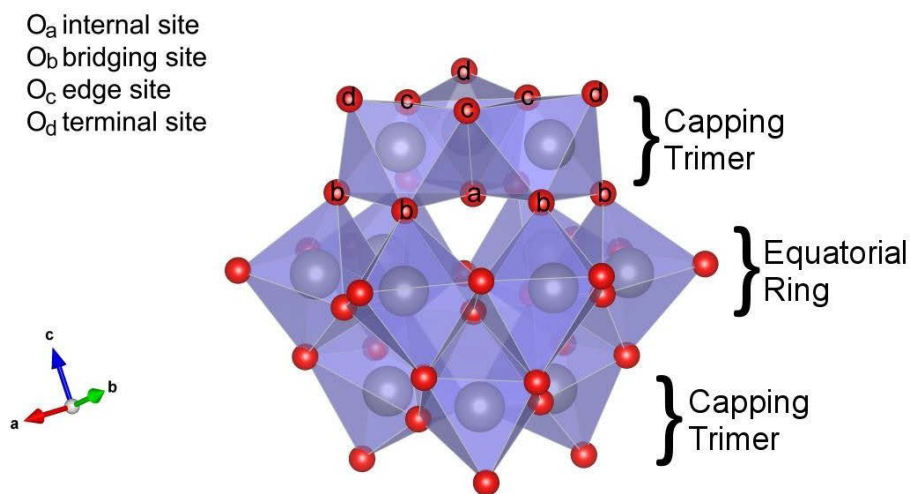


**Figure 5.1.2.** Structure of the Keggin anion depicting the edge-sharing capping trimers and the corner-sharing equatorial ring that comprise the anion, as well as the types of oxygen bonds that connect the octahedra.

Contracted W=O bonds ( $O_d$ ) terminate the surface of the anion, similar to those described previously, whilst interior oxygen bonds ( $O_a$ ) connect the  $WO_6$  octahedral cage to the interior ‘hetero-atom’.<sup>230, 231</sup> The hetero-atom, usually denoted as X is multi-valent cation, typically  $P^V$ ,  $S^{II}$ ,  $Si^{IV}$ ,  $Al^{III}$ ,  $Co^{II-III}$ ,  $Cu^{II}$  or  $H_2$ , that contributes to the anions redox properties and serves as template for the surrounding  $W_3O_{36}$  cage during synthesis from tungstate solutions. When  $H_2$  serves as the hetero-atom, the Keggin anion is termed a *metatungstate*, and the protons are non-labile (i.e. do not readily exchange). When any other cation serves as the heteroatom the anion is termed a *polyoxometalate*, although this latter term has been regularly used to describe any transition-metal oxo-anion cluster in recent times. The ability of the central  $XO_4^{n-}$  unit to change valence in response to the changing electronic charge of the outer photo-redox active W-octahedra strongly influences the redox properties of the anion and the extent to which the cluster can be reduced.<sup>230, 232</sup>

### 5.1.2 Band-gap structure of the Keggin anion

In the completely oxidized state, oxygen non-bonding 2p  $\pi$ -orbitals form the highest occupied molecular orbital (HOMO) of the Keggin anion (~95%), along with some mixing of low-lying W 5d orbitals.<sup>62, 227, 233</sup> The lowest unoccupied molecular orbital (LUMO) of the

anion largely consists of W 5d orbitals. Due to the considerable distortion of the  $\text{WO}_6$  octahedra away from the simple  $O_h$  symmetry, Figure 5.1.1, and the similar symmetry of the metallic  $d_{xy}$ -type and ligand  $\pi$ -type p-orbitals, there is increased interaction between the electron orbitals of these groups.<sup>234</sup> This interaction destabilizes the five d-orbitals that comprise the  $e_g$  and  $t_{2g}$  levels such that  $e_g$  levels are slightly increased and the the  $t_{2g}$  orbitals are further split into inequivalent states, Figure 5.1.3.<sup>62, 227, 233, 234</sup>

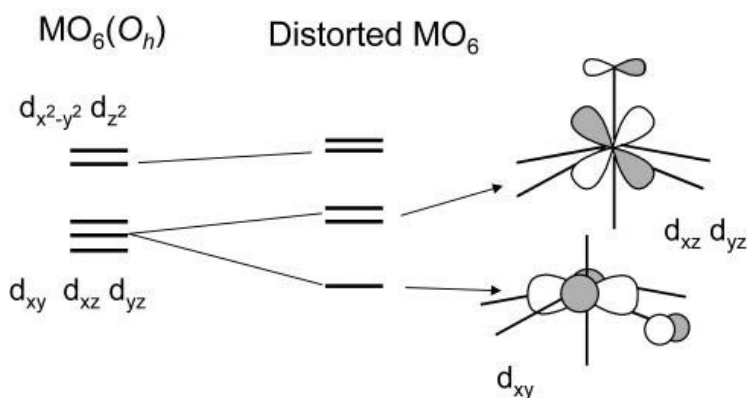


**Figure 5.1.3.** Splitting of the  $t_{2g}$  d-orbitals in Keggin and other polyoxometalates due to the distortion of  $\text{MO}_6$  octahedra away from idealised  $O_h$  symmetry (M = group 5 or 6 transition-metal).<sup>62</sup>

The splitting induced by the departure from  $O_h$  symmetry causes the metallic  $d_{xy}$  orbital to be the lowest lying metallic d-orbital in all polyanions, and hence forms the LUMO in such structures.<sup>62, 233, 234</sup> This distortion of the  $t_{2g}$  orbitals is greatest at the surface  $\text{W}=\text{O}_d$  sites, due to the significant contraction of these bonds towards the cluster, Figure 5.1.1. Because of this, the gap between the HOMO and LUMO levels of a Keggin anion is always smallest between O 2p orbitals of  $\text{W}=\text{O}_d$  bonds (HOMO) and W 5 $d_{xy}$  orbitals (LUMO) of the same octahedra. The energy gap between these two levels forms the band-gap,  $E_g$ , of a Keggin anion which and is usually on the order of 2.5 – 3.5 eV, dependent on the presence and type of hetero-atoms, counter-cations and solvents.<sup>62, 227, 233, 235</sup>

Absorption of light greater than  $\sim 3$  eV thus instigates an excitation of a high-lying O 2p HOMO electron to the W 5 $d_{xy}$  orbital, usually at a  $\text{W}=\text{O}_d$  site.<sup>58, 236</sup> This process of a transfer of charge from an oxygen ligand to a metallic cation is regularly referred to as an

oxygen-to-metal ligand-to-metal charge-transfer ( $O \rightarrow M$  LMCT) in photoelectric-based fields of study such as photo-catalysis and photochromism. The transfer of an electron ( $e^-$ ) away from the oxygen ligand results in the formation of an electron-hole ( $h^+$ ) at the photo-oxidized site. If the separation of these charges is maintained (as will be discussed in detail below) the electron within the semi-occupied W 5d orbital can undergo transition within the separated levels of the  $t_{2g}$  and  $e_g$  orbitals, thusly named d-d transitions, or exchange between neighbouring  $WO_6$  octahedra upon absorption of appropriate energy.<sup>48, 58, 237</sup>

### 5.1.3 Electronic structure of the Keggin anion

The structural stability of such large cyclic-geometries in polyanions arises from the significant mixing of metallic tungsten d-orbitals and oxygen p-orbitals across W-O bonds.<sup>170, 234</sup> The interaction between the metallic  $d_{xy}$ -type and ligand  $\pi$ -type orbitals described in the previous section culminates in mixing of the orbitals and hence (d-p) $\pi$  conjugation across W-O bonds.<sup>234, 238</sup> In addition to this, each edge-sharing  $O_c$  site possesses a lone-pair of electrons and shares  $\sigma$ -type bonds with its two W neighbours. This repeating pattern of out-of-plane  $\sigma$  and  $\pi$  orbital interactions resultant from the  $-O^{2-}-W^{6+}-O^{2-}$  closed loops, Figure 5.1.4(c), affords the ring structures considerable covalency.<sup>62, 170, 239</sup> In fact, it has been calculated that the removal of one  $O^{2-}$  from the cage of a Lindqvist anion,  $[W_6O_{19}]^{2-}$  requires  $>20$  eV.<sup>238</sup> These  $\sigma$  and  $\pi$  interactions are maximally overlapped across  $W-O_b-W$  and  $W-O_c-W$  sites. Consequently, the greater the number of these  $-O^{2-}-W^{6+}-O^{2-}$  closed loops, and the more  $\sigma$  and  $\pi$  interaction within them, the greater the stability of the polyanion. The Keggin-structure contains four of these closed-loops, Figure 5.1.4, more than any other type of isopolyanion, and is one of the reasons that the anion is the most widely used POM in research and industry today.<sup>170</sup>

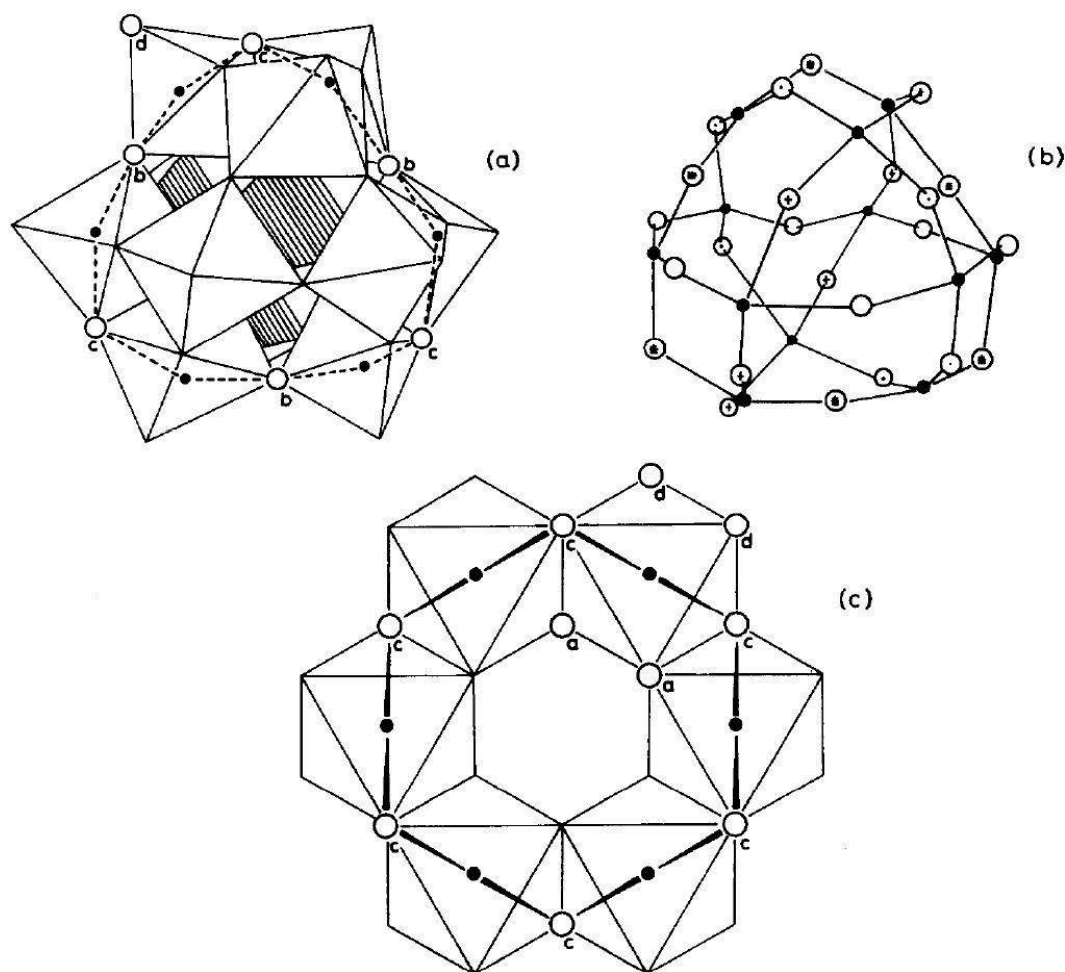


**Figure 5.1.4.** (a) Structure of the Keggin-anion, d = terminal-oxygen ( $O_d$ ), b = corner-sharing oxygen ( $O_c$ ), c = edge-sharing oxygen ( $O_b$ ). (b) ionic representation of the Keggin structure. (c) an example of one of the closed  $-O^{2-}-W^{6+}-O^{2-}$  loops formed within the anions cyclic-geometry.<sup>170</sup>

Due to the overlapping and mixing of the O 2p ligand  $\pi$ -orbitals and metallic W 5d orbitals across the  $WO_6$ -loops, electrons that are excited to the W 5d orbitals can easily be transferred between  $WO_6$  octahedra at ambient temperatures. Charge transfer across corner-sharing oxygen sites is more favourable due to the more linear W- $O_b$ -W bridges between these octahedra, thus optimizing orbital overlap.<sup>48, 240</sup> In this way reduced Keggin anions can delocalize charge across the entire six-membered octahedral ring present between the two apical trimers, Figures 5.1.2 and 5.1.4. The delocalization of charge across mixed  $d_{xy}$ -type

orbitals is the reason why the W 5d is often referred to as the *conduction band* in POM photoelectric descriptions. Additional charge is delocalized across the Keggin anion up to 6e<sup>-</sup> reduction. Beyond this stage, and up to 24e<sup>-</sup>, the additional electrons are localized within a single edge-sharing W<sub>3</sub>O<sub>13</sub> trimer (Figure 5.1.2).<sup>241, 242</sup>

W-O<sub>b</sub>-W, W-O<sub>c</sub>-W and W-O<sub>b</sub>-W-O<sub>c</sub>-W closed-loops (and combinations of them) are necessary for redox activity in polyoxometalates and isopolyanions.<sup>170, 243</sup> Polyanions without such loops, such as the Mo<sub>6</sub>O<sub>4</sub><sup>4-</sup> anion, are highly condensed and are largely intra-connected via edge-sharing and face-sharing bonds between octahedra, which mutually results in a greater number of terminal W=O<sub>d</sub> bonds per WO<sub>6</sub> octahedra. The increased number of contracted W=O<sub>d</sub> bonds results in a greater degree of distortion in the octahedra, causing the stabilized d<sub>xy</sub> orbitals, Figure 5.1.3, to be subject to a larger degree of covalent π-bonding with the W=O<sub>d</sub> ligands.<sup>170</sup> Correspondingly, no such stabilization of the d<sub>xy</sub> orbital occurs, resulting in a greatly increased E<sub>g</sub>, impeding reduction of the anion. The absence of W-O<sub>b/c</sub>-W closed loops, and the resulting (d-p)π conjugation across the connected octahedra, also prohibits delocalization of excited electrons across the anion. Delocalization mechanisms are necessary for colouration of the anion, as will be discussed in detail below, and their absence is the reason why anions that do not contain W-O<sub>b/c</sub>-W closed-loops, such as the paratungstate-A anion, [XW<sub>12</sub>O<sub>42</sub>]<sup>n-</sup> (where X = H<sub>2</sub> or relevant hetero-atom), are not photochromic.<sup>170, 243</sup>

#### 5.1.4 Photochromism of POM materials

As described in the above sections, an O→M LMCT is instigated in POMs by the absorption of above E<sub>g</sub> light, resulting in a reduced W<sup>5+</sup> centre and a h<sup>+</sup> at the photo-oxidized O<sub>d</sub> ligand. The negative charge on the reduced W<sup>5+</sup>-containing octahedra is delocalized amongst neighbouring oxygen ligands, due to the significant mixing of metallic d-orbitals and ligand p-orbitals. This increase in negative charge throughout the WO<sub>6</sub> octahedra is sufficient to attract protons hydrogen-bonded to the POM from their host molecule and form a hydroxyl bond with the O<sub>b</sub> site connected to the reduced W<sup>5+</sup> centre.<sup>48, 49, 58</sup> In organic-POM hybrids that contain alkyl-ammonium cations, this proton comes from the ammonium head-group, which then frees the N 2p\* non-bonding orbital that was previously occupied by the proton. The free N 2p\* orbital then associates with the h<sup>+</sup> at the photo-oxidized O<sub>d</sub> ligand, which

stabilizes the separation of the positive charge ( $h^+$ ) from the neighbouring reduced  $W^{5+}$  centre.<sup>48, 58, 244</sup> This stabilized excited state between the reduced POM and the oxidized organic species is aptly named the *charge-transfer complex*, Figure 5.1.5.

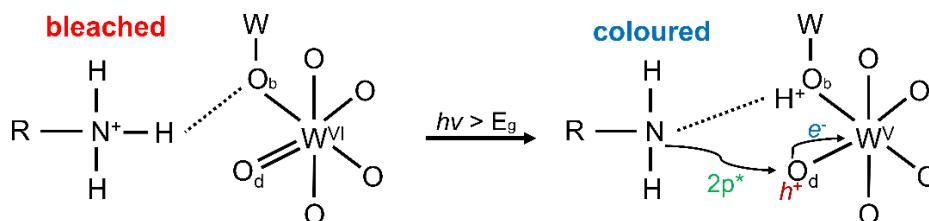
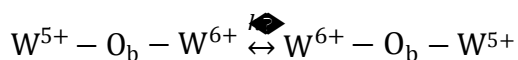


**Figure 5.1.5.** Formation of the photo-coloured charge-transfer complex from the bleached state in typical alkyl-ammonium-POM photochromic materials. R = alkyl-chain.

It is appropriate to mention here that there is another competing theory regarding the generation and stabilization of the charge-transfer-complex in POM alkyl-ammonium hybrids. This theory proposes that the  $h^+$  at the  $O_d$  site is stabilized by the transfer of a hydrogen atom from the ionically attached organic ammonium cation, thereby forming a hydroxyl group with the  $O_d$  site bonded to the reduced  $W^{5+}$  centre, and negating the need for the separation of  $h^+$  and  $e^-$  charges to be maintained by the freed N  $2p^*$  non-bonding orbital.<sup>70</sup>

As mentioned above, the (d-p) $\pi$  conjugation of the metallic d-orbitals and oxo-ligand p-orbitals allows for delocalization of electrons within these orbitals across connected corner-sharing octahedra. In this way (d-p) $\pi$  electrons can be delocalized across the Keggin anion equatorial ring, Figure 5.1.2, via ‘hopping’ of the electrons from one octahedron to another via the corner sharing ligand. This hopping process can be described as an intervalance charge-transfer (IVCT) from the reduced  $W^{5+}$  site, with the semi-occupied d-orbital as the HOMO (or valance band), to a  $W^{6+}$  where the doubly-occupied O 2p orbitals form the HOMO (or valance band).<sup>110, 233, 245</sup> The hopping process is thermally activated, and can also be instigated by the absorption of a photon at ambient temperatures ( $h\nu \approx 1-2$  eV)<sup>240, 246, 247</sup> as described in Scheme 5.1.1:



**Scheme 5.1.1**

The excited electrons within the semi-occupied d-orbitals (which comprise the majority of the (d-p) $\pi$  conjugated orbitals) can also undergo d-d transitions between the split and further distorted  $t_{2g}$  and  $e_g$  orbitals via the absorption of photons,<sup>240, 244, 248</sup> Figure 5.1.6.

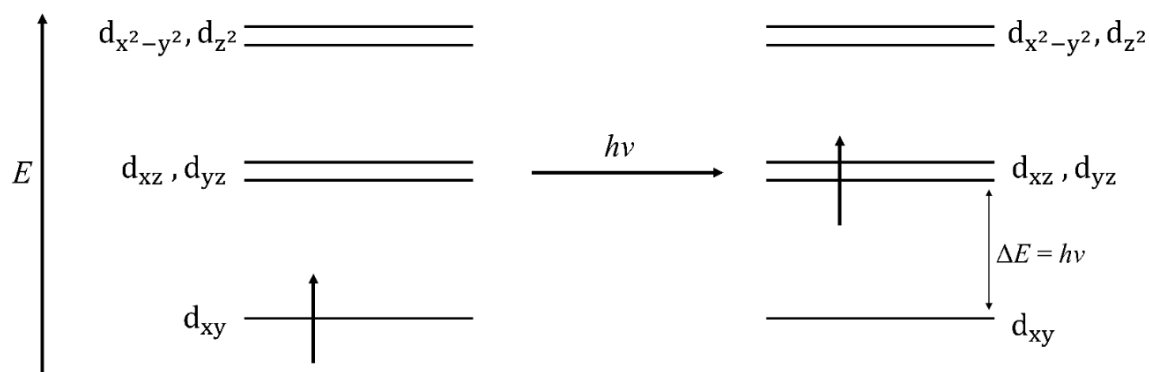
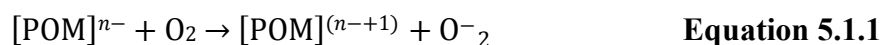


**Figure 5.1.6.** Diagram of photon absorption instigated electronic d-d transitions of excited electrons within the distorted W 5d band.

Via these excitation processes, POMs, and many other TMO-based materials can absorb incoming radiation. If this radiation is visible light, such as in the IVCT process, then these materials appear to be coloured. In the case of Keggin anions, the absorption of red and near-IR light turns materials bearing these polyanions blue. This reduction-instigated colouration is why reduced, coloured POMs are termed ‘*heteropoly blues*’.<sup>10, 248, 249</sup>

Oxidizing agents, such as peroxide,  $H_2O_2$ , and atmospheric oxygen,  $O_2$ , are able to oxidize the reduced  $W^{5+}$  centres in coloured charge-transfer-complexes by instigating a metal-to-oxygen metal-to-ligand charge-transfer ( $M \rightarrow O$  MLCT), the reverse of the  $O \rightarrow M$  LMCT excitation process.<sup>21, 73, 94, 95, 248, 250-254</sup> This causes the excited d-electrons to recombine with the  $h^+$ , and thus reducing the previously photo-oxidized  $O_d$  ligand, Equation 5.1.1.



The recombination of charges de-populates the d-band, and thus, the radiative absorption processes described previously can no longer occur, resulting in de-colouration of the material and a restoration of the material’s original state. The reliance on oxidizing agents to

reduce POMs is further confirmed by the near indefinite stability of the photo-coloured material when stored in inert atmospheres, such as N<sub>2</sub> or Ar. This reverse reaction of the colouration processes is termed *bleaching* in the study of photochromism.<sup>21, 93, 255</sup>

The light-absorption colouration followed by O<sub>2</sub> instigated bleaching is termed a materials *photochromic cycle*. The degree to which the original state of the material is restored upon bleaching and the degree to which the material colours again upon each iteration of the photochromic cycle is termed the material's reversibility or switchability. Switchability is an important property of all photochromic materials as it heavily determines the lifetime of a photochromic device. As of yet, few organic-POM materials exhibit complete reversibility, severely limiting commercial applications.<sup>58, 92, 94</sup> The reasons for this irreversibility are not yet completely understood, though authors usually cite two possible causes; unavoidable photo-redox side-reactions to the organic portion during colouration and/or bleaching,<sup>92-94</sup> or, the generation of deep W<sup>5+</sup> defect-states upon colouration such that O<sub>2</sub> is unable to diffuse and oxidize them at ambient pressures and temperature.<sup>256</sup> It is also quite possible that both of these processes occur mutually within organic-POM photochromic materials.

Slow bleaching times also disadvantage organic-POM photochromic materials, which further limits commercial viability.<sup>21, 92-95</sup> This could be due to the slow diffusion of atmospheric O<sub>2</sub> across the hydrophobic and hydrophilic spaces of POM-hybrid materials at room temperatures. Evidently, increasing the partial pressure of O<sub>2</sub>, and/or the bleaching temperature greatly accelerates bleaching times, however, such methods usually lead to decreased colouration upon subsequent photochromic cycles.<sup>21</sup>

### 5.1.5 Photocatalysis of POMs

By far the largest commercial application of POMs in industry is their use in catalysis.<sup>13, 16, 27, 37, 257, 258</sup> Not only can reduced POMs donate electrons or acidic-protons to reactions, the redox process between organic species and the anions that forms the coloured charge-transfer complexes can also be used to produce desired chemical products. The formation of the charge-transfer complex leads to the reduction of the POM due to the transfer of an electron from a suitable organic species (oxidation). With this method, oxidative homogeneous and heterogenous reactions of organic molecules can be catalysed by POMs.<sup>13, 41, 42, 257, 259</sup>

Furthermore, because these mechanisms can be instigated with UV light, many POMs and POM-hybrid systems have found further applications in photo-catalysis.<sup>14, 15, 48, 49</sup>

As detailed in the previous section, and Figure 5.1.5, the formation of the charge-transfer-complex between the POM and an organic species requires the transfer of a proton from the organic to the POM. When the proton originates from an amine group, the transfer is reversible as the primary amine (R-NH<sub>2</sub>) thus formed is stable and basic, and therefore, the ammonium amine (R-NH<sub>3</sub>) is regenerated upon oxidation of the charge-transfer-complex when the proton is transferred back. The proton-transfer reaction is still possible with any other organic proton-containing group, such as alkane (CH<sub>2</sub>), methyl (CH<sub>3</sub>), alcohol (C-OH) and hybridised carbon,<sup>42, 43, 260</sup> however, proton-transfer from these groups results in the formation of radical species (e.g. CH<sub>2</sub><sup>•</sup> from CH<sub>3</sub>), that react quickly with neighbouring molecules to form more stable groups. Also, the removal of a proton may in itself produce a stable product (e.g. C=C from CH<sub>2</sub>, and C=O from C-OH) that is unable to further accept protons. Of course, in each of these cases the proton that is removed from the parent organic molecules is the one that is most weakly attached (due to electron withdrawing neighbouring species such as N, O and halides). Via these methods, polyoxometalates are able to photo-catalyze dehydrogenation reactions of appropriate organic species with high selectivity.<sup>15, 103</sup> Furthermore, the oxidative cleavage of C-H bonds can be used in the presence of other reactive species to further produce desired molecules, Figure 5.1.7.

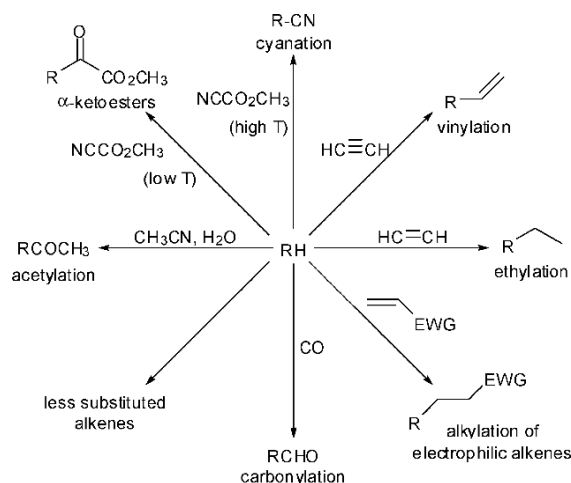
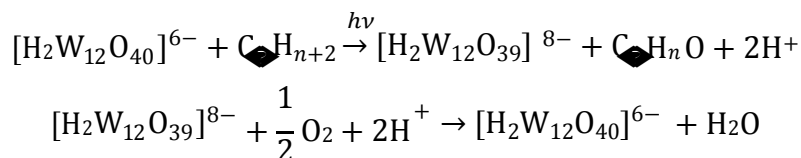


**Figure 5.1.7.** Photo-catalysed C-H bond activation-mediated reactions of organic molecules and the decatungstate anion,  $[W_{10}O_{32}]^{4-}$ . R = alkane, EWG = ‘electron withdrawing group’ (such as those containing N, O or halides).<sup>15</sup> Tzirakis, M. Lykakis, I. Orfanopoulos, M., Decatungstate as an Efficient Photocatalyst in Organic Chemistry. *Chem. Soc. Rev.* **2009**, 38, 2609–2621.

In the presence of oxidative oxygenated reactants (e.g.  $O_2$ ,  $H_2O$ ,  $OH^-$ ,  $CO$ ,  $NO_x$ ) the activation of C-H bonds produces the respective carbonyl, alkanol and peroxy species.<sup>103, 261, 262</sup> However, reactions involving atmospheric  $O_2$  as an oxygen source is uncommon, due to the prevalence of side or otherwise undesired reactions between  $O_2$  and the organic radical ( $C_nH_n^\bullet$ ). This non-selectivity with  $O_2$  can be overcome by using the POMs in a two-stage process. First, the oxidative reaction is carried out in anaerobic conditions, whereby the source of oxygen in the oxygenation reaction is the structural oxygen of the POM cluster. This of course produces oxygen-vacancies in the reduced POM which can then be re-oxidized with atmospheric  $O_2$ , thus regenerating the original POM structure and charge.<sup>103, 263, 264</sup> This two-stage *Mars-van Krevelen*-type oxidation reaction is depicted in Equation 5.1.2 using metatungstates,  $[H_2W_{12}O_{40}]^{6-}$ , and an alkane,  $C_nH_{n+2}$ , as an example.

**Equation 5.1.2.**

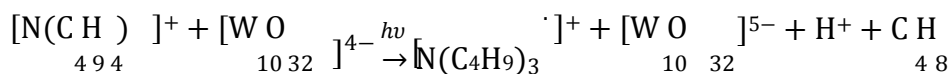


In the absence of definite weakly bound C-H sites, such as in long-chain aliphatic compounds, the location of the deprotonation site and subsequent oxygenation is more random.

### 5.1.6 Photochromism of quaternary-ammonium POM hybrids

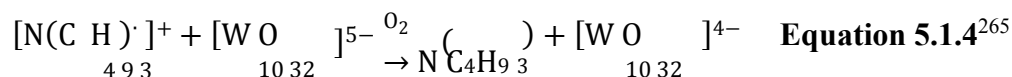
The photochromic mechanism described in Section 5.1.4, Figure 5.1.5, adequately describes the colouration of photochromic materials via the formation of a charge-transfer complex by transfer of a proton from the organic to the photo-reduced POM and the simultaneous interaction of the now free N 2p\* orbital with the  $h^+$  left at the oxidized O\* site (where the L → M IVCT took place).<sup>48, 58, 244</sup> This mechanism applies to all organic species containing labile proton transferable functional groups, e.g. R-N<sup>+</sup>-H<sub>3</sub>, whereby upon the transfer of the labile proton, a stable functional group results that is able to accept back the transferred proton upon bleaching, e.g. R-N-H<sub>2</sub>.<sup>33, 94</sup> The charge-transfer complex that is formed during quaternary-ammonium POM hybrid photochromism is, however, less understood. If the previously described mechanism is applied to this case, this would imply proton transfer from a CH<sub>3</sub> head-group or CH<sub>2</sub> tail site. However, this would not result in a free N 2p\* orbital as the long alkyl-chain and the three methyl groups surrounding the cation nitrogen would remain. The coloured charge-transfer complex must therefore arise by a different mechanism in quaternary-ammonium POM photochromic materials.

T. Yamase *et al* were the first to investigate this question in their study of the photochemistry of (TBA)<sub>4</sub>[W<sub>10</sub>O<sub>32</sub>], where TBA = tetrabutylammonium cation (N(C<sub>4</sub>H<sub>11</sub>)<sub>4</sub><sup>+</sup>).<sup>265</sup> Via employment of gas chromatography and mass spectrometry of a UV irradiated sample in a water-acetonitrile solution, the presence of 1-butene was observed, along with minor concentrations of butyraldehyde, tributylamine and dibutylamine. In light of these results, T. Yamase *et al* proposed the following photochromic mechanism of (TBA)<sub>4</sub>[W<sub>10</sub>O<sub>32</sub>] in a water-acetonitrile solution.

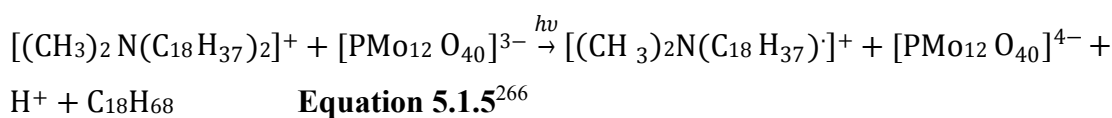


**Equation 5.1.3**<sup>265</sup>

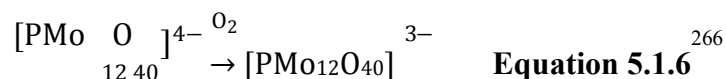
Therefore, according to this mechanism, the oxidation of TBA<sup>+</sup> due to the photoreduction of [W<sub>10</sub>O<sub>32</sub>]<sup>4-</sup> causes the removal and deprotonation of one of the quaternary alkyl groups (C<sub>4</sub>H<sub>9</sub>). This proton is then able to bond with the photo-reduced anion to form [HW<sub>10</sub>O<sub>32</sub>]<sup>4-</sup>, which is then stabilized by the newly available 2 Np\* orbital from [N(C<sub>4</sub>H<sub>9</sub>)<sub>3</sub>]<sup>+</sup>, thus forming the coloured charge-transfer complex. This complex would then bleach by electron transfer from the reduced anion to the oxidized amine, thus forming tributylamine (N(C<sub>4</sub>H<sub>9</sub>)) in support of the gas chromatography data.



The presence of butyraldehyde, C<sub>4</sub>H<sub>8</sub>O, was explained by reaction of [N(C<sub>4</sub>H<sub>9</sub>)<sub>3</sub>]<sup>+</sup> with H<sub>2</sub>O, as no butyraldehyde was detected when irradiation was conducted in the absence of H<sub>2</sub>O. Quaternary-ammonium POM photochromism was later investigated by T. Zhang *et al* in their investigation of the photo-chemical activity of (DODA)<sub>3</sub>[PMO<sub>12</sub>O<sub>40</sub>] (where DODA = dimethyldioctadecylammonium cation, [(CH<sub>3</sub>)<sub>2</sub>N(C<sub>18</sub>H<sub>37</sub>)<sub>2</sub>]<sup>+</sup>).<sup>266</sup> In this investigation (DODA)<sub>3</sub>[PMO<sub>12</sub>O<sub>40</sub>] was irradiated in the dry-state under ambient conditions, thus prohibiting side reactions with solvents as was described in the previous investigation. Similarly, T. Zhang *et al* explained the formation of the coloured charge-transfer complex by oxidation of DODA<sup>+</sup>, causing the loss of one (C<sub>18</sub>H<sub>37</sub>) side-chain and production of H<sup>+</sup>.



The bleaching reaction was described as:



It was also suggested that [(CH<sub>3</sub>)<sub>2</sub>N(C<sub>18</sub>H<sub>37</sub>)]<sup>+</sup> could undergo disproportionation, deprotonation or hydrolysis to form various products. Evidence for the production of these products was not collected however. Furthermore, FT-IR of (DODA)<sub>3</sub>[PMO<sub>12</sub>O<sub>40</sub>] was

collected on the as-prepared sample, directly after 80 minutes of UV irradiation (coloured), after 24 hrs of the coloured sample held at 70°C in air (bleached) and directly after a further 80 min of UV irradiation (re-coloured). The spectra revealed the presence of C=O and N-H after irradiation. N-H disappeared upon bleaching and re-appeared upon further irradiation, however the presence of C=O seemed to be permanent, Figure 5.1.7:.

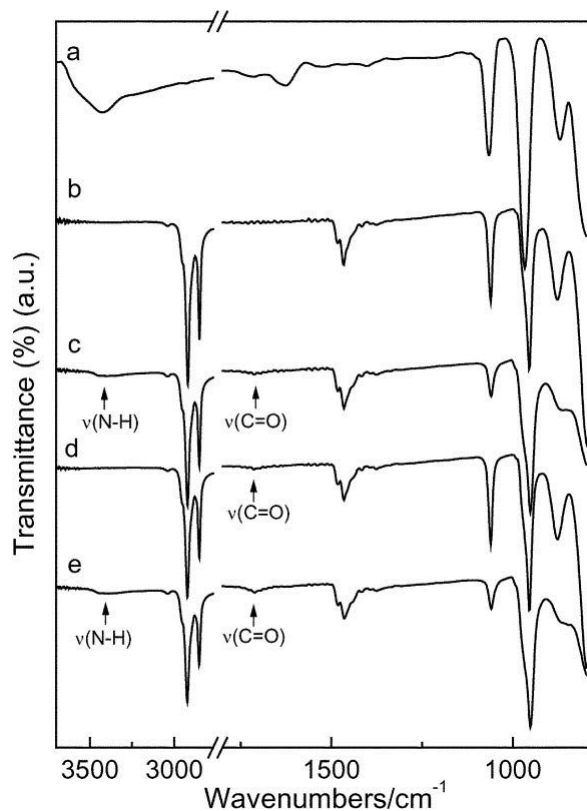


**Figure 5.1.7.** FT-IR spectra of (a)  $\text{H}_3\text{PMo}_{12}\text{O}_{40}$  polyoxometalate in a KBr pellet, (b) pristine  $(\text{DODA})_3[\text{PMo}_{12}\text{O}_{40}]$  film, (c)  $(\text{DODA})_3[\text{PMo}_{12}\text{O}_{40}]$  after 80min UV irradiation, (d)  $(\text{DODA})_3[\text{PMo}_{12}\text{O}_{40}]$  film after heating photo-coloured film at 70°C for 24hrs in air, and (e) after further UV irradiation of the bleached film for 80 min.<sup>266</sup>

Unfortunately, the presence of these species was not further explained, only referred to as ‘oxidation of DODA’, and were not referred to during the explanation of the photochromic mechanism from which Equations 5.1.5 and 5.1.6 were formulated. However, it is highly likely that the observed C=O species originated from either a Mars-van Krevelen-like mechanism described above, or, oxidation of a carbo-cation radical by  $\text{O}_2$ . Furthermore, the

possibility of methyl,  $\text{CH}_3^+$ , removal from the oxidation of DODA was also not considered. The understanding of quaternary-ammonium POM photochromism therefore seems to be incomplete and further study into the possible colouration mechanisms and resulting products is warranted.

## **5.2 Photochromism of CTA- $\text{W}_{12}$**

Above band gap irradiation of CTA- $\text{W}_{12}$  instigates an  $\text{O} \rightarrow \text{M}$  LMCT, as described in Section 4.1.2, from the HOMO which is mainly comprised of O 2p orbital to the LUMO which is mainly comprised of W 5d orbitals. The charge-transfer reduces a tungsten centre within the POM,  $\text{W}^{6+} \rightarrow \text{W}^{5+}$ , leaving a  $h^+$  at the oxygen ligand from where the  $\text{O} \rightarrow \text{M}$  LMCT took place. Proton-transfer from a suitable species to an  $\text{O}_b$  site of the photo-reduced octahedron containing the  $\text{W}^{5+}$  defect stabilizes the separation of charges. The electron within the singly populated W 5d can further undergoes IVCT and d-d transitions via the adsorption of red and NIR light, thus causing reduced CTA- $\text{W}_{12}$  to appear blue. Exposure of coloured CTA- $\text{W}_{12}$  to oxidizing environments causes the back-reaction of the previously described mechanism, depopulating the W 5d band and bleaches the material back to white, thus completing the photochromic cycle. The photochromic mechanism and cycle of CTA- $\text{W}_{12}$  was studied in detail in the present PhD and analysis and discussion is presented below.

### **5.2.1 Colouration of CTA- $\text{W}_{12}$ in alcohols**

CTA- $\text{W}_{12}$  in MeOH presents as a white/colourless suspension of fine particles. UV-vis of the as-prepared suspension reveals the location of the band-edge at 345 nm and displays no absorbance bands in the visible region, Figure 5.2.1. UV irradiation of CTA- $\text{W}_{12}$  in the presence of MeOH causes a slight blue-shift of the band-edge to 330nm and the formation of two broad absorbance bands centred at 624 and 877nm, thus turning the sample blue, Figure 5.2.1(insert). Irradiation in the presence of other primary alcohols such as EtOH produced the same results.

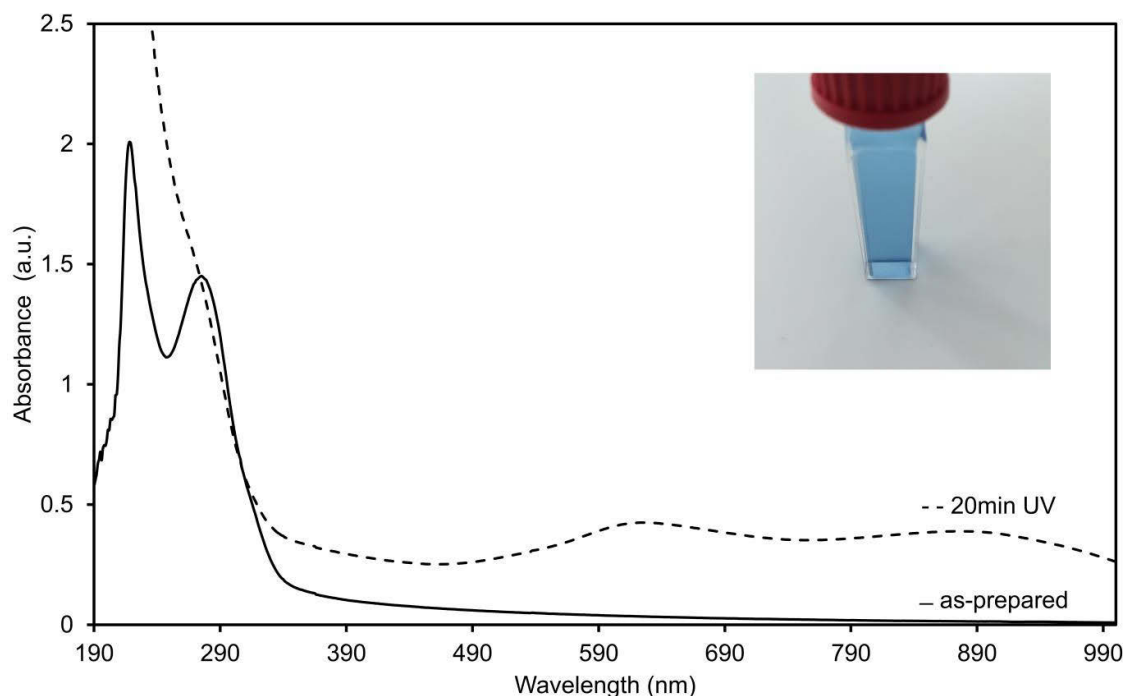
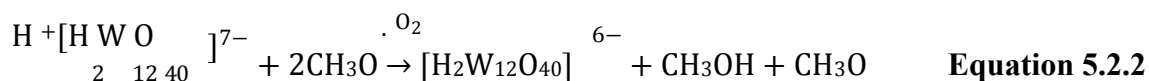
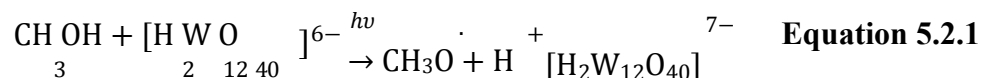


**Figure 5.2.1.** UV-vis spectra of CTA-W<sub>12</sub> in MeOH as-prepared and after 20min of UV irradiation. **Insert:** Quartz cuvette containing the described photo-reduced CTA-W<sub>12</sub> in MeOH.

The increase in absorption between 190 and ~300 nm is assigned to d-d transitions of excited electrons between the distorted, split  $t_{2g}$  and  $e_g$  levels within the semi-occupied W 5d band, Fig. 4.1.6. The broad bands at 624 and 877 nm are assigned to IVCT between corner-sharing octahedra, scheme 4.1.

Exposure of the photo-coloured suspension to air caused the suspension to revert back to white/colourless. Considering the proton-transfer mediated mechanism of POM photochromism,<sup>48, 265</sup> the colouration and decolouration of CTA-W<sub>12</sub> in MeOH is explained in Equations 5.2.1 and 5.2.2:



Introduction of H<sub>2</sub>O into the cuvette containing the CTA-W<sub>12</sub> and MeOH suspension decreased the degree of colouration upon irradiation proportional to the amount of H<sub>2</sub>O added. Irradiation of solely CTA-W<sub>12</sub> and H<sub>2</sub>O suspensions did not result in any colouration. This inhibition is due to the oxidation potential of H<sub>2</sub>O being greater than the reduction potential of [H<sub>2</sub>W<sub>12</sub>O<sub>40</sub>]<sup>6-</sup>.<sup>267</sup>

### **5.2.2 Colouration of CTA-W<sub>12</sub> in air**

UV-vis reflectance spectra of dry CTA-W<sub>12</sub> powder dispersed on a glass-slide is predominantly flat across the visible range, in accordance with the observed white/colourless colour, Figure 5.2.2. Upon incidence of above band-gap irradiation in the dry-state CTA-W<sub>12</sub> also undergoes a colour change from white/colourless, Figure 5.2.2, which is due to the formation of a broad absorbance band centred at 783nm with prominent shoulder at 645nm.

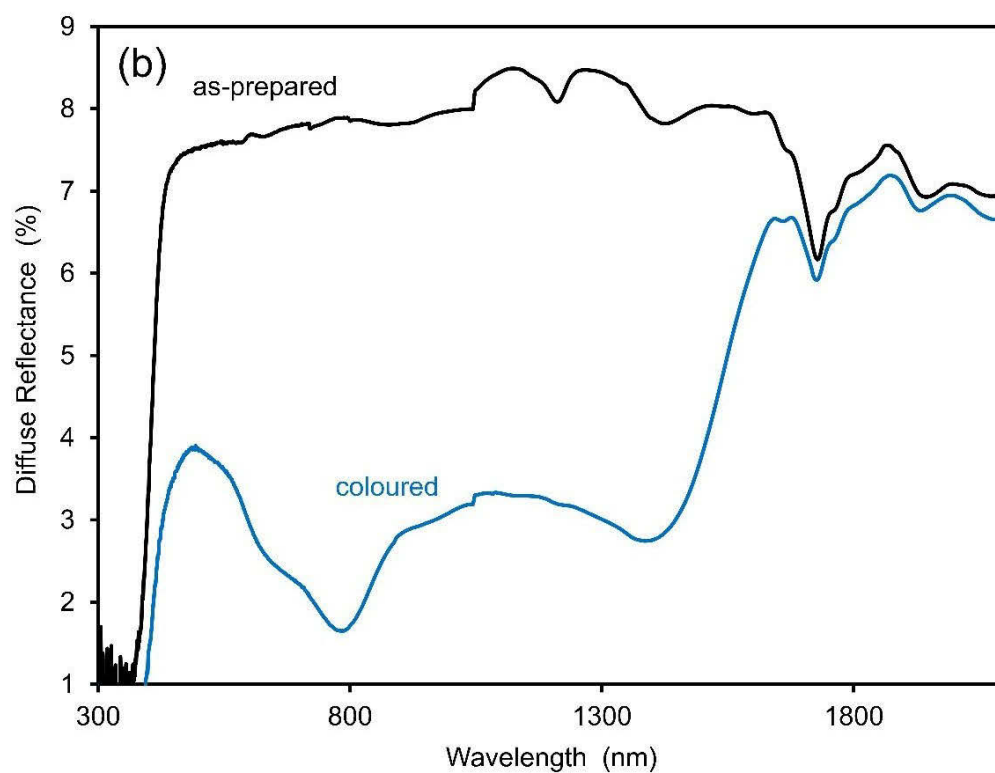


**Figure 5.2.2.** (a) CTA- $W_{12}$  particles directly after incident irradiation of UV displaying the coloured (blue) and as-prepared/bleached (whit/courless) states. (b) UV-vis reflectance spectra of CTA- $W_{12}$  as prepared and after 1hr of UV irradiation.

CTA-W<sub>12</sub> colours fairly quickly with the majority of colour change occurring during the first hour of exposure, with incremental increases in absorbance (or decreases in reflectivity) occurring up to 2 hrs, Figure 5.2.3(a). Colouration saturates at 2 hrs with little change in reflectivity occurring beyond this exposure time.

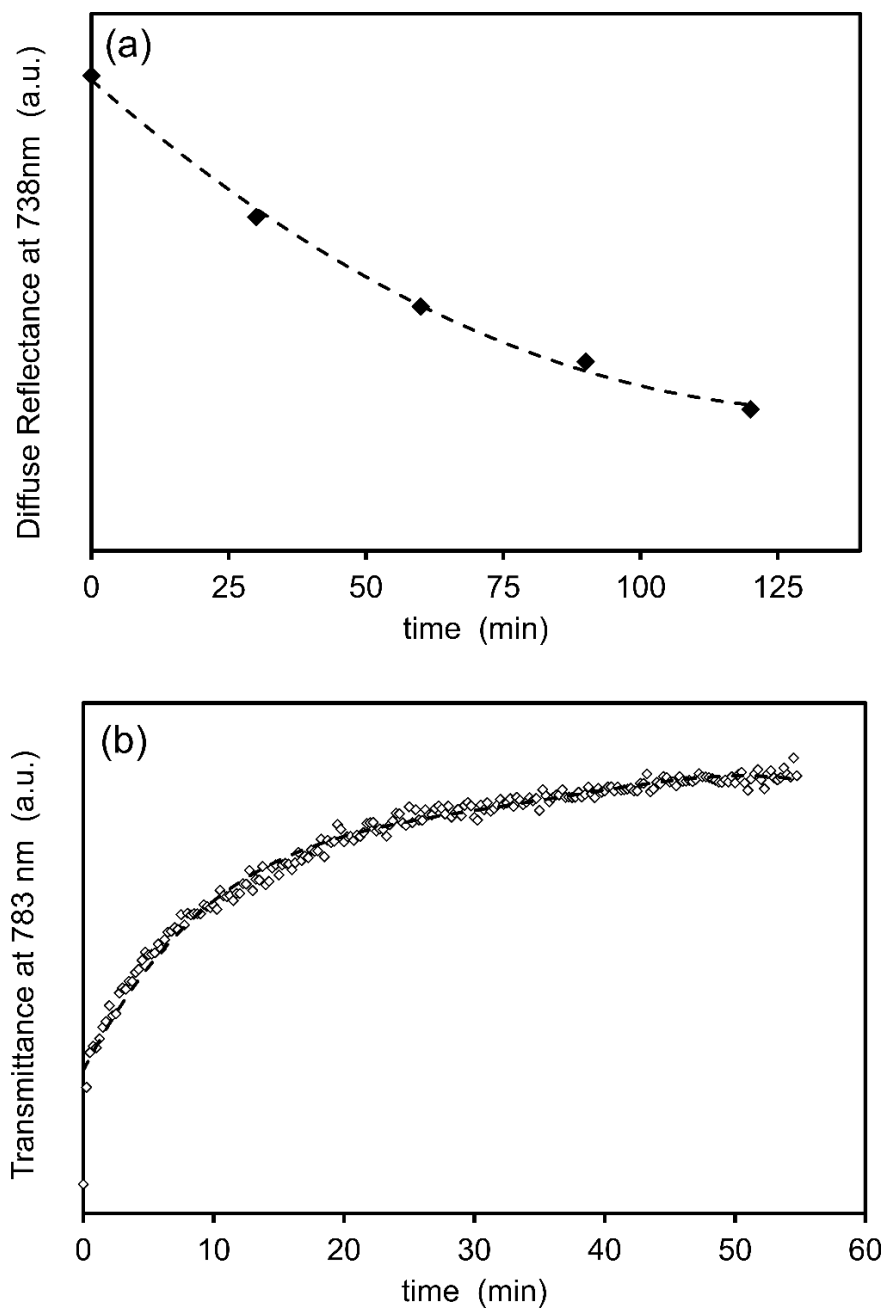


**Figure 4.2.3.** (a) Colouration rate of CTA-W<sub>12</sub> displayed as diffuse reflectance vs UV exposure time, and (b) bleaching rate of coloured CTA-W<sub>12</sub> (from 2 hrs UV exposure).

The rate of photo-colouration and bleaching can be modelled using the empirical relationship.

$$y = a + b \cdot e^{-ct} \quad \text{Equation 5.2.3}$$

Where  $y$  is the diffuse reflectance or transmittance at time  $t$  in seconds,  $c$  is the rate of change in 1/seconds while  $a$  and  $b$  account for the scaling of the vertical axis. The characteristic time constant,  $t_{1/2}$ , the halfway complete time for the process can be obtained from.

$$t_{1/2} = \frac{\ln(2)}{c} \quad \text{Equation 5.2.4}$$

The value of  $c$  for photo-colouration is  $5 \pm 3 \times 10^{-4} \text{ s}^{-1}$ , which corresponds to a  $t_{1/2}$  of about 1400 seconds, Figure 4.2.3(a). The  $c$  value for bleaching is about  $6 \pm 1 \times 10^{-4} \text{ s}^{-1}$ , corresponding to a  $t_{1/2}$  of about 1500 seconds. Of course, the values found here are highly dependent on our experimental set-up, such as the photon flux and energy of the UV lamp during photo-colouration, and the temperature and humidity of the room during bleaching. The long  $t_{1/2}$  value is attributed to the slow diffusion of  $\text{O}_2$  across the hydrophobic and hydrophilic layers,<sup>93, 250, 268</sup> as has been found previously for similar photochromic materials.<sup>21, 93</sup>

### 5.2.3 XPS of CTA-W<sub>12</sub>

XPS was conducted on CTA-W<sub>12</sub> as-prepared and after 3hrs of UV irradiation, Figure 5.2.4.

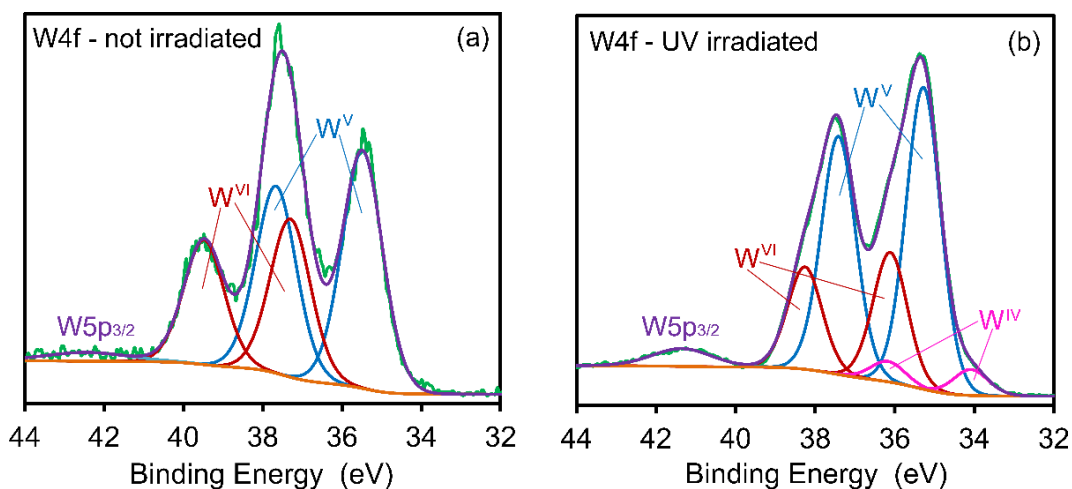


**Figure 5.2.4.** XPS of CTA- $W_{12}$  as-prepared (a) and directly after 3 hrs of UV irradiation (b).

As-prepared (not irradiated) CTA- $W_{12}$  exhibits strong signals assigned to  $W^{VI}4f_{7/2}$  and  $W^{VI}4f_{5/2}$  orbitals ( $W^{6+}$ ) at 37.28 and 39.48 eV, respectively, which represent 40% of all tungsten centers in the measured sample. Signals assigned to  $W^V4f_{7/2}$  and  $W^V4f_{5/2}$  orbitals ( $W^{5+}$ ) are also present and appear at 35.48 and 37.68 eV, respectively, accounting for 60% of all tungsten centers measured. The  $W5p_{3/2}$  satellite appears at 42.59 eV. The presence of the large  $W^{5+}$  concentration in the ‘not-irradiated’ sample is attributed to photoreduction of tungsten sites by incident x-rays from the instrument before the presented W4f spectrum was collected. X-ray induced reduction by measurement techniques is a well-known phenomenon in the study of organic-inorganic hybrids, and could have easily occurred in CTA- $W_{12}$  during initial survey scans.<sup>26,27,29,32</sup>

After exposing the material to UV light for 3 hours, a significant decrease in the intensity of the  $W^{VI}4f_{7/2}$  and  $W^{VI}4f_{5/2}$  peaks ( $W^{6+}$ ) is observed, from 40.0% to 28.4%, together with an increase in the intensity of the  $W^V4f_{7/2}$  and  $W^V4f_{5/2}$  signals ( $W^{5+}$ ), from 60.0% to 66.0%. The locations of the peaks are also seen to decrease in binding-energy once irradiated, with the  $W^{VI}4f_{7/2}$  and  $W^{VI}4f_{5/2}$  peaks shifting to 36.18 and 38.28 eV, respectively, and the  $W^V4f_{7/2}$  and  $W^V4f_{5/2}$  peaks shifting to 35.28 and 37.43 eV, respectively, post irradiation. Peaks at 34.08 and 36.23 eV are also apparent in the irradiated sample and are assigned to  $W^{IV}4f_{7/2}$  and  $W^{IV}4f_{5/2}$  states, respectively, accounting for 5.7% of tungsten centers measured.<sup>21, 269-272</sup>

The increase of  $W^{5+}$  and  $W^{4+}$  states at the expense of  $W^{6+}$  states is in accordance to with the photochromic mechanism of tungsten oxides, including isopolytungstates, as described in Section 5.1.4.<sup>73, 272, 273</sup> An increase in reduced  $W^{5+}$  and  $W^{4+}$  concentrations leads to a greater amount of IVCT processes,  $(W^{5+}-O_b-W^{6+}) \rightarrow (W^{6+}-O_b-W^{5+})$ , and d-d transitions within the semi-occupied W 5d orbitals, occurring in the sample, thus coloured the material.

### **5.3 Reversibility of CTA- $W_{12}$ photochromism**

CTA- $W_{12}$  photochromism is not completely reversible and the compound does not completely revert back to the as-prepared state by bleaching under dark ambient laboratory conditions, Figure 5.2.2, as measured by UV-vis reflectance. However, this incompletely bleached CTA- $W_{12}$  is still able to colourize to the same extent as the first instance of colourization, Figure 5.3.1.

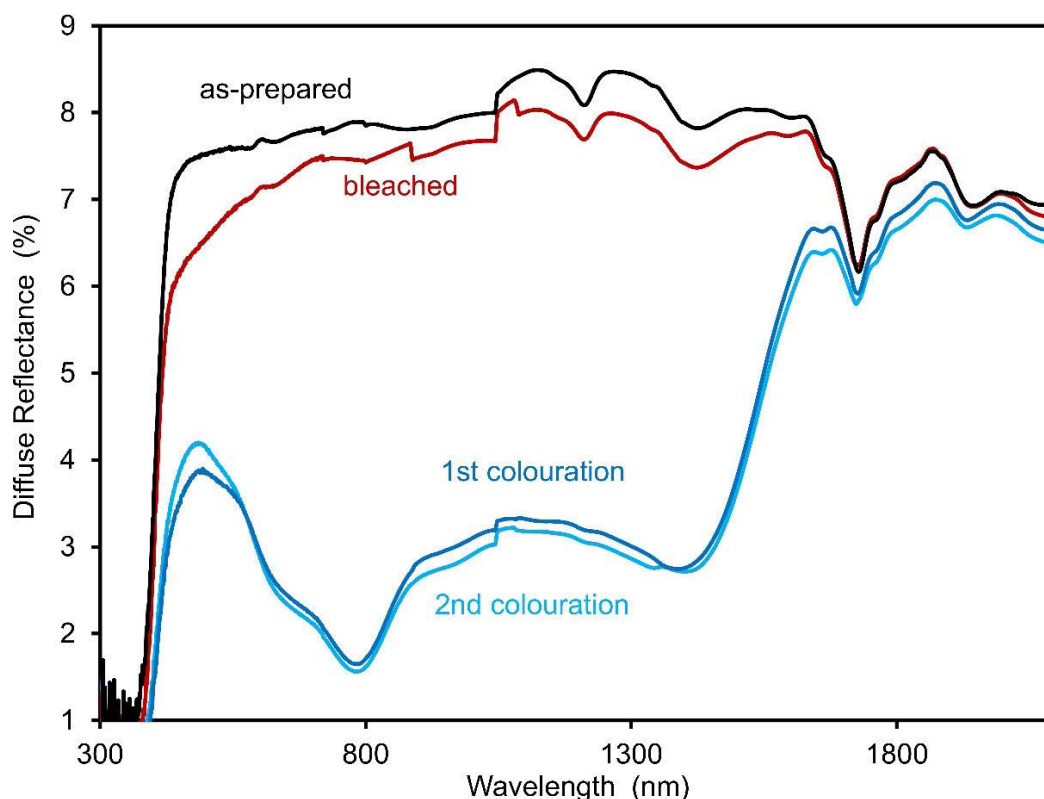


**Figure 5.3.1.** UV-vis reflectance spectra of CTA- $W_{12}$  as-prepared, directly after 1hr of UV irradiation (1<sup>st</sup> colouration), bleached (48 hours in dark ambient) and after a subsequent 1hr of UV irradiation (2<sup>nd</sup> Colouration).

Due to this irreversibility, a hysteresis study along with measurements to probe the chemical changes of CTA-W<sub>12</sub> during photochromism was conducted in order to determine the permanent changes to the material upon each cycle.

### 5.3.1 Hysteresis study of CTA-W<sub>12</sub> photochromism

The methodology of the hysteresis study is outlined in Section 2.1.12, and the results are depicted in Figure 5.3.2:

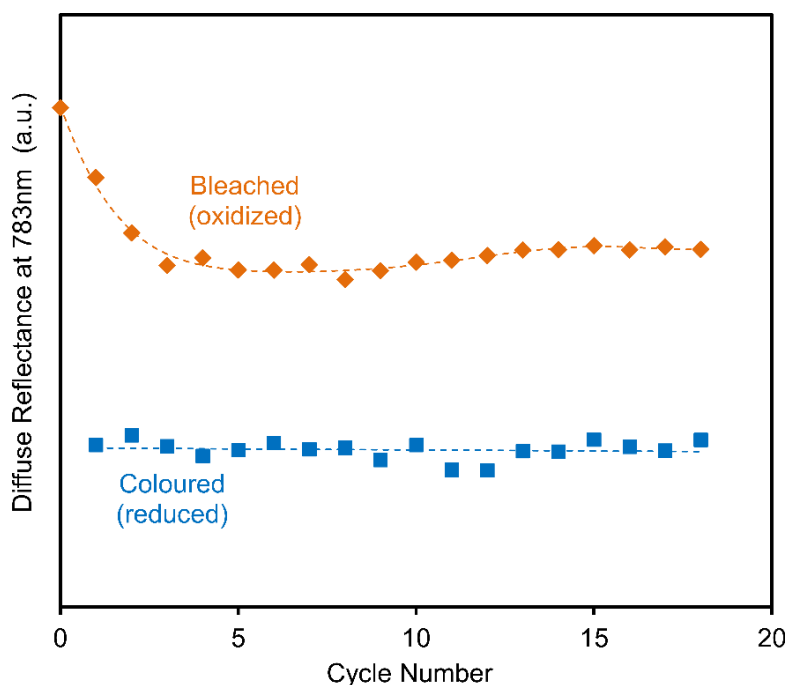


**Figure 5.3.2.** Hysteresis study of CTA-W<sub>12</sub> photochromism. Coloured measurements are conducted directly after 2hrs of UV irradiation. Bleached measurements are conducted 48hrs after UV irradiation.

The reflectance of the bleached state, and the change in reflectance,  $\Delta R$ , upon colouration decreases for four photochromic cycles until which no further decrease in reflectance or  $\Delta R$  is measured (for the 18 cycles measured). Conversely, the reflectance of the coloured state remains stable across the entire hysteresis study.

This indicates that for four photochromic cycles, or a total of 8 hours of UV irradiation, permanent changes accumulate in CTA-W<sub>12</sub> that have a detrimental effect on the photochromic performance of the material ( $\Delta R$ ). However, these changes are only seen to affect the reflectance of the bleached state, and CTA-W<sub>12</sub> is seen to produce the same coloured state upon each iteration of the photochromic cycles, or at least for 18 cycles. Considering the above performance, CTA-W<sub>12</sub> could be placed into the ‘semi-reversible’ photochromic category as performance is maintained beyond four cycles.

### **5.3.2 Chemical changes to CTA-W<sub>12</sub> during photochromism**

XPS, FT-IR and Raman spectroscopy was employed to probe the possible chemical changes in CTA-W<sub>12</sub> that causes the permanent change in  $\Delta R$ . XPS spectra of the organic species in CTA-W<sub>12</sub> before and after UV irradiation is displayed in Figure 5.3.3:

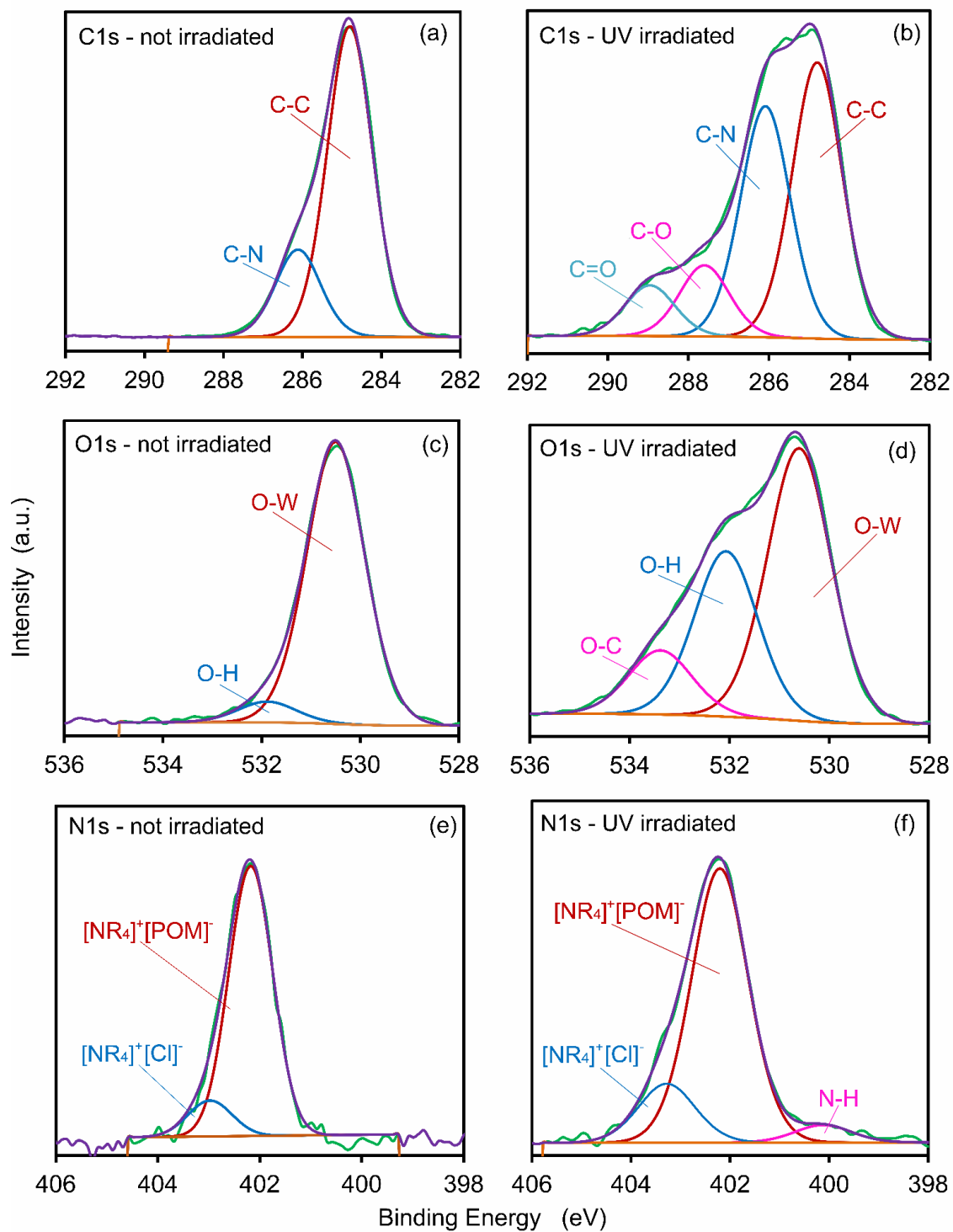


**Figure 5.3.3.** XPS spectra of CTA- $\text{W}_{12}$  showing binding energies for C1s energy levels in (a) un-irradiated and (b) UV irradiated (3hrs) material, O1s energy levels in (c) un-irradiated and (d) UV irradiated, and N1s energy levels in (e) un-irradiated and (f) UV irradiated.

Two carbon environments are apparent within the C1s spectrum of as-prepared CTA-W<sub>12</sub>, Figure 5.3.3(a). These correspond to carbon atoms within the methyl-groups that are attached to the cationic-nitrogen head-groups of CTA<sup>+</sup>, C-N, and to carbon atoms within the alkyl-chains, C-C, at 286.1 and 284.8eV, respectively.<sup>161, 274</sup> Upon irradiation, two new bands appear in the C1s spectrum, Figure 5.3.3(b), centered at 288.98 and 287.58eV, which are assigned to carbon atoms in C=O and C-O groups,<sup>275</sup> respectively. Thus, upon irradiation, some degree of oxidation of the carbon atoms in the CTA<sup>+</sup> group occurs. Two bands in the O1s spectrum of as-prepared CTA-W<sub>12</sub>, Figure 5.3.3(c), are assigned to oxygen atoms located within the Keggin anion, O-W, at 531.88 eV, and adsorbed moisture or protonated octahedra, O-H, at 530.48 eV. A new band emerged in the spectrum of the irradiated material, Figure 5.3.3(d), at 533.38eV, and is assigned to oxygen bonded to carbon.<sup>254</sup> This is consistent with the C1s spectrum that shows formation of C=O and C-O groups. The intensity of the band assigned to O-H groups increased upon irradiation, which is consistent with the proton-transfer mechanism of photochromism discussed in Section 5.1.4.<sup>58</sup> Two bands with binding-energies of 402.18 and 402.28 eV are observed in the N1s spectrum of CTA-W<sub>12</sub>, Figure 5.3.3(e). We assign these to quaternary alkyl-ammonium (NR<sub>4</sub><sup>+</sup>) groups of the CTA<sup>+</sup> cation bound to chloride, [NR<sub>4</sub>]<sup>+</sup>[Cl]<sup>-</sup>, at 402.28 eV, and to [H<sub>2</sub>W<sub>12</sub>O<sub>40</sub>]<sup>6-</sup>, [NR<sub>4</sub>]<sup>+</sup>[POM]<sup>-</sup>, at 402.18 eV. The [N-R<sub>4</sub><sup>+</sup>][Cl<sup>-</sup>] band appears at slightly higher binding energy than [NR<sub>4</sub>]<sup>+</sup>[POM]<sup>-</sup> due to the weaker basicity of the Cl<sup>-</sup> anion compared to [H<sub>2</sub>W<sub>12</sub>O<sub>40</sub>]<sup>6-</sup>.<sup>274</sup> A peak at 400.09 eV appears after UV irradiation, and is ascribed to nitrogen bonded to hydrogen, N-H.

ATR FT-IR spectra of CTA-W<sub>12</sub> in the bleached state after successive numbers of photochromic are displayed in Figures 5.3.4 and 5.3.5.

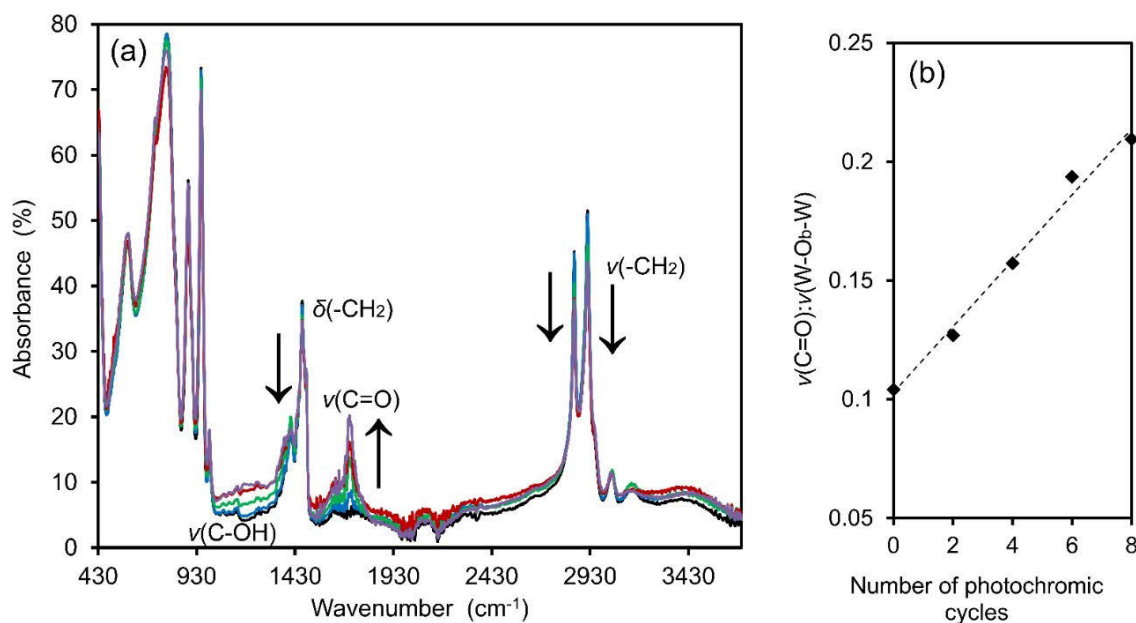


**Figure 5.3.4.** (a) ATR FT-IR spectra of CTA- $\text{W}_{12}$  as-prepared (-), and after two (-), four photochromic cycles (-) and six photochromic cycles (-), an eight photochromic cycles (-). All spectra were collected 24hrs after 1hr of UV irradiation. (b)  $\nu(\text{C=O}):\nu(\text{W-O}_b\text{-W})$  peak-area ratio vs total exposure time.

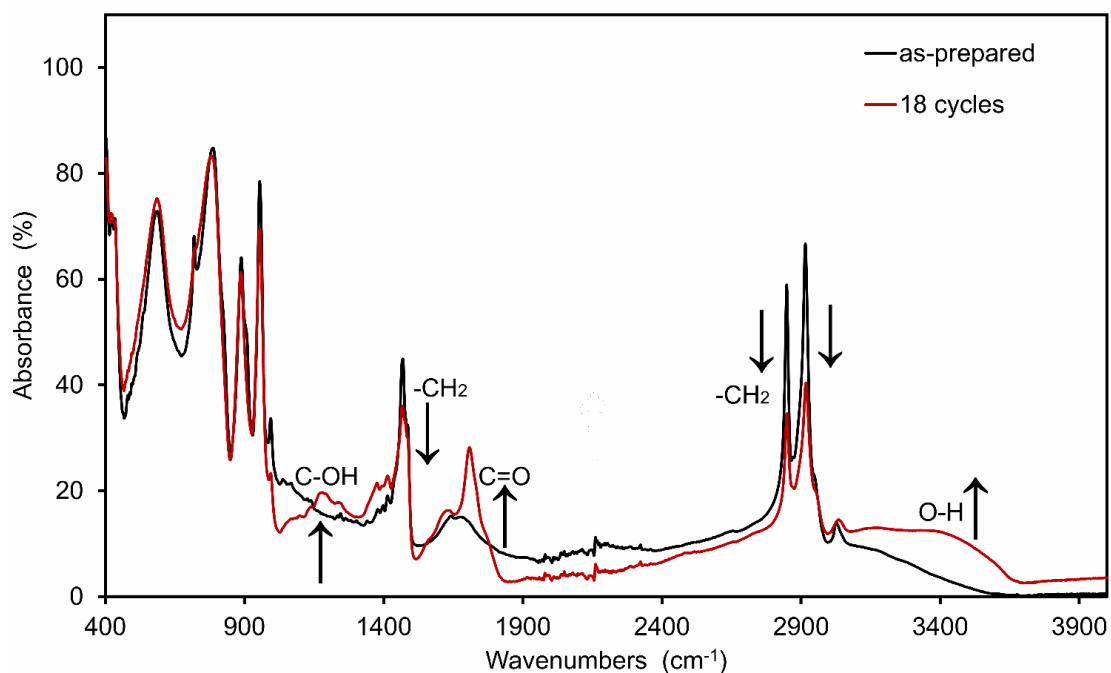


**Figure 5.3.5.** ATR FT-IR spectra of CTA- $\text{W}_{12}$  as-prepared and after 18 photochromic cycles (i.e. spectrum of sample after hysteresis study, Figure 5.3.2).

Both spectra, Fig. 4.3.4-6, display evidence of oxygenation of CTA<sup>+</sup>, consistent with the XPS spectra of Figure 5.3.3. The  $\nu(\text{C}=\text{O})$  vibration is seen to increase in intensity upon each iteration of the photochromic cycle, Figure 5.3.4, confirming the permanence and resulting accumulation of oxygenation to CTA-W<sub>12</sub> during photochromism. Decreases in -CH<sub>2</sub> content is also observed, as evidenced by the reduction of  $\delta(-\text{CH}_2)$  and  $\nu_{\text{as/ss}}(-\text{CH}_2)$  intensities at 1468, 2848 and 2916cm<sup>-1</sup>, respectively. A strong increase in O-H content is also seen, evidenced by the increase in the broad  $\nu(\text{O-H})$  band centred at ~3400cm<sup>-1</sup>.

Increases in oxygen content, C=O and C-OH, seem to mutually occur with decreases in -CH<sub>2</sub> content. This would suggest that CH<sub>2</sub> sites are the species being converted to C=O and C-OH during photochromism, which is perhaps not surprising considering the likely activation of C-H bonds during photochromism in the presence of O<sub>2</sub>, Section 5.1.5. To clarify possible concurrent increases and decreases of vibrational bands, the intensities of these FT-IR peaks were plotted against the number of photochromic cycles, Figure 5.3.6.

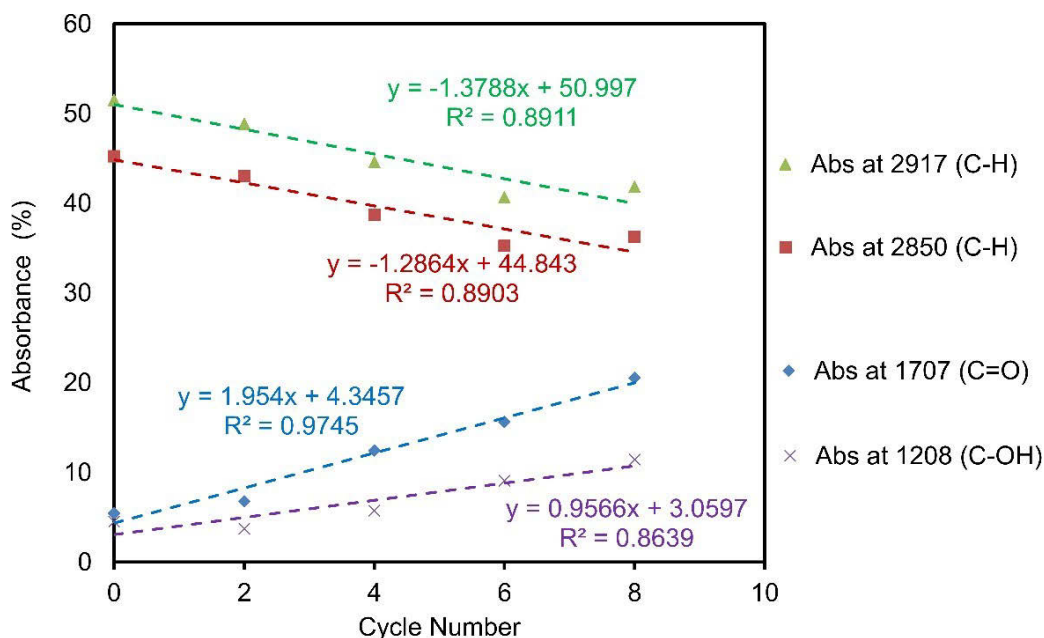


**Figure 5.3.6.** Intensities of  $\nu_{\text{as}}(-\text{CH}_2)$ ,  $\nu_{\text{ss}}(-\text{CH}_2)$ ,  $\nu(\text{C}=\text{O})$  and  $\nu(\text{C-OH})$  FT-IR bands vs number of photochromic cycles.

Figure 5.3.6 confirms that the increase of C=O and C-OH species occurs mutually with the decrease of C-H species. C=O species are seen to increase at a greater rate than C-OH. To ensure that the observed oxidation to CTA<sup>+</sup> was not being instigated by UV irradiation alone, CTA-Br was also subject to the same irradiation-bleaching cycles as described in Figure 5.3.4. The corresponding spectra are displayed in Figure 5.3.7.

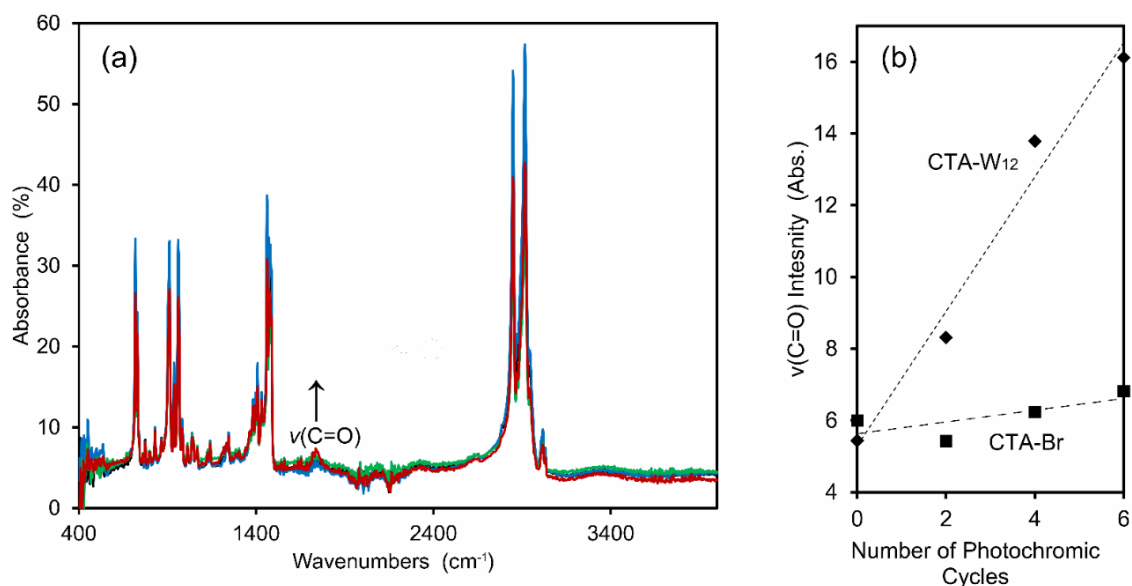


**Figure 5.3.7.** (a) ATR FT-IR spectra of CTA-Br as-received (-), after two (-), four (-) and six UV irradiation cycles (-). All spectra were collected 24hrs after 1hr of UV irradiation. (b)  $\nu(\text{C}=\text{O})$  intensity in CTA-Br and CTA-W<sub>12</sub> vs number of photochromic (or otherwise UV irradiation) cycles.

Some oxidation and mutual growth of  $\nu(\text{C}=\text{O})$  is seen to occur when CTA-Br is irradiated by UV. However, the increase in  $\nu(\text{C}=\text{O})$  intensity in CTA-Br due to UV irradiation is seen to occur nearly 12 times less than the rate of increase in CTA-W<sub>12</sub>, Figure 5.3.7(b). This large difference in  $\nu(\text{C}=\text{O})$  growth rate confirms that the majority of C=O creation in CTA-W<sub>12</sub> is due to the mutual presence of the  $[\text{H}_2\text{W}_{12}\text{O}_{40}]^{6-}$  anion and not to processes instigated by UV photons to CTA<sup>+</sup> in isolation.

The formation of C=O and C-OH oxygenated species within the otherwise pristine CTA<sup>+</sup> matrix would cause the material to ‘yellow’ and could account for the observed decreases in  $\Delta R$  with early cycle numbers, Figure 5.3.2. This discolouring photo-degradation

is regularly observed in polymers due ionization of polymeric units by UV light and subsequent reaction with O<sub>2</sub>. The oxygenated products of these processes are observed to absorb visible-light which causes the material to appear yellow.<sup>276-279</sup> However, the production of these absorbing oxygenated species seems to taper-off by the fourth photochromic cycle, whereby no further decreases in ΔR are observed.

### **5.3.3 Long-lived W<sup>5+/4+</sup> sites**

Raman spectroscopy similarly reveals decreases in CH<sub>2</sub> and CH<sub>3</sub> content, as evidenced by the decreases in the intensity of bands between 2700 – 3300 cm<sup>-1</sup>, Figure 5.3.8. Another feature which is also evident in the Raman spectrum is a broad photo-luminescence peak with a maximum emission at 725 nm (633nm + 2000 cm<sup>-1</sup>), corresponding to red light. Such features in TMOs are usually caused by oxygen-vacancies defects in sub-stoichiometric tungsten-oxide lattice.<sup>280</sup> This is interesting as the spectrum was collected three days after the final UV irradiation of the sample that underwent 18 photochromic cycles. This suggests some photo-produced oxygen-vacancy sites, and by extension reduced W<sup>5+</sup> species, are very long-lived. Further evidence for long-lived W<sup>5+</sup> centres can be found within Figure 5.3.1, where small absorbance bands at 783 and 1432 nm are still apparent in the bleached sample (24 hours after cessation of UV irradiation).

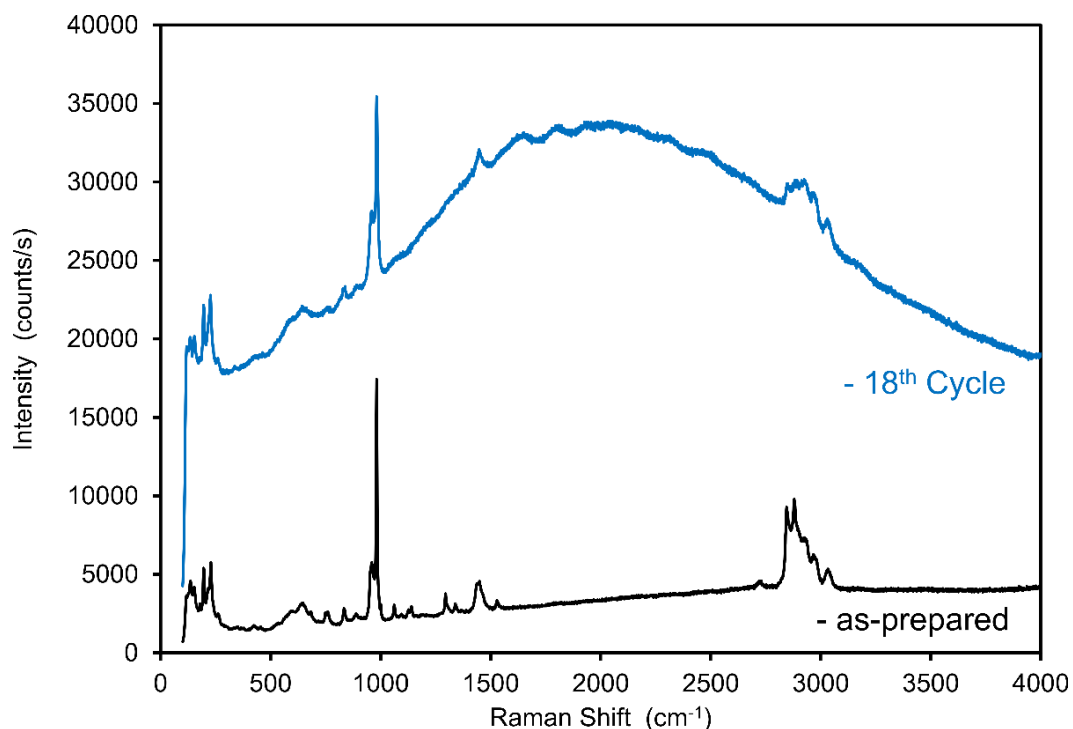


**Figure 5.3.8.** Raman spectra of CTA- $W_{12}$  as-prepared and after 18 photochromic cycles (i.e. spectrum of sample after hysteresis study, Figure 5.3.2, and same sample as depicted in Figure 5.3.5)

It is possible that some of the photo-redox processes between  $CTA^+$  and  $[H_2W_{12}O_{40}]^{6-}$  that yield the observed carbonyl species involve a Mars-van Krevelen-type mechanism, whereby lattice/cluster-oxygen of the POM is consumed by the reaction.<sup>263, 264</sup> If these oxygen-vacancies are created sufficiently deep within the sample, then it is possible that very long times (greater than three days) would be needed for  $O_2$  to eventually diffuse across the hydrophobic-hydrophilic layers of CTA- $W_{12}$  and replenish the vacancy.

However, the concentration of long-lived  $W^{5+}$  sites seems to be constant after four photochromic cycles, Figure 5.3.2, indicating a possible equilibrium point between the creation of deep, long-lived  $W^{5+}$  sites and the oxidation of these sites by the diffusion of atmospheric  $O_2$  into the sample.

### 5.3.4 Products of CTA-W<sub>12</sub> photochromism

Due to the detection of oxidized CTA<sup>+</sup> species produced during the photochromic cycle of CTA-W<sub>12</sub>, further chemical analysis was performed on bleached CTA-W<sub>12</sub> to characterize these products and determine if these oxidized products were volatile (i.e. leaving the material). To do this, CTA-W<sub>12</sub> was subject to prolonged UV exposure (48 hours). Weighing of the sample before and after the irradiation revealed a mass loss of 9%, indicating that indeed volatile molecules were being produced during photo-colouration. Furthermore, a strong fish-like odour, indicative of methyl-amines, was easily sensed upon collection of the irradiated sample, alluding to the likely volatilized species.

To confirm this hypothesis, gas chromatography-mass spectroscopy (GC-MS) was performed on irradiated and un-irradiated CTA-W<sub>12</sub>. Results are depicted in Figure 5.3.9.

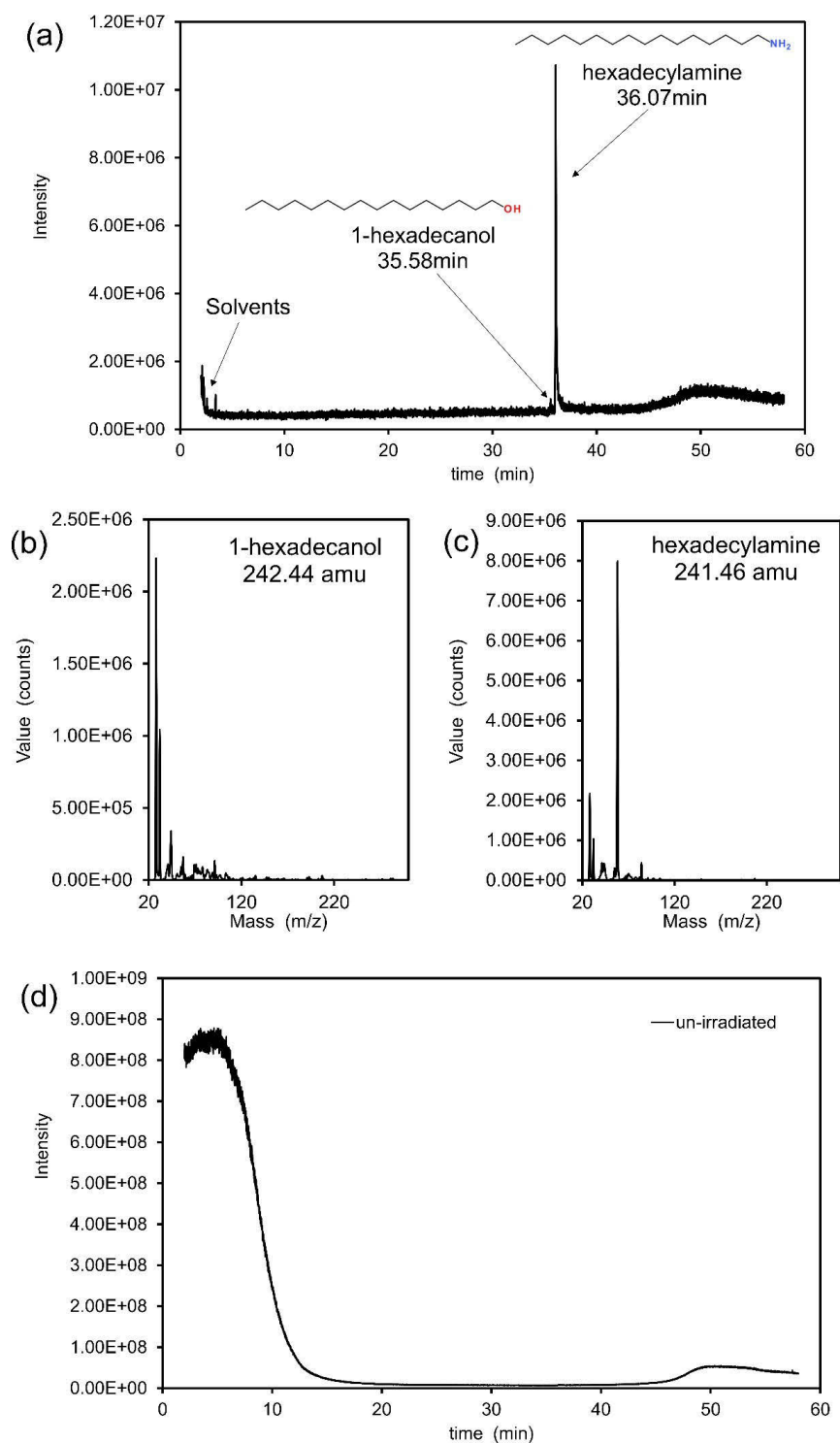


**Figure 5.3.9.** GC-MS spectra of CTA-W<sub>12</sub> after 48hrs of UV irradiation (a) GC of irradiated CTA-W<sub>12</sub> in CHCl<sub>3</sub> including molecular representations of identified compounds (b) Mass spectrum of detected 1-hexadecanol (c) Mass spectrum of detected hexadecylamine (d) GC of un-irradiated CTA-W<sub>12</sub>.

Hexadecylamine and 1-hexadecanol were detected as the only products from CTA-W<sub>12</sub> photochromism that could be dissolved in CHCl<sub>3</sub>. Hexadecylamine is identified as the major product, and 1-hexadecanol as the minor product, with only a trace amount detected. No CHCl<sub>3</sub> soluble products were detected in un-irradiated CTA-W<sub>12</sub>, Figure 5.3.9(d).

Both of these products are 16 carbons in length, suggesting that some photo-redox processes between CTA<sup>+</sup> and [H<sub>2</sub>W<sub>12</sub>O<sub>40</sub>]<sup>6-</sup> also involve head-group of CTA<sup>+</sup> and the C–N bonds therein. Cleavage of C–N bonds between the methyl-groups of the head-group and the cationic nitrogen would eventually result in the formation of hexadecylamine. The detection of hexadecylamine compliments the observation of N-H groups in N 1s spectra post UV irradiation, Figure 5.3.3. Additionally, cleavage of the C–N bond between the cationic-nitrogen and the alkyl-chain (C<sub>α</sub>, Figure 4.2.1) would result in a 16 carbon long alkyl-chain that could undergo further reaction with atmospheric O<sub>2</sub> or crystallographic H<sub>2</sub>O to form 1-hexadecanol. Methylamines were not detected by GC-MS, however, this is not surprising considering the volatility of such compounds (b.p. ≈ 5°C). Methane, a product that likely form after methyl-group abstraction from CTA<sup>+</sup> and subsequent reaction with H<sup>+</sup>, was also not detected, likely due to the similar volatility (b.p. = -161.5°C).

Molecules containing carbonyl, C=O, groups were not detected via GC-MS, although their presence in CTA-W<sub>12</sub> after UV irradiation is easily detected by FT-IR, Figures 5.3.4-5, and XPS, Figure 5.3.3(b). This is also not surprising as the reactions that likely form these groups, either a Mars-van Krevelen-type mechanism whereby the POM cluster is the source of oxygen, or, a C-H bond cleaved, deprotonated radical-CTA reacting with O<sub>2</sub> or H<sub>2</sub>O, do not produce non-ionic products soluble in CHCl<sub>3</sub>, Section 5.1.5. Secondary and tertiary forms of hexadecylamine that contained methyl groups around the head-group nitrogen were also not detected. This is interesting and suggests that photo-colouration of CTA-W<sub>12</sub> coincides with the removal of all methyl-groups from the CTA<sup>+</sup> head-group, or, CTA<sup>+</sup> products from photo-colouration remain cationic until the eventual formation of hexadecylamine.

Alternatively, methylated forms of hexadecylamine may not have been detected by GC-MS due to decomposition in the heated column before arrival at the detector. Hexadecylamine is detected at 36.07 min into the experiment, Figure 5.5.1(a). At this time the instrument was at 205°C, a temperature at which Hoffman degradation of alkyl-amines

can easily occur, as was realized by studying the thermal decomposition of CTA-W<sub>12</sub>, Chapter 3. Therefore, it is perhaps more likely that secondary and tertiary methylated forms of hexadecylamine were produced by photo-redox reactions between CTA<sup>+</sup> and [H<sub>2</sub>W<sub>12</sub>O<sub>40</sub>]<sup>6-</sup>, however these species decomposed in the GC-MS instrument before detection, and hence, only registered as the singular hexadecylamine species.

The formation of primary and secondary forms of hexadecylamine could explain the maintained  $\Delta R$  at extended photochromic cycle numbers, Figure 5.3.2. Because such molecules contain labile N<sup>+</sup>-H bonds, unlike the quaternary N<sup>+</sup>-CH<sub>3</sub> bonds of CTA<sup>+</sup>, the deprotonation of these molecules during photo-colouration and subsequent re-protonation during bleaching would be more reversible (as compared to N<sup>+</sup>-CH<sub>3</sub>), and follow the more typical surfactant-POM photochromic mechanism as described in Figure 5.1.5.<sup>58</sup> This would mean that the concentration of N<sup>+</sup>-H bonds is sufficient by four photochromic cycles (eight hours of UV irradiation) such that the formation of carbonyl groups from -CH<sub>2/3</sub> sites is severely diminished.

#### **5.4 Structural changes during CTA-W<sub>12</sub> photochromism**

Changes to the aliphatic chains of CTA<sup>+</sup> by abstraction of CH<sub>2</sub> groups should affect the lamellar mesostructure of CTA-W<sub>12</sub> considerably, as it is these hydrophobic alkyl-chains that support the separation of the hydrophilic POM containing sheets, Section 3.4. To observe these possible changes, *in-situ* synchrotron P-XRD was conducted on CTA-W<sub>12</sub> during a number of different exposure regimes.

##### **5.4.1 CTA-W<sub>12</sub> photo-decomposition**

*In-situ* low-angle synchrotron P-XRD of CTA-W<sub>12</sub> during UV irradiation is presented below, Figure 5.4.1:

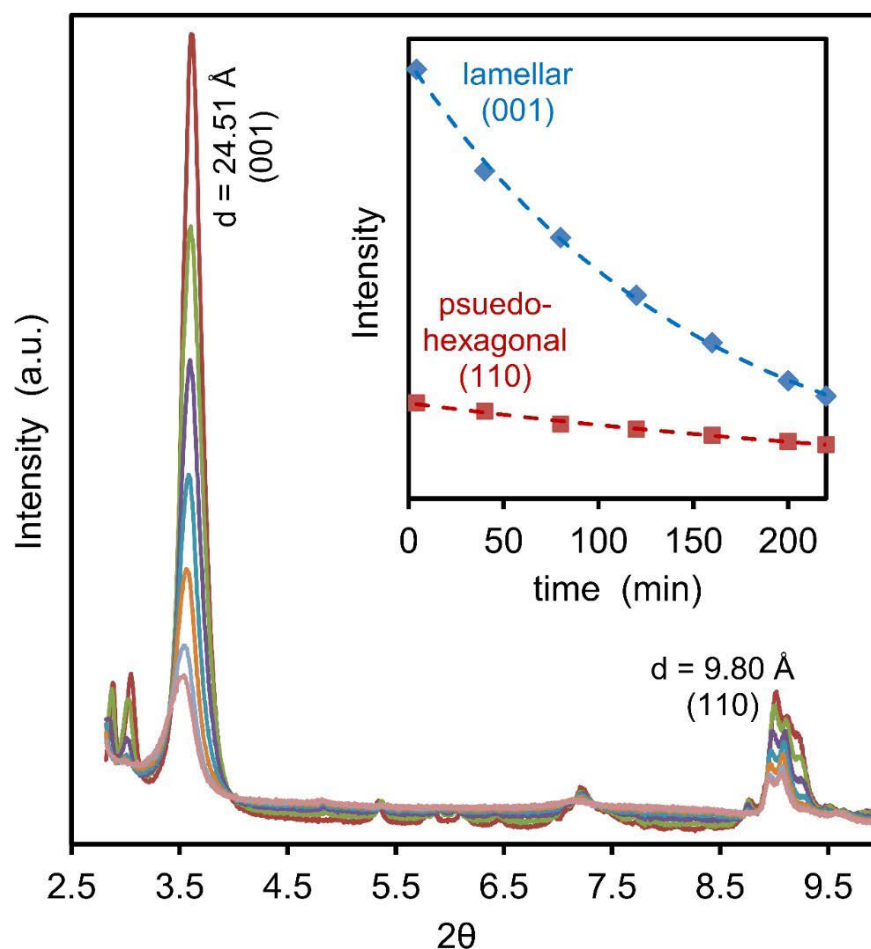


**Figure 5.4.1.** *in-situ* low-angle synchrotron P-XRD patterns of CTA- $W_{12}$  during UV irradiation; (-) 4min UV irradiation, (-) 40min, (-) 80min, (-) 120min, (-) 160min, (-) 200min, (-) 220 min. **Insert:** (001) and (110) peak intensities vs irradiation time.

The intensity of all low-angle diffraction peaks ( $< 10^\circ 2\theta$ ) is seen to sharply decrease upon irradiation by UV light. This peak erosion is seen to be greatest with the (001) diffraction peak, which is indicative of the lamellar-separation between the sheets of pseudo-hexagonally arranged POMs, Section 3.4. Peak erosion is also seen to occur to a large extent to the (110) diffraction peak, which is indicative of the separation between the pseudo-hexagonally arranged POMs within the hydrophilic layer. Mutually, the intensity of the background diffraction pattern increases with irradiation time and the concurrent peak erosion, which is indicative of decreasing order and increasing amorphization of the material. Interestingly, the

location of the (001) peaks shifts to lower  $2\theta$  with increasing irradiation time which corresponds to an increase in the lamellar distance.

To ensure that these effects were caused by UV irradiation and not by the synchrotron X-ray source, a baseline was recorded where the sample was repeatedly imaged by the X-ray beam without any UV irradiation, Figure 5.4.2. A further experiment was conducted where UV irradiation was intermittently incident upon the sample to further clarify the role of UV in CTA- $W_{12}$  amorphization.

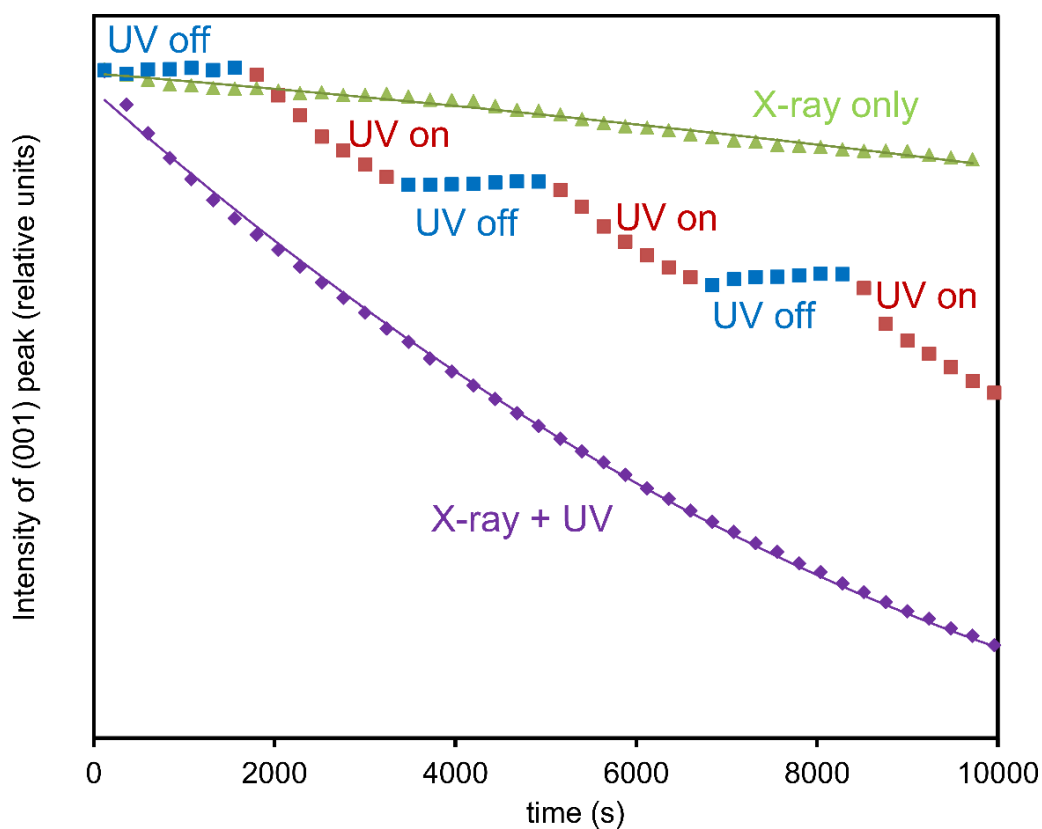


**Figure 5.4.2.** (001) peak intensity vs X-ray only irradiation (baseline), X-ray with intermittent UV irradiation (UV on, UV off), and continuous UV and X-ray irradiation (same trend as depicted in Figure 5.4.1).

Some degradation of the (001) peak is observed to occur due to the synchrotron X-ray beam alone, however, it is clear that UV irradiation greatly accelerates this process. This is further clarified within the intermittent run, where periods of UV irradiation are seen to greatly

increase the rate of peak decomposition as compared with periods where UV light was not incident. Interestingly, peak intensity is seen to increase during the first ‘UV off’ segment (0 – 1600s). It is not entirely understood as to why this occurs, although it is most likely be due to movement of the sample within the silica capillary as it rotates within the sample mount. This hypothesis is supported by the slight oscillations in intensity observed within the X-ray only baseline.

#### 5.4.2 Lattice expansion and contraction during photochromism

Periods when the UV irradiation is turned off following periods of UV irradiation seems to coincide with an increase in (001) peak intensity. This sharp increase in intensity directly after UV irradiation is likely due to a decrease in temperature, as the CTA<sup>+</sup> amphiphiles adopt a less disordered structure upon cooling, restoring a more regular interlamellar distance across the layers. The intensity of the (001) peak during each ON-OFF cycle vs time from when the UV irradiation was turned on is displayed below, Figure 5.4.3 (the individual data segments were translated in time and intensity so that they could be overlaid on a common graph).

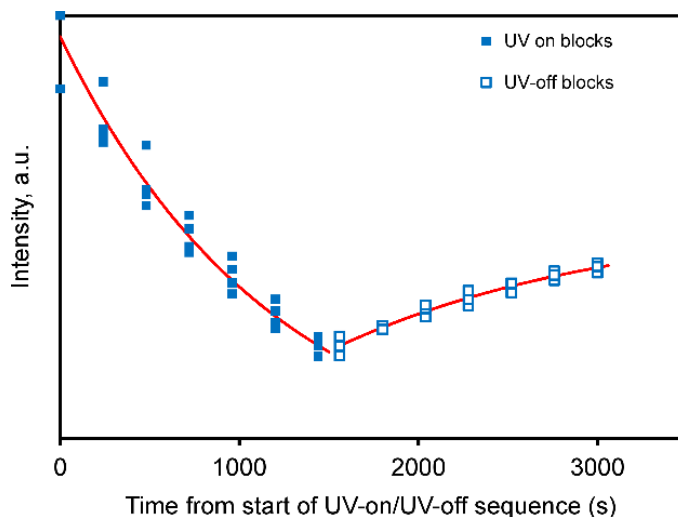


**Figure 5.4.3.** (001) peak intensity for each UV ON-OFF cycle. Time = 0 corresponds to when the UV was turned on for each cycle.

It is clear that changes to the inter-lamellar distance occur not only during times of UV irradiation, but also in the preceding minutes after it is turned off. Furthermore, these changes seem to be constant, with equal decreases in intensity occurring with every exposure cycle, and equal increases in intensity during every period when the lamp was turned off. To see whether these changes were caused by expansion due to heating alone, the coefficient of thermal expansion of CTA- $W_{12}$  between 25 and 90°C was calculated using data detailed in Section 4.3, Figure 5.4.4.

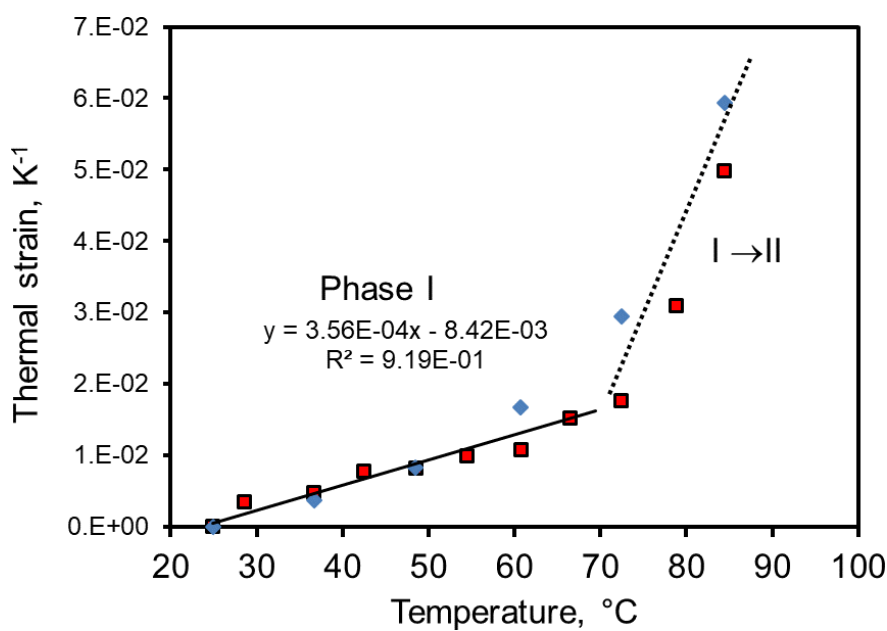


**Figure 5.4.4.** Thermal expansion of CTA- $W_{12}$  in the [001] direction (normal to the planes containing the pseudo-hexagonally arranged POMs). CTA- $W_{12}$  undergoes a phase transformation (phase I  $\rightarrow$  II) at  $\sim 70^\circ\text{C}$ .

Using this data, a coefficient of thermal expansion of  $3.56 \times 10^{-4} \text{ }^\circ\text{C}^{-1}$  in the [001] direction between 25 to 70°C is deduced. Applying this to the UV on-off trend of Figure 5.4.2, it is found that turning the UV irradiation on or off instigates a  $\pm 6^\circ\text{C}$  change in temperature. This change in temperature would stabilize within the small quartz capillary after a few minutes. Therefore, changes to the lattice parameter beyond this period must be caused by the

irradiation alone. The effects of UV irradiation on the lamellar distance in CTA-W<sub>12</sub> is present in Figure 5.4.5.

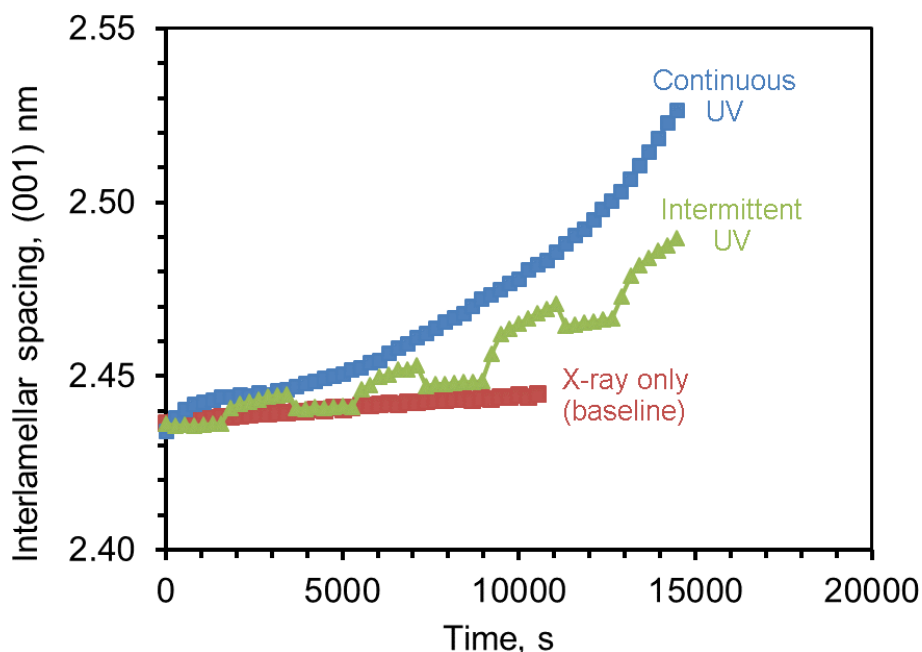


**Figure 5.4.5.** Interlamellar spacing vs X-ray-only irradiation time (baseline), X-ray and intermittent UV irradiation (UV on/off) and continuous X-ray and UV irradiation.

Two distinct expansion regimes are observed within the intermittent UV experiment; an initial rapid increase in interlamellar distance directly following the incidence of UV irradiation, and a longer term more gradual increase in interlamellar distance following the initial rapid increase. This initial rapid increase is also seen within the UV continuous experiment (0 to ~1000s). Importantly, the trend of the X-ray only baseline closely resembles that of periods when the UV irradiation was turned off in the intermittent experiment.

The consistent increase in lattice parameter during the intermittent experiment with every period when the UV lamp was turned on, after the thermal affects have been taken into account, highlights permanence of the expansion. However, partial restoration of the lattice parameter is observed at every instance when the lamp was turned off. Clearly a semi-reversible process is occurring in CTA-W<sub>12</sub> during each cycle of UV irradiation. The interlamellar space of CTA-W<sub>12</sub> is highly dependent on the conformation of the aliphatic

CTA<sup>+</sup> alkyl-tails, as detailed in the previous two chapters. Therefore, changes in the interlamellar space are likely due to changes in the conformation of these alkyl-tails, such as changes in interdigitation or electrostatic bond-angle (relative to the lamellar interface). The increasing lamellar distance and mutual decrease in lamellar peak intensity when UV irradiation is incident upon the sample suggests that Keggin anions become disordered and further separated during photo-colouration and become more ordered and less separated during periods of bleaching. In other words, UV irradiation instigates lamellar distance increase and amorphization, which is then partially reversed when irradiation ceases.

Changes in the electrostatic bond-angle between the POM anion and CTA<sup>+</sup> due to the reduction of the WO<sub>6</sub> octahedral-unit and the altered electronic environment around the cationic nitrogen during the formation of the coloured charge-transfer complex, Figure 5.1.5, could account for these observations. Re-oxidation of the reduced POM and recovery of the electronic environment around the cationic nitrogen upon bleaching would then account for the increase in crystallographic order and reduction in interlamellar distance during times when the UV lamp was turned off. Conversion of the oxidized  $\alpha$ -Keggin anion structure to the reduced  $\beta$ -Keggin anion structure during photo-reduction, and restoration of the  $\alpha$ -Keggin anion structure when the UV lamp is turned off could also account for the changes in lattice parameter.<sup>230</sup> In any case, it is clear structural, not only optical, changes occur in surfactant-POM hybrid systems during photochromism.

### **5.5 Conclusion: Photochromism of quaternary-ammonium polytungstate hybrids**

CTA-W<sub>12</sub> performed as a photochromic material, although with only partial reversibility during the initial (four) colour-bleaching cycles. This irreversibility manifested as a decrease in the  $\Delta R$  between the bleached and coloured states, due to a decrease in reflectance with each bleaching cycle, Figure 5.3.2. No changes in the reflectance of the coloured state was observed i.e. the reflectance of the first coloured state was maintained with every successive colouration across the materials observed life-time. After four photochromic cycles, CTA-W<sub>12</sub> functioned as a completely reversible photochromic material.

The initial decreases in  $\Delta R$  during the first four photochromic cycles were ascribed to two mutually occurring processes; permanent oxidation to CTA<sup>+</sup> via the formation of carbonyl species, Figures 5.3.3-6, and long-lived reduction of the POM likely due to the

formation of  $W^{5+}$  sites deep within the material that could not be oxidized by the diffusion of  $O_2$  into the sample (within the observed time-scale), Figures 5.3.1 and 5.3.8. The constant  $\Delta R$  after four photochromic cycles was ascribed to the formation of more reversible proton-transfer groups (as compared to  $-CH_{2/3}$ ), such as primary and secondary amines, which would limit further carbonyl formation. The presence of these amines was confirmed with XPS (Figure 5.3.3) and GC-MS (Figure 5.3.9). An equilibrium between the concentration of long-lived  $W^{5+}$  sites and the diffusion of  $O_2$  into the sample to oxidize them may also explain or contribute to the maintained  $\Delta R$ .

Structural changes were also observed to mutually occur during CTA- $W_{12}$  photochromism. UV irradiation and consequent colouring was observed to coincide with disordering of the Keggin anions and increases in the interlamellar distance, as evidenced by XRD peak intensity and position. Periods when the UV lamp was turned off following UV irradiation and consequent bleaching of the sample was observed to coincide with increases in Keggin anion order and decreases in interlamellar distance.

## Chapter 6. Photochromic Reduction During XPS Measurements

The work presented in this chapter is a result of an investigation into the *in situ* reduction of CTA- $W_{12}$  during measurement by XPS. The investigation included the extent of photoreduction during a studied time-frame, the rate of photoreduction, as well as the possible causes of the observed photoreduction. For a complete introduction on X-ray-based measurement photoreduction of studied samples, and its significance in the fields of photochromism and photo-catalysis see Section 1.7.

### 6.1 Background theory

#### 6.1.1 X-ray/Matter interactions

X-rays can be loosely defined as photons with an energy between 100 eV to 100 keV (or a wavelength of 10 to 0.01 nm). The probability,  $p$ , that an x-ray photon interacts with a solid can be roughly expressed as.

$$p \propto Z^3 / E_\gamma^3 \quad \text{Equation 6.1.1}^{281}$$

Where  $Z$  is an element's atomic number and  $E_\gamma$  is energy of the incident x-ray photon. With this expression, the dependence of x-ray penetration on a material's dominant element can be easily realized. This dependence is the reason why x-rays can be used to image the skeletal structures of animals, due to the contrast between Ca ( $Z = 20$ ) found mostly in bones, and that of the surrounding soft tissues made up of mostly C, H and N ( $Z = 6, 1$  and  $7$  respectively).<sup>281</sup> Also easily recognized in Equation 6.1.1 is the dependence of x-ray interaction on photon energy, with higher  $E_\gamma$  x-rays less likely to interact. This dependence is the reason why high-energy x-rays are used in medical imaging, so as to minimize the amount of energy deposited into sensitive organic molecules such as DNA.

Because of this energy-dependent difference in interaction probability, x-rays are usually further characterized into lower-energy soft x-rays and higher-energy hard x-rays. Hard x-rays are typically described as having a photon energy of  $> 10$  keV whilst soft x-rays

are typically described as containing photons of  $< 10$  keV.<sup>282</sup> Typically, soft x-rays are completely absorbed by solid matter whilst hard x-rays are partially absorbed and scattered.

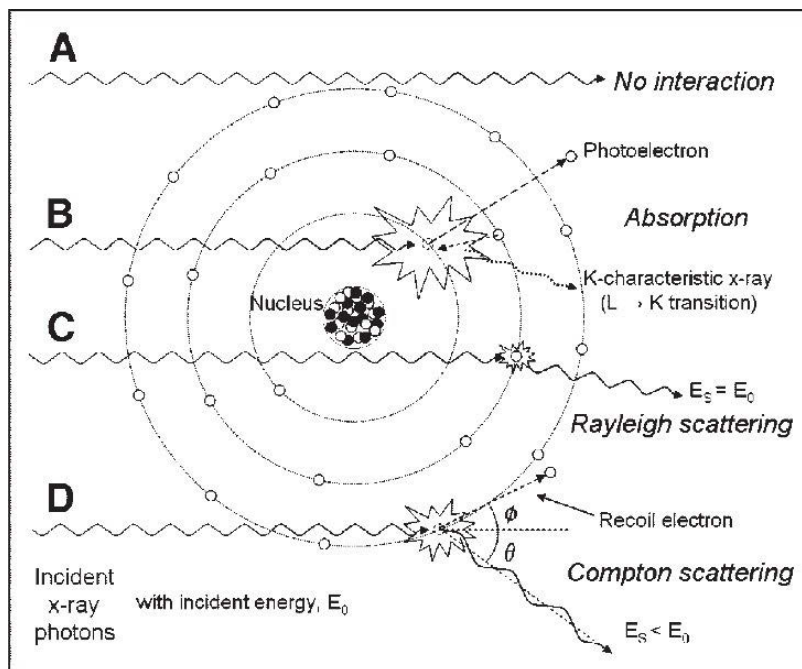


**Figure 6.1.1.** Diagram of all possible x-ray/matter interactions.<sup>281</sup>

X-rays can interact with matter via four main mechanisms, as illustrated in Figure 6.1.1. X-rays can either pass through matter without any interaction (A in Figure 6.1.1), be absorbed by an electron resulting the emission of a photoelectron (B in Figure 6.1.1), be elastically scattered which is termed *Rayleigh Scattering*, or inelastically scattered which is termed *Compton Scattering*.<sup>281, 283</sup> Typically, high-energy x-rays (i.e. hard x-rays) primarily interact with matter through mechanisms A, C and D (transmission or scattering), whilst lower energy electrons (i.e. soft x-rays) interact through mechanism C (absorption), as Equation 6.1.1 suggests. Because lower-energy soft x-rays have the highest probability of depositing energy into a sample, their interaction with matter will be the focus of this chapter's literature review.

Absorption of x-rays by an atom's electron results in the production of photoelectrons, or photoionization of the atom, due to the very high energies of x-rays relative to the binding energies of electrons to the atom's nucleus. If the electron that absorbs an x-ray is a core-electron, i.e. residing in an orbital deeper than the HOMO (or valence

band), than an electron in a higher energy orbital will relax down to fill the core vacancy. Usually the relaxation is radiative, meaning that the difference between the higher energy orbital and the core orbital is emitted as a photon. However, if the photoelectron is created from a deep core-orbital, then this relaxation energy is more likely transferred to the relaxing electron in the form of kinetic energy and is thus ejected from the atom. This is termed the *Auger process* or *Auger mechanism* and electrons ejected via this method are termed *Auger electrons*.<sup>102, 284, 285</sup>

The (kinetic) energy of the ejected photo- or Auger-electron is itself is also relatively high, and therefore x-ray instigated photo-ionization events usually result in ionization cascades, where the primary photo-ionized electron induces further ionization of surrounding atoms by means of kinetic energy transfer.<sup>281</sup> Depending on the elemental make-up of the irradiated solid, a single x-ray photoionization event can result in the production of millions ejected electrons, otherwise known as *hot* or *secondary* electrons.

### **6.1.2 Measurement induced x-ray damage**

It is clear from the above section that the interaction, mainly absorption, of x-rays can change a sample's chemistry considerably, through oxidative photo- and electron ionization events, and subsequent cascades of reductive electrons throughout the interaction volume. Furthermore, high-magnification x-ray instruments can deposit a large amount of energy onto a sample surface within a small spot size. If this energy is not dissipated away from the interaction volume, through the mechanisms listed above, it is transformed into heat. Because of this, the small interaction volume can increase in temperature, sufficient to decompose sensitive organic molecules or promote reactions with neighbouring or adsorbed atoms and molecules.<sup>4, 286-288</sup>

Because of all these mechanisms, samples can be severely damaged when subject to measurement techniques that involve the incidence of x-ray radiation.<sup>4, 103, 282, 289</sup> Due to the dependence of absorption on photon energy, techniques that employ soft x-rays, such as XPS and XAS, have a greater potential to damage samples than those that employ hard x-rays, such as XRD and SAXS.<sup>282, 289</sup> The amount of damage inflicted on a sample is dependent on sample composition, temperature, as well as incident x-ray flux and energy.<sup>282</sup> Covalent bonds are more subject to being broken by the movement of the electrons that comprise them,

relative to the more delocalized ionic and much more delocalized metallic bonds. It is for this reason that samples that are largely comprised of covalently bonded atoms, such as organic molecules, are more susceptible to x-ray induced damage than samples comprised of ionically bonded atoms, and much more than samples comprised of metallically bonded atoms.<sup>4</sup> Of course, thermally-induced degradation will also be greatest in organic samples, due to the decomposition and minimal heat conduction of organic molecules.<sup>4</sup> An illustration of the many types of damage that can be induced by x-ray based measurements on a sample is given in Figure 6.1.2.

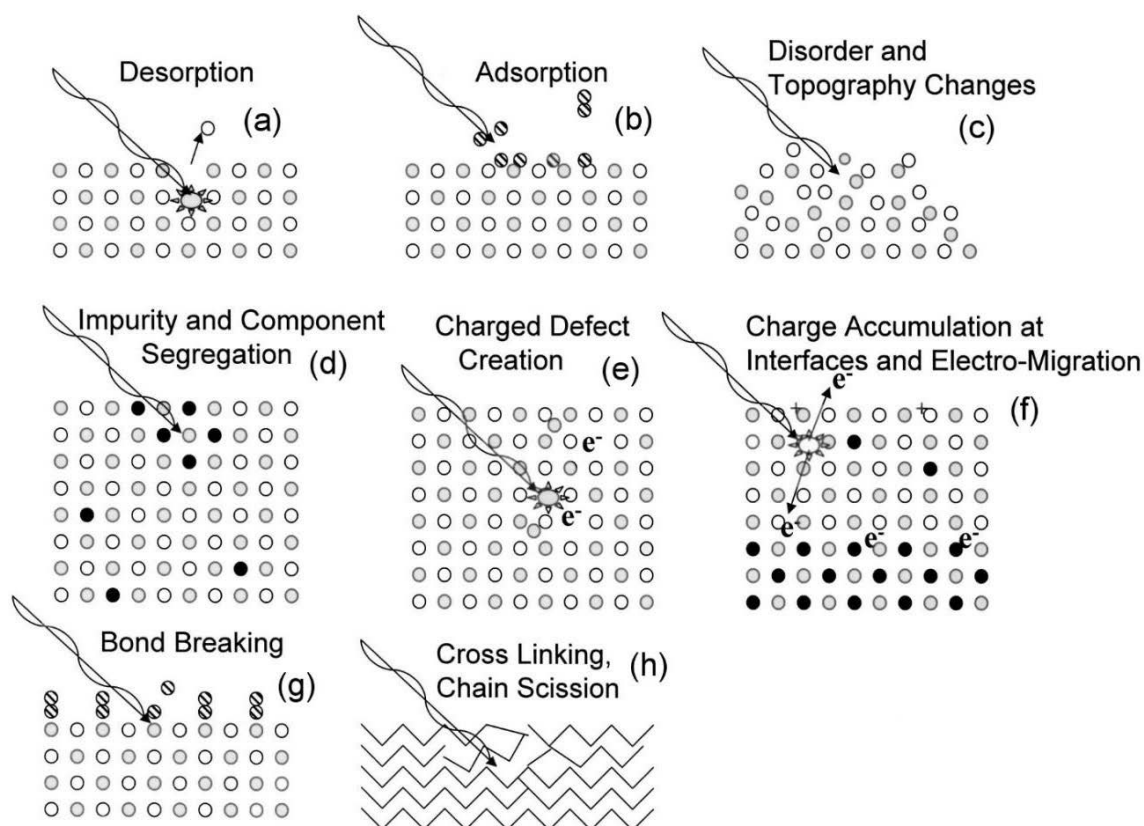


**Figure 6.1.2.** Examples of x-ray induced damage that can be induced by measurement of a sample.<sup>290</sup>

Ionic and organic samples are susceptible to desorption processes, Figure 6.1.2(a), whereby incident x-rays and consequential ionization and secondary electron cascades modify the chemistry of the sample surface, resulting in the formation of volatile species. For example, the breaking up of organic molecules can result in the production of volatile short-chain

hydrocarbons and alcohols which quickly desorb from the sample surface in the UHV environment of the instrument, Figure 6.1.2(g). Photoionization and ensuing ionization and Auger cascades can also significantly alter the net charge in local volumes of ionic compounds, turning anions cationic. The repulsion between the newly formed cationic species and neighbouring metallic cations can result in the desorption of the newly formed cations, significantly altering the surface chemistry and charge of a sample.<sup>4, 70, 101, 102, 285</sup>

Adsorption of molecules and atoms from the gas phase onto the sample surface during x-ray-based measurements can also modify surface chemistry, Figure 6.1.2(b). X-rays are sufficiently energetic to be able to break the strong bonds between diatomic gases, such as O<sub>2</sub> and N<sub>2</sub>, as well as other small molecules such as H<sub>2</sub>O and short-chain hydrocarbons which regularly persist in sample chambers after being pumped-down to UHV levels. These molecules can be broken down into reactive free-radicals by x-ray photoionization which then react quickly with the sample surface resulting in chemisorbed states, again changing the surface chemistry of the sample.<sup>4, 270, 291</sup>

The production of relatively inert species by x-ray instigated reaction with the sample can result in their accumulation within the sample, Figure 6.1.2(d). For example, reduction of metallic cations due to the production of secondary electron cascades can result in the formation of completely reduced metallic atoms. The migration of these M<sup>0</sup> defects (where M is a metal) results in the formation of metallic particulates near the sample surface. In organic samples, the preferential abstraction of N, H and O from the sample surface by x-ray photoionization may result in the formation of inert graphitic deposits at the sample surface.<sup>98, 100, 242, 261, 284, 292, 293</sup>

Of course, the release of negative charge away from the sample surface by x-ray photoionization, Figure 6.1.2(e), results in the production of positive charge within the interaction volume, Figure 6.1.2(f). In samples with poor electrical conduction, such as organic and ionic compounds, this positive charge can accumulate at the sample surface. This positive charge not only changes the surface chemistry, which could lead to desorption (Figure 6.1.2(a)) or reaction with neighbouring or adsorbed atoms and molecules, but also attenuates the further release of electrons from the surface of the sample due to the attraction between the differing charges. This attenuation can influence measurements which analyse photoelectron energy, such as XPS, resulting in the collection of erroneous data.<sup>4, 242</sup>

As previously mentioned, organic samples, and the covalent bonds therein, are especially susceptible to x-ray induced damage.<sup>4, 242, 289</sup> Photoionization, and the resulting ionization and secondary electron cascades can result in the formation of reactive free-radical components or otherwise induce reactions between neighbouring molecules. In polymeric samples, and other samples that contain long-chained organic species, this can result in chain scission, and/or cross-linking, Figure 6.1.2(h), significantly modifying the sample surface. Of course, all the above processes listed here are all examples of disorder and topography changes, Figure 6.1.2(c).

### 6.1.3 Photoreduction during x-ray measurements

Processes such as photoionization and desorption of previously anionic components obviously lead to reduction within the interaction volume of the incident x-rays. In oxide and other metallic-cation-based inorganic materials, this can result in substoichiometry and the reduction of the metallic cations to lower oxidation states.<sup>4, 70, 100-102, 242, 261, 285, 294</sup> In materials comprising of high reduction potential noble metal cations, such as Hg<sup>2+</sup>, Ag<sup>+</sup>, Pt<sup>2+</sup> and Au<sup>3+</sup>, progressive reduction of the sample induced by x-ray irradiation can eventually lead to the production of noble metal nanoparticles.<sup>100, 295-297</sup>

More specific to the case of x-ray imaged oxides is the previously mentioned release of O<sup>+</sup> and the corresponding formation of oxygen vacancies, a phenomenon otherwise known as ‘*Coulombic explosion*’.<sup>70, 100-102, 249, 261, 285, 298</sup> Because of their relatively high *Z*, x-ray interaction and resulting photoionization in metal-oxide compounds are usually concentrated at the heavier metallic cation sites (Equation 6.1.1). Photoionization of sufficiently core-level electrons results in Auger electron release from the metallic-cation.<sup>102, 285</sup> If the metallic-cation is maximally oxidized and there are no outer-shell valence-electrons (i.e. *d*<sup>0</sup>), then an electron from a neighbouring oxo-ligand will fill the hole left at the metallic-cation via electron-transfer, thus oxidizing the oxo-ligand in the process. If this process occurs three times, then the previously O<sup>2-</sup> oxo-anion becomes cationic:



These created  $O^+$  are quickly desorbed from the sample, due to their proximity to the sample surface and the repulsion between them and the likely-charged metallic-cations. Consequently, oxygen-vacancies are created in the oxide, leading to substoichiometry and overall reduction of the sample.<sup>101, 294, 299, 300</sup> Of course, if valence electrons are present on the outer-shell of the metallic cations, than these electrons are able to relax into the core-vacancies without Auger processes and thus, this particular mechanism of photoreduction is subdued. The process of Coulombic explosion is illustrated in Figure 6.1.3.

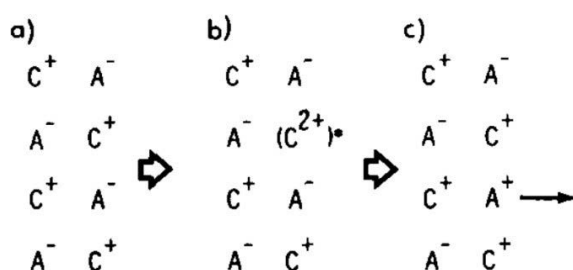


**Figure 6.1.3.** Process of ‘Coulombic explosion’ in ionic compounds. If a maximally-oxidized cation,  $C^+$ , in an ionic material (a), is further oxidized,  $C^{2+}$ , then the only source of electrons to reduced it is from neighbouring anions,  $A^+$  (b). If the maximally-oxidized cations are repeatedly oxidized, this will eventually render anions cationic,  $A^+$ , which are quickly ejected from the sample due to repulsion from the neighbouring like-charge cations (c).<sup>102</sup>

More typical mechanisms of light-adsorption induced photoreduction also occur. The adsorption of x-rays in ionic compounds results the production of photoelectrons and likely leads to secondary electron cascades within the material. The relaxation of these hot electrons likely takes place at metallic cations regardless of the origin of the secondary-electron, due to the attraction between the dislike charges, resulting in a net movement of negative charge away from ligands and onto metals. Of course, such transfer of electrons from ligands to metallic-cations reduces the oxidation level of the metal and causes mutual oxidation of the ligand. X-ray induced photo- and/or redox decomposition of more complex ligands and the resulting release of covalently bonded electrons has also been observed.<sup>293, 301</sup> These x-ray absorption induced ligand-to-metal charge-transfer ( $L \rightarrow M$  CT) processes can also lead to the

production of oxygen- and analogous ligand-vacancies via the desorption of O<sub>2</sub>, Cl<sub>2</sub>, etc, as has been observed during the x-ray-based measurements of CuO<sub>2</sub>,<sup>292, 293, 302</sup> Re<sub>2</sub>O<sub>7</sub>,<sup>303</sup> H<sub>2</sub>AuCl<sub>4</sub>,<sup>295, 296</sup> Fe<sup>3+/4+</sup>-based,<sup>301, 304, 305</sup> and Ce<sup>4+</sup>-based materials.<sup>287, 288, 306, 307</sup>

The process of x-ray photoreduction of metal centres in ionic materials seems to compete with x-ray photooxidation.<sup>301, 306</sup> As mentioned in the previous section (Figure 6.1.2(b)), residual O<sub>2</sub> in the instrument chamber left after pump-down can be broken-down into reactive monoatomic components by the absorption of x-rays which quickly react with the sample surface. This competition of x-ray induced processes causes lower oxidation-state metallic-cations and pristine metal sites, M<sup>0</sup> (where M = metal), to usually undergo oxidation during soft x-ray-based measurements, while highly oxidized metals usually undergo reduction.<sup>270, 301</sup> This was clearly observed by S. George *et al* in their study of the XPS of a series of Fe<sup>0</sup>- to Fe<sup>4+</sup>-based materials.<sup>301</sup> Here, Fe cations with a charge greater than 2+ were observed to undergo photoreduction during XPS, whilst Fe<sup>0</sup> was observed to undergo photooxidation, and Fe cations with a charge of 2+ did not undergo any significant change.

#### 6.1.4 X-ray photoreduction of organic-inorganic hybrids

The mutual presence of organic and metallic components in a sample can significantly increase the rate of x-ray-induced photoreduction of the metallic component, and photooxidation of the organic component. This has been known for many decades in the study of metallo-proteins, where even the incidence of more transmissive hard x-rays, such as those used in XRD and SAXS, induce significant damage to measured samples.<sup>292, 293, 295, 301</sup> As described above in the previous sections, organic molecules are highly susceptible to x-ray induced damage due to presence of rigid covalent bonds which break upon x-ray induced redox processes, releasing previously bound electrons into the sample which reduce neighbouring metallic-cations.<sup>305</sup> The accurate determination of the oxidation-state of the metal-centres is a priority during these measurements, due to their redox activity in biological processes, such as Fe<sup>2+↔Fe<sup>3+</sup></sup> in haem, Cu<sup>1+↔Cu<sup>2+</sup></sup> in azurin and Mn<sup>2+↔Mn<sup>3+</sup></sup> in dismutase.<sup>292, 295</sup> Because of this, great care is taken with the set-up and conduction of experiments involving x-rays and metallo-proteins to limit the amount energy deposited into the sample, such as limiting x-ray flux, ensuring good thermal and electrical conductivity away from the sample and cooling samples to cryogenic temperatures.<sup>292, 295</sup>

The presence of organic components in simpler organic-inorganic hybrids is also known to accelerate x-ray induced photoreduction processes.<sup>70</sup> Even surface contamination of samples, such as adventitious surface carbon and volatile hydrocarbons left in the instrument chamber after pump-down, can significantly accelerate the photoreduction of metallic-cations.<sup>103, 308</sup> This is especially a concern in the case of measuring Cr<sup>6+</sup> bearing compounds, where residual volatile hydrocarbons accelerate the ‘Coulombic explosion’ process. The holes ( $h^+$ ) created in the oxo-ligands by the inter-atomic Auger processes within maximally oxidized metallic-cations (Section 6.1.3) are highly oxidizing and react readily with the electron reservoirs of adsorbed hydrocarbons, producing volatile products such as CO and CH<sub>4</sub>O, figure 6.1.4. These volatile products quickly desorb from the sample surface in the UHV environment, accelerating the formation of oxygen-vacancies.<sup>100, 103, 308</sup>

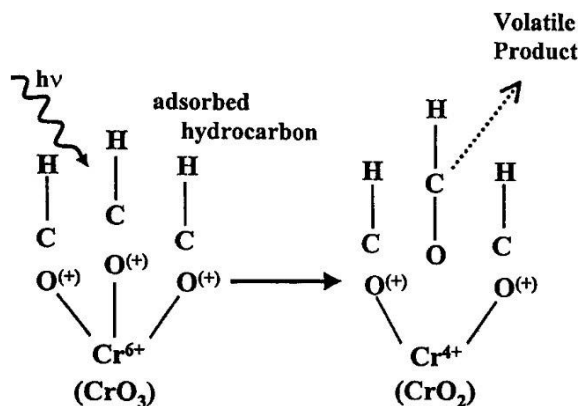


**Figure 6.1.4.** The presence of organic material accelerates oxygen-vacancy generation and x-ray photoreduction of chromium oxides by reacting with photo-oxidized O<sup>+</sup> species.<sup>308</sup>

The nano- and meso-structure of organic-inorganic hybrids can also influence the photoreduction kinetics of a sample.<sup>4, 242, 249, 303</sup> Dimensionally constrained samples, such as nanoparticles, nanowires and thin-films, are more susceptible to x-ray adsorption-induced modification. These samples lack long-range thermal and electrical conductivity and are therefore less able to conduct electrical charge (produced through charging effects, Section 6.1.2) and heat (produced through inelastic non-radiative adsorption, Section 6.1.2) away from the sample. Build-up of electrical charge and heat can accelerate the processes

previously listed, such as decomposition of the organic component, or reaction of the organic component with itself, with the oxide or residual atmosphere.<sup>4</sup>

As previously mentioned in Section 6.1.2, attached organic groups interact with x-rays to differing degrees.<sup>70, 98, 289</sup> Generally, organic N, H and O containing groups are removed from the surface of organic and organic-inorganic hybrid samples with x-ray exposure, resulting in increasing C concentration with exposure/measurement time.<sup>70, 98, 242, 289</sup> This is due to the highly covalent nature of the bonds between these elements and C, and the relatively delocalized, hybridized bonds that can form between C atoms. Bonds between carbon and other elements are also usually weaker than the hybridized bonds between carbon atoms.<sup>180, 184</sup> Furthermore, photo-decomposition products that form with N, H and O tend to be volatile and have low molecular-weight, which easily desorb from the sample under the UHV instrument environment.<sup>98</sup> Alternatively, C atoms can be added to C-based samples near indefinitely, again due to the hybridized bonds between C atoms and their formation into non-volatile carbonaceous deposits. The presence of C-N, C-H and C-O and similar bonds in organic-inorganic hybrids can accelerate to the photoreduction of metallic-cation centres due to the relative instability of these groups.<sup>70</sup>

## 6.2 XPS-induced reduction of CTA-W<sub>12</sub>

As has been described previously, above band-gap (3.6 eV) radiation incident on the sample instigates an oxygen-to-metal ligand-to-metal charge-transfer (O→M LMCT), reducing W<sup>6+</sup> to W<sup>5+</sup> which results in the formation of a visible-light absorbing charge-transfer complex (Chapter 5).<sup>58, 60, 73, 95</sup> It was also discovered (in the same chapter) that repeated synchrotron XRD measurements resulted in increasing disorder of CTA-W<sub>12</sub>, figures 5.4.1-2 and 5.4.5. This occurred largely through the deterioration of the lamellar peak at  $d = 24.5\text{\AA}$ , which is indicative of CTA alkyl-tail confirmation (Section 5.4).

It is therefore likely that soft x-ray irradiation (1.486 keV), such as that routinely used in XPS measurements, will induce similar metallic-cation reduction and other possible changes to the inorganic-organic hybrids CTA-W<sub>12</sub>. To investigate this CTA-W<sub>12</sub> was subjected to repeated XPS scans, using the same measurement parameters that produced Figures 5.2.4 and 5.3.3.

### 6.2.1 W4f core-level spectra during XPS induced reduction

The first, fifteenth, thirtieth and fiftieth scans of the W4f core-level XPS spectra of CTA-W<sub>12</sub> are displayed in Figure 6.2.1. W4f<sub>5/2</sub> and W4f<sub>7/2</sub> spin-orbit doublets of the W<sup>6+</sup> and W<sup>5+</sup> states appear at 39.4 and 37.2, and 37.6 and 35.4 eV, respectively. W4f<sub>5/2</sub> and W4f<sub>7/2</sub> spin-orbit doublets of the W<sup>4+</sup> state, apparent within the fifteenth, thirtieth and fiftieth scans, appear at 36.3 and 34.1 eV. To the best of our knowledge, this is the first report of W4f XPS of a metatungstate (i.e. a Keggin polyoxotungstate containing 2H<sup>+</sup> as the ‘hetero-atom’). As such, the binding-energies (BEs) reported here are somewhat different to that of analogues organic-polyoxometalate materials, with the W4f<sub>5/2</sub> W<sup>6+</sup> state being around 1.4 eV higher than the regularly reported 37.5-38.5 eV for example.<sup>73, 101, 106</sup>

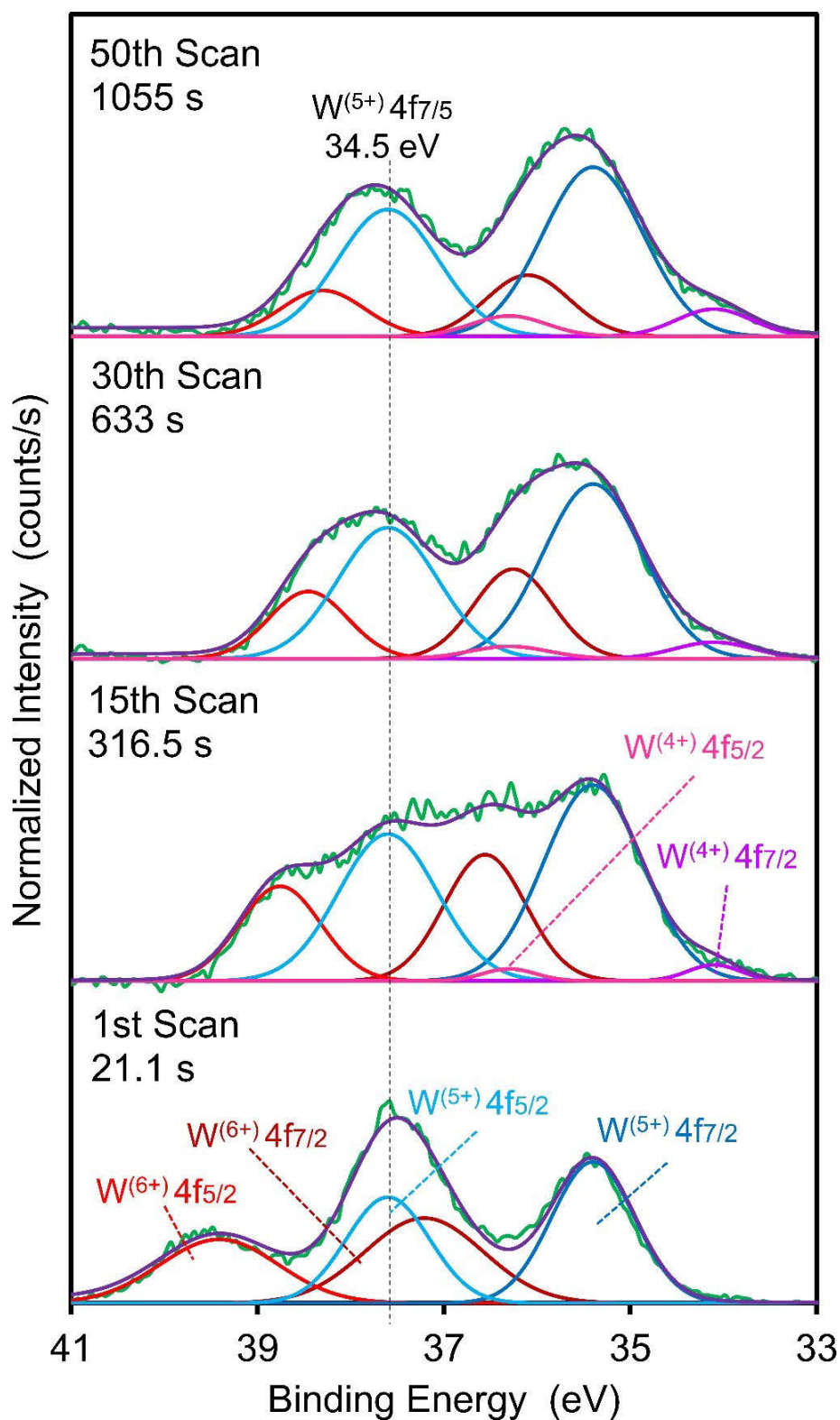


**Figure 6.2.1.** The first, fifteenth, thirtieth and fiftieth scans of the W4f core-level XPS spectra of CTA-W<sub>12</sub>.

The relative concentrations of the differing tungsten oxidation states which contribute to the W4f core-level XPS spectra change significantly with successive XPS scans. The first scan reveals a W<sup>6+</sup> and W<sup>5+</sup> concentration of 46.1 and 53.9%, respectively, indicating that the very first x-ray irradiation induces a considerable degree of reduction to the hybrid material, as was observed in Figure 5.2.4. The relative fraction of the reduced W<sup>5+</sup> states increases with increasing scan number until it constitutes 70.3% of the W4f spectrum by the fiftieth scan (a change of 16.4%), whilst the fraction of maximally oxidized W<sup>6+</sup> states decreases to 21.2% by the fiftieth scan (a change of 24.9%). This trend of increasing reduction with scan/irradiation time is further reflected in the evolution of W<sup>4+</sup> concentration, where it constitutes 0.0% of the W4f spectra within the first scan (within fitting errors) and 8.5% by the fiftieth scan. The evolution of the tungsten oxidation states across successive XPS scans is summarized within Table 6.2.1.

**Table 6.2.1.** Relative concentration (%) of W<sup>6+</sup>, W<sup>5+</sup> and W<sup>4+</sup> oxidation states across successive XPS scans.

<b>Scan Number</b>	<b>W<sup>6+</sup> (%)</b>	<b>W<sup>5+</sup> (%)</b>	<b>W<sup>4+</sup> (%)</b>
1	46.1	53.9	0.0
15	33.7	63.5	2.8
30	25.7	68.7	5.6
50	21.2	70.3	8.5

The large concentration of W<sup>5+</sup> at the start of the experiment is attributed to initial survey and test scans of CTA-W<sub>12</sub>, before the W4f spectrum was continually measured.

The sample exhibited a strong blue colour after these XPS measurements were taken, contributing to the evidence that reduced W<sup>5+</sup> and W<sup>4+</sup> species were produced during x-ray irradiation (Section 5.1.4). It can be said then, that x-rays irradiation also induces a photochromic response (or at least photo-colouration) in CTA-W<sub>12</sub>, somewhat similar to that of UV irradiation (Section 5.2). However, the reversibility of x-ray-induced photochromism has not been studied.

### 6.2.2 Kinetics of XPS induced reduction

The relative concentration of  $W^{6+}$ ,  $W^{5+}$  and  $W^{4+}$  oxidation states as a function of total XPS scan/irradiation time is displayed in Figure 6.2.2. The trends depicted complements the data displayed in Figure 6.2.1 and Table 6.2.1, showing an increasing reduced  $W^{5+}$  and  $W^{4+}$  concentration at the expense of maximally oxidized  $W^{6+}$ . Reduction of CTA- $W_{12}$  occurs the quickest during the first ~500 seconds (23 scans), before slowing and finally reaching a saturation point by ~900 seconds (42 scans). This initially fast and later slower behaviour can be adequately described with first-order kinetics, which is typical of many chemical reactions.<sup>295, 296</sup> Similar x-ray photoreduction kinetics have been observed by R. Steinberger *et al*<sup>298</sup> and F. Mercier-Bon *et al*<sup>70</sup> in their studies on the XPS-induced photoreductions of  $Cr^{6+}$  and  $U^{6+}$  compounds, respectively. However, the growth of  $W^{4+}$  seems to be relatively linear throughout the measured time, although this may be an artefact due to its much lower relative concentration.

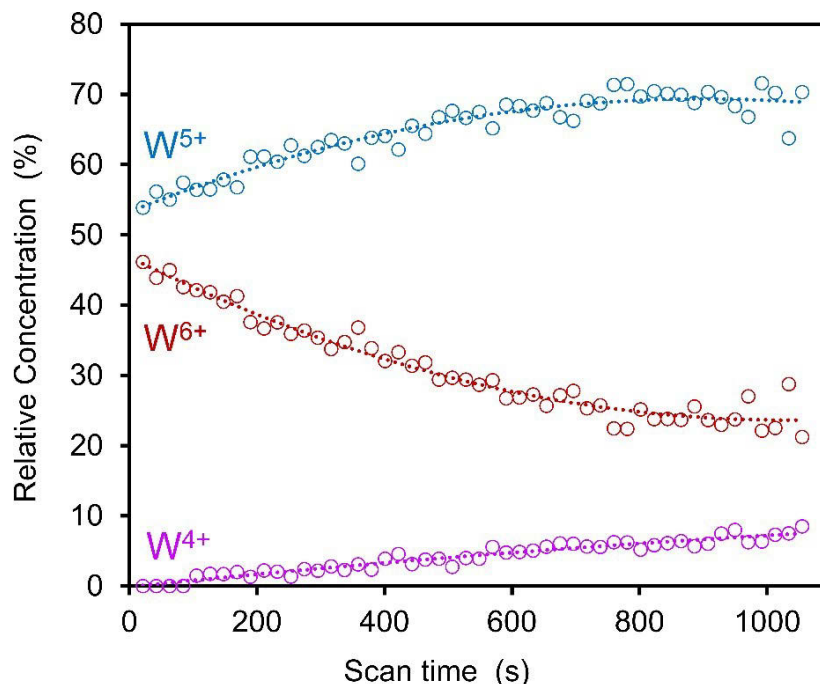


**Figure 6.2.2.** Relative concentration of  $W^{6+}$ ,  $W^{5+}$  and  $W^{4+}$  oxidation states as a function of scan time.

Quadratic polynomials provided the best fit to the trends of tungsten oxidation-state evolution, and are expressed in Equations 6.2.1-3:

$$W^{6+}(\%) = 2 \times 10^{-5} t^2 - 0.045 t + 46.81 \quad \text{Equation 6.2.1}$$

$$W^{5+}(\%) = -2 \times 10^{-5} t^2 + 0.0357 t + 52.395 \quad \text{Equation 6.2.2}$$

$$W^{4+}(\%) = 2 \times 10^{-6} t^2 - 0.0093 t - 0.1045 \quad \text{Equation 6.2.3}$$

Where  $t$  is measured irradiation/scan time in seconds. The  $R^2$  values of the  $W^{6+}(\%)$ ,  $W^{5+}(\%)$  and  $W^{4+}(\%)$  trends are 0.96, 0.91 and 0.93, respectively. Of course, the kinetics displayed here are highly specific to the current experiment, and strongly depend on the composition of the sample studied and the parameters of the measurement, such as photon energy and flux, temperature of the stage and the UHV's properties. However, these equations do reinforce the observed trend that  $W^{5+}$  and  $W^{4+}$  reduced specie concentrations are growing with irradiation/scan time at the expense of maximally-oxidized  $W^{6+}$ .

### 6.2.3 Binding Energy of W oxidation-states during XPS induced reduction

Figure 6.2.3 contains a 3D surface plot (Figure 6.2.3(a)) and a colour-map (Figure 6.2.3(b)) which displays all recorded W4f spectra (one to fifty) as a function of scan number. Within figure 3, the trend towards the growth of reduced, lower oxidation states on the lower binding-energy side of the spectra at the expense of more oxidized, higher oxidation states on the higher binding-energy side is clearly visible.

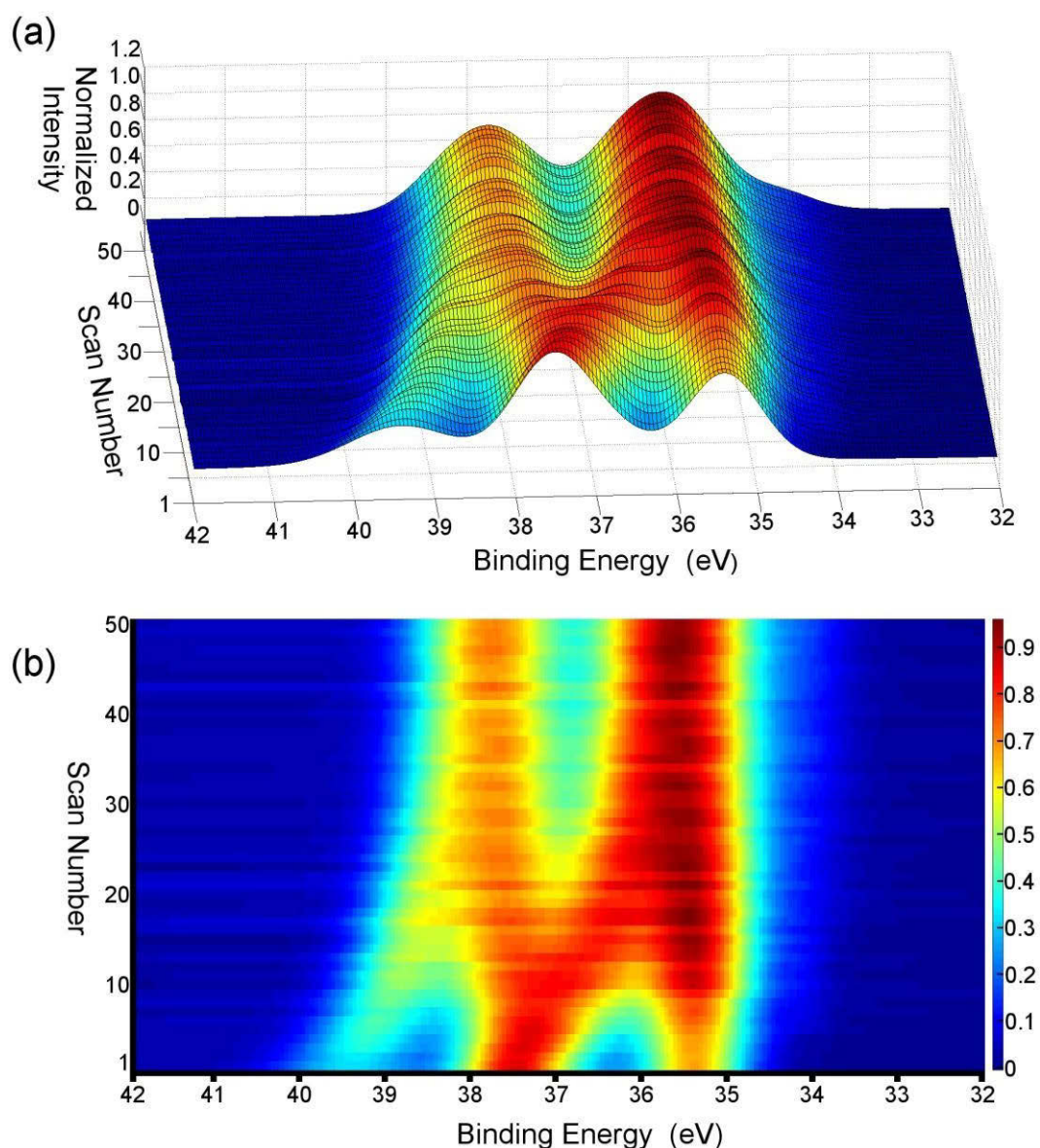


**Figure 6.2.3.** Surface plot (a) and coloured heat-map (b) of W4f x-ray photoelectron intensity as a function of XPS scan number.

Three local maxima are apparent within the first 20 recorded spectra, largely corresponding to the additive sum of the  $4f_{7/2}$  and  $4f_{5/2}$   $W^{6+}$  and  $W^{5+}$  doublets. During this time, the position (maximum intensity) of the  $W^{6+}$  attributed peaks is seen to shift from 39.4 eV towards lower binding-energies, residing at 38.3 eV by the fiftieth scan. F. Xie *et al* observed a similar behaviour of the  $W^{6+}$  oxidation state in their study of  $Ar^+$  bombarded  $WO_3$ .<sup>270</sup> By the 25<sup>th</sup> scan, the  $W^{6+}$  doublets are largely enveloped by the increasingly prominent  $W^{5+}$  peaks,

resulting in only two discernible local maxima in the W4f spectra by this time. These two dominant local maxima persist until the end of the experiment, with the lower-binding energy local-maxima slowly increasing in intensity and area during this time.

### 6.3.1 Probable causes of XPS induced Reduction

The above results suggest that the tungsten centres within the surfactant-POM organic-inorganic hybrid undergo a significant degree of reduction when measured by XPS. Because the above measurements were not conducted at elevated temperatures ( $> \sim 250^\circ$ ), it is highly unlikely that the UHV environment present in the XPS chamber ( $10^{-9}$  mbar) was sufficient to cause the evaporation of oxygen from the sample, and hence create oxygen-vacancies which would be able to reduce neighbouring tungsten cations.<sup>248, 309-311</sup> Therefore, the reduction of the sample must have been caused by the incidence of high-energy x-rays alone.

Considering Equation 6.1.1, x-ray interaction with CTA-W<sub>12</sub> would most likely occur at W-centres, since the atomic number of W ( $Z = 74$ ) is much higher than any other element present in the sample (Cl is the next highest with  $Z = 17$ , then O with  $Z = 8$ ). Since the W initially present in CTA-W<sub>12</sub> is at its highest oxidation-state, W<sup>6+</sup>, it is highly likely that the process of ‘Coulombic explosion’ (Section 6.1.3) is occurring with increasing scan/irradiation time.<sup>101, 102, 249, 261, 285</sup> However, x-ray induced photoreduction of purely inorganic tungsten oxide samples, i.e. WO<sub>3</sub>, seems to be a slow process, due to the small, positive reduction potential of W<sup>6+</sup> (+0.04 V vs hydrogen). For example, Suzer *et al* observed a small W<sup>5+</sup> concentration increase after 80 hours of x-ray irradiation.<sup>100</sup> In contrast, W<sup>5+</sup> and W<sup>4+</sup> concentration within CTA-W<sub>12</sub> increases significantly within 1055 seconds (~18 min). Therefore, other x-ray induced photoreduction processes must also be occurring.

The x-ray absorbing W-centres in CTA-W<sub>12</sub> are confined to the hydrophilic planes containing the POMs, CTA<sup>+</sup> cationic head-groups and water (Section 3.4.1). These planes are separated by the hydrophobic regions containing the alkyl-tails of CTA<sup>+</sup>, Figure 3.4.1. Considering the composition of the alkyl-tails, comprising of saturated C-H bonds, this plane would be electrically non-conductive. Therefore, the hydrophilic planes could be considered to be ‘thin-films’ containing the photo-reducible W<sup>6+</sup> and photo-oxidisable O<sup>2-</sup> sites, which are separated by insulating organic layers. This confinement would lead to a build-up of charge in these layers, which, considering the x-ray induced mechanisms of photoionization

and Coulombic explosion and the fact that tungsten-oxides are large band-gap semiconductors, would most likely be positive charge in the form of  $O^-$ ,  $O^0$  and  $O^+$  sites, figure 6.1.3.<sup>242, 249, 261</sup>

The proximity of organic groups, the  $CTA^+$  alkyl-tails, to the positively charged layers containing the  $O^+$  groups would likely accelerate oxygen-vacancy generation due to the reaction between  $O^+$  and C-H species, Figure 6.1.4.<sup>70, 100</sup> Furthermore, the C-N bonds within the  $CTA^+$  head-groups would be especially sensitive to x-ray induced photodecomposition (section 6.1.4), further injecting electrons into the sample.<sup>70, 98, 289</sup> It is likely all these factors; the confinement of photo-generated  $O^+$  species, and their proximity to oxidisable organic molecules, as well as x-ray sensitive C-N bonds, contribute to the relatively fast photo-reduction of the  $W^{6+}$  sites in  $CTA-W_{12}$  observed here.

Of course, as previously stated, the knowledge that x-ray-based measurements of such samples changes the sample's chemistry is not new.<sup>73, 95, 104, 106</sup> Even within this PhD, it was observed that continual synchrotron XRD caused structural disorder in  $CTA-W_{12}$ , as evidenced by the erosion of the (001) and (110) peaks, indicative of the lamellar and pseudo-hexagonal arrangement of POMs, respectively (Figures 5.4.1-2 and 5.4.5). The position and intensity of these peaks is highly dependent on  $CTA$  alkyl-tail conformality (interdigitation) and head-group order, which would be disrupted by the photo-decomposition of C-N bonds within the cationic head-group, and by the reaction of photo-oxidized  $O^+$  with C-H bonds within the alkyl tail, as postulated here. These realisations show that both hard (XRD) and soft (XPS) x-rays have the potential to change photo-redox active organic-inorganic materials during measurement time.

#### **6.4.1 Conclusions: XPS measurements of metal-oxide based inorganic-organic hybrids**

The results presented here show that care must be taken when considering data collected from XPS of photo-reducible metal-oxide hybrids, especially when these measurements are used to determine degrees of reduction within the sample. Many redox-active, photo-responsive oxide-containing organic-inorganic hybrids have similarly confined oxide-phases surrounded by organic species, such as surfactant-encapsulated or polymer-coated nanoparticles, nanowires and quantum-dots, and these would also be highly susceptible to soft x-ray induced photoreduction.<sup>21, 22, 254, 291</sup> Efforts should be made to minimize total

incident x-ray flux on such samples, especially when determining concentrations of (photo-)reduced metal-cations. Such photoreduction-minimization methods include decreasing the intensity of the incident beam, decreasing acquisition time or cryogenic cooling of the sample before and during measurement.<sup>4, 294, 295</sup> If these methods are not possible, then comments of final-states should be compared with spectra of as-prepared samples, with quantitative determinations of  $M^{n+}/M^{(n-1)+}$  ratios always being tentative.

## Chapter 7. Conclusions and prospective future work

### 7.1. Conclusions

The work undertaken in this PhD was aimed at addressing unanswered questions concerning the thermal- and photo-stability of polyoxometalate-surfactant hybrid materials. This was accomplished by synthesizing and studying a compound comprised of CTA<sup>+</sup> surfactants and isopolytungstate metatungstates in a lamellar structure. I designated this ‘CTA-W<sub>12</sub>’.

CTA-W<sub>12</sub> was formed by the hydrolysis of WCl<sub>6</sub> in CTA<sup>+</sup> micelles followed by alkalization to pH 7.5 with NH<sub>4</sub>OH. WCl<sub>6</sub> hydrolysis without the presence of CTA<sup>+</sup> unsurprisingly yielded WO<sub>3</sub>·2H<sub>2</sub>O. WCl<sub>6</sub> hydrolysis in the presence of CTA<sup>+</sup> but without further NH<sub>4</sub>OH addition yielded sheets of WO<sub>3</sub>·2H<sub>2</sub>O separated by the alkyl-tails of CTA<sup>+</sup>, similar to the lamellar structure of CTA-W<sub>12</sub>. Only the initially described method produced CTA-W<sub>12</sub>. WO<sub>3</sub>·2H<sub>2</sub>O/CTA<sup>+</sup> suspensions alkalized up to pH 7 did not change significantly, probably due to the hydrophobic Stern layer formed around the micelles. This would restrict the entry of OH<sup>-</sup> and prevent reaction with WO<sub>3</sub>·2H<sub>2</sub>O to produce metatungstates, [H<sub>2</sub>W<sub>12</sub>O<sub>40</sub>]<sup>6-</sup>. WO<sub>3</sub>·2H<sub>2</sub>O/CTA<sup>+</sup> suspensions that were alkalized beyond pH 8 and subsequently acidified with HCl to pH below 7.5 did not produce CTA-W<sub>12</sub> within three weeks due to the slow equilibrium kinetics of tungstate solutions. WO<sub>3</sub>·2H<sub>2</sub>O suspensions that were alkalized with NH<sub>4</sub>OH followed by the addition of CTA<sup>+</sup> did not produce CTA-W<sub>12</sub> either, also due to slow tungstate equilibrium kinetics. It therefore concluded that WO<sub>3</sub>·2H<sub>2</sub>O alkalization in the presence of methyl-ammonium cations is the fastest method to produce metatungstate with a high yield from WCl<sub>6</sub>.

The empirical formula of (CTA)<sub>7</sub>Cl[H<sub>2</sub>W<sub>12</sub>O<sub>40</sub>]<sup>6-</sup>·2H<sub>2</sub>O was confirmed via TGA and C, H and N micro-analysis. The lamellar structure of CTA-W<sub>12</sub> was confirmed with XRD and TEM, which revealed a bilayer thickness of ~24.5Å. A spread of similar distances around 24.5Å was also measured, which, along with the asymmetry of the (110) reflection indicative of POM organization, revealed inhomogeneity within the sample. This inhomogeneity was attributed to hyperdigitation of the CTA<sup>+</sup> surfactants, which occurs when a POM:surfactant ratio of 1:4 is exceeded. This caused the CTA<sup>+</sup> head-groups to bind to the POMs at inequivalent locations in the bilayer interface, causing the alkyl-tails to interdigitate with each other to differing degrees within the inter-lamellar gallery.

The purpose of the thermal studies was to gain an understanding of polyoxometalate-surfactant hybrid instability at higher temperatures and to determine the feasibility of producing porous networks of tungstates from polyoxometalate-surfactant precursors. Overall, CTA- $W_{12}$  underwent eight phase transitions from 30 to 800°C, which coincided with one major endothermic event and three major exothermic events during thermal decomposition in air. Less oxidizing environments were found to accelerate decomposition. Decomposition from 30 to ~200°C involved dehydration of the material, and an expansion of the lamellar distance caused by the CTA<sup>+</sup> alkyl-tails adopting a more normal orientation with respect to the bilayer interface. CTA<sup>+</sup> surfactants began decomposing at ~180°C in air by Hoffman degradation, then by cracking from ~245°C, and finally by combustion at ~320°C. Carbonaceous soft-coke persisted in the pores of the decomposing material, which slowly combusted from ~400°C until no further mass loss occurred by ~520°C. The metatungstate anion began decomposing at ~230°C in air into smaller fragments that rearranged into a highly crystalline HCP network before further decomposing to a bulk oxide at ~320°C. The production of a porous network of the HCP phase was attempted by removing organic material via Soxhlet extraction with  $CHCl_3$ . However, it was found that a significant portion of organic material remained after extraction, ~20 weight %, largely in the form of cationic methyl-ammonium species. This rendered the material non-porous. Surprisingly, the extracted  $CHCl_3$ -soluble fraction contained ~62 weight %  $WO_3$ , which revealed the mutual presence of two distinct tungsten-oxide phases within the HCP phase. One phase was found to be highly crystallographic and contained no organically-soluble alkyl-chain units, and the other was less crystallographic and contained organically-soluble alkyl-chain units. ATR FT-IR also confirmed the presence of different isopolytungstates within each of the two samples, which further revealed the complex thermal decomposition processes of surfactant-polyoxometalate hybrids. Organic material bound to the inorganic phase persisted until ~520°C, however porous phases were only stable up to ~320°C. Because of this, it is concluded that the production of porous tungstate or tungsten-oxide materials from surfactant-polyoxometalate precursors would be exceedingly difficult.

CTA- $W_{12}$  underwent a colour change from white to blue upon the incidence of UV irradiation, due to the formation of a broad absorption band centred on about 780 nm. This band was attributed to absorption-instigated IVCT processes between  $W^{6+}$  and photo-reduced

$W^{5+}$  sites. The formation of  $W^{5+}$  due to UV irradiation was confirmed by XPS. Coloured CTA- $W_{12}$  slowly faded in the presence of  $O_2$ . CTA- $W_{12}$  coloured to the same degree every time it was irradiated with UV light, however, the reflectance of the bleached state decreased upon the completion of each cycle during the first four cycles. This decreased reflectance in the bleached state was observed as a yellowing of the material. The change in absorbance between the bleached and coloured states,  $\Delta R$ , was constant beyond the fourth cycle, up to the final measurement of 18 cycles. CTA<sup>+</sup> was oxidized during photochromism, as evidenced by XPS, due to the formation of C-O, C=O and N-H groups. This chemical change was permanent, as evidenced by ATR FT-IR spectroscopy, and progressively increased with each photochromic cycle. Concurrently, the concentration of proton-donating C-H sites decreased with increasing photochromic cycles, also evidenced by ATR FT-IR spectroscopy. This suggested that protons were being donated from C-H groups to form the coloured charge-transfer complex, whereby the donated positive-charge stabilizes the reduced POM. The presence of N-H groups was also confirmed by GC-MS, due to the detection of 1-hexadecylamine after UV irradiation. A 9% mass loss was measured after 72 hours of UV irradiation, confirming the formation of volatile species during photochromism. Raman spectroscopy revealed the presence of long-lived oxygen-vacancy defects and, by extension,  $W^{5+}$  sites, in CTA- $W_{12}$  three days after UV irradiation. The consistency of  $\Delta R$  that was maintained beyond four photochromic cycles was ascribed to the formation of more reversible N-H proton transfer groups, as opposed to C-H sites which permanently oxidized upon proton-donation. An equilibrium between the formation of deep long-lived  $W^{5+}$  sites and the diffusion of  $O_2$  beyond four cycles may also contribute to the nearly constant  $\Delta R$ . It was concluded that CTA- $W_{12}$  should be reversibly photochromic as long as appropriate proton-transfer groups, such as C-H and N-H sites, were present to stabilize the reduced POM and the coloured charge-transfer complex. It has been suggested in previous publications that the irreversibility observed in many inorganic-organic photochromic compounds is due to side-reactions involving the permanent oxidation of the organic species, however, the present work may be the first time that this has been studied in detail. It is hoped that the new insights will enable researchers to design more durable photochromic materials in the future.

Structural changes accompanied the photochromic process of CTA- $W_{12}$ , as evidenced by XRD, UV irradiation, and subsequent colouration, was observed to coincide with an

increase in the lamellar distance, and a disorganization of the POMs. This was evidenced by the (001) peak shifting to lower  $2\theta$  and decreasing in intensity. Bleaching coincided with a partial restoration of the interlamellar distance and reordering of the POMs into a more regular arrangement, as evidenced by a partial restoration of the (001) peak to its original location and intensity. X-ray irradiation alone, from the synchrotron source, also caused disordering of the POMs. This is the first report, as far as I know, on structural changes that accompany photochromism, and it is hoped that this new insight leads to such materials also being considered in possible applications for their photo-mechanical properties.

X-ray irradiation affected CTA- $W_{12}$ , as evidenced by the presence of  $W^{5+}$  in the W4f XPS spectrum prior-to UV irradiation, as well as the disordering of the POMs during synchrotron XRD. To investigate the effects of X-ray irradiation further, the W4f spectrum of CTA- $W_{12}$  was continually scanned by XPS. The concentration of reduced  $W^{5+}$  and  $W^{4+}$  species increased at the expense of maximally oxidized  $W^{6+}$  as the scans accumulated. The increase of  $W^{5+}$  and  $W^{4+}$  concentrations occurred at a faster rate during the earlier scans as opposed to the later scans, indicative of first-order rate kinetics. Overall  $W^{6+}$  reduction occurred at a much faster rate in CTA- $W_{12}$  as compared to  $WO_3$  in previous studies. This was ascribed to the electrical isolation of the photo-reducible  $W^{6+}$  sites and photo-oxidizable  $O^{2-}$  sites within the thin hydrophilic layers by the surrounding non-conductive hydrophobic layers. This caused an accumulation of  $h^+$  in the valence-bands of the oxo-ligands within the layer, which readily reacted with neighbouring C-H sites producing volatile products and accelerated oxygen-vacancy generation. It is concluded that  $M^{n+}/M^{(n-1)+}$  (where  $M$  = metal and  $n$  = oxidation state) ratios of UV or visible-light photo-reduced samples determined by XPS should always be compared to non-irradiated controls. If this is not possible, then care must be taken to limit x-ray-induced photoreduction of the sample, such as limiting photon flux, reducing acquisition time or conducting the measurement under cryogenic conditions.

It is hoped the work undertaken during my PhD will contribute to the growing field of polyoxometalate-hybrid compounds, especially within the context of the stability of these compounds.

## **7.2. Future Work**

A number of possible avenues for future investigation have been opened from the work completed within this PhD. This includes revisiting the thermal decomposition of surfactant-POM hybrid compounds and their possible use as precursors to porous TMO materials. To try to avoid the collapse of the porous isopolytungstate/ $\text{WO}_x$  phase at high temperatures ( $\sim 300^\circ\text{C}$ ), organic matrices with low thermal stability, such as low thermal stability polymers, and/or weak association with the anionic POM, such as non-anionic surfactants, will need to be chosen. Other precursor mesophases, such as hexagonally arranged tubes of POMs, rather than the lamellar phase presented within this work (see Figure 1.1.8), could also aid in organic component removal at lower temperatures before the collapse of porosity.

It may also be beneficial to investigate the  $\text{CHCl}_3$ -insoluble fraction of phase V (from the thermal decomposition of CTA- $\text{W}_{12}$ ) in greater detail. This could include proton-conduction measurements or to assess its applicability as a battery anode. Products from the thermal decomposition of other POM-hybrid precursors described above could also be assed for the same applications.

A closer inspection of the photo-mechanical properties of photochromic materials is also warranted, and to identify possible applications of this process. It would be of interest to identify the reason for the initial rapid lamellar expansion when UV radiation is subjected to CTA- $\text{W}_{12}$ , and the quick semi-restoration of the lamellar space after irradiation has ceased. This may include monitoring the conformation of the  $\text{CTA}^+$  surfactants before, during and after UV irradiation, as well as the environment surrounding the cationic nitrogen within he head-group. Monitoring the structural conformation of the POM clusters themselves and the octahedra within them before, during and after UV irradiation may also yield insight.

Soft X-ray irradiation (such as XPS) with *in situ* Raman or IR spectroscopy could directly detect the production of volatile species during measurement and confirm the mechanism of accelerated W photoreduction hypothesized here. Monitoring the environment surrounding other elements in CTA- $\text{W}_{12}$ , such as the C 1s, O 1s and N1s orbitals, may also provide useful information as to why and how the samples undergoes such rapid photoreduction in comparison to other tungsten oxides. It may also be of interested to investigate the rate of in situ soft X-ray photoreduction in other related TMO-hybrid materials.

## References

1. Colusso, A.; Cortie, M.; Dowd, A.; McDonagh, A., Thermal stability of mesoscopic compounds of cetyltrimethylammonium and Keggin metatungstates. *Dalton Trans.* **2017**, 46, 11053–11062.
2. Colusso, A.; McDonagh, A.; Gentle, A.; Cortie, M., Photomechanical photochromism in a cetyltrimethylammonium isopolytungstate. *RSC Adv.* **2018**, 8, 18776–18783.
3. Colusso, A.; McDonagh, A.; Cortie, M., X-ray-induced reduction of a surfactant/polyoxotungstate hybrid compound. *Surf. Interface Anal.* **2018**.
4. Weinstock, I.; Schreiber, R.; Neumann, R., Dioxygen in Polyoxometalate Mediated Reactions. *Chem. Rev.* **2018**, 118, 2680–2717.
5. Tucher, J.; Wu, Y.; Nye, L.; Ivanovic-Burmazovic, I.; Khusniyarov, M.; Streb, C., Metal substitution in a Lindqvist polyoxometalate leads to improved photocatalytic performance. *Dalton Trans.* **2012**, 41, 9938–9943.
6. Clemente-Juan, J.; Coronado, E.; Gaita-Arin, A., Magnetic Polyoxometalates: From Molecular Magnetism to Molecular Spintronics and Quantum Computing. *Chem. Soc. Rev.* **2012**, 41, 7464–7478.
7. Proust, A.; Thouvenot, R.; Gouzerh, P., Functionalization of polyoxometalates: towards advanced applications in catalysis and materials science. *Chem. Commun.* **2008**, 2008, 1837–1852.
8. Uchida, S.; Mizuno, N., Design and syntheses of nano-structured ionic crystals with selective sorption properties. *Coord. Chem. Rev.* **2007**, 251, 2537–2546.
9. Leroy, F.; Miro, P.; Poblet, J.; Bo, C.; A'valos, J., Keggin Polyoxoanions in Aqueous Solution: Ion Pairing and Its Effect on Dynamic Properties by Molecular Dynamics Simulations. *J. Phys. Chem. B* **2008**, 112, 8591–8599.
10. Borrffis-Almenar, J.; Clemente, J.; Coronado, E.; Tsukerblat, B., Mixed-valence Polyoxometalate Clusters. I. Delocalization of Electronic Pairs in Dodecanuclear Heteropoly Blues with Keggin Structure. *Chem. Phys.* **1995**, 195, 1-15.
11. Hill, C.; Prosser-McCartha, C., Homogeneous Catalysis by Transition Metal Oxygen Anion Clusters. *Coord. Chem. Rev.* **1995**, 143, 407-455.

12. Weinstock, I., Homogeneous-Phase Electron-Transfer Reactions of Polyoxometalates. *Chem. Rev.* **1998**, 98, 113–170.
13. Kozhevnikov, I., Sustainable heterogeneous acid catalysis by heteropoly acids. *J. Mol. Catal. A: Chem.* **2007**, 262, 86–92.
14. Guo, Y.; Hu, C., Heterogeneous Photocatalysis by Solid Polyoxometalates. *J. Mol. Catal. A: Chem.* **2007**, 262, 136–148.
15. Tzirakis, M.; Lykakis, I.; Orfanopoulos, M., Decatungstate as an efficient photocatalyst in organic chemistry. *Chem. Soc. Rev.* **2009**, 38, 2609-2621.
16. Walsh, J.; Bond, A.; Forster, R.; Keyes, T., Hybrid Polyoxometalate Materials for Photo(Electro-) Chemical Applications. *Coord. Chem. Rev.* **2016**, 306, 217–234.
17. Ammam, M., Polyoxometalates: formation, structures, principal properties, main deposition methods and application in sensing. *J. Mater. Chem. A* **2013**, 1, 6291–6312.
18. Herrmann, S.; Ritchie, C.; Streb, C., Polyoxometalate – Conductive Polymer Composites for Energy Conversion, Energy Storage and Nanostructured Sensors. *Dalton Trans.* **2015**, 44, 7092–7104.
19. Ye, T.; Wang, J.; Dong, G.; Jiang, Y.; Feng, C.; Yang, Y., Recent Progress in the Application of Polyoxometalates for Dye-sensitized/Organic Solar Cells. *Chin. J. Chem.* **2016**, 34, 747—756.
20. Sivakumar, R.; Thomas, J.; Yoon, M., Polyoxometalate-based Molecular/Nano Composites: Advances in Environmental Remediation by Photocatalysis and Biomimetic Approaches to Solar Energy Conversion. *J. Photochem. Photobiol., C* **2012**, 13, 277– 298.
21. He, T.; Yao, J., Photochromism in composite and hybrid materials based on transition-metal oxides and polyoxometalates. *Prog. Mater Sci.* **2006**, 51, 810–879.
22. Wang, M.; Xu, G.; Zhang, Z.; Guo, G., Inorganic–organic hybrid photochromic materials. *Chem. Commun.* **2010**, 46, 361–376.
23. Baetens, R.; Jelle, B.; Gustavsen, A., Properties, Requirements and Possibilities of Smart Windows for Dynamic Daylight and Solar Energy Control in Buildings: A State-Of-The-Art Review. *Sol. Energy Mater. Sol. Cells* **2010**, 94, 87–105.
24. Liu, S.; Mohwald, H.; Volkmer, D.; Kurth, D., Polyoxometalate-Based Electro- and Photochromic Dual-Mode Devices. *Langmuir* **2006**, 22, 1949-1951.

25. Kortz, U.; Müller, A.; Slageren, J.; Schnack, J.; Dalal, N.; Dressel, M., Polyoxometalates: Fascinating Structures, Unique Magnetic Properties. *Coord. Chem. Rev.* **2009**, 253, 2315–2327.
26. Rhule, J.; Hill, C.; Judd, D., Polyoxometalates in Medicine. *Chem. Rev.* **1998**, 98, 327–357.
27. Dolbecq, A.; Dumas, E.; Mayer, C.; Mialane, P., Hybrid Organic-Inorganic Polyoxometalate Compounds: From Structural Diversity to Applications. *Chem. Rev.* **2010**, 110, 6009–6048.
28. Ito, T., Inorganic–Organic Hybrid Surfactant Crystals: Structural Aspects and Functions. *Crystals* **2016**, 6, 1-21.
29. Yin, P.; Li, D.; Liu, T., Solution Behaviors and Self-Assembly of Polyoxometalates as Models of Macroions and Amphiphilic Polyoxometalate–Organic Hybrids as Novel Surfactants. *Chem. Soc. Rev.* **2012**, 41, 7368–7383.
30. Nisar, A.; Wang, X., Surfactant-Encapsulated Polyoxometalate Building Blocks: Controlled Assembly and Their Catalytic Properties. *Dalton Trans.* **2012**, 41, 9832–9845.
31. Yan, Y.; Wu, L., Polyoxometalate-Incorporated Supramolecular Self-Assemblies: Structures and Functional Properties. *Isr. J. Chem.* **2011**, 51, 181 – 190.
32. Zhang, T.; Brown, J.; Oakley, R.; Faul, C., Towards Functional Nanostructures: Ionic Self-Assembly of Polyoxometalates and Surfactants. *Curr. Opin. Colloid Interface Sci.* **2009**, 14, 62–70.
33. Wu, H.; Yang, H.; Wang, W., Covalently-linked Polyoxometalate–polymer Hybrids: Optimizing Synthesis, Appealing Structures and Prospective Applications. *New J. Chem.* **2015**, 40, 886--897.
34. Peng, Z., Rational Synthesis of Covalently Bonded Organic– Inorganic Hybrids. *Angew. Chem. Int. Ed.* **2004**, 43, 930 –935.
35. Deshlahra, P.; Carr, R.; Iglesia, E., Ionic and Covalent Stabilization of Intermediates and Transition States in Catalysis by Solid Acids. *J. Am. Chem. Soc.* **2014**, 136, 15229–15247.
36. Wang, S.; Yang, G., Recent Advances in Polyoxometalate-Catalyzed Reactions. *Chem. Rev.* **2015**, 115, 4893–4962.

37. Katsoulis, D., A Survey of Applications of Polyoxometalates. *Chem. Rev.* **1998**, *98*, 359–387.
38. Du, D.; Qin, J.; Li, S.; Su, Z.; Lan, Y., Recent Advances in Porous Polyoxometalate-Based Metal–Organic Framework Materials. *Chem. Soc. Rev.* **2014**, *43*, 4615–4632.
39. Proust, A.; Matt, B.; Villanneau, R.; Guillemot, G.; Gouzerha, P.; Izzet, G., Functionalization and post-functionalization: a step towards polyoxometalate-based materials. *Chem. Soc. Rev.* **2012**, *41*, 7605–7622.
40. Liu, D.; Gui, J.; Park, Y.; Lu, F.; Sun, Z., New Simple Synthesis Route for Decatungstate Hybrids: Novel Thermo-Regulated Phase Transfer Catalysts for Selective Oxidation of Alcohols. *Catal. Lett.* **2012**, *142*, 1330–1335.
41. Qi, W.; Wang, Y.; Li, W.; Wu, L., Surfactant-Encapsulated Polyoxometalates as Immobilized Supramolecular Catalysts for Highly Efficient and Selective Oxidation Reactions. *Chem. Eur. J.* **2010**, *16*, 1068–1078.
42. Holles, J.; Dillon, C.; Labinger, J.; Davis, M., A Substrate-versatile Catalyst for the Selective Oxidation of Light Alkanes I. Reactivity. *J. Catal.* **2003**, *218*, 42–53.
43. Renneke, R.; Pasquali, M.; Hill, C., Polyoxometalate Systems for the Catalytic Selective Production of Nonthermodynamic Alkenes from Alkanes. Nature of Excited-State Deactivation Processes and Control of Subsequent Thermal Processes in Polyoxometalate Photoredox Chemistry. *J. Am. Ceram. Soc.* **1990**, *112*, 6585–6594.
44. Zhao, M.; Ou, S.; Wu, C., Porous Metal–Organic Frameworks for Heterogeneous Biomimetic Catalysis. *Acc. Chem. Res.* **2014**, *47*, 1199–1207.
45. Sun, C.; Liu, S.; Liang, D.; Shao, K.; Ren, Y.; Su, Z., Highly Stable Crystalline Catalysts Based on a Microporous Metal–Organic Framework and Polyoxometalates. *J. Am. Ceram. Soc.* **2009**, *131*, 1883–1888.
46. Zou, C.; Zhang, Z.; Xu, X.; Gong, Q.; Li, J.; Wu, C., A Multifunctional Organic–Inorganic Hybrid Structure Based on Mn<sup>III</sup>–Porphyrin and Polyoxometalate as a Highly Effective Dye Scavenger and Heterogenous Catalyst. *J. Am. Ceram. Soc.* **2012**, *134*, 87–90.
47. Song, J.; Luo, Z.; Britt, D.; Furukawa, H.; Yaghi, O.; Hardcastle, K.; Hill, C., A Multiunit Catalyst with Synergistic Stability and Reactivity: A Polyoxometalate–Metal

- Organic Framework for Aerobic Decontamination. *J. Am. Ceram. Soc.* **2011**, 133, 16839–16846.
48. Yamase, T., Photoredox Chemistry of Polyoxometalates as a Photocatalyst. *Catal. Surv. Asia* **2003**, 7, 203-217.
49. Marci, G.; García-López, E.; Palmisano, L., Heteropolyacid-Based Materials as Heterogeneous Photocatalysts. *Eur. J. Inorg. Chem.* **2014**, 2014, 21–35.
50. Maldotti, A.; Molinari, A., Design of Heterogeneous Photocatalysts Based on Metal Oxides to Control the Selectivity of Chemical Reactions. *Top. Curr. Chem.* **2011**, 303, 185-216.
51. Troupis, A.; Gkika, E.; Hiskia, A.; Papaconstantinou, E., Photocatalytic Reduction of Metals using Polyoxometallates: Recovery of Metals or Synthesis of Metal Nanoparticles. *C. R. Chimie* **2006**, 9, 851–857.
52. Dave, M.; Streb, C., Oxidative Photoreactivity of Mono-transition-metal Functionalized Lacunary Keggin Anions. *Dalton Trans.* **2015**, 44, 18919–18922.
53. Kornarakis, I.; Lykakis, I.; Vordosc, N.; Armatas, G., Efficient Visible-light Photocatalytic Activity by Band Alignment in Mesoporous Ternary Polyoxometalate–Ag<sub>2</sub>S–CdS Semiconductors. *Nanoscale* **2014**, 6, 8694–8703.
54. Shi, H.; Zhang, T.; Ana, T.; Li, B.; Wang, X., Enhancement of photocatalytic activity of nano-scale TiO<sub>2</sub> particles co-doped by rare earth elements and heteropolyacids. *J. Colloid Interface Sci.* **2012**, 380, 121–127.
55. Pearson, A.; Zheng, H.; Kalantar-zadeh, K.; Bhargava, S.; Bansal, V., Decoration of TiO<sub>2</sub> Nanotubes with Metal Nanoparticles Using Polyoxometalate as a UV-Switchable Reducing Agent for Enhanced Visible and Solar Light Photocatalysis. *Langmuir* **2012**, 28, 14470–14475.
56. Zhou, W.; Cao, M.; Li, N.; Su, S.; Zhao, X.; Wang, J.; Li, X.; Hu, C., Ag@AgHPW as a plasmonic catalyst for visible-light photocatalytic degradation of environmentally harmful organic pollutants. *Mater. Res. Bull.* **2013**, 48, 2308–2316.
57. Xu, L.; Wang, G.; Ma, F.; Zhao, Y.; Lu, N.; Guo, Y.; Yang, X., Photocatalytic Degradation of an Aqueous Sulfamethoxazole over the Metallic Silver and Keggin Unit Codoped Titania Nanocomposites. *Appl. Surf. Sci.* **2012**, 258, 7039–7046.

58. Yamase, T., Photo- and electrochromism of polyoxometalates and related materials. *Chem. Rev.* **1998**, 98, 307–325.
59. Luo, X.; Yang, C., Photochromic Ordered Mesoporous Hybrid Materials Based on Covalently Grafted Polyoxometalates. *Phys. Chem. Chem. Phys.* **2010**, 13, 7892–7902.
60. Xu, B.; Xu, L.; Gao, G.; Jin, Y., Nanosized multilayer films with concurrent photochromism and electrochromism based on Dawson-type polyoxometalate. *Appl. Surf. Sci.* **2007**, 253, 3190–3195.
61. Ji, Y.; Huang, L.; Hu, J.; Streb, C.; Song, Y., Polyoxometalate-functionalized Nanocarbon Materials for Energy Conversion, Energy Storage and Sensor Systems. *Energy Environ. Sci.* **2015**, 8, 776–789.
62. Poblet, J.; López, X.; Bo, C., Ab initio and DFT modelling of complex materials: towards the understanding of electronic and magnetic properties of polyoxometalates. *Chem. Soc. Rev.* **2005**, 32, 297–308.
63. Y.Song; McMillan, N.; Long, D.; Thiel, J.; Ding, Y.; Chen, H.; Gadegaard, N.; Cronin, L., Design of Hydrophobic Polyoxometalate Hybrid Assemblies Beyond Surfactant Encapsulation. *Chem. Eur. J.* **2008**, 14, 2349 – 2354.
64. Yang, Y.; Wang, Y.; Li, H.; Li, W.; Wu, L., Self-Assembly and Structural Evolution of Polyoxometalate-Anchored Dendron Complexes. *Chem. Eur. J.* **2010**, 16, 8062–8071.
65. Zhang, B.; Yin, P.; Haso, F.; Hu, L.; Liu, T., Soft Matter Approaches for Enhancing the Catalytic Capabilities of Polyoxometalate Clusters. *J. Clust. Sci.* **2014**, 25, 695–710.
66. Sun, H.; Li, H.; Bu, W.; Xu, M.; Wu, L., Self-Organized Microporous Structures Based on Surfactant-Encapsulated Polyoxometalate Complexes. *J. Phys. Chem. B* **2006**, 110, 24847-24854.
67. Zhang, J.; Li, W.; Wu, C.; Li, B.; Zhang, J.; Wu, L., Redox-Controlled Helical Self-Assembly of a Polyoxometalate Complex. *Chem. Eur. J.* **2014**, 2013, 8129 – 8135.
68. Nisar, A.; Lu, Y.; Wang, X., Assembling Polyoxometalate Clusters into Advanced Nanoarchitectures. *Chem. Mater.* **2010**, 22, 3511–3518.
69. Nisar, A.; Zhuang, J.; Wang, X., Cluster-Based Self-Assembly: Reversible Formation of Polyoxometalate Nanocones and Nanotubes. *Chem. Mater.* **2009**, 21, 3745–3751.

70. Dessapt, R.; Collet, M.; Coue', V.; Bujoli-Doeuff, M.; Jobic, S.; C.Lee; M.Whangbo, Kinetics of Coloration in Photochromic Organoammonium Polyoxomolybdates. *Inorg. Chem.* **2009**, 48, 574-580.
71. Mestl, G.; Ilkenhans, T.; Spielbauer, D.; Dieterle, M.; Timpe, O.; Kröhnerta, J.; Jentoft, F.; Knözinger, H.; Schlögl, R., Thermally and Chemically Induced Structural Transformations of Keggin-type Heteropoly Acid Catalysts. *Appl. Catal. A* **2001**, 210, 13–34.
72. Soler-Illia, G.; Sanchez, C.; Lebeau, B.; Patarin, J., Chemical Strategies To Design Textured Materials: from Microporous and Mesoporous Oxides to Nanonetworks and Hierarchical Structures. *Chem. Rev.* **2002**, 102, 4093–4138.
73. Feng, W.; Ding, Y.; Liu, Y.; Lu, R., The photochromic process of polyoxometalate-based nanocomposite thin film by in situ AFM and spectroscopy. *Mater. Chem. Phys.* **2006**, 98, 347–352.
74. Nair, H.; Miller, J.; Stach, E.; Baertsch, C., Mechanism of Dynamic Structural Reorganization in Polyoxometalate Catalysts. *J. Catal.* **2010**, 270, 40–47.
75. Janik, M.; Bardin, B.; Davis, R.; Neurock, M., A Quantum Chemical Study of the Decomposition of Keggin Structured Heteropolyacids. *J. Phys. Chem. B* **2006**, 110, 4170-4178.
76. Damyanova, S.; Gomez, L.; Banares, M.; Fierro, J., Thermal Behavior of 12-Molybdophosphoric Acid Supported on Zirconium-Loaded Silica. *Chem. Mater.* **2000**, 12, 501-510.
77. Huang, Z.; Song, J.; Pan, L.; Zhang, X.; Wang, L.; Zou, J., Tungsten Oxides for Photocatalysis, Electrochemistry, and Phototherapy. *Adv. Mater.* **2015**, 27, 5309–5327.
78. Cong, S.; Geng, F.; Zhao, Z., Tungsten Oxide Materials for Optoelectronic Applications. *Adv. Mater.* **2016**, 28, 10518–10528.
79. Ciesla, U.; Schuth, F., Ordered mesoporous materials. *Microporous and Mesoporous Mater.* **1999**, 27, 131–149.
80. Ciesla, U.; Demuth, D.; Leon, R.; Petroff, P.; Stucky, G.; Unger, K.; Schüth, F., Surfactant controlled preparation of mesostructured transition-metal oxide compounds. *J. Chem. Soc., Chem. Commun.* **1994**, 0, 1387-1388.

81. Larson, P., X-ray Induced Photoelectron and Auger Spectra of Cu, CuO, Cu<sub>2</sub>O and Cu<sub>2</sub>S Thin Films. *J. Electron. Spectrosc. Relat. Phenom.* **1974**, 4, 213-218.
82. Lozzi, L.; Ottaviano, L.; Passacantando, M.; Santucci, S.; Cantalini, C., The influence of air and vacuum thermal treatments on the NO<sub>2</sub> gas sensitivity of WO thin films prepared by thermal evaporation. *Thin Solid Films* **2001**, 391, 224-228.
83. Nelder, J.; Mead, R., A Simplex Method for Function Minimization. *The Computer Journal* **1965**, 7, 308-313.
84. Stein, A.; Fendorf, M.; Jarvie, T.; Mueller, K.; Benesi, A.; Mallouk, T., Salt-Gel Synthesis of Porous Transition-Metal Oxides. *Chem. Mater.* **1995**, 7, 304-313.
85. Poirier, G.; Nalin, M.; Cescato, L.; Messaddeq, Y.; Ribeiro, S., Bulk Photochromism in a Tungstate-Phosphate Glass: A New Optical Memory Material? *J. Chem. Phys.* **2006**, 125, 161101-161103.
86. Granqvist, C., Electrochromic tungsten oxide films: Review of progress 1993-1998. *Sol. Energy Mater. Sol. Cells* **1999**, 60, 201-262.
87. Djaoued, Y.; Balaji, S.; Bruning, R., Electrochromic Devices Based on Porous Tungsten Oxide Thin Films. *J. Nanomater.* **2012**, 2012, 1-9.
88. Heravi, M.; Sadjadi, S., Recent Developments in Use of Heteropolyacids, Their Salts and Polyoxometalates in Organic Synthesis. *J. Iran. Chem. Soc.* **2009**, 6, 1-54.
89. Wang, X.; Wei, Z.; Yu, C.; Zhang, X.; Zhang, Y., Reversible Wettability of Tungsten Trioxide Films with Novel Dandelion-like Structures. *Z. Anorg. Allg. Chem.* **2012**, 638, 231-235.
90. Wang, S.; Feng, X.; Yao, J.; Jiang, L., Controlling Wettability and Photochromism in a Dual-Responsive Tungsten Oxide Film. *Angew. Chem. Int. Ed.* **2006**, 45, 1264-1267.
91. Zhang, L.; Gu, W.; Dong, Z.; Liu, X.; Li, B.; Liu, M., Syntheses, structures and properties of a series of photochromic hybrids based on Keggin tungstophosphates. *J. Solid State Chem.* **2009**, 182, 1040-1044.
92. Zhang, T.; Feng, W.; Lu, R.; Zhang, X.; Jina, M.; Lia, T.; Zhao, Y.; Yao, J., Synthesis and Characterization of Polymetalate Based Photochromic Inorganic-Organic Nanocomposites. *Thin Solid Films* **2002**, 402, 237-241.
93. Poulos, A.; Constantin, D.; Davidson, P.; Imperor, M.; Pansu, B.; Panine, P.; Nicole, L.; Sanchez, C., Photochromic Hybrid Organic-Inorganic Liquid-Crystalline

Materials Built from Nonionic Surfactants and Polyoxometalates: Elaboration and Structural Study. *Langmuir* **2008**, *24*, 6285-6291.

94. Ai, L.; Feng, W.; Chen, J.; Liu, Y.; Cai, W., Evaluation of Microstructure and Photochromic Behavior of Polyvinyl Alcohol Nanocomposite Films Containing Polyoxometalates. *Mater. Chem. Phys.* **2008**, *109*, 131–136.

95. Colusso, A.; Cortie, M.; Dowd, A.; McDonagh, A., Thermal stability of mesoscopic compounds of cetyltrimethylammonium and Keggin metatungstates. *Dalton Trans.* **2017**, *46*, 11053–11062.

96. Xu, J.; Volfova, H.; Mulder, R.; Goerigk, L.; Bryant, G.; Riedle, E.; Ritchie, C., Visible-Light-Driven “On”/“Off” Photochromism of a Polyoxometalate Diarylethene Coordination Complex. *J. Am. Chem. Soc.* **2018**, *140*, 10482–10487.

97. Fong, Y.; Visser, B.; Gascooke, J.; Cowie, B.; Thomsen, L.; Metha, G.; Buntine, M.; Harris, H., Photoreduction Kinetics of Sodium Tetrachloroaurate under Synchrotron Soft X-ray Exposure. *Langmuir* **2011**, *27*, 8099–8104.

98. Kuepper, K.; Taubitz, C.; Taubitz, D.; Wiedwald, U.; Scheurer, A.; Sperner, S.; Saalfrank, R.; Kappler, J.; Joly, L.; Ziemann, P.; Neumann, M., Magnetic Ground-State and Systematic X-ray Photoreduction Studies of an Iron-Based Star-Shaped Complex. *J. Phys. Chem. Lett.* **2011**, *2*, 1491–1496.

99. Halada, G.; Clayton, C., Photoreduction of hexavalent chromium during X-ray photoelectron spectroscopy analysis of electrochemical and thermal films. *J. Electrochem. Soc.* **1991**, *138*, 2921-2927.

100. George, S.; Fub, J.; Guob, Y.; Drury, O.; Friedrich, S.; Rauchfuss, T.; Volkers, P.; Peters, J.; Scott, V.; Browne, S.; Thomase, C.; Cramer, S., X-ray photochemistry in iron complexes from Fe(0) to Fe(IV) – Can a bug become a feature? *Inorg. Chim. Acta* **2008**, *361*, 1157–1165.

101. Chen, Y.; Wang, S.; Xue, L.; Zhang, Z.; Li, H.; Wu, L.; Wang, Y.; Li, F.; Zhang, F.; Li, Y., Insights into the working mechanism of cathode interlayers in polymer solar cells via [(C<sub>8</sub>H<sub>17</sub>)<sub>4</sub>N]<sub>4</sub>[SiW<sub>12</sub>O<sub>40</sub>]. *J. Mater. Chem. A* **2016**, *4*, 19189–19196.

102. Steinberger, R.; Duchoslav, J.; Greunz, T.; Arndt, M.; Stifter, D., Investigation of the chemical stability of different Cr(VI) based compounds during regular X-ray photoelectron spectroscopy measurements. *Corros. Sci.* **2015**, *90*, 562–571.

103. Harb, S.; Santos, F. d.; Caetano, B.; Pulcinelli, S.; Santilli, C.; Hammer, P., Structural properties of cerium doped siloxane–PMMA hybrid coatings with high anticorrosive performance. *RSC Adv.* **2015**, *5*, 15414–15424.
104. Ku, Z.; Jin, S.; Zhou, H., Synthesis and characterization of two charge-transfer salts based on Keggin-type polyoxometalates and morpholinebiguanide. *Koord. Khim.* **2009**, *35*, 195–199.
105. Ottaviano, L.; Bussolotti, F.; Lozzi, L.; Passacantando, M.; Rosa, S. L.; Santucci, S., Core level and valence band investigation of WO thin films with synchrotron radiation. *Thin Solid Films* **2003**, *436*, 9-16.
106. Feldman, V.; Zezin, A.; Abramchuk, S.; Zezina, E., X- ray Induced Formation of Metal Nanoparticles from Interpolyelectrolyte Complexes with Copper and Silver Ions: The Radiation-Chemical Contrast. *J. Phys. Chem. C* **2013**, *117*, 7286–7293.
107. Cottineau, T.; Rouet, A.; Fernandez, V.; Brohana, L.; Richard-Plouet, M., Intermediate band in the gap of photosensitive hybrid gel based on titanium oxide: role of coordinated ligands during photoreduction. *J. Mater. Chem.* **2014**, *2*, 11499–11508.
108. Skinner, W.; Prestidge, C.; Smart, R., Irradiation Effects During XPS Studies of Cu(II) Activation of Zinc Sulphide. *Surf. Interface Anal.* **1996**, *24*, 620-626.
109. Kepert, D., Isopolytungstates. *Prog. Inorg. Chem.* **1962**, *4*, 200-273.
110. Lopez, X.; Carbo, J.; Bo, C.; Poblet, J., Structure, Properties and Reactivity of Polyoxometalates: A Theoretical Perspective. *Chem. Soc. Rev.* **2012**, *41*, 7537–7571.
111. Bilal, B.; Haufe, P.; Moller, R., Raman Spectroscopic and Electrochemical Study of Polymerization of Tungsten (VI) in a Hydrothermal Solution up to 1 kbar and 200°C. *Physica B+C* **1986**, *139-140*, 721-724.
112. Hastings, J.; Howarth, O., A <sup>183</sup>W, <sup>1</sup>H and <sup>17</sup>O Nuclear Magnetic Resonance Study of Aqueous Isopolytungstates. *J. Chem. Soc. Dalton Trans.* **1992**, *1992*, 209-215.
113. Prasad, S., Tungstate Polyanions: An Electrometric Study. *Quimica Nova* **1994**, *17*, 31-34.
114. Cruywagen, J.; Merwe, L., Tungsten(VI) Equilibria: A Potentiometric and Calorimetric Investigation. *J. Chem. Soc. Dalton Trans.* **1987**, *1987*, 1701-1705.

115. Oliva, A. d. I.; Sans, V.; Miras, H.; Long, D.; Cronin, L., Coding the Assembly of Polyoxotungstates with a Programmable Reaction System. *Inorg. Chem.* **2017**, *56*, 5089–5095.
116. Holclajtner-Antunovic, I.; Bajuk-Bogdanovic, D.; Todorovic, M.; Mioc, U.; Zakrzewska, J.; Uskokovic-Markovic, S., Spectroscopic Study of Stability and Molecular Species of 12-Tungstophosphoric Acid in Aqueous Solution. *Can. J. Chem.* **2008**, *86*, 996–1004.
117. Smith, B.; Patrick, V., Quantitative Determination of Aqueous Dodecatungstophosphoric Acid Speciation by NMR Spectroscopy. *Aust. J. Chem.* **2004**, *57*, 261–268.
118. Smith, B.; Patrick, V., Quantitative Determination of Sodium Dodecatungstosilicate Speciation by  $^{183}\text{W}$  Nuclear Magnetic Resonance Spectroscopy. *Aust. J. Chem.* **2002**, *55*, 281–286.
119. Keggin, J., The structure and formula of 12-phosphotungstic acid. *Proc. Royal Soc. London. Series A.* **1934**, *144*, 75-100.
120. Zavalij, P.; Guo, J.; Whittingham, M.; Jacobson, R.; Pecharsky, V.; Bucher, C.; Hwu, S., Keggin Cluster Formation by Hydrothermal Reaction of Tungsten Trioxide with Methyl Substituted Ammonium: The Crystal Structure of Two Novel Compounds,  $[\text{NH}_2(\text{CH}_3)_2]_6\text{H}_2\text{W}_{12}\text{O}_{40}\cdot 4\text{H}_2\text{O}$  and  $[\text{N}(\text{CH}_3)_4]_2]_6\text{H}_2\text{W}_{12}\text{O}_{40}\cdot 2\text{H}_2\text{O}$ . *J. Solid State Chem.* **1996**, *123*, 83–92.
121. Chaumont, A.; Wipf, G., Ion aggregation in concentrated aqueous and methanol solutions of polyoxometallates Keggin anions: the effect of counterions investigated by molecular dynamics simulations. *Phys. Chem. Chem. Phys.* **2008**, *10*, 6940–6953.
122. Pradeep, C.; Long, D.; Cronin, L., Cations in Control: Crystal Engineering Polyoxometalate Clusters using Cation Directed Self-assembly. *Dalton Trans.* **2010**, *39*, 9443–9457.
123. Balázs, C.; Wang, L.; Zayim, E.; Szilágyi, I.; Sedlackova, K.; Pfeifer, J.; Tóth, A.; Gouma, P., Nanosize hexagonal tungsten oxide for gas sensing applications. *J. Eur. Ceram. Soc.* **2008**, *28*, 913–917.
124. Knoth, W.; Harlow, R., New Tungstophosphates:  $\text{Cs}_6\text{W}_5\text{P}_2\text{O}_{23}$ ,  $\text{Cs}_7\text{W}_{10}\text{PO}_{36}$ , and  $\text{Cs}_7\text{Na}_2\text{W}_{10}\text{O}_{37}$ . *J. Am. Ceram. Soc.* **1981**, *103*, 1865-1867.

125. Canny, J.; Tize, A.; Thouvenot, R.; Heme, G., Disubstituted Tungstosilicates. 1. Synthesis, Stability, and Structure of the Lacunary Precursor Polyanion  $\gamma$ -SiW<sub>10</sub>O<sub>36</sub><sup>8-</sup>. *Inorg. Chem.* **1986**, *25*, (13), 2114-2119.
126. Daniel, M.; Desbat, B.; Lassegues, J.; Gerand, B.; Figlarz, M., Infrared and Raman Study of WO<sub>3</sub> Tungsten Trioxides and WO<sub>3</sub>·xH<sub>2</sub>O Tungsten Trioxide Hydrates. *J. Solid State Chem.* **1987**, *67*, 235-247.
127. Whittingham, M.; Guo, J.; Chen, R.; Chirayil, T.; Janauer, G.; Zavalij, P., The Hydrothermal Synthesis of New Oxide Materials. *Solid State Ionics* **1995**, *75*, 257-268.
128. Whittingham, M.; Chen, R.; Chirayil, T.; Zavalij, P., The Intercalation and Hydrothermal Chemistry of Solid Electrodes. *Solid State Ionics* **1997**, *94*, 227-238.
129. Ban, T.; Ito, T.; Ohya, Y., Phase Transition between Layered Tungstates and Polyoxotungstates in Aqueous Solutions. *Inorg. Chem.* **2013**, *52*, 10520–10524.
130. Li, W.; Sasaki, A.; Oozu, H.; Aoki, K.; Kakushima, K.; Kataoka, Y.; Nishiyama, A.; Sugii, N.; Wakabayashi, H.; Tsutsui, K.; Natori, K.; Iwai, H., Improvement of charge/discharge performance for lithium ion batteries with tungsten trioxide electrodes. *Microelectronics Reliability* **2015**, *5*, 402–406.
131. Yoon, S.; Jo, C.; Noh, S.; Lee, C.; Song, J.; Lee, J., Development of a high-performance anode for lithium ion batteries using novel ordered mesoporous tungsten oxide materials with high electrical conductivity. *Phys. Chem. Chem. Phys.* **2011**, *13*, 11060–11066.
132. Asami, M.; Ichida, H.; Sasaki, Y., The Structure of Hexakis(tetramethylammonium) Dihydrogendodecatungstate Enneahydrate, [(CH<sub>3</sub>)<sub>4</sub>N]<sub>6</sub>[H<sub>2</sub>W<sub>12</sub>O<sub>40</sub>].9H<sub>2</sub>O. *Acta Cryst.* **1984**, *C40*, 35-37.
133. Huo, Q.; Margolese, D.; Ciesla, U.; Demuth, D.; Feng, P.; Gier, T.; Sieger, P.; Firouzi, A.; Chmelka, B.; Schuth, F.; Stucky, G., Organization of Organic Molecules with Inorganic Molecular Species into Nanocomposite Biphase Arrays. *Chem. Mater.* **1994**, *6*, 1176-1191.
134. Nyman, M.; Ingersoll, D.; Singh, S.; Bonhomme, F.; Alam, T.; Brinker, C.; Rodriguez, M., Comparative Study of Inorganic Cluster-Surfactant Arrays. *Chem. Mater.* **2005**, *17*, 2885-2895.

135. Nyman, M.; Rodriguez, M.; Anderson, T.; Ingersoll, D., Two Structures Toward Understanding Evolution from Surfactant-Polyoxometalate Lamellae to Surfactant-Encapsulated Polyoxometalates. *Cryst. Growth Des.* **2009**, *9*, 3590–3597.
136. Wang, Y.; Li, W.; Wu, L., Organic-Inorganic Hybrid Supramolecular Gels of Surfactant-Encapsulated Polyoxometalates. *Langmuir* **2009**, *25*, 13194–13200.
137. Tan, C., Self-assembly and Morphology Change of Four Organic-Polyoxometalate Hybrids with Different Solid Structures from 2D Lamellar to 3D Hexagonal Forms. *J. Mol. Struct.* **2017**, *1130*, 276-283.
138. Rangan, K.; Kanatzidis, M., Mesolamellar thiogermanates  $[\text{C}_n\text{H}_{2n+1}\text{NH}_3]_4\text{Ge}_4\text{S}_{10}$ . *Inorg. Chim. Acta* **2004**, *357*, 4036–4044.
139. Ito, T.; Nakagawa, M.; Kobayashi, J.; Matsumoto, T.; Otobe, S.; Naruke, H., Layered and Molecular-structural Control in Polyoxomolybdate Hybrid Crystals by Surfactant Chain Length. *J. Mol. Struct.* **2016**, *1106*, 220-226.
140. Tanev, P.; Liang, Y.; Pinnavaia, T., Assembly of Mesoporous Lamellar Silicas with Hierarchical Particle Architectures. *J. Am. Chem. Soc.* **1997**, *119*, 8616-8624.
141. Polarz, S.; Landsmann, S.; Klaiber, A., Hybrid Surfactant Systems with Inorganic Constituents. *Angew. Chem. Int. Ed.* **2014**, *53*, 946-954.
142. Sayari, A.; Liu, P., Non-Silica Periodic Mesoporous Materials: Recent Progress. *Microporous Mater.* **1997**, *12*, 149-177.
143. Huo, Q.; Margolese, D.; Stucky, G., Surfactant Control of Phases in the Synthesis of Mesoporous Silica-Based Materials. *Chem. Mater.* **1996**, *8*, 1147-1160.
144. Szleifer, I.; Kramer, D.; Ben-Shaul, A.; Roux, D.; Gelbart, W., Curvature Elasticity of Pure and Mixed Surfactant Films. *Phys. Rev. Lett.* **1988**, *60*, 1966-1969.
145. Li, W.; Wu, L., Nano-Hybrid Liquid Crystals from the Self-Assembly of Surfactant-Encapsulated Polyoxometalate Complexes. *Chin. J. Chem.* **2015**, *33*, 15-23.
146. Li, W.; Yi, S.; Wu, Y.; Wu, L., Thermotropic Mesomorphic Behavior of Surfactant-Encapsulated Polyoxometalate Hybrids. *J. Phys. Chem. B* **2006**, *110*, 16961-16966.
147. Bonhomme, F.; Kanatzidis, M., Structurally Characterized Mesoporous Hybrid Surfactant-Inorganic Lamellar Phases Containing the Adamantane  $[\text{Ge}_4\text{S}_{10}]_4^-$  Anion: Synthesis and Properties. *Chem. Mater.* **1998**, *10*, 1153-1159.

148. Yang, Y.; Yue, L.; Li, H.; Maher, E.; Li, Y.; Wang, Y.; Wu, L.; Yam, V., Photo-Responsive Self-Assembly of an Azobenzene-Ended Surfactant-Encapsulated Polyoxometalate Complex for Modulating Catalytic Reactions. *Small* **2012**, *8*, 3105–3110.
149. Monnier, A.; Schuth, F.; Huo, Q.; Kumar, D.; Margolese, D.; Maxwell, R.; Stucky, G.; Krishnamurty, M.; Petroff, P.; Firouzi, A.; Janicke, M.; Chmelka, B., Cooperative Formation of Inorganic-Organic Interfaces in the Synthesis of Silicate Mesostructures. *Science* **1993**, *261*, 1299-1303.
150. Fogden, A.; Ninham, B., The Bending Modulus of Ionic Lamellar Phases. *Langmuir* **1991**, *7*, 590-595.
151. Li, J.; Marler, B.; Kessler, H.; Soulard, M.; Kallus, S., Synthesis, Structure Analysis, and Characterization of a New Thiostannate,  $(C_{12}H_{25}NH_3)_4[Sn_2S_6] \cdot 2H_2O$ . *Inorg. Chem.* **1997**, *36*, 4697-4701.
152. Gabb, D.; Pradeep, C.; Boyd, T.; Mitchell, S.; Miras, H.; Long, D.; Cronin, L., A general route for the transfer of large, highly-charged polyoxometalates from aqueous to organic phase. *Polyhedron* **2013**, *52*, 159–164.
153. Redkin, A.; Bondarenko, G., Raman Spectra of Tungsten-Bearing Solutions. *J. Solution Chem.* **2010**, *39*, 1549–1561.
154. Himeno, S.; Yoshihara, M.; Maekawa, M., Formation of voltammetrically-active isopolyoxotungstate complexes in aqueous  $CH_3CN$  media. *Inorg. Chim. Acta* **2000**, *298*, 165-171.
155. Buckley, R.; Clark, R., Structural and Electronic Properties of some Polymolybdates Reducible to Molybdenum Blues. *Coord. Chem. Rev.* **1985**, *65*, 167-218.
156. Rocchiccioli-Deltcheff, C.; Fournier, M.; Franck, R.; Thouvenot, R., Vibrational investigations of polyoxometalates. 2. Evidence for anion-anion interactions in molybdenum(VI) and tungsten(VI) compounds related to the Keggin structure. *Inorg. Chem.* **1983**, *22*, 207-216.
157. Thouvenot, R.; Fournier, M.; Franck, R.; Rocchiccioli-Deltcheff, C., Vibrational Investigations of Polyoxometalates. 3. Isomerism in Molybdenum(VI) and Tungsten(VI) Compounds Related to the Keggin Structure. *Inorg. Chem.* **1984**, *23*, 598-605.

158. Ingham, B.; Chong, S.; Tallon, J., Layered Tungsten Oxide-Based Organic-Inorganic Hybrid Materials: An Infrared and Raman Study. *J. Phys. Chem. B* **2005**, 109, 4936-4940.
159. Venkataraman, N.; Vasudevan, S., Interdigitation of an Intercalated Surfactant Bilayer. *J. Phys. Chem. B* **2001**, 105, 7639-7650.
160. Vaia, R.; Teukolsky, R.; Giannelis, E., Interlayer Structure and Molecular Environment of Alkylammonium Layered Silicates. *Chem. Mater.* **1994**, 6, 1017-1022.
161. Yu, X., The Preparation and Characterization of Cetyltrimethylammonium Intercalated Muscovite. *Microporous Mesoporous Mater.* **2007**, 98, 70–79.
162. Jakubowska, A., Stability of Anion Binding with Monomers of a Cationic Surfactant. *ChemPhysChem* **2008**, 9, 829 – 831.
163. Chacon, C.; Rodriguez-Perez, M.; Oskam, G.; Rodri'guez-Gattorno, G., Synthesis and characterization of WO<sub>3</sub> polymorphs: monoclinic, orthorhombic and hexagonal structures. *J. Mater. Sci: Mater. Electron.* **2015**, 26, 5526–5531.
164. Zheng, J.; Song, G.; Hong, J.; Van, T.; Pawar, A.; Kim, D.; Kim, C.; Haider, Z.; Kang, Y., Facile Fabrication of WO<sub>3</sub> Nanoplates Thin Films with Dominant Crystal Facet of (002) for Water Splitting. *Cryst. Growth Des.* **2014**, 14, 6057–6066.
165. Yang, J.; Li, W.; Li, J.; Sun, D.; Chen, Q., Hydrothermal synthesis and photoelectrochemical properties of vertically aligned tungsten trioxide (hydrate) plate-like arrays fabricated directly on FTO substrates. *J. Mater. Chem.* **2012**, 22, 17744–17752.
166. Kida, T.; Nishiyama, A.; Yuasa, M.; Shimanoe, K.; Yamazoe, N., Highly sensitive NO<sub>2</sub> sensors using lamellar-structured WO<sub>3</sub> particles prepared by an acidification method. *Sens. Actuators B: Chem.* **2009**, 135, 568–574.
167. Holland, B.; Isbester, P.; Munson, E.; Stein, A., Transformation of layered polyoxometallate cluster salts into mesoporous materials. *Mater. Res. Bull.* **1999**, 34, 471-482.
168. Picquart, M.; Castro-Garcia, S.; Livage, J.; Julien, C.; Haro-Poniatowski, E., Structural Studies During Gelation of WO<sub>3</sub> Investigated by In-situ Raman Spectroscopy. *J. Sol-Gel Sci. Technol.* **2000**, 18, 199-206.

169. Highfield, J.; Moffat, J., Characterization of 12-Tungstophosphoric Acid and Related Salts Using Photoacoustic Spectroscopy in the Infrared Region. *J. Catal.* **1984**, *88*, 177-187.
170. Nomiya, K.; Miwa, M., Structural Stability Index of Heteropoly- and Isopoly-Anions. *Polyhedron* **1984**, *3*, 341-346.
171. Ortner, H., Characterization of Isopolytungstates by Molecular Sieve Chromatography. *Anal. Chem.* **1975**, *47*, 162-165.
172. Bunton, C.; Ohmenzetter, K.; Sepulveda, L., Binding of Hydrogen Ions to Anionic Micelles. *J. Phys. Chem.* **1977**, *81*, (21).
173. Bunton, C.; Gan, L.; Moffatt, J.; Romsted, L., Reactions in Micelles of Cetyltrimethylammonium Hydroxide. Test of the Pseudophase Model for Kinetics. *J. Phys. Chem.* **1981**, *85*, 4118-4125.
174. Chaimovich, H.; Bonilha, J.; Poltli, M.; Quina, F., Ion Exchange in Micellar Solutions. 2.<sup>1</sup> Binding of Hydroxide Ion to Positive Micelles. *J. Phys. Chem.* **1979**, *83*, 1851-1854.
175. Baker, L.; Glick, D., Present General Status of Understanding of Heteropoly Electrolytes and a Tracing of Some Major Highlights in the History of Their Elucidation. *Chem. Rev.* **1998**, *98*, 3-49.
176. Gibson, L., Mesosilica materials and organic pollutant adsorption: part A removal from air. *Chem. Soc. Rev.* **2014**, *43*, 5163-5172.
177. Brinker, C., Hydrolysis and Condensation of Silicates: Effects on Structure. *J. Non-Cryst. Solids* **1988**, *100*, 31-50.
178. Yang, P.; Zhao, D.; Margolese, D.; Chmelka, B.; Stucky, G., Block Copolymer Templating Syntheses of Mesoporous Metal Oxides with Large Ordering Lengths and Semicrystalline Framework. *Chem. Mater.* **1999**, *11*, 2813-2826.
179. Shi, L.; Wang, Y.; Li, B.; Wu, L., Polyoxometalate complexes for oxidative kinetic resolution of secondary alcohols: unique effects of chiral environment, immobilization and aggregation. *Dalton Trans.* **2014**, *43*, 9177-9188.
180. Xie, W.; Gao, Z.; Pan, W.; Hunter, D.; Singh, A.; Vaia, R., Thermal Degradation Chemistry of Alkyl Quaternary Ammonium Montmorillonite. *Chem. Mater.* **2001**, *13*, 2979-2990.

181. Kleitz, F.; Schmidt, W.; Schüth, F., Evolution of mesoporous materials during the calcination process: structural and chemical behaviour. *Microporous Mesoporous Mater.* **2001**, 44-45, 95-109.
182. Goworek, J.; Kierys, A.; Gac, W.; Borówka, A.; Kusak, R., Thermal degradation of CTAB in as-synthesized MCM-41. *J. Thermal Anal. Calorimetry* **2009**, 96, 375-382.
183. Kruk, M.; Jaroniec, M.; Sayari, A., A Unified Interpretation of High-Temperature Pore Size Expansion Processes in MCM-41 Mesoporous Silicas. *J. Phys. Chem. B* **1999**, 103, 4590-4598.
184. March, J., *Advanced Organic Chemistry, Reactions, Mechanisms and Structures*. 4th ed.; John Wiley and Sons: New York, 1992.
185. Corma, A.; Kan, Q.; Navarro, M.; Perez-Pariente, J.; Rey, F., Synthesis of MCM-41 with Different Pore Diameters without Addition of Auxiliary Organics. *Chem. Mater.* **1997**, 9, 2123-2126.
186. Bertus, L.; Duta, A., Synthesis of WO<sub>3</sub> Thin Films by Surfactant Mediated Spray Pyrolysis. *Ceram. Int.* **2012**, 38, 2873–2882.
187. Wienold, J.; Timpe, O.; Ressler, T., In Situ Investigations of Structure-Activity Relationships in Heteropolyoxomolybdates as Partial Oxidation Catalysts. *Chem. Eur. J.* **2003**, 9, 6007-6017.
188. Zheng, H.; Ou, J.; Strano, M.; Kaner, R.; Mitchell, A.; Kalantar-zadeh, K., Nanostructured Tungsten Oxide – Properties, Synthesis, and Applications. *Adv. Funct. Mater.* **2011**, 21, 2175–2196.
189. Zheng, J.; Haider, Z.; Van, T.; Pawar, A.; Kang, M.; Kim, C.; Kang, Y., Tuning of the crystal engineering and photoelectrochemical properties of crystalline tungsten oxide for optoelectronic device applications. *CrystEngComm* **2015**, 17, 6070–6093.
190. Roussel, P.; Labbe, P.; Groult, D., Symmetry and twins in the monophosphate tungsten bronze series (PO<sub>2</sub>)<sub>4</sub>(WO<sub>3</sub>)<sub>2m</sub> (2 < m < 14). *Acta Crystallogr. B* **1999**, B56, 377-391.
191. Polaczek, A.; Pekata, M.; Obuszko, Z., Magnetic susceptibility and thermoelectric power of tungsten intermediary oxides. *J. Phys.: Condens. Matter* **1994**, 6, 7909-7919.

192. Lin, H.; Zhou, F.; Liu, C.; Ozolins, V., Non-Grotthuss Proton Diffusion Mechanism in Tungsten Oxide Dihydrate from First-principles Calculations. *J. Mater. Chem. A* **2014**, 2, 12280–12288.
193. Kuti, L.; Bhella, S.; Thangadurai, V., Revisiting Tungsten Trioxide Hydrates (TTHs) Synthesis - Is There Anything New? *Inorg. Chem.* **2009**, 48, 6804–6811.
194. Yoon, S.; Woo, S.; Jung, K.; Song, H., Conductive surface modification of cauliflower-like WO<sub>3</sub> and its electrochemical properties for lithium-ion batteries. *J. Alloys Compd.* **2014**, 613, 187–192.
195. Garcia-Sanchez, R.; Ahmido, T.; Casimir, D.; Baliga, S.; Misra, P., Thermal Effects Associated with the Raman Spectroscopy of WO<sub>3</sub> Gas-Sensor Materials. *J. Phys. Chem. A* **2013**, 117, 13825–13831.
196. Li, D.; Chandra, D.; Saito, K.; Yui, T.; Yagi, M., Unique and facile solvothermal synthesis of mesoporous WO<sub>3</sub> using a solid precursor and a surfactant template as a photoanode for visible-light-driven water oxidation. *Nanoscale Res. Lett.* **2014**, 9, 542–550.
197. Lee, Y.; Lee, T.; Jang, W.; Soon, A., Unraveling the Intercalation Chemistry of Hexagonal Tungsten Bronze and Its Optical Responses. *Chem. Mater.* **2016**, 28, 4528–4535.
198. Szilágyi, I.; Pfeifer, J.; Balázs, C.; Tóth, A.; Varga-Josepovits, K.; Madarász, J.; Pokol, G., Thermal Stability of Hexagonal Tungsten Trioxide in Air. *J. Therm. Anal. Calorim.* **2008**, 94, 499–505.
199. Potin, V.; Bruyere, S.; Gillet, M.; Domechini, B.; Bourgeois, S., Growth, Structure, and Stability of K<sub>x</sub>WO<sub>3</sub> Nanorods on Mica Substrate. *J. Phys. Chem. C* **2012**, 116, 1921–1929.
200. Szilágyi, I.; Madarász, J.; Pokol, G.; Király, P.; Tárkányi, G.; Saukko, S.; Mizsei, J.; Toth, A.; Szabo, A.; Varga-Josepovits, K., Stability and Controlled Composition of Hexagonal WO<sub>3</sub>. *Chem. Mater.* **2008**, 20, 4116–4125.
201. Szilágyi, I.; Hange, F.; Madarász, J.; Pokol, G., In situ HT-XRD Study on the Formation of Hexagonal Ammonium Tungsten Bronze by Partial Reduction of Ammonium Paratungstate Tetrahydrate. *European Journal of Inorganic Chemistry* **2006**, 2006, 3413–3418.

202. Liu, G.; Wang, S.; Nie, Y.; Sun, X.; Zhang, Y.; Tang, Y., Electrostatic-induced synthesis of tungsten bronze nanostructures with excellent photo-to-thermal conversion behavior. *J. Mater. Chem. A* **2013**, 1, 10120–10129.
203. Griffith, C.; Luca, V., Ion-Exchange Properties of Microporous Tungstates. *Chem. Mater.* **2004**, 16, 4992-4999.
204. Pfeifer, J.; Balazsi, C.; Kiss, B.; Pecz, B.; Toth, A., The influence of residual sodium on the formation and reductive decomposition of hexagonal tungsten oxide. *J. Mater. Sci. Lett.* **1999**, 18, 1103– 1105.
205. Balazsi, C.; Pfeifer, J., Development of tungsten oxide hydrate phases during precipitation, room temperature ripening and hydrothermal treatment. *Solid State Ionics* **2002**, 151, 353–358.
206. Kooli, F.; Mianhui, L.; Alshahateet, S.; Chen, F.; Yinghuai, Z., Characterization and thermal stability properties of intercalated Na-magadiite with cetyltrimethylammonium (C16TMA) surfactants. *J. Phys. Chem. Solids* **2006**, 67, 926–931.
207. Bielariski, A.; Malecka, A.; Kubelkova, L., Infrared Study of the Thermal Decomposition of Heteropolyacids of the Series  $H_{3+x}PMo_{12-x}V_xO_{40}$ . *J. Chem. Soc., Faraday Trans. 1* **1989**, 85, 2847-2856.
208. Damyanova, S.; Fierro, J., Structural Features and Thermal Stability of Titania-Supported 12-Molybdophosphoric Heteropoly Compounds. *Chem. Mater.* **1998**, 10, 871-879.
209. Klotsmana, S.; Kaigorodova, V.; Ermakovb, A.; Rudenko, V., Formation Enthalpies of Vacancy–Oxygen Complexes and Single Vacancies in the Core of Grain Boundaries in Polycrystalline Cr, Ta, and W. *Mater. Lett.* **2005**, 59, 166–170.
210. Cope, A.; Trumbull, E., *Organic Reactions 11*. 1st ed.; John Wiley and Sons: New York, 1960.
211. Meng, X.; Wang, H.; Song, S.; Zhang, H., Proton-Conducting Crystalline Porous Materials. *Chem. Soc. Rev.* **2017**, 46, 464-480.
212. Mioc, U.; Todorovic, M.; Davidovic, M.; Colomban, P.; Holclajtner-Antunovic, I., Heteropoly compounds–From proton conductors to biomedical agents. *Solid State Ionics* **2005**, 176, 3005 – 3017.

213. Chen, C.; Wang, Q.; Lei, P.; Song, W.; Ma, W.; Zhao, J., Photodegradation of Dye Pollutants Catalyzed by Porous K3PW12O40 under Visible Irradiation. *Environ. Sci. Technol.* **2006**, 40, 3965-3970.
214. Karuppasamy, A.; Subrahmanyam, A., Electron beam induced coloration and luminescence in layered structure of WO<sub>3</sub> thin films grown by pulsed dc magnetron sputtering. *J. Appl. Phys.* **2007**, 101, 113522-113527.
215. Feng, M.; Pan, A.; Zhang, H.; Li, Z.; Li, F.; Liu, H.; Shi, D.; Zou, B.; Gao, H., Strong photoluminescence of nanostructured crystalline tungsten oxide thin films. *Appl. Phys. Lett.* **2005**, 86, 141901-141903.
216. Lambert, J., *Introduction to Organic Spectroscopy*. Macmillan: New York, 1987.
217. Busca, G., Differentiation of mono-oxo and polyoxo and of monomeric and polymeric vanadate, molybdate and tungstate species in metal oxide catalysts by IR and Raman spectroscopy. *J. Raman Spectrosc.* **2002**, 33, 348-358.
218. Atia, H.; Armbruster, U.; Martin, A., Dehydration of glycerol in gas phase using heteropolyacid catalysts as active compounds. *J. Catal.* **2008**, 258, 71–82.
219. López-Salinas, E.; Hernández-Cortéz, J.; Schifter, I.; Torres-García, E.; Navarrete, J.; Gutiérrez-Carrillo, A.; López, T.; Lottici, P.; Bersani, D., Thermal stability of 12-tungstophosphoric acid supported on zirconia. *Appl. Catal., A* **2000**, 193, 215–225.
220. Lee, K.; Mizuno, N.; Okuhara, T.; Misono, M., Catalysis by Heteropoly Compounds XIII. An Infrared Study of Ethanol and Diethyl Ether in Pseudoliquid Phase of 12-Tungstophosphoric Acid. *Bull. Chem. Soc. Jpn.* **1989**, 62, 1731-1739.
221. Zhang, F.; Wu, H.; Xu, Y.; Li, Y.; Jiao, H., Structure and stability of neutral polyoxometalate cages: (Mo<sub>2</sub>O<sub>6</sub>)<sub>m</sub> (m = 1–13). *J. Mol. Model.* **2006**, 12, 551–558.
222. Southward, D.; Vaughan, J.; O'Connor, C., Infrared and Thermal Analysis Studies of heteropoly Acids. *J. Catal.* **1994**, 153, 293-303.
223. Madarász, J.; Szilágyi, I.; Hangeb, F.; Pokol, G., Comparative evolved gas analyses (TG-FTIR, TG/DTA-MS) and solid state (FTIR, XRD) studies on thermal decomposition of ammonium paratungstate tetrahydrate (APT) in air. *J. Anal. Appl. Pyrolysis* **2004**, 72, 197–201.
224. Hunyadi, D.; Sajo, I.; Szilágyi, I., Structure and thermal decomposition of ammonium metatungstate. *J. Therm. Anal. Calorim.* **2014**, 116, 329–337.

225. Tian, Z.; Tong, W.; Wang, J.; Duan, N.; Krishnan, V.; Suib, S., Manganese Oxide Mesoporous Structures - Mixed-Valent Semiconducting Catalysts. *Science* **1997**, 276, 926-930.
226. Meija, J.; Coplen, T.; Berglund, M.; Brand, W.; Bièvre, P.; Gröning, M.; Holden, N.; Irrgeher, J.; Loss, R.; Walczyk, T.; Prohaska, T., Atomic Weights of the Elements 2013 (IUPAC Technical Report). *Pure Appl. Chem.* **2016**, 88, 265–291.
227. Jansen, S.; Singh, D.; Wang, S., Cluster Fragmentation and Orbital Analysis: A Theoretical Study of Cohesive Interactions and Electronic Properties of Polyoxometalates with the Keggin Structure. *Chem. Mater.* **1994**, 6, 146-155.
228. Berzelius, J., Beitrag zur naheren Kenntnifs des Molybdans. *Annalen Der Physik* **1826**, 82, 369–392.
229. Keggin, J., Structure of the Molecule of 12-Phosphotungstic Acid. *Nature* **1933**, 131, 908-909.
230. Zhang, F.; Zhang, X.; Wu, H.; Jiao, H., Structural and Electronic Properties of Hetero-Transition-Metal Keggin Anions: A DFT Study of a/B-[XW<sub>12</sub>O<sub>40</sub>]<sup>n-</sup> (X = Cr<sup>VI</sup>, V<sup>V</sup>, Ti<sup>IV</sup>, Fe<sup>III</sup>, Co<sup>III</sup>, Ni<sup>III</sup>, Co<sup>II</sup>, and Zn<sup>II</sup>) Relative Stability. *J. Phys. Chem. A* **2007**, 111, 159-166.
231. Uehara, K.; Miyachi, T.; Nakajima, T.; Mizuno, N., Effects of Heteroatoms on Electronic States of DivanadiumSubstituted  $\gamma$ -Keggin-type Polyoxometalates. *Inorg. Chem.* **2014**, 53, 3907–3918.
232. Fernandez, J.; Lopez, X.; Poblet, J., A DFT study on the effect of metal, anion charge, heteroatom and structure upon the relative basicities of polyoxoanions. *J. Mol. Catal. A: Chem.* **2006**, 262, 236–242.
233. Maestre, J.; Lopez, X.; Bo, C.; Poblet, J.; Casan-Pastor, N., Electronic and Magnetic Properties of R-Keggin Anions: A DFT Study of [XM<sub>12</sub>O<sub>40</sub>]<sup>n-</sup>, (M ) W, Mo; X ) Al<sup>III</sup>, Si<sup>IV</sup>, P<sup>V</sup>, Fe<sup>III</sup>, Co<sup>II</sup>, Co<sup>III</sup> ) and [SiM<sub>11</sub>VO<sub>40</sub>]<sup>m-</sup> (M ) Mo and W). *J. Am. Chem. Soc.* **2001**, 123, 3749-3758.
234. Li, J., Electronic Structures, (d-p) $\pi$  Conjugation Effects, and Spectroscopic Properties of Polyoxometalates: M<sub>6</sub> O<sub>19</sub><sup>2-</sup> (M=Cr, Mo,W). *J. Cluster Sci.* **2001**, 13, 137-163.

235. Zhong, X.; Liu, Y.; Tang, X.; Wu, Q.; Li, L.; Yu, Y., Polyoxometalate cured epoxy resins with photochromic properties. *Colloid Polym. Sci.* **2012**, 290.
236. Knotek, M.; Feibelman, P., Stability of ionically bonded surfaces in ionizing environments. *Surf. Sci.* **1979**, 90, 78-90.
237. Zhao, W.; Wang, Z.; Shen, X.; Li, J.; Xu, C.; Gan, Z., Hydrogen generation via photoelectrocatalytic water splitting using a tungsten trioxide catalyst under visible light irradiation. *Int. J. Hydrogen Energy* **2012**, 37, 908-915.
238. Bridgeman, A.; Cavigliasso, G., Structure and Bonding in [M6O19]<sup>n-</sup> Isopolyanions. *Inorg. Chem.* **2002**, 41, 1761-1770.
239. Barton, D.; Shtein, M.; Wilson, R.; Soled, S.; Iglesia, E., Structure and Electronic Properties of Solid Acids Based on Tungsten Oxide Nanostructures. *J. Phys. Chem. B* **1999**, 103, 630-640.
240. Livage, C. S. J.; Launay, J.; Fournier, M., Electron Delocalization in Mixed-Valence Tungsten Polyanions. *J. Am. Chem. Soc.* **1983**, 105, 6817-6823.
241. Jeannin, Y.; Launay, J.; Sedjadi, M. S., Crystal and Molecular Structure of the Six-Electron-Reduced Form of Metatungstate  $\text{Rb}_4\text{H}_8[\text{H}_2\text{W}_{12}\text{O}_{40}] \cdot \sim 18\text{H}_2\text{O}$ : Occurrence of a Metal-Metal Bonded Subcluster in a Heteropolyanion Framework. *Inorg. Chem.* **1980**, 19, 2933-2935.
242. Smith, S.; Christian, J., Mechanism of the coupled 24-electron reduction and transformations among the “blues”, the “browns” and the “reds” of ammonium metatungstate. *Electrochim. Acta* **2008**, 53, 2994-3001.
243. Pope, M., Heteropoly and Isopoly Anions as Oxo Complexes and Their Reducibility to Mixed-Valence “Blues”. *Inorg. Chem.* **1972**, 11, 1973-1974.
244. Feibelman, P.; Knotek, M., Reinterpretation of electron-stimulated desorption data from chemisorption systems. *Phys. Rev. B: Condens. Matter* **1978**, 18, 6531-6539.
245. Zubavichus, Y.; Zharnikov, M.; Shaporenko, A.; Fuchs, O.; Weinhardt, L.; Heske, C.; Umbach, E.; Denlinger, J.; Grunze, M., Soft X-ray induced decomposition of phenylalanine and tyrosine: A comparative study. *J. Phys. Chem. A* **2004**, 108, 4557-4565.
246. Jing, X.; Zou, D.; Meng, Q.; Zhang, W.; Zhang, F.; Feng, W.; Hanb, X., Fabrication and visible-light photochromism of novel hybrid inorganic-organic film based on polyoxometalates and ethyl cellulose. *Inorg. Chem. Commun.* **2014**, 46, 149-154.

247. Hiskia, A.; Mylonas, A.; Papaconstantinou, E., Comparison of the photoredox properties of polyoxometallates and semiconducting particles. *Chem. Soc. Rev.* **2001**, *30*, 62–69.
248. Leghari, S.; Sajjad, S.; Zhang, J., A time saving and cost effective route for metal oxides activation. *RSC Adv.* **2014**, *4*, 5248–5253.
249. Cazaux, J., About the charge compensation of insulating samples in XPS. *J. Electron Spectrosc. Relat. Phenom.* **2000**, *113*, 15–33.
250. Chen, J.; Liu, Y.; Xiong, D.; Feng, W.; Cai, W., Preparation and photochromic behavior of crosslinked polymer thin films containing polyoxometalates. *Thin Solid Films* **2008**, *516*, 2864–2868.
251. Gomez-Romero, P.; Casan-Pastor, N., Photoredox Chemistry in Oxide Clusters. Photochromic and Redox Properties of Polyoxometalates in Connection with Analog Solid State Colloidal Systems. *J. Phys. Chem.* **1996**, *100*, 12448–12454.
252. Huang, Y.; Pan, Q.; Dong, X.; Cheng, Z., Synthesis and Photochromism of a Novel Organic–Inorganic Hybrid Film Embedded with Polyoxometalates. *Mater. Chem. Phys.* **2006**, *97*, 431–436.
253. Jr., M. d. O.; Souza, A. d.; Schneider, J.; Rodrigues-Filho, U., Local Structure and Photochromic Response in Ormosils Containing Dodecatungstophosphoric Acid. *Chem. Mater.* **2011**, *23*, 953–963.
254. Pruethiarenun, K.; Isobe, T.; Matsushita, S.; Ye, J.; Nakajima, A., Comparative study of photoinduced wettability conversion between  $[\text{PW}_{12}\text{O}_{40}]^{3-}$ /brookite and  $[\text{SiW}_{12}\text{O}_{40}]^{4-}$ /brookite hybrid film. *Mater. Chem. Phys.* **2014**, *144*, 327e334.
255. Jiang, M.; Wang, E.; Wei, G.; Xu, L.; Li, Z., Photochromic Inorganic–Organic Multilayer Films Based on Polyoxometalates and Poly(ethylenimine). *J. Colloid Interface Sci.* **2004**, *275*, 596–600.
256. Feng, W.; Zhang, T.; Liu, Y.; Lu, R.; Li, T.; Zhao, Y.; Yao, J., Novel Hybrid Inorganic-organic Film Based on the Tungstophosphate Acid-polyacrylamide System: Photochromic Behavior and Mechanism. *J. Mater. Res.* **2002**, *17*, 133–136.
257. Kozhevnikov, I., Catalysis by Heteropoly Acids and Multicomponent Polyoxometalates in Liquid-Phase Reactions. *Chem. Rev.* **1998**, *98*, 171–198.

258. Kozhevnikov, I.; Matveev, K., Homogeneous Catalysts based on Heteropoly Acids (Review). *Appl. Catal.* **1982**, 5, 135-150.
259. Neumann, R., Polyoxometalate Complexes in Organic Oxidation Chemistry. *Prog. Inorg. Chem.* **1998**, 47, 317-370.
260. Hill, C.; Bouchard, D., Catalytic Photochemical Dehydrogenation of Organic Substrates by Polyoxometalates. *J. Am. Chem. Soc.* **1985**, 107, 5148-5157.
261. Cazaux, J., Mechanisms of charging in electron spectroscopy. *J. Electron Spectrosc. Relat. Phenom.* **1999**, 105, 155-185.
262. Knotek, M.; Feibelman, P., Ion desorption by core-hole Auger decay. *Phys. Rev. Lett.* **1978**, 40, 964-967.
263. Khenkin, A.; Neumann, R., Low-Temperature Activation of Dioxygen and Hydrocarbon Oxidation Catalyzed by a Phosphovanadomolybdate: Evidence for a Mars ± van Krevelen Type Mechanism in a Homogeneous Liquid Phase. *Angew. Chem. Int. Ed.* **2000**, 39, 4088-4090.
264. Khenkin, A.; Weiner, L.; Wang, Y.; Neumann, R., Electron and Oxygen Transfer in Polyoxometalate,  $H_5PV_2Mo_{10}O_{40}$ , Catalyzed Oxidation of Aromatic and Alkyl Aromatic Compounds: Evidence for Aerobic Mars-van Krevelen-Type Reactions in the Liquid Homogeneous Phase. *J. Am. Chem. Soc.* **2001**, 123, 8531-8542.
265. Yamase, T.; Takabayashi, N.; Kaji, M., Solution Photochemistry of Tetrakis(tetrabutylammonium) Decatungstate(VI) and Catalytic Hydrogen Evolution from Alcohols. *J. Chem. Soc. Dalton Trans.* **1984**, 1984, 793-799.
266. Zhang, T.; Feng, W.; Fu, Y.; Lu, R.; Bao, C.; Zhang, X.; Zhao, B.; Sun, C.; Li, T.; Zhao, Y.; Yao, J., Self-assembled organic-inorganic composite superlattice thin films incorporating photo- and electro-chemically active phosphomolybdate anion. *J. Mater. Chem.* **2002**, 12, 1453-1458.
267. Baer, D.; Engelhard, M.; Lea, A., Introduction to surface science spectra data on electron and x-ray damage: Sample degradation during XPS and AES measurements. *Surf. Sci. Spectra* **2003**, 10, 47-56.
268. Bechinger, C.; Oefinger, G.; Herminghaus, S.; Leiderer, P., On the fundamental role of oxygen for the photochromic effect of  $WO_3$ . *J. Appl. Phys.* **1993**, 74, 4527-4533.

269. Santucci, S.; Cantalini, C.; Crivellari, M.; Lozzi, L.; Ottaviano, L.; Passacantando, M., X-ray Photoemission Spectroscopy and Scanning Tunneling Spectroscopy Study on the Thermal Stability of WO<sub>3</sub> Thin Films. *J. Vac. Sci. Technol. A* **2000**, 18, 1077-1082.
270. Xie, F.; Gong, L.; Liu, X.; Tao, Y.; Zhang, W.; Chen, S.; Meng, H.; Chen, J., XPS Studies on Surface Reduction of Tungsten Oxide Nanowire Film by Ar<sup>+</sup> Bombardment. *J. Electron. Spectrosc. Relat. Phenom.* **2012**, 185, 112– 118.
271. Dixon, R.; Williams, J.; Morris, D.; Rebane, J.; Jones, F.; Egdell, R.; Downes, S., Electronic States at Oxygen Deficient WO<sub>3</sub>(001) Surfaces: A Study by Resonant Photoemission. *Surf. Sci.* **1998**, 399, 199-211.
272. Leftheriotis, G.; Papaefthimiou, S.; Yianoulis, P.; Siokou, A., Effect of the Tungsten Oxidation States in the Thermal Coloration and Bleaching of Amorphous WO<sub>3</sub> Film. *Thin Solid Films* **2001**, 384, 298-306.
273. Altenau, J.; Pope, M.; Prados, R.; So, H., Models for Heteropoly Blues. Degrees of Valence Trapping in Vanadium(IV)- and Molybdenum(V)- Substituted Keggin Anions. *Inorg. Chem.* **1975**, 14, (2), 417-421.
274. Blundell, R.; Licence, P., Quaternary Ammonium and Phosphonium Based Ionic liquids: A Comparison of Common Anions. *Phys.Chem.Chem.Phys.* **2014**, 16, 15278-15288.
275. Beamson, G.; Briggs, D., *High Resolution XPS of Organic Polymers: The Scienta ESCA300 Database*. 1st ed.; Wiley: New York, 1992; p 306.
276. Castro, M. L. d.; Priego-Capote, F., Soxhlet extraction: Past and present panacea. *J. Chromatogr. A* **2010**, 1217, 2383–2389.
277. Nair, H.; Gatt, J.; Miller, J.; Baertsch, C., Mechanistic insights into the formation of acetaldehyde and diethyl ether from ethanol over supported VO<sub>x</sub>, MoO<sub>x</sub>, and WO<sub>x</sub> catalysts. *J. Catal.* **2011**, 279, 144–154.
278. Kim, T.; Burrows, A.; Kiely, C.; Wachs, I., Molecular/electronic structure–surface acidity relationships of model-supported tungsten oxide catalysts. *J. Catal.* **2007**, 246, 370–381.
279. Wachs, I.; Kim, T.; Ross, E., Catalysis science of the solid acidity of model supported tungsten oxide catalysts. *Catal. Today* **2006**, 116, 162–168.

280. A. Karuppasamy, A. S., Electron beam induced coloration and luminescence in layered structure of WO<sub>3</sub> thin films grown by pulsed dc magnetron sputtering. *Applied Physics Letters* **2007**, 101, 5.
281. Gutmann, S.; Wolak, M.; Conrad, M.; Beerbom, M.; Schlaf, R., Effect of ultraviolet and x-ray radiation on the work function of TiO<sub>2</sub> surfaces. *J. Appl. Phys.* **2010**, 107, 103705-103713.
282. Gregoratti, L.; Menten, T.; Locatelli, A.; Kiskinova, M., Beam-induced effects in soft X-ray photoelectron emission microscopy experiments. *J. Electron Spectrosc. Relat. Phenom.* **2008**, 170, 13–18.
283. Isaacs, E.; Platzman, P., Inelastic X-Ray Scattering in Condensed Matter Systems. *Physics Today* **1996**, 49, (2), 40-45.
284. Larson, P., X-ray induced photoelectron Cu<sub>2</sub>O and Cu<sub>2</sub>S thin films. *J. Electron Spectrosc. Relat. Phenom.* **1974**, 4, 213-218.
285. Feibelman, P.; Knotek, M., Reinterpretation of electron-stimulated desorption data from chemisorption systems. *Phys. Rev. B* **1978**, 18, (12), 6531-6539.
286. Kagwade, S.; Clayton, C.; Halada, G., Causes and prevention of photochemical reduction of hexavalent chromium during x-ray photoelectron spectroscopy. *Surf. Interface Anal.* **2001**, 31, 442–447.
287. Oku, M., Kinetics of photoreduction of Fe(III) in solid solution K<sub>3</sub>(Fe,M)(CN)<sub>6</sub> (where M is Cr, Co) during XPS measurement. *J. Electron. Spectrosc. Relat. Phenom.* **1994**, 67, 401-407.
288. Hammer, P.; Schiavetto, M.; Santos, F. d.; Benedetti, A.; Pulcinelli, S.; Santilli, C. V., Improvement of the corrosion resistance of polysiloxane hybrid coatings by cerium doping. *J. Non-Cryst. Solids* **2010**, 356, 2606–2612.
289. Gulino, A., Structural and electronic characterization of self-assembled molecular nanoarchitectures by X-ray photoelectron spectroscopy. *Anal. Bioanal. Chem.* **2013**, 405, 1479–1495.
290. Chidambaram, D.; Halada, G.; Clayton, C., Development of a technique to prevent radiation damage of chromate conversion coatings during X-ray photoelectron spectroscopic analysis. *Appl. Surf. Sci.* **2001**, 181, 283-295.

291. Mercier-Bion, F.; Drot, R.; Ehrhardt, J.; Lambert, J.; Roques, J.; Simoni, E., X-ray photoreduction of U(VI)-bearing compounds. *Surf. Interface Anal.* **2011**, *43*, 777–783.
292. Skinner, W.; Prestidge, C.; Smart, R., Irradiation effects during XPS studies of Cu(II) activation of zinc sulphide. *Surf. Interface Anal.* **1996**, *24*, 620–626.
293. Yang, J.; Regier, T.; Dynes, J.; Wang, J.; Shi, J.; Peak, D.; Hu, T.; Chen, Y.; Tse, J.; Y. Zhao, Soft X-ray induced photoreduction of organic Cu(II) compounds probed by X-ray absorption near-edge (XANES) spectroscopy. *Anal. Chem.* **2011**, *83*, 7856–7862.
294. Fernandes, D.; Julião, D.; Pereira, C.; Ananias, D.; Balula, S.; Freire, C., Hybrid layer-by-layer films based on lanthanide-bridged silicotungstates and poly(ethylenimine). *Colloids Surf. A: Physicochem. Eng. Aspects* **2012**, *415*, 302–309.
295. Karadas, F.; Ertas, G.; Ozkaraoglu, E.; Suzer, S., X-ray-Induced Production of Gold Nanoparticles on a SiO<sub>2</sub>/Si System and in a Poly(methyl methacrylate) Matrix. *Langmuir* **2005**, *21*, 437–442.
296. Tanielian, C.; Schweitzer, C.; Seghrouchni, R.; Esch, M.; Mechin, R., Polyoxometalate sensitization in mechanistic studies of photochemical reactions: The decatungstate anion as a reference sensitizer for photoinduced free radical oxygenations of organic compounds. *Photochem. Photobiol. Sci.* **2003**, *2*, 297–305.
297. Feldman, V.; Zezin, A.; Abramchuk, S.; Zezina, E., X-ray Induced Formation of Metal Nanoparticles from Interpolyelectrolyte Complexes with Copper and Silver Ions: The Radiation-Chemical Contrast. *J. Phys. Chem. C* **2013**, *117*, 7286–7293.
298. Papparazzo, E., XPS Studies of Damage Induced by X-ray Irradiation on CeO<sub>2</sub> Surfaces. *Surf. Sci.* **1990**, *234*, L253–L258.
299. Chatten, R.; Chadwick, A.; Rougier, A.; Lindan, P., The Oxygen Vacancy in Crystal Phases of WO<sub>3</sub>. *J. Phys. Chem. B* **2005**, *109*, 3146–3156.
300. Wang, F.; Valentin, C.; Pacchioni, G., Semiconductor-to-Metal transition in WO<sub>3-x</sub>: Nature of the Oxygen Vacancy. *Phys. Rev. B: Condens. Matter* **2011**, *84*, 073103–073105.
301. George, S.; Fu, J.; Guo, Y.; Drury, O.; Friedrich, S.; Rauchfuss, T.; Volkers, P.; Peters, J.; Scott, V.; Brown, S.; Thomas, C.; Cramer, S., X-ray photochemistry in iron complexes from Fe(0) to Fe(IV) – Can a bug become a feature? *Inorg. Chim. Acta* **2008**, *361*, 1157–1165.

302. Plackowski, C.; Hampton, M.; Nguyen, A.; Bruckard, W., The effects of X-ray irradiation and temperature on the formation and stability of chemical species on enargite surfaces during XPS. *Miner. Eng.* **2013**, 45, 59–66.
303. Iqbal, S.; Shozi, M.; Morgan, D., X-ray induced reduction of rhenium salts and supported oxide catalysts. *Surf. Interface Anal.* **2017**, 49, 223–226.
304. Paparazzo, E.; Ingo, G.; Zacchetti, N., X-ray induced reduction effects at CeO<sub>2</sub> surfaces: An x-ray photoelectron spectroscopy study. *J. Vac. Sci. Technol. A* **1991**, 9, 1416-1420.
305. Wang, J.; Morin, C.; Li, L.; Hitchcock, A.; Scholl, A.; Doran, A., Radiation damage in soft X-ray microscopy. *J. Electron. Spectrosc. Relat. Phenom.* **2009**, 170, 25–36.
306. Hammer, P.; Schiavetto, M.; Santos, F. d.; Benedetti, A.; Pulcinelli, S.; Santilli, C., Improvement of the corrosion resistance of polysiloxane hybrid coatings by cerium doping. *J. Non-Cryst. Solids* **2010**, 356, 2606–2612.
307. Iqbal, S.; Shozi, M.; Morgan, D. J., X-ray induced reduction of rhenium salts and supported oxide catalysts. *Surf. Interface Anal.* **2017**, 49, 223–226.
308. Suzer, S., XPS investigation of X-ray-induced reduction of metal ions. *Appl. Spectrosc.* **2000**, 54, (11), 1716-1718.
309. Lozzia, L.; Ottaviano, L.; Passacantando, M.; Santuccia, S.; Cantalini, C., The Influence of Air and Vacuum Thermal Treatments on the NO<sub>2</sub> Gas Sensitivity of WO Thin Films Prepared by Thermal Evaporation. *Thin Solid Films* **2001**, 391, 224-228.
310. Ottaviano, L.; Bussolotti, F.; Lozzi, L.; Passacantando, M.; Rosa, S. L.; Santucci, S., Core level and valence band investigation of WO<sub>3</sub> thin films with synchrotron radiation. *Thin Solid Films* **2003**, 436, 9–16.
311. Gilleta, M.; Aguirra, K.; Lemire, C.; Gilleta, E.; Schierbaum, K., The structure and electrical conductivity of vacuum-annealed WO<sub>3</sub> thin films. *Thin Solid Films* **2004**, 467, 239–246.